UNIVERSITY OF CALIFONRIA

Los Angeles

# Constraints on Dual Clumped Isotope
# Equilibrium and Kinetic Effects

A dissertation submitted in partial satisfaction of the

requirements for the degree

Doctor of Philosophy in Geochemistry

by

Jamie Kaaren Lucarelli

2022

# ABSTRACT OF THE DISSERTATION

# Constraints on Dual Clumped Isotope Equilibrium and Kinetic Effects

By

Jamie Kaaren Lucarelli
Doctor of Philosophy in Geochemistry
University of California, Los Angeles, 2022
Professor Aradhna K. Tripati, Co-Chair
Professor Robert Eagle Tripati, Co-Chair

A powerful tool for reconstructing past temperatures is based on the extent of carbonate ions in carbonate minerals with more than one heavy isotope substitution, termed carbonate clumped isotopes. The use of the clumped isotope thermometer assumes that the mineral formed under isotopic equilibrium conditions, however, some carbonate minerals can form from dissolved inorganic carbon pools that are not equilibrated. Here, we use dual clumped isotope measurements of mass 47 and mass 48 ($^{13}C^{18}O^{16}O$ - $\Delta_{47}$; $^{12}C^{18}O^{18}O$ - $\Delta_{48}$) $CO_2$ from gas liberated by acid digestion of carbonate minerals to constrain equilibrium clumped isotope relationships and kinetic isotope effects. In one manuscript, we present results for widely used laboratory standards that lay a strong foundation for the measurement and application of paired

$\Delta_{47}$ and $\Delta_{48}$. In a second manuscript, the results from controlled inorganic calcite precipitation experiments constrain kinetic isotope effects in $\Delta_{47}$ and $\Delta_{48}$ from hydration and hydroxylation and compared to theory, and enzymatic effects are studied. Non-linear mixing effects in $\Delta_{47}$ and $\Delta_{48}$ are also determined using experiments and theory. In a third manuscript, we report $\Delta_{47}$ and $\Delta_{48}$ for amorphous calcium magnesium carbonates and transformation products, and show they are distinct from mineral equilibrium. We propose a new mechanism for disequilibrium clumped and oxygen isotope values in carbonate minerals that precipitate from an amorphous calcium carbonate precursor. Results indicate that the dissolution of an amorphous precursor may cause disequilibrium in the dissolved inorganic pool during transformation to a crystalline phase, that can impact final mineral dual clumped isotope and oxygen isotope values.

The dissertation of Jamie Kaaren Lucarelli is approved.

Abby Kavner

Tina Irene Treude

Robert Eagle Tripati, Committee Co-Chair

Aradhna K. Tripati, Committee Co-Chair

University of California, Los Angeles

2022

# DEDICATION

To Steve, for his advice, patience, faith in me, and because he always understood.

To our beautiful babies, Jameson and Juliet, for giving me endless love, motivation, and inspiration.

Special thanks to Kristen, for lifelong friendship and unwavering belief that I could complete this.

## TABLE OF CONTENTS

SUPPLEMENTARY INFORMATION

## LIST OF FIGURES

### CHAPTER 1

Chapter 1 Supplementary Figures

Chapter 1 Appendix Figures

### CHAPTER 2

Chapter 2 Appendix Figures

**CHAPTER 3**

Chapter 3 Supplementary Figures

# LIST OF TABLES

## CHAPTER 1

## CHAPTER 2

## CHAPTER 3

Chapter 3 Supplementary Tables

# ACKNOWLEDGEMENTS

I would like to acknowledge my advisor, Aradhna Tripati, for her constant support of my efforts, which started during my undergraduate degree. My life has been forever impacted by her mentorship. She has supported and advocated for me in real ways that have made my graduate education possible and given me an example to follow for how to advocate for myself and others in significant ways. Her fair and honest feedback has made me grow as a person and scientist through iterative self-reflection and hard work. I am deeply thankful for the scientific and social knowledge I have gained during my time as a graduate student, as I am a better version of myself than I thought was possible.

# VITA

University of California, Los Angeles, 2018

M.S. Geochemistry

University of California, Los Angeles, 2016

B.S., Chemistry

Los Angeles City College, 2014

Completed coursework necessary for transfer

## PUBLICATIONS

**Jamie Lucarelli**, Bettina Purgstaller, Martin Dietzel, Robert Eagle, Aradhna Tripati (in review). Paired $\Delta_{47}$ and $\Delta_{48}$ analyses and model calculations constrain equilibrium, experimentally-manipulated kinetic isotope effects, and mixing effects in calcite, *Geochimica et Cosmochimica Acta.*

**Jamie Lucarelli,** Hannah Carroll, Ben M. Elliot, Robert Eagle, Aradhna Tripati (in preparation). Equilibrated gas and carbonate standard-derived paired clumped isotope ($\Delta_{47}$ and $\Delta_{48}$) values on the absolute reference frame, *Geochemistry, Geophysics, Geosystems.*

**Jamie Lucarelli**, Bettina Purgstaller, Robert Ulrich, Zeeshan Parvez, Albrecht Leis, Katja Goetschl, Robert Eagle, Martin Dietzel, Aradhna Tripati (in preparation). Dual clumped isotope data for amorphous carbonates and transformation products reveal a novel mechanism for nonequilibrium effects, *Proceedings of the National Academy of Sciences.*

**Jamie Lucarelli**, Yama Dixit, Maxence Guillermic, Whitney Doss, Ryan Dill, Fengming Chang, Aradhna Tripati (in preparation), Evidence for past dramatic changes in Amazon outflow, *Science Advances.*

Deepshikha Upadhyay, **Jamie Lucarelli**, Alexandrea Arnold, Randy Flores, Hayley Bricker, Robert N. Ulrich, Gregory Jesmok, Lauren Santi, William Defliese, Robert A. Eagle, Hannah M. Carroll, Jesse Bloom Bateman, Victoria Petryshyn, Sean J. Loyd, Jianwu Tang, Antra Priyadarshi, Ben Elliott, Aradhna Tripati (2021). Carbonate clumped isotope analysis ($\Delta_{47}$) of 21 carbonate standards determined via gas source isotope ratio mass spectrometry on four instrumental configurations using carbonate-based standardization and multi-year datasets, *Rapid Communications in Mass Spectrometry*. doi.org/10.1002/rcm.9143.

Stefano Bernasconi, Mathieu Daeron, Kristin Bergmann, Magali Bonifacie, Nele Meckler, Hagit Affek, Noah Anderson, David Bajnai, Eugeni Barkan, Emily Beverly, Dominique Blamart, Landon Burgener, Damien Calmels, Carine Chaduteau, Mathieu Clog, Brett Davidheiser-Kroll, Amelia Davies, Florian Dux, John Eiler, Ben Elliott, Anne Fetrow, Jens Fiebig, Samuel Goldberg, Michael Hermosos, Katharine Huntington, Ethan Hyland, Miquela Ingalls, Madalina Jaggi, Cedric John, Adam Jost, Sarah Katz, Julia Kelson, Tobias Kluge, Ilja Kocken, Amzad Laskar, Thomas Leutert, Mao-Chang Liang, **Jamie Lucarelli**, Tyler Mackey, Xavier Mangenot, Niklas Meinicke, Sevasti Modestou, Inigo Muller, Sean Murray, Ashling Neary, Natalie Packard, Benjamin Passey, Elise Pelletier, Sierra Petersen, Alison Piaskecki, Andrew Schauer, Kathryn Snell, Peter Swart, Aradhna Tripati, Deepshikha Upadhyay, Torsten Bennemann, Ian Winkelstern, Drake Yarianm Naohiro Yoshidam Naizhong Zhang, Martin Ziegler (2021). InterCarb: A community effort to improve inter-laboratory standardization of the carbonate clumped isotope thermometer using carbonate standards, *Geochemistry, Geophysics, Geosystems*. doi.org/10.1029/2020GC009588.

Zeeshan Parvez, **Jamie Lucarelli**, Ben Elliott, Robert Eagle, John N. Christensen, Aradhna Tripati (in preparation). Using clumped isotope systems and modeling to study dissolved inorganic carbon transformation in natural high pH waters related to serpentinization, *Proceedings of the National Academy of Sciences.*

Robert N. Ulrich, **Jamie K. Lucarelli**, Rachel Han, Julia Campbell, Abbas Hakim, Shayleen Singh, Justin B. Ries, Aradhna Tripati, and Robert A. Eagle (in preparation). Coupled $\Delta_{47}$–$\Delta_{48}$ clumped isotope analysis indicates origins of kinetic isotope effects in cultured biogenic marine carbonates, *Geochimica et Cosmochimica Acta*.

# INTRODUCTION

Carbonate clumped isotope thermometry is a powerful tool for reconstructing temperature. Developed in the early 2000s, this technique studies the distributions of naturally occurring carbonate isotopologues that contain more than one rare isotope (Wang et al., 2004; Ghosh et al., 2006; Schauble et al., 2006). Mass spectrometry is used to determine the extent to which $^{13}C$ and $^{18}O$, and two $^{18}O$ atoms are bonded within carbonate ion groups within a carbonate mineral (Eiler and Schauble, 2004; Ghosh et al., 2006). A unique attribute of carbonate clumped isotope thermometry is it only depends on formation temperature and does not depend on the isotopic composition of the precipitation fluid, as with oxygen isotope-based ($\delta^{18}O$) temperature reconstructions. It has been shown to have wide ranging applications, including terrestrial paleothermometry (i.e., Passey et al., 2010; Eagle et al., 2013; Hren et al., 2013; Santi et al., 2020), ocean temperatures (i.e., Tripati et al., 2010, 2014; Leutert et al., 2019; Modestou et al., 2020), tectonic uplift (i.e., Huntington and Lechler, 2015; Wang et al., 2021), and extinct vertebrate body temperature (Eagle et al., 2011).

A potential caveat to carbonate clumped isotope thermometry is that the relationship to formation temperature depends on the mineral precipitating at isotopic equilibrium conditions. Previous studies have indicated the decoupling of clumped isotope values and temperature from kinetic isotope effects that result from hydration and hydroxylation reactions in abiotic carbonate minerals (i.e., Affek et al., 2008, Kluge et al., 2014; Meckler et al., 2015; Falk et al., 2016) and carbonate minerals found in wide ranging taxa (i.e., Saenger et al., 2012; Tripati et al., 2015; Spooner et al., 2016;

Bajnai et al., 2020; Davies and John, 2019). The enzyme carbonic anhydrase catalyzes the hydration reaction, and is present in most organisms at varying concentrations, yet the effect of carbonic anhydrase on clumped isotope values has only begun to be examined (Tripati et al., 2015) and has not been systematically explored. Additionally, disequilibrium clumped isotope values have been observed in organisms such as corals (i.e., Tripati et al., 2015; Spooner et al., 2016) and mollusks (Eagle et al., 2013; Henkes et al., 2013) that precipitate their calcium carbonate skeleton from an amorphous precursor.

The dual clumped isotope measurement of the most abundant *m/z* 47 ($^{13}C^{18}O^{16}O$ - $\Delta_{47}$) and *m/z* 48 ($^{12}C^{18}O^{18}O$ - $\Delta_{48}$) isotopologues can be used to determine if a carbonate mineral has precipitated at quasi-equilibrium (Tripati et al., 2015; Bajnai et al., 2020). Further, recent work has suggested that paleotemperatures can be determined from carbonates exhibiting kinetic biases using characteristic $\Delta_{47}$-$\Delta_{48}$ slopes (Bajnai et al., 2020); however, there are no experimental constraints on kinetic $\Delta_{47}$- $\Delta_{48}$ slopes for hydration and hydroxylation.

In this dissertation, equilibrium and kinetic isotope relationships between $\Delta_{47}$-$\Delta_{48}$, $\Delta_{47}$ -$\delta^{18}O$, and $\Delta_{48}$ -$\delta^{18}O$ in carbonate minerals are explored using experimental data and modeling. In Chapter 1, we determined $\Delta_{47}$ and $\Delta_{48}$ values for a suite of carbonate standards and samples. The values were compared to theoretical equilibrium values, previously published values, and values for calcite that was precipitated at quasi-equilibrium to further constrain the equilibrium $\Delta_{47}$-$\Delta_{48}$ regression. In Chapter 2, calcite was precipitated under controlled temperature and pH with and without carbonic anhydrase to constrain equilibrium isotope values and kinetic slopes for hydration and hydroxylation. We used modeling to explore and the effect of precipitation rate on the magnitude of inherited kinetic clumped and oxygen isotope values. Mixing experiments using two isotopically distinct endmembers were performed and compared to nonlinear mixing model results to constrain mixing effects in the dual clumped isotope system. In Chapter 3, we examined the potential isotopic effects on high Magnesium calcite that was precipitated from an amorphous precursor. We also used modeling to simulate the extent of disequilibrium in the dissolved inorganic carbon (DIC) pool that would occur from the dissolution of the amorphous precursor during transformation into a crystalline product. A nonlinear mixing model was used to simulate mixing effects from the crystalline product forming from an evolving DIC pool.

## REFERENCES

Affek, H.P., Bar-Matthews, M., Ayalon, A., Matthews, A. and Eiler, J.M., 2008. Glacial/interglacial temperature variations in Soreq cave speleothems as recorded by 'clumped isotope'thermometry. *Geochimica et Cosmochimica Acta*, *72*(22), pp.5351-5360.

Bajnai, D., Guo, W., Spötl, C., Coplen, T.B., Methner, K., Löffler, N., Krsnik, E., Gischler, E., Hansen, M., Henkel, D. and Price, G.D., 2020. Dual clumped isotope thermometry resolves kinetic biases in carbonate formation temperatures. *nature communications*, *11*(1), pp.1-9.

Davies, A.J. and John, C.M., 2019. The clumped (13C18O) isotope composition of echinoid calcite: Further evidence for "vital effects" in the clumped isotope proxy. *Geochimica et Cosmochimica Acta*, *245*, pp.172-189.

Eagle, R.A., Schauble, E.A., Tripati, A.K., Tütken, T., Hulbert, R.C. and Eiler, J.M., 2010. Body temperatures of modern and extinct vertebrates from 13C-18O bond abundances in bioapatite. *Proceedings of the National Academy of Sciences*, *107*(23), pp.10377-10382.

Eagle, R.A., Eiler, J.M., Tripati, A.K., Ries, J.B., Freitas, P.S., Hiebenthal, C., Wanamaker Jr, A.D., Taviani, M., Elliot, M., Marenssi, S. and Nakamura, K., 2013. The influence of temperature and seawater carbonate saturation state on 13 C–18 O bond ordering in bivalve mollusks. *Biogeosciences*, *10*(7), pp.4591-4606.

Falk, E.S., Guo, W., Paukert, A.N., Matter, J.M., Mervine, E.M. and Kelemen, P.B., 2016. Controls on the stable isotope compositions of travertine from hyperalkaline springs in Oman: Insights from clumped isotope measurements. *Geochimica et Cosmochimica Acta*, *192*, pp.1-28.

Ghosh, P., Adkins, J., Affek, H., Balta, B., Guo, W., Schauble, E.A., Schrag, D. and Eiler, J.M., 2006. 13C–18O bonds in carbonate minerals: a new kind of paleothermometer. *Geochimica et Cosmochimica Acta*, *70*(6), pp.1439-1456.

Henkes, G.A., Passey, B.H., Wanamaker Jr, A.D., Grossman, E.L., Ambrose Jr, W.G. and Carroll, M.L., 2013. Carbonate clumped isotope compositions of modern marine mollusk and brachiopod shells. *Geochimica et Cosmochimica Acta*, *106*, pp.307-325.

Hren, M.T., Sheldon, N.D., Grimes, S.T., Collinson, M.E., Hooker, J.J., Bugler, M. and Lohmann, K.C., 2013. Terrestrial cooling in Northern Europe during the Eocene–Oligocene transition. *Proceedings of the National Academy of Sciences*, *110*(19), pp.7562-7567.

Huntington, K.W. and Lechler, A.R., 2015. Carbonate clumped isotope thermometry in continental tectonics. *Tectonophysics*, *647*, pp.1-20.

Kluge, T., Affek, H.P., Zhang, Y.G., Dublyansky, Y., Spötl, C., Immenhauser, A. and Richter, D.K., 2014. Clumped isotope thermometry of cryogenic cave carbonates. *Geochimica et Cosmochimica Acta*, *126*, pp.541-554.

Leutert, T.J., Sexton, P.F., Tripati, A., Piasecki, A., Ho, S.L. and Meckler, A.N., 2019. Sensitivity of clumped isotope temperatures in fossil benthic and planktic foraminifera to diagenetic alteration. *Geochimica et Cosmochimica Acta*, *257*, pp.354-372.

Meckler, A.N., Affolter, S., Dublyansky, Y.V., Krüger, Y., Vogel, N., Bernasconi, S.M., Frenz, M., Kipfer, R., Leuenberger, M., Spötl, C. and Carolin, S., 2015. Glacial–interglacial temperature change in the tropical West Pacific: A comparison of stalagmite-based paleo-thermometers. *Quaternary Science Reviews*, *127*, pp.90-116.

Modestou, S.E., Leutert, T.J., Fernandez, A., Lear, C.H. and Meckler, A.N., 2020. Warm middle Miocene Indian Ocean bottom water temperatures: Comparison of clumped isotope and Mg/Ca-based estimates. *Paleoceanography and Paleoclimatology*, *35*(11), p.e2020PA003927.

Passey, B.H., Levin, N.E., Cerling, T.E., Brown, F.H. and Eiler, J.M., 2010. High-temperature environments of human evolution in East Africa based on bond ordering in paleosol carbonates. *Proceedings of the National Academy of Sciences*, *107*(25), pp.11245-11249.

Saenger, C., Affek, H.P., Felis, T., Thiagarajan, N., Lough, J.M. and Holcomb, M., 2012. Carbonate clumped isotope variability in shallow water corals: Temperature dependence and growth-related vital effects. *Geochimica et Cosmochimica Acta*, *99*, pp.224-242.

Santi, L.M., Arnold, A.J., Ibarra, D.E., Whicker, C.A., Mering, J.A., Lomarda, R.B., Lora, J.M. and Tripati, A., 2020. Clumped isotope constraints on changes in latest Pleistocene hydroclimate in the northwestern Great Basin: Lake Surprise, California. *GSA Bulletin*, *132*(11-12), pp.2669-2683.

Schauble, E.A., Ghosh, P. and Eiler, J.M., 2006. Preferential formation of 13C–18O bonds in carbonate minerals, estimated using first-principles lattice dynamics. *Geochimica et Cosmochimica Acta*, *70*(10), pp.2510-2529.

Spooner, P.T., Guo, W., Robinson, L.F., Thiagarajan, N., Hendry, K.R., Rosenheim, B.E. and Leng, M.J., 2016. Clumped isotope composition of cold-water corals: A role for vital effects?. *Geochimica et Cosmochimica Acta*, *179*, pp.123-141.

Tripati, A.K., Eagle, R.A., Thiagarajan, N., Gagnon, A.C., Bauch, H., Halloran, P.R. and Eiler, J.M., 2010. 13C–18O isotope signatures and ‘clumped isotope’thermometry in foraminifera and coccoliths. *Geochimica et cosmochimica acta*, *74*(20), pp.5697-5717.

Tripati, A.K., Sahany, S., Pittman, D., Eagle, R.A., Neelin, J.D., Mitchell, J.L. and Beaufort, L., 2014. Modern and glacial tropical snowlines controlled by sea surface temperature and atmospheric mixing. *Nature Geoscience*, *7*(3), pp.205-209.

Wang, Z., Schauble, E.A. and Eiler, J.M., 2004. Equilibrium thermodynamics of multiply substituted isotopologues of molecular gases. *Geochimica et Cosmochimica Acta*, *68*(23), pp.4779-4797

Wang, Y., Passey, B., Roy, R., Deng, T., Jiang, S., Hannold, C., Wang, X., Lochner, E. and Tripati, A., 2021. Clumped isotope thermometry of modern and fossil snail shells from the Himalayan-Tibetan Plateau: Implications for paleoclimate and paleoelevation reconstructions. *GSA Bulletin*, *133*(7-8), pp.1370-1380.

# CHAPTER 1

## Equilibrated gas and carbonate standard-derived paired clumped isotope ($\Delta_{47}$ and $\Delta_{48}$) values on the absolute reference frame

Jamie K. Lucarelli[1], Hannah M. Carroll[1], Ben M. Elliott[1], Tyler B. Coplen[2], Robert A. Eagle[1], Aradhna Tripati[1]

[1]Department of Earth, Planetary, and Space Sciences, Department of Atmospheric and Oceanic Sciences, Institute of the Environment and Sustainability, Center for Diverse Leadership in Science, UCLA, Los Angeles, CA 90095 USA.
[2]US Geological Survey, 12201 Sunrise Valley Drive, Reston, VA, 20192, USA
Correspondence to: jklucarelli@gmail.com and atripati@g.ucla.edu

**Rationale:** Carbonate clumped isotope geochemistry has primarily focused on mass spectrometric determination of *m/z* 47 $CO_2$ for geothermometry, but theoretical calculations and recent experiments indicate paired analysis of the *m/z* 47 ($^{13}C^{18}O^{16}O$) and *m/z* 48 ($^{12}C^{18}O^{18}O$) isotopologues (referred to as $\Delta_{47}$ and $\Delta_{48}$) can be used to study non-equilibrium isotope fractionations and refine temperature estimates. We utilize a multi-year and multi-instrument dataset to constrain $\Delta_{47}$ and $\Delta_{48}$ values for 27 samples, including standards and Devils Hole cave calcite, and study equilibrium $\Delta_{47}$-$\Delta_{48}$, $\Delta_{47}$-temperature, and $\Delta_{48}$-temperature relationships.

**Methods:** A total of 5,465 $\Delta_{47}$ and 3,400 $\Delta_{48}$ measurements of carbonates, and 183 $\Delta_{47}$

and 195 $\Delta_{48}$ measurements of gas standards from 2015-2021 from multiple mass spectrometers were used. We compare results to previously published findings.

**Results:** We report $\Delta_{47}$ and $\Delta_{48}$ values for 27 carbonates. We provide further experimental constraints on the equilibrium relationship between $\Delta_{47}$ and $\Delta_{48}$. We report $\Delta_{47}$ and $\Delta_{48}$ relationships with temperature using a combination of theory and experimental regression-form acid digestion fractionation factors, $\Delta^*_{63-47}$ and $\Delta^*_{64-48}$.

**Conclusions:** This large dataset provides $\Delta_{48}$ values of carbonate standards for use in carbonate standard-based standardization. A robust $\Delta_{47}$-$\Delta_{48}$ equilibrium regression was determined with data presented here and from previously published datasets. Regressions for $\Delta_{47}$ and $\Delta_{48}$ relationships with temperature are also presented.

## 1. INTRODUCTION

Equilibrium constants for internal isotope exchange reactions in carbonate minerals are directly related to their formation temperature.[1,2] This temperature dependence is the basis for carbonate clumped isotope thermometry, a tool for paleotemperature reconstruction in the geosciences. For minerals that form in isotopic equilibrium, the frequency with which rare, heavy isotopes in carbonate minerals are bonded to each other (instead of bonded to much more common light isotopes) relative to a stochastic (random) distribution is proportional to precipitation temperature.

There are multiple clumped isotopologues containing paired heavy isotopes in carbonate minerals that can potentially be used for geothermometry. The abundance of the dominant *m/z* 63 isotopologue ($^{13}C^{18}O^{16}O_2$) forms the basis of the most widely used thermometer. The acid digestion of minerals containing carbonate ion groups with *m/z* of 63 yields *m/z* 47 $CO_2$, which can then be measured by isotope ratio mass spectrometry.[1] Theory predicted that the lower abundance *m/z* 48 $CO_2$ isotopologue derived from acid digestion of *m/z* 64 ($^{12}C^{18}O_2{}^{16}O$) carbonate ion groups in equilibrium precipitates could be used for geothermometry [1,3–6] and this has recently been confirmed through experimentation.[7–10]

The abundance of the $^{13}C^{18}O^{16}O$ and $^{12}C^{18}O^{18}O$ isotopologues is denoted with $\Delta_{47}$ and $\Delta_{48}$ notation.[11] These are defined as:

$$\Delta_{47} = [(R47_{\text{sample}}/R47_{\text{stochastic}} - 1) \qquad \text{Equation 1}$$

$$\Delta_{48} = (R48_{\text{sample}}/R48_{\text{stochastic}} - 1) \qquad \text{Equation 2}$$

where $Ri_{\text{sample}}$ is the measured ratio of i/44 $CO_2$ isotopologues in the sample, $Ri_{\text{stochastic}}$ is the ratio of i/44 $CO_2$ isotopologues that would be expected in a random distribution, and $\Delta_{47}$ and $\Delta_{48}$ values are typically multiplied by a factor of 1000 and given in permil (‰).[2,12] The most abundant *m/z* 48 $CO_2$ isotopologue ($^{12}C^{18}O^{18}O$) has two $^{18}O$ substitutions and is therefore in extremely low abundance at 4.1 ppm in air, which is an order of magnitude lower than *m/z* 47 isotopologues (45 ppm).[1] The minor *m/z* 48 $CO_2$ isotopologue ($^{13}C^{18}O^{17}O$) has an abundance of 16.7 ppb.[1]

The precise measurement of $\Delta_{47}$ was enabled by modification of the Thermo MAT 253, specially configured with *m/z* 47-49 Faraday cups and digestion and purification methods for carbonate minerals.[1,11] On this instrument, *m/z* 48 isotopologues were used only to screen for contaminants. Measurements of $\Delta_{48}$ have recently emerged as a tool for the study of equilibrium and kinetic isotope effects due to the use of $10^{13}$ Ω resistors for *m/z* 47-49 Faraday cups in the Thermo MAT 253 Plus[7–10], and secondary electron suppression in the Nu Perspective IS. These advances contribute to increased accuracy and precision for determination of $\Delta_{48}$ values, and paired $\Delta_{47}$ and $\Delta_{48}$ values on the absolute reference frame.

A unique attribute of carbonate clumped isotope thermometry based on $\Delta_{47}$ or $\Delta_{48}$ is that it does not depend on the bulk oxygen isotope composition ($\delta^{18}$O) of the water the carbonate precipitated from[1], unlike the more widely used oxygen isotope thermometer[13]. $\Delta_{47}$ measurements have been used for the reconstruction of numerous paleo-environmental parameters, including but not limited to land[14] and ocean[5,15] paleotemperatures, paleoelevation[16,17], and dinosaur body temperature[18], while simultaneously estimating water $\delta^{18}$O. Previous research has shown that kinetic isotope effects observed in abiotic and biogenic carbonates, including speleothems[19,20] and coral[8,21–23], may affect the accuracy of $\Delta_{47}$-based temperature reconstructions. However, the paired analysis of $\Delta_{47}$ and $\Delta_{48}$ has been shown by theory[2,4,5,24,25] and experimentation[7–10] to have a characteristic equilibrium relationship to temperature which may be used to identify and study kinetic effects in carbonates, if sufficiently accurate and precise measurements can be made.

Several studies have proposed the use of new methods to advance the consistency of measurements between laboratories and have improved the accuracy and precision of $\Delta_{47}$ determinations by mass spectrometry. Interlaboratory reproducibility of $\Delta_{47}$ values was advanced by using accurately determined carbonate standard values that are anchored to the absolute reference frame, using a reference frame constructed using primary gas standards, secondary carbonate standards, or a mixture of gas and carbonate standards, detailed by Dennis et al.[26], allowing for interlaboratory standardization. Recent work from Bernasconi et al.[27] has proposed nominal carbonate standard $\Delta_{47}$ values and the use of carbonate standards for standardization in the 90 °C reference frame. These advances form the foundation for assessing whether carbonate standardization can be used to yield $\Delta_{48}$ values, and paired $\Delta_{47}$ and $\Delta_{48}$ values, on the absolute reference frame that are intercomparable between instruments.

Here, we utilize large datasets collected over multiple years on multiple instruments for this purpose. Due to the low abundance of *m/z* 48 $CO_2$ isotopologues and potential for analytical error, the development of robust standard values is critical in ensuring accurate determination of unknown sample $\Delta_{48}$ values. Given the size of the dataset and the use of multiple instruments, we assessed if there were standardized methods of outlier analysis. In the literature, for outlier identification, one group of publications used outlier tests. Zaarur et al.[28] used a Peirce outlier test to identify and remove replicate $\Delta_{47}$, $\delta^{18}O$, and $\delta^{13}C$ values that were statistical outliers, resulting in the exclusion of ~2% of data. They report this affected $\Delta_{47}$ in the third decimal place. Burgener et al.[29] used this same test to determine one sample $\Delta_{47}$ value was an outlier relative to the other samples in the dataset. Peral et al.[30] used Grubbs' outlier test to show that a $\Delta_{47}$ value for a foraminifera sample was an outlier when compared to the rest of their sample set. A second group of publications have used absolute deviations from mean values as cutoffs. Meckler et al.[31] excluded standard replicates with an offset greater than ± 0.03 ‰ from the mean value in each run. Upadhyay et al.[32] excluded replicates with an offset greater than ± 0.075 ‰ from the mean value. A third group of publications uses ancillary data. Tripati et al.[5] used $\Delta_{48}$ values of > 1 per mil ($\Delta_{48}$ excess) to be potentially indicative of contamination, and screened data if replicate level $\delta^{13}C$ or $\delta^{18}O$ values differed from the population mean by more than 3σ. Tripati et al.[33] used $\Delta_{48}$ excess, and also used a Q-test (which identifies outliers at a 5σ level), for data quality assurance. Bernasconi et al.[27] worked with data that was provided by laboratories, based on each laboratory's own criteria for quality assurance to produce publication-grade results.

Here, we used both equilibrated gas and carbonate-based standardization to report the isotopic composition of 27 carbonates, including standards and 4 Devils Hole calcite samples[34,35], determined on different mass spectrometer configurations over multiple years. We use this data and theory to explore clumped isotope equilibrium relationships. We also report statistical methods for data processing of large datasets. We compared use of a 3σ and 5σ cutoff for outlier exclusion. We determine regression-form acid digestion fractionation factors for the phosphoric acid digestion of *m/z* 63 and *m/z* 64 $CO_3^{2-}$ to *m/z* 47 and *m/z* 48 $CO_2$, respectively.

## 2. METHODS

### 2.1 Carbonates analyzed

In total, 27 different carbonates were analyzed for clumped and bulk isotope compositions on mass spectrometers in the Tripati Lab at University of California, Los Angeles. Table 1 contains a description of the mineralogy and origin of all carbonates, modified from Upadhyay et al.[32] These materials were chosen for analysis because many of them are standards used widely among clumped isotope laboratories, such as the ETH standards and Carrara Marble. Others are used commonly in a certain region or country, such as ISTB-1, TB-1, and TB-2, which are clumped isotope standards from the China University of Geosciences. Additionally, this suite of samples encompasses numerous carbonate types, including biogenic materials, and carbonates of different mineralogies. Some of the materials are presumed to have near equilibrium clumped isotope values, such as Devils Hole mammillary calcite, ETH-1, and ETH-2. Many also have a large number of analyses (n > 50) on one or multiple instruments that can be used to provide robust standard values for $\Delta_{47}$ and $\Delta_{48}$ measurements on the absolute reference frame.

### 2.2 Devils Hole calcite

We analyzed four Devils Hole (Amargosa Desert, Nevada) mammillary calcite samples from core DH-2 for paired $\Delta_{47}$ and $\Delta_{48}$ values, including DH-10 (172 ± 4 ka), DH-11 (163 ± 5 ka), DH-12 (57 ± 5 ka), and DH-13 (151 ± 4 ka)[34], that previously were measured for $\Delta_{47}$ in Tripati et al.[5] The samples were re-analyzed on Nu Perspective mass spectrometers. Devils Hole calcite is assumed to have precipitated near isotopic equilibrium due to an extremely slow precipitation rate (0.1-0.8 μm year$^{-1}$) in water with a low calcite saturation index (0.16-0.21).[35,36] Devils Hole is thought to have had a stable temperature of 33.7 (±0.8) °C throughout the Holocene.[34–37]

### 2.3 Instrumentation

Standards and samples were analyzed on 3 mass spectrometers using 5 configurations (Table 2), including Nu Perspective-EG, Nu Perspective-1, Nu Perspective-1a, Nu-Perspective-2, and MAT 253. Nu Perspective-EG, Nu Perspective-1, and Nu Perspective-1a use the same mass spectrometer with differences in the acid digestion system, ion beam intensity, and integration time. Nu Perspective-EG is the only configuration that analyzed equilibrated gases. On both the MAT 253 and Nu Perspective mass spectrometers, the detectors for *m/z* 44 through 46 are registered through $3 \times 10^8$, $3 \times 10^{10}$, and $10^{11}$ Ω resistors, respectively, while detectors for *m/z* 47 through 49 are registered with $10^{12}$ Ω resistors.

The most notable difference between Nu Instruments Perspective and the more widely used older generation Thermo Fisher MAT 253 is the implementation in the former of electrostatic analyzers (ESAs) before the *m/z* 47-49 detectors. These ESAs consist of two curved plates with a voltage difference placed directly in front of each of the Faraday collectors. The addition of the ESAs as well as ion lenses following the magnetic sector of the flight tube removes secondary ion and electron signals from the mass detection. This removal results in a drastic reduction in the interfering signals on all masses (*m/z* 44-49) during operation, producing flatter and more stable baselines, relative to the older MAT 253 (Figure S1). In addition, the lowered interference from secondary electrons in the Nu Perspectives results in greater intensities and lowered noise in the signals from the higher masses, especially *m/z* 48 and 49. This advancement has contributed to a $\Delta_{47}$ non-linearity slope for the Nu Perspective (median slope observed was -0.00005) that ranges from one to two orders of magnitude less than the MAT 253 (median slope observed was -0.007), and a $\Delta_{48}$ non-linearity slope for the Nu Perspective (median slope observed was -0.004) that is an order of magnitude less than the MAT 253 (median slope observed was -0.013).

Nu Perspective-EG, Nu Perspective-1, Nu Perspective-1a, and MAT 253 use an in-house constructed autosampler that is similar to the setup detailed in Passey et al.[38] The configuration uses a stainless steel Costech Zero Blank autosampler and a 105 % phosphoric acid bath that digests calcium carbonate samples at 90 °C. The sample gas passes through cryogenic purification traps that use dry ice-cooled ethanol and liquid nitrogen to remove contaminant gases that have low vapor pressure, mostly consisting of water vapor. The $CO_2$ gas then passes through elemental silver wool (Sigma-Aldrich) to remove sulfur compounds, followed by a gas chromatograph (GC) column with helium carrier gas that contains Porapak Type-Q™ 50/80 mesh column packing material to remove organic compounds. The GC column is maintained at a constant temperature of -20 °C during sample purification. Large samples weighing 4-7 mg are analyzed on the MAT 253 in bellows with a total integration time of 720 s. Small samples weighing 0.5 mg are analyzed in bellows on Nu Perspective-EG and Nu Perspective-1 mass spectrometer (they use the same mass spectrometer) with 3 blocks of 20 cycles, with a total integration time of 1600 s. Nu Perspective-1a also uses the same mass spectrometer, but the sample and working gas volumes are depleted in microvolume mode at precisely matched rates, with *m/z* 44 ranging from 80-30 nA during sample acquisition, with an integration time of 1200 s. The sample preparation system is operated by custom software in Labview that controls the sampler, GC column, cryogenic dewar lifters, and valves. The Labview software is integrated with the Perspective Stable Gas Control software interface that controls the Nu Perspective mass spectrometer.

Nu Perspective-2 uses a Nu Carb Sample Digestion System instead of a common acid bath, where 0.5 mg of calcium carbonate is reacted at 70 $^{o}$C in individual glass vials with 105 wt% phosphoric acid. The sample gas is cryogenically purified in liquid nitrogen-cooled tubes called coldfingers before passing through a relatively short GC column packed with Porapak Type-Q$^{TM}$ 50/80 and silver wool. This instrument operates under vacuum pressure and does not use a carrier gas. The sample and working gas volumes are matched precisely during depletion into the mass spectrometer, with *m/z* 44 ranging from 80-30 nA. Sample data is analyzed in 3 blocks of 20 cycles, with each cycle integrating for 20 s, for a total integration time of 1200 s.

### 2.4 Equilibrated gas standards

We analyzed 195 equilibrated gas standards on a Nu Instruments Perspective mass spectrometer, here called Nu Perspective-EG. We utilized two gases with differing bulk isotope values, with a ~60 ‰ difference in $\delta_{47}$ values, prepared using standard procedures[1,26]. The heavy isotope depleted $\delta_{47}$ gas is from an Airgas $CO_2$ gas cylinder and was equilibrated with 5-10 mL of 25 $^{o}$C deionized (DI) water. The heavy isotope enriched $\delta_{47}$ gas is produced by phosphoric acid digestion of a Carrara Marble carbonate standard. The resulting carbon dioxide was equilibrated with evaporated DI water held at 25 °C. Aliquots of the two 25 °C gases are re-equilibrated at 1000 °C by heating the gases in quartz tubes inside a muffle furnace for >1 hour, and then flash cooled, to produce gases with near stochastic $\Delta_{47}$ values.

### 2.5 Data processing and normalization

Raw data files from all instrument configurations were transferred into Easotope[39] (64-bit version from release 20201231), where corrections and final $\Delta_{47}$ and $\Delta_{48}$ values for replicates were calculated. All data used the IUPAC parameter set.[40,41] $\Delta_{47}$ and $\Delta_{48}$ data from Nu Perspective-EG is reported on the Carbon Dioxide Equilibrium Scale (CDES 90; Dennis et al.[26]), meaning it was normalized to $CO_2$ equilibrated at 25 °C and 1000 °C at an acid digestion temperature of 90 °C. $\Delta_{47}$ data from Nu Perspective-1, Nu Perspective-2, and MAT 253 is reported on the InterCarb-Carbon Dioxide Equilibrium Scale (I-CDES; Bernasconi et al.[27]), meaning it was normalized to carbonate standards including ETH-1, ETH-2, and ETH-3 at an acid digestion temperature of 90 °C. Note that the I-CDES and CDES 90 reference frames should be equivalent if properly standardized. $\Delta_{48}$ data for Nu Perspective-1, Nu Perspective-2, and MAT 253 are reported on the CDES 90 scale, normalized to carbonate standards including ETH-1, ETH-2, and ETH-3 at an acid digestion temperature of 90 °C. Since it currently is convention to describe $\Delta_{48}$ values digested at 90 °C as CDES 90 whether they are normalized to equilibrated $CO_2$ or carbonate standards, we want to note again that the only instrument here that used equilibrated $CO_2$ normalization was Nu Perspective-EG, while the others use exclusively carbonate standard based normalization.

Figure 1 contains a flow chart detailing the standards used in data normalization for each instrument configuration. Methods detailed in Dennis et al. (2011) were used to normalize data to the CDES 90 and I-CDES reference frames, including a nonlinearity correction and transfer function (Figures 1, 2). We do not perform pressure baseline corrections; however, a background correction is performed for all masses (*m/z* 44-49) on all instruments before any further data normalization. The background is measured (in amps on the Nu Perspective instruments; mV on the MAT 253) at the start of an analysis and is subtracted from the measurement. For the nonlinearity slope correction, a slope was determined over a 10-day moving average for the regression lines between $\delta_{47\ \mathrm{raw}}$ and $\Delta_{47\ \mathrm{raw}}$, and $\delta_{48\ \mathrm{raw}}$ and $\Delta_{48\ \mathrm{raw}}$ values for $CO_2$ gas standards equilibrated at 25 $^{o}$C and 1000 $^{o}$C or ETH-1 and ETH-2 (Figure 2A, B, E, F). Nonlinearity slope corrections are applied to all analyses using equations 3 and 4:

$$\Delta_{47\ \mathrm{sc}} = \Delta_{47\ \mathrm{raw}} - (m_{47} \times \delta_{47\ \mathrm{raw}}) \qquad \text{Equation 3}$$

$$\Delta_{48\ \mathrm{sc}} = \Delta_{48\ \mathrm{raw}} - (m_{48} \times \delta_{48\ \mathrm{raw}}) \qquad \text{Equation 4}$$

where $\Delta_{47\ \mathrm{sc}}$ and $\Delta_{48\ \mathrm{sc}}$ values are the nonlinearity slope-corrected values, and $m_{47}$ and $m_{48}$ are the regression slopes, with nomenclature adapted from Fiebig et al.[7] For the transfer function, the 10-day moving average slope and intercept was determined for the linear relationship between either theoretically calculated $\Delta_{47}$ values for 25 $^{o}$C and

1000 °C, 0.925 ‰[42] and 0.027 ‰[26], respectively, or carbonate standard values, and $\Delta_{47\ sc}$ values (Fig. 2C, D, G, H). Where carbonate standards where used, $\Delta_{47}$ values determined in Bernasconi et al.[27] of 0.2052 ‰, 0.2085 ‰, and 0.6132 ‰ were used as standard values for ETH-1, ETH-2, and ETH-3, respectively. For Nu Perspective-2, the additional standards Carmel Chalk and Veinstrom were used, with $\Delta_{47}$ values of 0.674 ‰ and 0.715 ‰, respectively. Before Carmel Chalk and Veinstrom were used in data normalization, their long-term average values were determined on Nu Perspective-1 and MAT 253. For $\Delta_{48}$, the 10-day moving average slope and intercept was determined for the linear relationship between either theoretically calculated $\Delta_{48}$ values for 25 °C and 1000 °C of 0.345 ‰[42] and 0.000 ‰[7], respectively, or carbonate standards, and $\Delta_{48\ sc}$. Where carbonate standards were used, the $\Delta_{48}$ values determined on Nu Perspective-EG for ETH-1, ETH-2, ETH-3, and Veinstrom (Table 3) were used for standard values. The transfer function (TF) slope and intercept from these regressions were used to create transfer functions, which are applied to all $\Delta_{47\ sc}$ and $\Delta_{48\ sc}$ values, and yields the fully corrected values $\Delta_{47}$ and $\Delta_{48}$ values using equations 5 and 6:

$$\Delta_{47\text{I-CDES; CDES 90}} = \Delta_{47\ sc} \times \text{TF slope} + \text{TF intercept} \qquad \text{Equation 5}$$

$$\Delta_{48\ \text{CDES 90}} = \Delta_{48\ sc} \times \text{TF slope} + \text{TF intercept} \qquad \text{Equation 6}$$

where $\Delta_{47}$ and $\Delta_{48}$ values are the fully corrected values in the I-CDES or CDES 90 reference frame, $\Delta_{47\ sc}$ and $\Delta_{48\ sc}$ values are the slope corrected values from equations 3 and 4, TF slope is the transfer function slope, and TF intercept is the transfer function intercept.

### 2.6 Use of statistical methods for robust determination of $\Delta_{47}$ and $\Delta_{48}$ values

We report a large historical dataset where many standards have >100 replicates. To streamline data analyses and ensure all replicate data was handled identically, we developed an R script that automated outlier identification, calculation of sample mean values (replicate pool average), error (replicate pool error reported as ±1 SE), and data statistics. In the Appendix we provide a detailed description of this method for replicate-level outlier identification and data pooling from multiple instruments. The R script is publicly available for review at https://github.com/Tripati-Lab/Lucarelli-et-al. This method is particularly useful for datasets with a large number of replicates where determining outliers manually can be time intensive; it also helps reduce potential human bias. We do not recommend this method for samples with less than 12 replicates, as this was the smallest number of replicates we successfully tested the method on. In short, a density function was determined for replicate level data for each sample on every instrumental configuration after an initial removal of very large outliers (i.e., $\Delta_{47}$ or $\Delta_{48}$ values of <-0.5) (Figure 3B). A 3σ or 5σ (3 standard deviations from the mean or 5 standard deviations from the mean) cut was then made for each density function (Figure 3C). Then, the final replicate pool for each sample was used to determine the average $\Delta_{47}$, $\Delta_{48}$, $\delta^{18}$O, and $\delta^{13}$C values, SE, and normality of the data distribution. We note the error reported here may not fully account for all error associated with transferring raw data into the final $\Delta_{47}$

values, described as “allogenic” errors by Daëron (2021). These errors may play a larger role for $\Delta_{48}$ given larger measurement uncertainties.

For data pooling between instrumental configurations, the $\Delta_{47}$ and $\Delta_{48}$ replicate distributions for standards and samples run on multiple instrument configurations (consistency standards) were directly compared. If no statistically significant differences were observed for standard and consistency standard values between configurations, replicates were pooled to calculate a combined average. $\Delta_{48}$ replicate values from the MAT 253 were not pooled with replicate values from the Nu Perspective instruments.

### 2.7 Calculation of $\Delta_{47}$-$T$ and $\Delta_{48}$-$T$ equilibrium relationships using regression-form acid fractionation factors

Temperature-dependent $\Delta_{47}$ and $\Delta_{48}$ equilibrium relationships were calculated using equilibrium calcite $\Delta_{63}$ and $\Delta_{64}$ values predicted by theory from Hill et al.[4] and Tripati et al.[5], combined with regression-form acid fractionation factors (AFFs), $\Delta^*_{63\text{-}47}$ and $\Delta^*_{64\text{-}48}$ using equations 7 and 8.

$$\Delta_{47\ \text{I-CDES EQ}} = \Delta_{63} + \Delta^*_{63\text{-}47} \qquad \text{Equation 7}$$

$$\Delta_{48\ \text{CDES 90 EQ}} = \Delta_{64} + \Delta^*_{64\text{-}48} \qquad \text{Equation 8}$$

Model calculations from Guo et al.[3] predicted that AFFs for when calcite mineral is digested in phosphoric acid, $\Delta^*_{63\text{-}47}$ and $\Delta^*_{64\text{-}48}$, should depend on the $\Delta_{63}$ and $\Delta_{64}$

values of the reactant carbonate, respectively. Thus, regression form AFFs were determined by taking the theoretical $\Delta_{63}$ and $\Delta_{64}$ values at two temperatures, 600 °C and 33.7 °C, and then subtracting the experimental $\Delta_{47}$ and $\Delta_{48}$ values for samples with known precipitation temperatures at 600 °C and 33.7 °C. Then, a linear regression was made between the $\Delta^*_{63-47}$ and $\Delta^*_{64-48}$ values for 600 °C and 33.7 °C and the corresponding theoretically predicted $\Delta_{63}$ and $\Delta_{64}$ values for 600 °C and 33.7 °C (Hill et al.[4]; Tripati et al.[5]). The experimental $\Delta_{47}$ and $\Delta_{48}$ values used for 600 °C were the pooled replicate values for ETH-1 and ETH-2 (Bernasconi et al.[43]), and the values used for 33.7 °C were from pooled replicate values for Devils Hole calcite (Coplen,[35]). Further details of this calculation are in Appendix Section A.2.

## 3. RESULTS

### 3.1 Use of statistical methods for robust determination of $\Delta_{47}$ and $\Delta_{48}$ values

We find there was a negligible difference in the number of replicates removed when a 3σ versus 5σ cutoff was used for outliers due to narrow peak widths (Figure S2, Table S1). To further ensure the robustness of this method, we compared our final $\Delta_{47}$ values to Upadayay et al.[32] which presented a subset of the data reported here using other methods for outlier removal and data processing (Table S2). The datasets are in good agreement, with an average offset of 0.011 ‰, despite the $\Delta_{47}$ data from their study being standardized differently than the data here, and then being transferred into the I-CDES reference frame using an equation from Appendix A in Bernasconi et al.[27].

### 3.2 Instrumental configuration comparison

We found no evidence of statistically significant differences in the final $\Delta_{47}$ or $\Delta_{48}$ values of samples analyzed on multiple configurations (Figure S3; Table S3, S4). However, $\Delta_{48}$ data from the MAT 253 was not pooled with Nu Perspective-1 and Nu Perspective-2 data because offsets were observed in $\Delta_{48}$ values for the standards ETH-1 and ETH-2 that did not exist in Nu Perspective-1 and Nu Perspective-2 (Table 4). The older generation MAT 253 does not use secondary electron suppression, and therefore, does not yield as precise $\Delta_{48}$ data as the Nu Perspective instruments, which do use secondary electron suppression. Additionally, we have not combined data produced using equilibrated gas-based standardization with data produced using carbonate-based standardization.

### 3.3 $\Delta_{47}$ and $\Delta_{48}$ results

$\Delta_{47}$ and $\Delta_{48}$ values were determined for 7 standards using 25 $^{o}$C and 1000 $^{o}$C equilibrated gas-based standardization, with a total of 324 $\Delta_{47}$ and 363 $\Delta_{48}$ replicate analyses performed from May 2015-June 2017 (Table 3). Additionally, $\Delta_{47}$ values were determined for 27 standards and samples (5,141 replicate analyses), and $\Delta_{48}$ values (3,037 replicate analyses) for 24 standards and samples using carbonate-based standardization, performed from April 2015-March 2021 (Table 4). All $\Delta_{47}$ sample replicate-level data were normally distributed, with the exception of ETH-3 analyzed on MAT 253 (Table S5). All $\Delta_{48}$ replicate-level data were normally distributed (Table S6).

We also present $\Delta_{48}$ data produced on the older generation MAT 253 mass spectrometer (Table 4). Due to higher error, lower precision, and offsets in ETH-1 and ETH-2 values, we did not pool $\Delta_{48}$ replicate data produced on the MAT 253 with the data produced on the Nu instruments. However, $\Delta_{48}$ data from the MAT 253 is included here due to the large amount of clumped isotope data produced on this instrument going back to 2014, given comments from J. Eiler (pers. comm.) indicating these instruments may produce usable $\Delta_{48}$ data. We sought to test as to whether this instrument, with sufficient replication and quality control, could produce reproducible $\Delta_{48}$ values. We observed that the MAT 253 produced similar sample average values for the majority of samples (Table 4; Figure S3), with larger SE than the Nu Perspective instruments, as expected. Thus, it may be worth mining past MAT 253 datasets to examine $\Delta_{48}$ depending on the reproducibility of measurements, although newer generation instrumentation is preferable for the measurement of $\Delta_{48}$ values.

### 3.3.1 Experimentally determined $\Delta_{47}$-$\Delta_{48}$ regression

The polynomial described by Equation 9 ($r^2 = 0.97$) was fit through experimentally determined $\Delta_{47}$ and $\Delta_{48}$ values for 20 samples, including standards and Devils Hole calcite (Figure 4A).

Equation 9

$$\Delta_{48\ \mathrm{CDES\ 90}} = (0.1179 \pm 0.0266) - (0.0398 \pm 0.1332)\Delta_{47\ \mathrm{I\text{-}CDES}} + (0.4407 \pm 0.1490)\Delta_{47\ \mathrm{I\text{-}CDES}}{}^{2}$$

All $\Delta_{47}$ and $\Delta_{48}$ values used to calculate this regression can be found in Table 4. Of the 21 total samples in Figure 4, all lie within 1 SE of the 95 % confidence interval of the regression, with the exception of Merck, Carmel Chalk, and 47407 Coral. 47407 Coral was the only sample not included in the regression due to its apparent offset from equilibrium.

### 3.4 Calculated $\Delta_{47}$-$T$, $\Delta_{48}$-T, and $\Delta_{47}$-$\Delta_{48}$ regressions using regression-form AFFs

The calculated $\Delta_{47}$ and $\Delta_{48}$ equilibrium values for 0-1000 $^{o}$C are in Table 5. These values were calculated using theoretical equilibrium $\Delta_{63}$ and $\Delta_{64}$ values for calcite (Hill et al.[4];Tripati et al.[5]) and regression-form AFFs determined here. The equilibrium $\Delta_{47}$ and $\Delta_{48}$ relationship (Figure 4A) is represented by equation 10.

Equation 10

$$\Delta_{48\ \mathrm{CDES\ 90\ EQ}} = 0.1123 + 0.01971\ \Delta_{47\ \mathrm{I\text{-}CDES\ EQ}} + 0.364(\Delta_{47\ \mathrm{I\text{-}CDES\ EQ}})^2$$

The temperature-dependent equilibrium relationships are described by equations 11 and 12,

Equation 11

$$\Delta_{47\ \text{I-CDES EQ}} = [0.6646 \pm (0.0009)] - [0.0032 \pm (3.033 \text{ x } 10^{-5})]T + [(1.012 \text{ x } 10^{-5}) \pm (2.449 \times 10^{-7})]T^2 - [(1.559 \times 10^{-8}) \pm (6.717 \times 10^{-10})]T^3 + [(9.251 \times 10^{-12}) \pm (5.802 \times 10^{-13})]T^4$$

Equation 12

$$\Delta_{48\ \text{CDES 90 EQ}} = [0.2842 \pm (0.0009)] - [0.0014 \pm (3.048 \times 10^{-5})]\mathrm{T} + [(5.741 \times 10^{-6}) \pm (2.437 \times 10^{-7})]T^2 - [(1.017 \times 10^{-8}) \pm (6.749 \times 10^{-10})]T^3 + [(6.570 \times 10^{-12}) \pm (5.830 \times 10^{-13})]T^4$$

where temperature is in Celsius.

The regression form AFFs are represented by equations 13 and 14,

$$\Delta^*_{63\text{-}47} = 0.0190 \times \Delta_{47\ \text{I-CDES}} + 0.1842$$ Equation 13

$$\Delta^*_{64\text{-}48} = 0.0077 \times \Delta_{48\ \text{CDES 90}} + 0.1290$$ Equation 14

where $\Delta^*_{63\text{-}47}$ and $\Delta^*_{64\text{-}48}$ are the AFFs. These values can be used to estimate calcite mineral $\Delta_{63}$ and $\Delta_{64}$ values via equations 7 and 8 for comparison the theory. The use of a regression form AFF is more important for $\Delta_{47}$ than $\Delta_{48}$, as there is a ~0.009 ‰ difference in $\Delta^*_{63-47}$ from 0-600 °C for $\Delta_{47}$, while there is only a ~0.001 ‰ difference in $\Delta^*_{64-48}$ over the same temperature range (Table 5).

## 4. DISCUSSION

### 4.1 Comparison of $\Delta_{47}$ and $\Delta_{48}$ values determined with equilibrated gas-based standardization

Since $\Delta_{48}$ is a relatively new proxy, the development of robust standard values is of the utmost importance to ensure intra- and inter-laboratory reproducibility. To establish carbonate standard $\Delta_{48}$ values that can be used in data normalization for unknown samples, $\Delta_{48}$ values for carbonate standards must first be determined relative to equilibrated gases. We have compared our $\Delta_{47}$ and $\Delta_{48}$ values for carbonate standards determined using equilibrated gas-based standardization to other recently published datasets with paired clumped isotope values for ETH standards, including Fiebig et al.[7], Bajnai et al.[8], and Swart et al.[9] (Figure 5, Table 3). There is good interlaboratory agreement for $\Delta_{47}$ values, with a range of 0.002 ‰ to 0.012 ‰ for $\Delta_{47}$ offsets for replicated samples. The $\Delta_{47}$ error, reported as 1 SE, was similar (0.001 ‰ to 0.006 ‰) for all studies. When the $\Delta_{47}$ values for carbonate standards determined in these studies were compared to the multi-laboratory study from Bernasconi et al.[27] which determined nominal $\Delta_{47}$ values for carbonate standards, there was similar agreement between laboratories, with offsets from 0.000 ‰ to 0.012 ‰ for replicated samples (Table 3). The interlaboratory $\Delta_{48}$ offsets were larger, with a range of 0.009 ‰ to 0.038 ‰ for replicated samples, although the majority of replicated samples were with within 1 SE of eachother (Table 3, Figure 5). The $\Delta_{48}$ error reported in Bajnai et al.[8] of 0.004 ‰ to 0.005 ‰ was lower than that for the other studies which have error ranging from 0.007 ‰ to 0.014 ‰, possibly from more replication, larger sample size (10 mg compared to 0.5 mg in this study), and longer mass spectrometric integration times than what was used here.

The use of equilibrated gases for standardization has been shown to be a potential source of error and interlaboratory offsets since the sample undergoes acid digestion and the gas standard does not, different laboratories use different setups to produce gas standards, and fractionations may occur from quenching during the production of heated gas standards[43]. However, interlaboratory $\Delta_{47}$ offsets up to 0.024 ‰ in Bernsconi et al.[27] were determined to be the result of random error which may be amplified during data normalization. The range in $\Delta_{47}$ offsets observed here are smaller than what was observed in Bernsconi et al.[27], likely from overall high replication. Additionally, we observed an average interlaboratory $\Delta_{48}$ offset of 0.018 ‰ (taken as the average of the absolute value of offsets of replicated samples in Table 3). These offsets are likely also from random error, considering that the *m/z* 48 isotopologue is an order of magnitude lower in abundance than the m/z 47 isotopologue[1], and this offset is still within the range of observed interlaboratory $\Delta_{47}$ offsets.

### 4.2 Carbonate based standardization for $\Delta_{47}$-$\Delta_{48}$ measurements

Previously, important contributions have demonstrated that carbonate standard-based standardization that uses readily available materials can produce robust $\Delta_{47}$ values and yield interlaboratory discrepancies that are consistent with analytical uncertainties[27,31,43]. We applied this approach, using ETH-1, ETH-2, and ETH-3 as carbonate standards on multiple instruments in our laboratory for the paired analysis of $\Delta_{47}$-$\Delta_{48}$. The combined instrument average from this study (Table 4) and Bernsconi et al.[27] had excellent agreement between ETH standard $\Delta_{47}$ values, with offsets of 0.001, 0.002, 0.004, and 0.005 for ETH-1, ETH-2, ETH-3, and ETH-4 (used as an unknown), respectively. This is likely because the nominal $\Delta_{47}$ values determined in Bernasconi et al.[27] for ETH standards were used here in transfer functions for data normalization, adding supporting evidence for the importance of laboratories using common standard values to yield reproducible results. Similarly, carbonate standard-based standardization yielded reproducible $\Delta_{48}$ results (Figure 6) across the two Nu Perspective mass spectrometer configurations presented in Table 4. The $\Delta_{48}$ offsets for the 3 standards treated as unknowns (consistency standards), Carrara Marble, CM Tile, and ETH-4, that were replicated on Nu Perspective-1 and Nu Perspective-2, ranged from 0.004 ‰ to 0.013 ‰. These offsets were reduced compared to interlaboratory $\Delta_{48}$ offsets observed for ETH standard values and Carrara Marble determined using equilibrated gas-based standardization (average: 0.018 ‰; minimum: 0.008 ‰; maximum: 0.038 ‰). Further, carbonate standard based standardization was successfully used by Bajnai et al.[44] for determining $\Delta_{48}$ values for Devils Hole cave calcite. There is currently no agreed upon $\Delta_{48}$ values for carbonate standards, thus, for laboratories that choose to employ carbonate-based standardization for $\Delta_{48}$ data and do not have in-house determined standard $\Delta_{48}$ values, the use of $\Delta_{48}$ values determined here for ETH-1 (0.132 ‰; n = 464), ETH-2 (0.132 ‰, n = 439), and ETH-3 (0.247 ‰; n = 236) may be used in carbonate-based standardization. Additional $\Delta_{48}$ values for materials that are widely used and may potentially be used as standards, such as Carrara Marble (n = 319), IAEA-C1 (n = 49), and IAEA-C2 (n = 59) are also in Table 4. Consistent with Daëron[45] and Kocken et al.[46], we recommend a 50:50 sample to standard ratio, which was what was utilized here.

### 4.3 Experimental $\Delta_{47}$-$\Delta_{48}$ equilibrium regression using samples and standards

We determined an experimental $\Delta_{47}$-$\Delta_{48}$ regression (equation 9) for 20 carbonate standards and samples (combined average values in Table 4). To have a constraint as to whether the materials included in the regression achieved quasi-equilibrium clumped isotope values, we compared the experimental regression to our equilibrium regression based on calcite mineral equilibrium theory[4,5] for $\Delta_{63}$-$\Delta_{64}$ (Figure 4A). The theoretical regression for $\Delta_{63}$-$\Delta_{64}$ equilibrium was transferred into $\Delta_{47}$-$\Delta_{48}$ space with an experimentally determined regression-form AFF (see Methods 2.7). The materials used to determine the regression-form AFF to transfer theoretical $\Delta_{63}$-$\Delta_{64}$ equilibrium values into $\Delta_{47}$-$\Delta_{48}$ equilibrium values were the extremely slow growing calcite from Devils Hole and pooled values for ETH-1 and ETH-2. These materials have well-constrained precipitation temperatures and are believed to have achieved quasi-equilibrium clumped isotope values[35,43,44]. When the experimental regression using 20 carbonates was compared to the theoretical/experimental AFF regression, they were found to be statistically indistinguishable (P = 0.39; F = 1.03; Table S7). This supports the assumption that the materials used in the experimental regression have achieved quasi-equilibrium clumped isotope values.

Of the materials used in the regression, all lie within 1 SE of the 95 % confidence interval of the regression, with the exception of Merck, Carmel Chalk, and 47407 Coral. The 47407 Coral was the only sample for which we determined a $\Delta_{48}$ value that was not included in the regression. The possibility that Merck, an ultra-pure synthetic calcite, and Carmel Chalk, a natural calcite chalk, are exhibiting subtle clumped isotope disequilibrium cannot be excluded. However, both Merck and Carmel Chalk deviated from the equilibrium regressions by <1 SD and therefore were included in the experimental regression, while 47407 Coral deviated from the regressions by >1 SD. 47407 Coral is a deep-sea coral of the genus *Desmophyllum* with an estimated growth temperature of 4.2 $^{o}$C.[21] Guo et al.[24] used model estimates to predict a negative correlation between $\Delta_{47}$ and $\Delta_{48}$ values for cold-water corals, with kinetic effects causing enrichments in $\Delta_{47}$ values and depletions in $\Delta_{48}$ values. We determined that the 47407 Coral exhibits an enrichment of 0.030 ‰ in $\Delta_{47}$ and depletion of -0.018 ‰ in $\Delta_{48}$ by defining nominal equilibrium as the regression through the remaining carbonates, and the offsets were determined by using a kinetic slope for $CO_2$ absorption in corals of -0.6[8,24]. Bajnai et al.[8] also measured $\Delta_{47}$ and $\Delta_{48}$ values for a coral of the same genus (*Desmophyllum*) and a brachiopod (*Magellania venosa*) and observed similar enrichments in $\Delta_{47}$ (0.038 ‰ to 0.069 ‰) and depletions in $\Delta_{48}$ (-0.0004 ‰ to -0.095 ‰). Additionally, modeling from Guo et al.[24] and Bajnai et al.[8] predicts deviations from equilibrium of a similar magnitude.

### 4.4 Constraining equilibrium $\Delta_{47}$-$\Delta_{48}$

The equilibrium $\Delta_{47}$-$\Delta_{48}$ relationship is of recent interest due to the potential for use to identify kinetic effects in biotic and abiogenic samples that are or could be used for paleotemperature reconstructions. As mentioned above, a recent study[8] used a kinetic slope calculated relative to a proposed equilibrium $\Delta_{47}$-$\Delta_{48}$ regression to recover temperature signals in kinetically controlled samples. To further develop the use of $\Delta_{47}$-$\Delta_{48}$ equilibrium as a proxy to constrain kinetic effects, the $\Delta_{47}$-$\Delta_{48}$ equilibrium relationship must be well constrained. Thus, we compared the experimentally determined $\Delta_{47}$-$\Delta_{48}$ regressions for quasi-equilibrium materials determined here (Equation 9) to those from Swart et al.[9] and Fiebig et al.[10] using a sum-of-squares F test (Table S7). This compares the fit of a regression through all datasets to the fit of individual regressions for each dataset, and tests whether the datasets differ sufficiently from each other to warrant separate regressions. The dataset from Swart et al.[9] contains 7 inorganic precipitations in 5 °C increments from 5 °C to 65 °C and carbonate standards ETH-1, ETH-2, ETH-3, and ETH-4. The dataset from Fiebig et al.[10] includes 16 carbonates, some of which are combined into averages, yielding 10 samples that are used for comparison here, including lake calcite, Devils Hole calcite, inorganic calcite precipitations, and calcite equilibrated at high temperatures, with crystallization temperatures for all samples ranging from 8 °C to 1100 °C. We found no evidence of statistically significant differences between the individual regressions (P = 0.86; F = 0.43; Table S7), and we therefore produced a combined regression (Figure 4B), described by equation 15, which is composed of 41 samples that are believed to have achieved quasi-equilibrium clumped isotope values.

Equation 15

$$\Delta_{48\ \mathrm{CDES}\ 90} = (0.1132 \pm 0.010) + (0.008 \pm 0.055)\ \Delta_{47\ \mathrm{CDES}\ 90} + (0.3692 \pm 0.065)\ \Delta_{47\ \mathrm{CDES}\ 90}{}^{2}$$

Of the 41 materials used in the combined regression, 35 are within 1 SE of the 95 % confidence interval. The samples outside of the confidence interval include Carmel Chalk, ETH-4, and Merck from this study; ETH-2 and ETH-4 from Swart et al.[9]; and a cave lake calcite sample from Fiebig et al.[10]. It is unlikely that ETH-2 is exhibiting kinetic effects since it has an equilibration temperature of 600 °C[43], and has near stochastic isotopic values[47].The cave lake calcite sample from Fiebig et al.[10] is from Laghetto Basso, Italy with a precipitation temperature of 7.9 ± 0.2 °C. Fiebig et al[10] and Daëron et al.[48] argued that this sample precipitated close to equilibrium due to long residence times of water in the lake, low calcite saturation index (< 0.3), slow precipitation rate (0.3 $\mu$m/yr), and consistent $\delta^{18}$O values for contemporaneously deposited calcite layers. It cannot be ruled out that ETH-4, the same commercially available calcite as ETH-2 but unheated[43], exhibits subtle kinetic effects. The ETH-4 sample from this study is much closer to the equilibrium regression than the ETH-4 sample from Swart et al.[9], mostly due to offsets in the $\Delta_{48}$ value (0.030 ‰) between the studies, which is larger than the offset for $\Delta_{47}$ (0.014 ‰). Both the $\Delta_{47}$ and $\Delta_{48}$ offsets between the studies are >2 SE but <1 SD, and within the threshold of observed scatter from random error[27], therefore, the difference in ETH-4 values between this study and Swart et al.[9] may be reflection of different standardization methods (carbonate-based standardization used here and equilibrated gas-based standardization in Swart et al.[9]) and measurement uncertainty. As discussed above in Section 4.3, it also cannot be ruled out that Carmel Chalk from this study exhibits subtle kinetic effects. However, the scatter for all samples and standards around the equilibrium line are well within what is expected from random error[27]. Further, the lack of statistical differences (P = 0.71; F = 0.46; Table S7) between the combined experimental regression and the theoretically based regression (equation 10) is evidence that equation 15 is a robust experimental representation of $\Delta_{47}$-$\Delta_{48}$ equilibrium and can be used to constrain unknown sample kinetic biases.

### 4.5 Constraining equilibrium $\Delta_{47}$-*T and* $\Delta_{48}$-T

To date, four groups have published relationships for both $\Delta_{47}$-*T* and $\Delta_{48}$-*T*. The regressions from Swart et al.[9] and Fiebig et al.[10] are based on experimentally constrained values (as discussed in Section 4.4), while the regressions from this study and Bajnai et al.[8] are based on a combination of calcite mineral $\Delta_{63}$-$\Delta_{64}$ equilibrium theory and experimental AFFs (see Methods 2.7). The $\Delta_{47}$-*T* and $\Delta_{48}$-*T* regressions from Bajnai et al.[8] was calculated for 0-40 °C, while the experimentally based regressions from Swart et al.[9] are for 0-65 °C. In this study we calculated $\Delta_{47}$-*T* and $\Delta_{48}$-*T* values from 0-1000 °C, and Fiebig et al.[10] has experimentally constrained values up to 1100 °C. Due to the regressions from this study and Bajnai et al.[8] being theoretically based and therefore difficult to accurately provide an error calculation, we were unable to perform the same type of statistical analysis that compares the regressions, as we did for the experimental $\Delta_{47}$-$\Delta_{48}$ regressions. Instead, we have compared the absolute difference between the regressions at 0 °C and 600 °C and compared this difference to measurement error observed in standards replicated between the laboratories. We used this metric to determine if it was appropriate to determine a combined regression. For $\Delta_{47}$-$T$, the largest difference at 0 °C was 0.007 ‰ between this study and Bajnai et al.[8]. At 600 °C, an offset of 0.001 ‰ was calculated between this study and Fiebig et al.[10]. For $\Delta_{48}$-$T$, the largest difference at 0 °C was 0.014 ‰ between this study and Bajnai et al.[8]. At 600 °C, an offset of 0.006 ‰ was calculated between this study and Fiebig et al.[10]. These offsets are well within the bounds of what we observed when comparing differences between ETH standard $\Delta_{47}$ and $\Delta_{48}$ values between laboratories (Section 4.1, Figure 5). This is a good metric for interlaboratory expected analytical error due to large numbers of replicates of ETH standards in all groups. The offsets are also within the bounds expected from random error in $\Delta_{47}$ measurements[27]. Therefore, we determined combined regressions for $\Delta_{47}$-$T$ and $\Delta_{48}$-$T$ (Figure 7), including this study, Bajnai et al.[8], Swart et al.[9], and Fiebig et al.[10], represented by equations 16 and 17

Equation 16

$$\Delta_{47\ \text{I-CDES; CDES 90}} = 0.2017 - 36.2 \times (1/T) + 16822 \times (1/T)^2 + 18878240 \times (1/T)^3 - 3064202063 \times (1/T)^4$$

Equation 17

$$\Delta_{48\ \mathrm{CDES}\ 90} = 0.1642 - 64.1 \times (1/T) + 32920 \times (1/T)^2 - 3140075 \times (1/T)^3 + 354396957 \times (1/T)^4$$

where T is in Kelvin. We also report the inverse of the relationships for ease of use for samples with unknown precipitation temperature in equations 18 and 19.

Equation 18

$$1/T = -0.003728 + 0.04027 \times \Delta_{47\ I-CDES;\ CDES\ 90} - 0.1048 \times (\Delta_{47\ I-CDES;\ CDES\ 90})^2 + 0.134 \times (\Delta_{47\ I-CDES;\ CDES\ 90})^3 - 0.06386 \times (\Delta_{47\ I-CDES;\ CDES\ 90})^4$$

Equation 19

$$1/T = -0.02296 + 0.425 \times \Delta_{48\ CDES\ 90} - 2.718 \times (\Delta_{48\ CDES\ 90})^2 + 7.936 \times (\Delta_{48\ CDES\ 90})^3 - 8.704 \times (\Delta_{48\ CDES\ 90})^4$$

To check the robustness of these equations, we solved the $\Delta_{47}$-$T$ equation (equation 16) for 10 °C, yielding a $\Delta_{47}$ value of 0.639 ‰. Then, solved the experimentally determined combined $\Delta_{47}$-$\Delta_{48}$ regression for $\Delta_{48}$ (equation 15) using 0.639 ‰ as the input $\Delta_{47}$. This returned a $\Delta_{48}$ value of 0.269 ‰, which is offset by 0.004 ‰ from the $\Delta_{48}$ value obtained when solving the $\Delta_{48}$-$T$ equation (equation 17) for 10 °C. While it may seem obvious that these equations would have good agreement, this may not necessarily have been the case given the large amount of data determined here for samples and standards that contributed to the experimental $\Delta_{47}$-$\Delta_{48}$ regression not having a constrained relationship to temperature, and it was therefore not used in the $\Delta_{47}$-$T$ and $\Delta_{48}$-$T$ regressions. Additionally, the theoretically based $\Delta_{47}$ and $\Delta_{48}$ values from Bajnai et al.[8] and this study were not included in the experimentally based $\Delta_{47}$-$\Delta_{48}$ regression. Thus, the excellent agreement between the combined experimental $\Delta_{47}$-$\Delta_{48}$ regression, and combined $\Delta_{47}$-$T$ and $\Delta_{48}$-$T$ regressions provides evidence that equations 15-19 are robust representations of clumped isotope $\Delta_{47}$-$\Delta_{48}$, $\Delta_{47}$-$T$, and $\Delta_{48}$-$T$ quasi-equilibrium relationships.

### 4.6 Comparison of Devils Hole $\Delta_{47}$ and $\Delta_{48}$

There are multiple lines of evidence that Devils Hole calcite has achieved very close to oxygen and clumped isotope equilibrium values[35,44] and has a well-constrained precipitation temperature of 33.7 °C[49–52]; therefore, samples from Devils Hole have been used to anchor clumped isotope equilibrium regressions[5,8,10], including in this study. To further constrain $\Delta_{47}$ and $\Delta_{48}$ values for Devils Hole, replicate-level values from this study were compared to previously published replicate-level values from Bajnai et al.[44] and Fiebig et al.[10]. This study used four samples from core DH-2, spanning 146-176 ka.[34] Bajnai et al.[44] used ten samples from cores DH-11, DHC2-8, and DHC2-3, spanning 4.5-508 ka. Fiebig et al.[10] used four samples from core DHC2-8, all of which were dated to 4.5-16.9 ka. The replicate pools from these three studies were compared using an ANOVA (Table S8), which is a statistical test comparing whether population means are significantly different. The mean $\Delta_{48}$ values from all three studies were statistically indistinguishable (P = 0.71; F = 0.34; Table S8). In contrast, the mean $\Delta_{47}$ values from this study and Bajnai et al.[44] were significantly different ($p < 0.0001$), as were mean $\Delta_{47}$ values from this study and Fiebig et al.[10] ($p < 0.0001$). The Devils Hole mean $\Delta_{47}$ value offset between this study and Bajnai et al.[44] is 0.012 ‰, and 0.018 ‰ between this study and Fiebig et al.[10] (Table 6). For comparison, the largest offset in replicated standard values between this study, Fiebig et al.[7], and Bajnai et al.[8] was 0.012 ‰ (Table 3), thus, the observed offset in Devils Hole $\Delta_{47}$ values could be from analytical error.

It is unlikely that the offsets are the result of Devils Hole samples exhibiting kinetic effects from $CO_2$ degassing from groundwater, which is observed in other speleothems[19,20,24,53–55]. Clumped isotope values that exhibit kinetic effects from degassing result in decreased $\Delta_{47}$ values and increased $\Delta_{48}$ values, with an approximately linear early departure from equilibrium that has a slope of ~-0.793[8,24]. The samples from Devils Hole do not follow this trend, as was concluded in Bajnai et al.[44] and here (red arrow in Figure 8). Although we cannot preclude the possibility there are small, yet resolvable differences in Devils Hole clumped isotope values from samples of different ages given that we did not measure the same samples, the evidence here does not provide sufficient evidence to support that conclusion.

The combined average $\Delta_{47}$ value from all replicates from samples in this study, Bajnai et al.[44], and Fiebig et al.[10], yielded a $\Delta_{47}$ value of 0.571 ± 0.001 ‰, which yields a temperature value of 33.9 ± 0.3 $^{o}$C from equation 18. The combined average $\Delta_{48}$ value 0.238 ± 0.007 yields a temperature value of 30.8 ± 6.8 $^{o}$C when input into equation 19. Both $\Delta_{47}$ and $\Delta_{48}$ reconstructed temperatures values are congruent with measured temperature values from Devils Hole ranging from 32.8-34.3 °C[49–52]. This provides further evidence that the observed interlaboratory offsets in Devils Hole samples are likely caused analytical error and/or error from data normalization, and the average interlaboratory $\Delta_{47}$ and $\Delta_{48}$ values for Devils Hole (Table 6) provide accurate equilibrium clumped isotope values for 33.7 °C.

## 5. CONCLUSIONS

This study, which contains 5,465 $\Delta_{47}$ and 3,400 $\Delta_{48}$ measurements of standards and samples, helps to establish $\Delta_{48}$ values that can be used in carbonate standard-based standardization. Our data supports previous $\Delta_{47}$ research[26,27,32,43] that carbonate-based standardization is a robust technique, and demonstrate that carbonate standard-based standardization produces statistically indistinguishable $\Delta_{48}$ data on varying instrumentation. Interlaboratory reproducibility of $\Delta_{48}$ values would likely be improved by the universal application of carbonate-based standardization using agreed upon carbonate standard values.

We have further constrained the equilibrium $\Delta_{47}$-$\Delta_{48}$ relationship with experimental values for standards and samples and formed a combined experimental regression with data from this study and previously published work. We constructed equilibrium $\Delta_{47}$-T and $\Delta_{48}$-T regressions using experimental and theoretically-based values and formed combined regressions using this study and previously published work. We compared $\Delta_{47}$-$\Delta_{48}$ values for Devils Hole calcite from this study and previously published work and determined that the overall combined average $\Delta_{47}$- and $\Delta_{48}$-reconstructed temperatures align with measured values of 33.7 $^{o}$C.

## Data Accessibility Statement

All code and raw data used in analyses are available for review at https://github.com/Tripati-Lab/Lucarelli-et-al.

## Acknowledgements

We thank laboratory members past and present for their work running standards, efforts in data entry, and contributions to discussions. This work was funded by DOE BES grant DE-FG02-13ER16402. HMC was supported through a postdoctoral fellowship by the Institutional Research and Academic Career Development Awards (IRACDA) program at UCLA (Award # K12 GM106996).

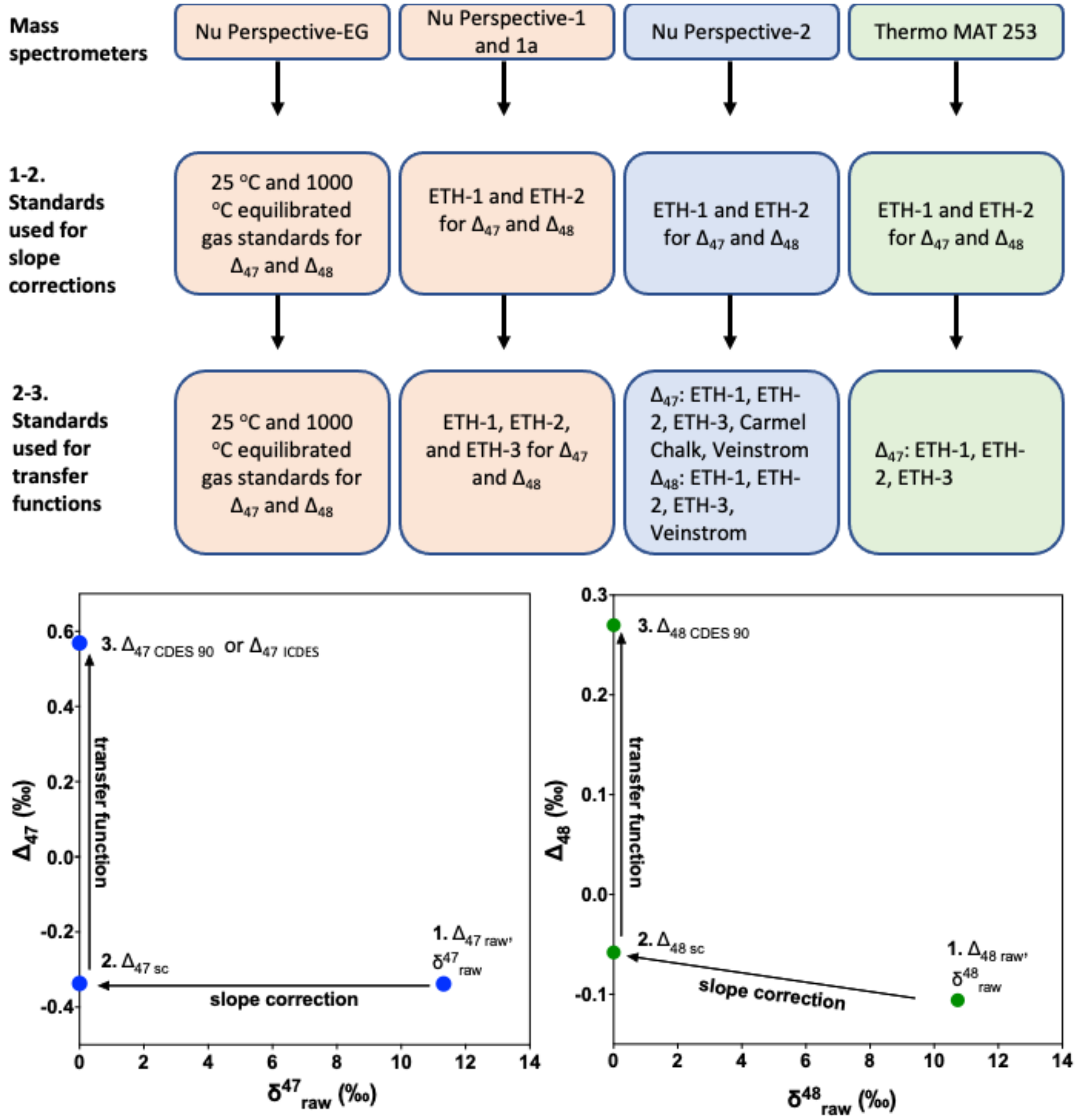

**Figure 1.** Flow chart indicating which standards are used for data normalization in each instrumental configuration, and how the data is transformed at each step. The bottom two panels are adapted from Dennis et al.[26].

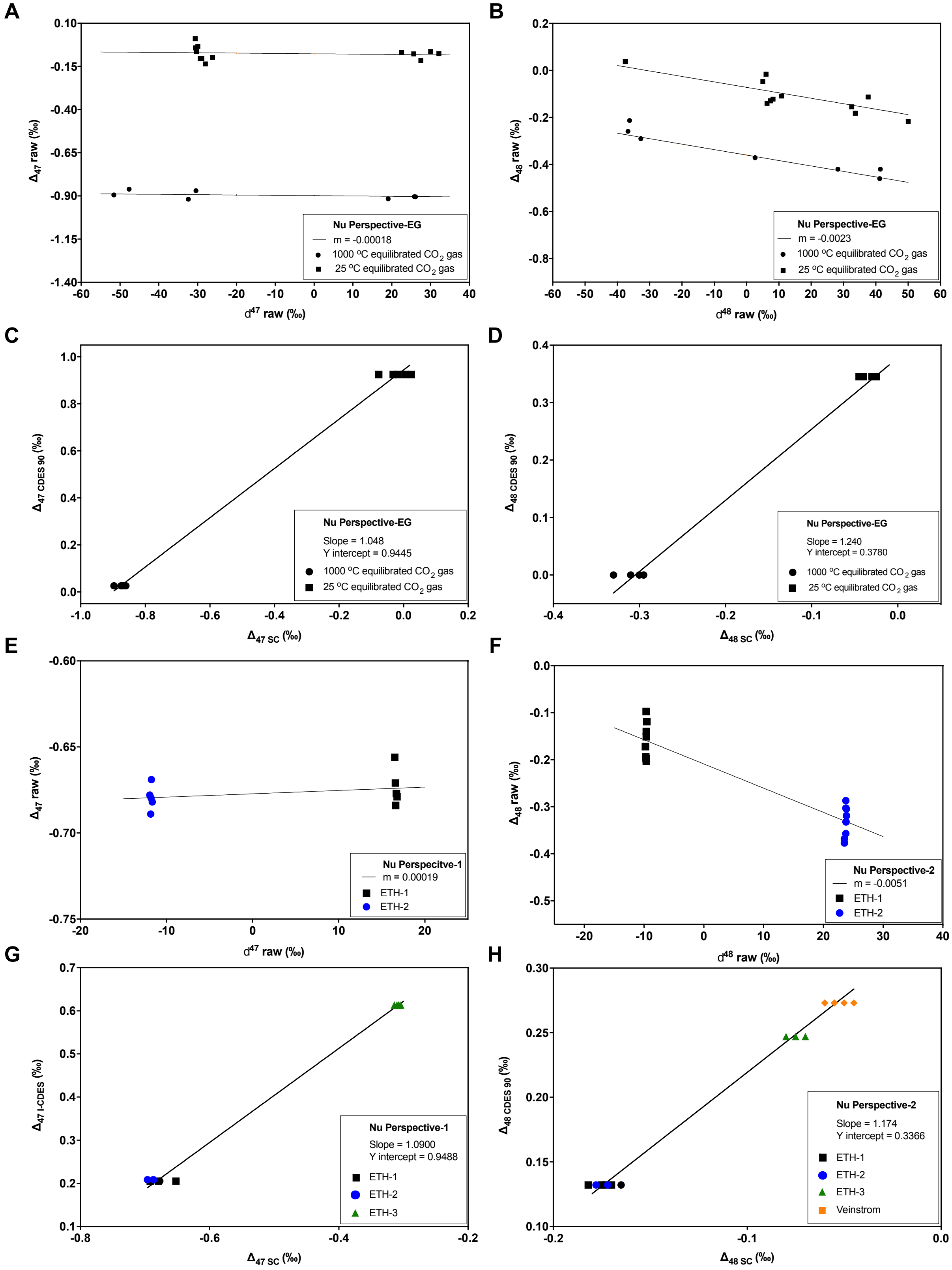
A
Δ47 raw (‰)
d47 raw (‰)
Nu Perspective-EG
m = -0.00018
1000 °C equilibrated CO2 gas
25 °C equilibrated CO2 gas
B
Δ48 raw (‰)
d48 raw (‰)
Nu Perspective-EG
m = -0.0023
1000 °C equilibrated CO2 gas
25 °C equilibrated CO2 gas
C
Δ47 CDES 90 (‰)
Δ47 SC (‰)
Nu Perspective-EG
Slope = 1.048
Y intercept = 0.9445
1000 °C equilibrated CO2 gas
25 °C equilibrated CO2 gas
D
Δ48 CDES 90 (‰)
Δ48 SC (‰)
Nu Perspective-EG
Slope = 1.240
Y intercept = 0.3780
1000 °C equilibrated CO2 gas
25 °C equilibrated CO2 gas
E
Δ47 raw (‰)
d47 raw (‰)
Nu Perspecitve-1
m = 0.00019
ETH-1
ETH-2
F
Δ48 raw (‰)
d48 raw (‰)
Nu Perspective-2
m = -0.0051
ETH-1
ETH-2
G
Δ47 I-CDES (‰)
Δ47 SC (‰)
Nu Perspective-1
Slope = 1.0900
Y intercept = 0.9488
ETH-1
ETH-2
ETH-3
H
Δ48 CDES 90 (‰)
Δ48 SC (‰)
Nu Perspective-2
Slope = 1.174
Y intercept = 0.3366
ETH-1
ETH-2
ETH-3
Veinstrom

**Figure 2.** Representative examples of slope corrections and transfer functions performed for data normalization. Panels A) and B) are the slope correction using equilibrated gas standards on Nu Perspective-EG for $\delta^{47}$ versus $\Delta_{47\ \mathrm{raw}}$ and $\delta^{48}$ and $\Delta_{48\ \mathrm{raw}}$, respectively. Panels C) and D) are transfer functions using equilibrated gas standards on Nu Perspective-EG for $\Delta_{47}$ and $\Delta_{48}$, respectively. Panels (E) and (F) are the slope correction using carbonate standards ETH-1 and ETH-2 on Nu Perspective-1 for $\delta^{47}$ versus $\Delta_{47\ \mathrm{raw}}$ and $\delta^{48}$ and $\Delta_{48\ \mathrm{raw}}$, respectively. Panels (G) and (H) are transfer functions using carbonate standards ETH-1, ETH-2, and ETH-3, and Veinstrom (for $\Delta_{48}$ only) on Nu Perspective-1 for $\Delta_{47}$ and $\Delta_{48}$, respectively. The slopes are determined on a 10-day moving interval to account for instrument drift and applied to standards and samples. Data normalization is performed similarly on all instruments.

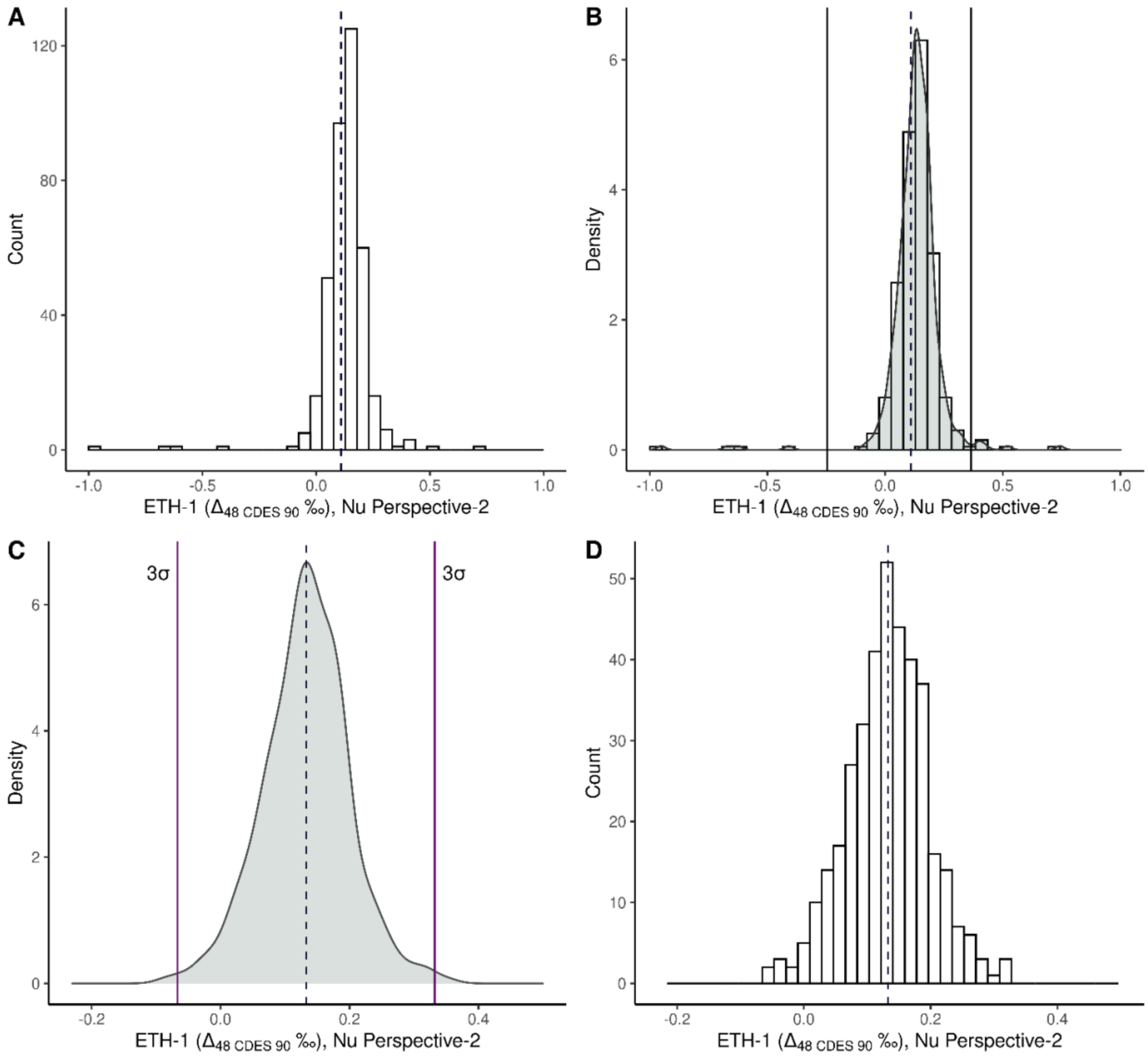

**Figure 3**. Example of data throughout the quality control process. In all panels, the dashed vertical line represents the mean value of sample replicates. A) Histogram of the raw replicate pool (N = 389, where N is the number of sample replicates). B) Density plot with histogram of the raw replicate pool and first outlier removal for large outliers (solid vertical lines). C) Density plot of the replicate pool following initial exclusions (N = 378); potential cutoff at 3σ (solid vertical lines) is shown. D) Histogram of the final replicate pool following a 3σ exclusion (mean = 0.133 ‰, SD = 0.065, N = 376). Note that the x and y axis scales differ between plots.

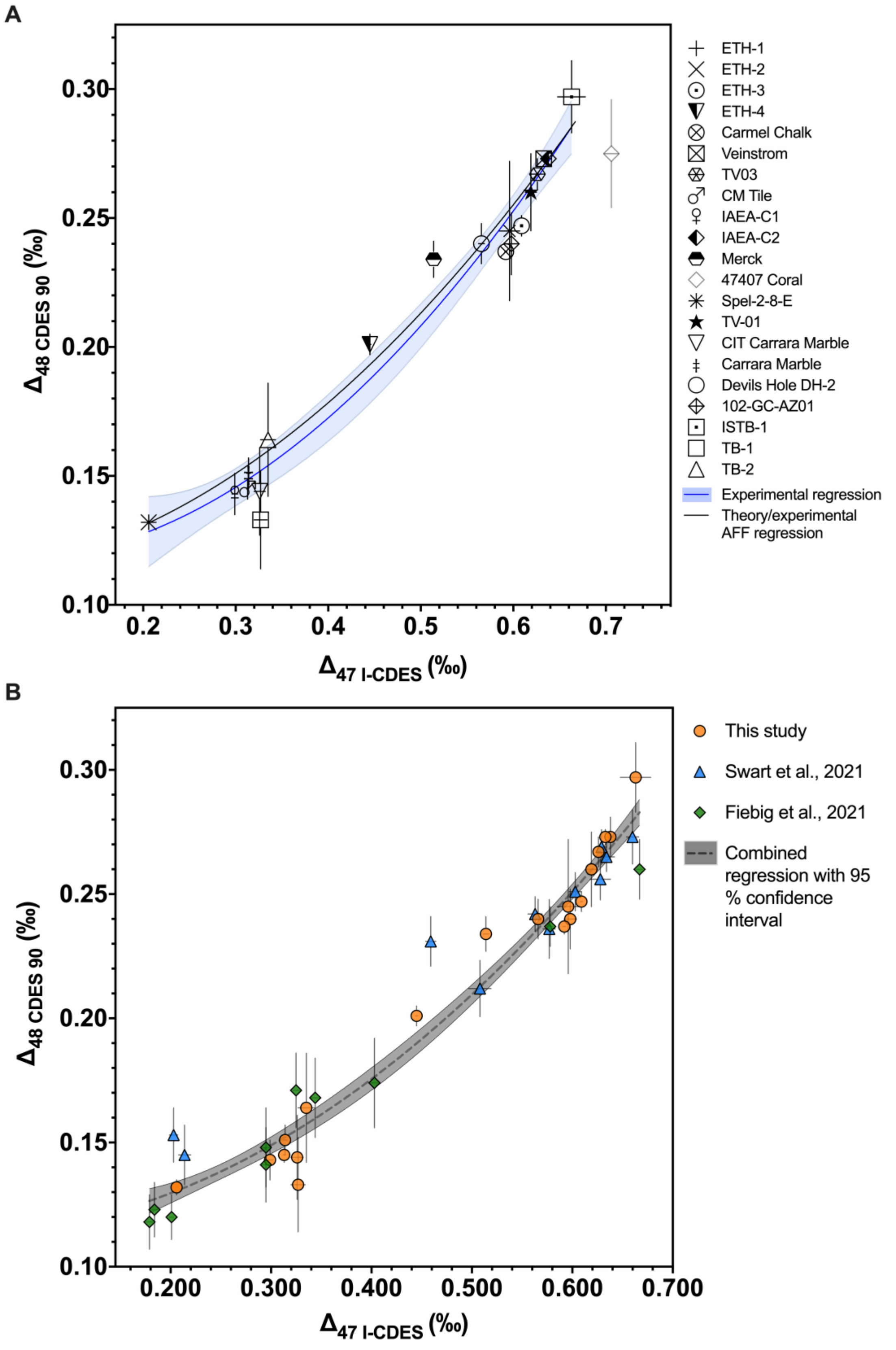
A
0.30
0.25
0.20
0.15
0.10
$\Delta_{48\ CDES\ 90}$ (‰)
0.2
0.3
0.4
0.5
0.6
0.7
$\Delta_{47\ I\text{-}CDES}$ (‰)
ETH-1
ETH-2
ETH-3
ETH-4
Carmel Chalk
Veinstrom
TV03
CM Tile
IAEA-C1
IAEA-C2
Merck
47407 Coral
Spel-2-8-E
TV-01
CIT Carrara Marble
Carrara Marble
Devils Hole DH-2
102-GC-AZ01
ISTB-1
TB-1
TB-2
Experimental regression
Theory/experimental AFF regression
B
0.30
0.25
0.20
0.15
0.10
$\Delta_{48\ CDES\ 90}$ (‰)
0.200
0.300
0.400
0.500
0.600
0.700
$\Delta_{47\ I\text{-}CDES}$ (‰)
This study
Swart et al., 2021
Fiebig et al., 2021
Combined regression with 95 % confidence interval

**Figure 4.** A) Plot showing for $\Delta_{47}$-$\Delta_{48}$ values for 21 samples including standards and Devils Hole (DH-2) cave calcite. A second order polynomial was fitted through all samples, with the exception of 47407 Coral, which may express kinetic bias. The light blue shading indicates the 95 % confidence interval. Also shown is an equilibrium regression calculated using theoretical calcite equilibrium $\Delta_{63}$ and $\Delta_{64}$[4,5] combined with experimental AFFs to determine $\Delta_{47}$-$\Delta_{48}$ values. Error bars indicate 1 SE. B) Experimental $\Delta_{47}$-$\Delta_{48}$ data from this study, Swart et al.[9], and Fiebig et al.[10] The data from this study are the same as for panel A, with the exception of 47407 Coral. The individual regressions fit through each dataset were determined to be statistically indistinguishable (P = 0.86; F = 0.43; Table S7), and a combined data regression was determined including all three datasets. The grey shading indicates the 95 % confidence interval for the combined regression.

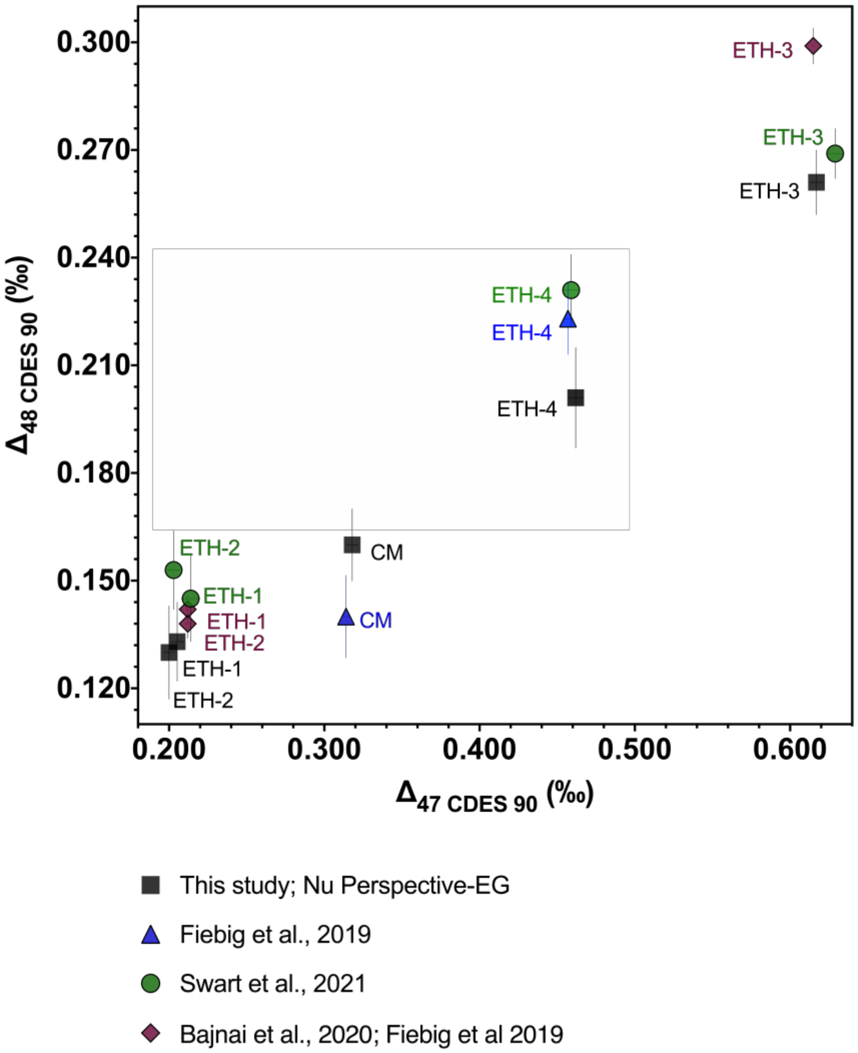

**Figure 5.** Plot showing comparison between $\Delta_{47}$-$\Delta_{48}$ values for ETH-1, ETH-2, ETH-3, ETH-4, and Carrara Marble (CM) from Nu Perspective-EG from this study with values from Fiebig et al.[7], Bajnai et al.[8], and Swart et al.[9] All data in this plot were standardized with 25 °C and 1000 °C equilibrated gas-based standardization. Error bars indicate 1 SE.

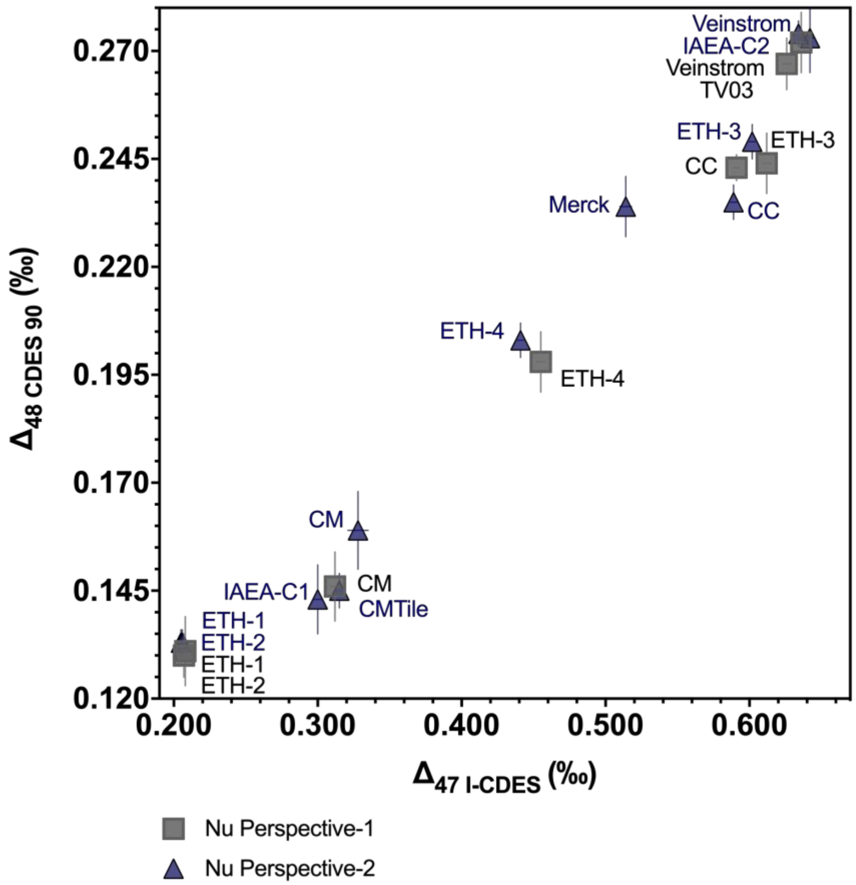

**Figure 6.** $\Delta_{47}$-$\Delta_{48}$ values for standards and samples determined using carbonate-based standardization on Nu Perpective-1 and Nu Perspective-2. Error bars indicate 1 SE.

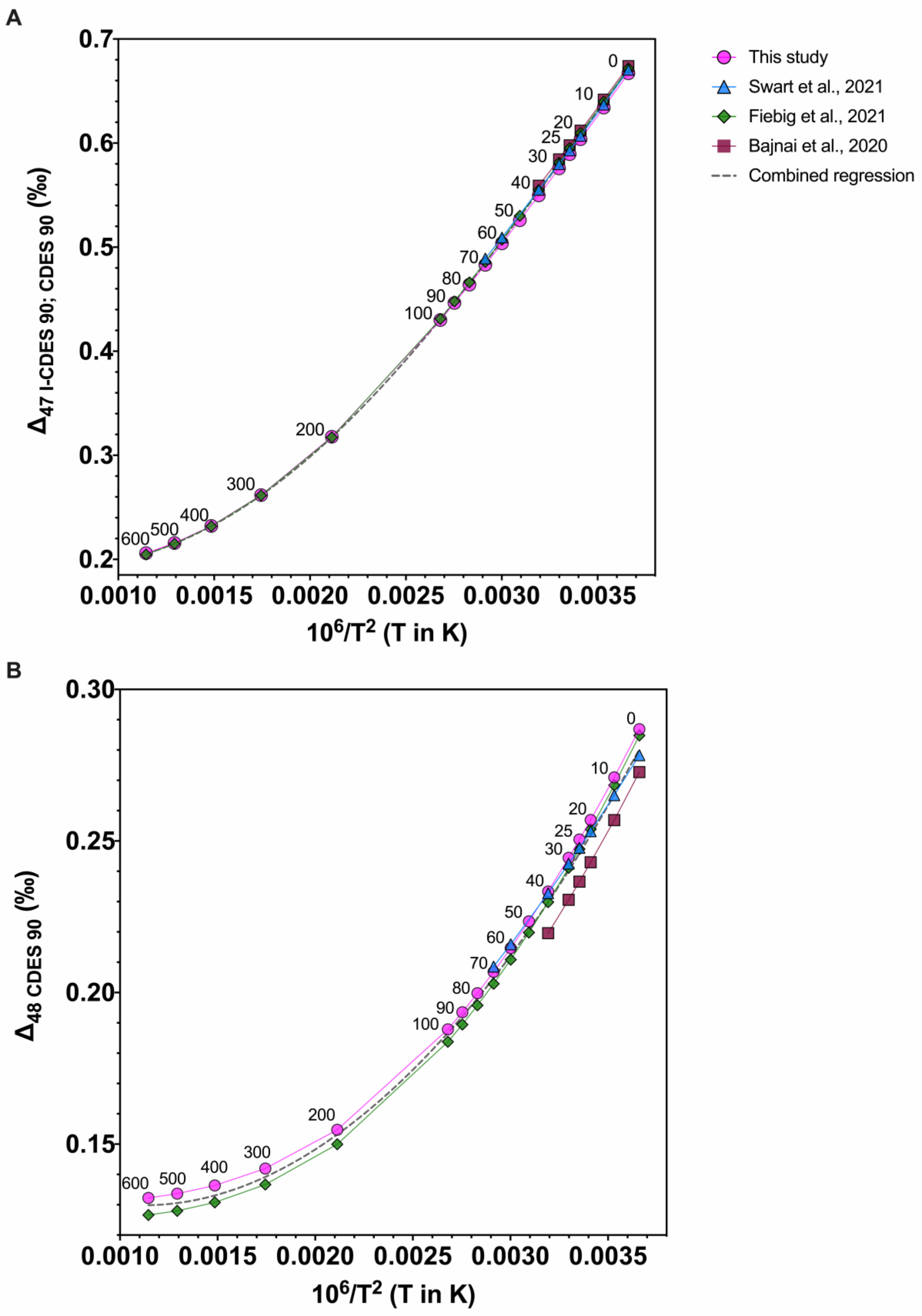
A
0.7
0.6
0.5
0.4
0.3
0.2
Δ47 I-CDES 90; CDES 90 (‰)
0.0010
0.0015
0.0020
0.0025
0.0030
0.0035
10⁶/T² (T in K)
0
10
20
25
30
40
50
60
70
80
90
100
200
300
400
500
600
This study
Swart et al., 2021
Fiebig et al., 2021
Bajnai et al., 2020
Combined regression
B
0.30
0.25
0.20
0.15
Δ48 CDES 90 (‰)
0.0010
0.0015
0.0020
0.0025
0.0030
0.0035
10⁶/T² (T in K)
0
10
20
25
30
40
50
60
70
80
90
100
200
300
400
500
600

**Figure 7. A)** $\Delta_{47}$-$T$ and B) $\Delta_{48}$-$T$ regressions from this study and Bajnai et al.[8] that rely on calcite $\Delta_{63}$-$\Delta_{64}$ equilibrium theory and experimental AFFs, and regressions from Swart et al.[9] and Fiebig et al.[10] that rely on experimentally constrained values. A combined regression for all datasets is represented by the gray dashed line. Numbers by the data points indicate temperature in Celsius.

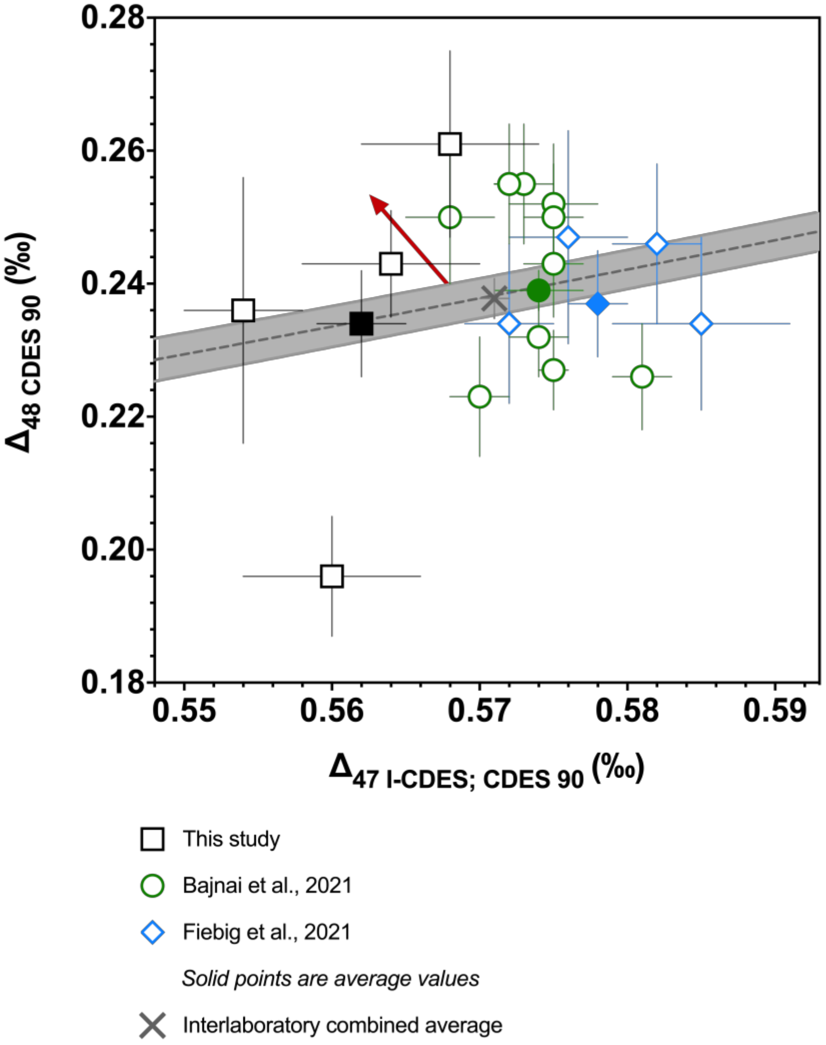

**Figure 8.** Plot showing $\Delta_{47}$-$\Delta_{48}$ values for Devils Hole cave calcite determined in this study, Bajnai et al.[44] and Fiebig et al.[10] The open points indicate individual samples, and solid points are the overall average from each study. The gray X is the combined average from all datasets. The gray dashed line is the combined experimental regression (equation 15 with the 95 % confidence interval).

| Standard | Mineralogy | Origin |
|---|---|---|
| **102-GC-AZ01** | calcite | Vein carbonate from Grand Canyon |
| **Carmel Chalk** | calcite | Chalk |
| **Carrara Marble** | calcite | Collected in Carrara, Tuscany, Italy. |
| **CM Tile** | calcite | Homogenized version of Carrara Marble (UCLA) |
| **47407 Coral** | aragonite | Deep sea coral, *Desmophyllum* |
| **DH-2-10** | calcite | Devils Hole - U.S. Geological Survey, Ash Meadows, Nevada. Core DH-2. 172 ± 4 ka |
| **DH-2-11** | calcite | Devils Hole - U.S. Geological Survey, Ash Meadows, Nevada. Core DH-2. 163 ± 5 ka |
| **DH-2-12** | calcite | Devils Hole - U.S. Geological Survey, Ash Meadows, Nevada. Core DH-2. 157 ± 5 ka |
| **DH-2-13** | calcite | Devils Hole - U.S. Geological Survey, Ash Meadows, Nevada. Core DH-2. 151 ± 4 ka |
| **ETH-1** | calcite | Carrara Marble, heated to 600°C at 155 MPa for 10 hours, sent from ETH Zurich |
| **ETH-2** | calcite | Reagent grade synthetic, subjected to same treatment as ETH-1, sent from ETH Zurich |
| **ETH-3** | calcite | Upper Cretaceous chalk (mostly coccoliths), Isle of Rügen, Germany, sent from ETH Zurich |
| **ETH-4** | calcite | Same reagent grade synthetic as ETH-2, but unheated, sent from ETH Zurich |
| **IAEA-C1** | calcite | Carrara Marble, from International Atomic Energy Agency |
| **IAEA-C2** | travertine | Collected in Bavaria. From International Atomic Energy Agency |
| **ISTB-1** | calcite | Speleothem from Yichang, Hubei province, China |
| **Mallinckrodt** | calcite | Synthetic, from Mallinckrodt Baker, Inc. |
| **MERCK** | calcite | Synthetic, from International Atomic Energy Agency |
| **NBS 19** | calcitic marble | Carrara Marble, from National Bureau of Standards |
| **Spel 2-8-E** | calcite | Speleothem |
| **SRM 88B** | dolomitic limestone | Collected from mine site near Skokie, Illinois, USA |
| **TB-1** | marble | Marble rock of marine origin from Quyang, Hebei province, China |
| **TB-2** | calcite | Hydrothermal calcite from Yanji, Jilin province, China |
| **TV01** | calcite | Travertine tile |
| **TV03** | calcite | Travertine tile |
| **Veinstrom** | calcite | Shallow carbonate vein collected from Tempiute Mountain, Nevada |

**Table 1**. Description of the mineralogy and origin for samples and standards analyzed in this study (Upadhyay et al., 2021; Chang et al., 2020; Bernasconi et al., 2018), including 4 samples of Devils Hole calcite. Uranium-series ages for Devils Hole vein calcite were determined by Winograd et al. (2006).

| Configuration | Mass spectrometer model | Acid digestion temperature | Acid Digestion System, sample size | m/z 44 ion beam intensity | Integration time | Use of equilibrated gas-based corrections | Use of carbonate-based corrections |
|---|---|---|---|---|---|---|---|
| **Nu Perspective- EG** | Nu Instruments Perspective | 90 °C | Common acid bath, 0.45-0.60 | 80 nA before 6/2017, 60 nA after | 1600 s | Yes, 25 and 1000 °C gases | No |
| **Nu Perspective-1** | Nu Instruments Perspective | 90 °C | Common acid bath,0.45-0.60 | 80 nA before 6/2017, 60 nA after | 1600 s | No | Yes |
| **Nu Perspective -1a** | Nu Instruments Perspective | 90 °C | Common acid bath, 0.45-0.60 | 80-30 nA | 1200 s | No | Yes |
| **Nu Perspective-2** | Nu Instruments Perspective | 70 °C | Nu Carb, 0.45-0.60 | 80-30 nA | 1200 s | No | Yes |
| **MAT 253** | Thermo Finnigan MAT 253 | 90 °C | Common acid bath, 5-7 mg | 16 V | 720 s | No | Yes |

**Table 2.** Description of mass spectrometer configurations used in this study.

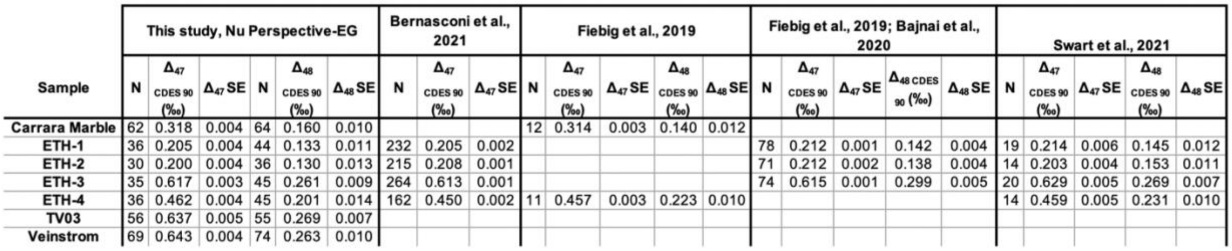

| | This study, Nu Perspective-EG | | | | | | Bernasconi et al., 2021 | | | Fiebig et al., 2019 | | | | | Fiebig et al., 2019; Bajnai et al., 2020 | | | | | Swart et al., 2021 | | | | |
|---|---|---|---|---|---|---|---|---|---|---|---|---|---|---|---|---|---|---|---|---|---|---|---|---|
| Sample | N | $\Delta_{47}$ CDES 90 (‰) | $\Delta_{47}$ SE | N | $\Delta_{48}$ CDES 90 (‰) | $\Delta_{48}$ SE | N | $\Delta_{47}$ CDES 90 (‰) | $\Delta_{47}$ SE | N | $\Delta_{47}$ CDES 90 (‰) | $\Delta_{47}$ SE | $\Delta_{48}$ CDES 90 (‰) | $\Delta_{48}$ SE | N | $\Delta_{47}$ CDES 90 (‰) | $\Delta_{47}$ SE | $\Delta_{48}$ CDES 90 (‰) | $\Delta_{48}$ SE | N | $\Delta_{47}$ CDES 90 (‰) | $\Delta_{47}$ SE | $\Delta_{48}$ CDES 90 (‰) | $\Delta_{48}$ SE |
| **Carrara Marble** | 62 | 0.318 | 0.004 | 64 | 0.160 | 0.010 | | | | 12 | 0.314 | 0.003 | 0.140 | 0.012 | | | | | | | | | | |
| **ETH-1** | 36 | 0.205 | 0.004 | 44 | 0.133 | 0.011 | 232 | 0.205 | 0.002 | | | | | | 78 | 0.212 | 0.001 | 0.142 | 0.004 | 19 | 0.214 | 0.006 | 0.145 | 0.012 |
| **ETH-2** | 30 | 0.200 | 0.004 | 36 | 0.130 | 0.013 | 215 | 0.208 | 0.001 | | | | | | 71 | 0.212 | 0.002 | 0.138 | 0.004 | 14 | 0.203 | 0.004 | 0.153 | 0.011 |
| **ETH-3** | 35 | 0.617 | 0.003 | 45 | 0.261 | 0.009 | 264 | 0.613 | 0.001 | | | | | | 74 | 0.615 | 0.001 | 0.299 | 0.005 | 20 | 0.629 | 0.005 | 0.269 | 0.007 |
| **ETH-4** | 36 | 0.462 | 0.004 | 45 | 0.201 | 0.014 | 162 | 0.450 | 0.002 | 11 | 0.457 | 0.003 | 0.223 | 0.010 | | | | | | 14 | 0.459 | 0.005 | 0.231 | 0.010 |
| **TV03** | 56 | 0.637 | 0.005 | 55 | 0.269 | 0.007 | | | | | | | | | | | | | | | | | | |
| **Veinstrom** | 69 | 0.643 | 0.004 | 74 | 0.263 | 0.010 | | | | | | | | | | | | | | | | | | |

**Table 3.** $\Delta_{47}$ and $\Delta_{48}$ for samples and standards analyzed on Nu Perspective-EG. All data in this table was standardized using only 25 and 1000 $^{o}$C equilibrated gases. Results are compared to values from Fiebig et al., (2019), Bajnai et al. (2020), and Swart et al. (2021).

| | Nu Perspective 1 | | | | | | | | Nu Perspective 2 | | | | | | | | MAT 253 | | | | | | | | Combined average (Nu Perspective 1, Nu Perspective 2, MAT 253 | | | | Combined average (Nu Perspective 1, Nu Perspective 1a, Nu Perspective 2) | | | |
|---|---|---|---|---|---|---|---|---|---|---|---|---|---|---|---|---|---|---|---|---|---|---|---|---|---|---|---|---|---|---|---|---|
| Standard | $\Delta_{47}$ I-CDES (‰) | N | $\Delta_{47}$ SD | $\Delta_{47}$ SE | $\Delta_{48}$ CDES 90 (‰) | N | $\Delta_{48}$ SD | $\Delta_{48}$ SE | $\Delta_{47}$ I-CDES (‰) | N | $\Delta_{47}$ SD | $\Delta_{47}$ SE | $\Delta_{48}$ CDES 90 (‰) | N | $\Delta_{48}$ SD | $\Delta_{48}$ SE | $\Delta_{47}$ I-CDES (‰) | N | $\Delta_{47}$ SD | $\Delta_{47}$ SE | $\Delta_{48}$ CDES 90 (‰) | N | $\Delta_{48}$ SD | $\Delta_{48}$ SE | $\Delta_{47}$ I-CDES (‰) | N | $\Delta_{47}$ SD | $\Delta_{47}$ SE | $\Delta_{48}$ CDES 90 (‰) | N | $\Delta_{48}$ SD | $\Delta_{48}$ SE |
| 102-GC-AZ01 | | | | | | | | | | | | | | | | | | | | | | | | | 0.598 | 24 | 0.028 | 0.006 | 0.240 | 24 | 0.057 | 0.012 |
| Carmel Chalk | 0.591 | 94 | 0.017 | 0.002 | 0.243 | 69 | 0.028 | 0.003 | *0.589 | 248 | 0.026 | 0.002 | 0.235 | 250 | 0.062 | 0.004 | 0.594 | 282 | 0.021 | 0.001 | 0.227 | 166 | 0.080 | 0.006 | 0.592 | 640 | 0.025 | 0.001 | 0.237 | 319 | 0.056 | 0.003 |
| Carrara Marble | 0.312 | 81 | 0.031 | 0.003 | 0.146 | 81 | 0.072 | 0.008 | 0.328 | 44 | 0.048 | 0.007 | 0.159 | 54 | 0.065 | 0.009 | 0.310 | 155 | 0.020 | 0.002 | 0.175 | 80 | 0.161 | 0.018 | 0.314 | 280 | 0.030 | 0.002 | 0.151 | 135 | 0.079 | 0.006 |
| Carrara Marble CIT | | | | | | | | | | | | | | | | | | | | | | | | | 0.326 | 21 | 0.027 | 0.006 | 0.144 | 24 | 0.081 | 0.017 |
| CMTile | | | | | 0.149 | 18 | 0.029 | 0.007 | 0.315 | 303 | 0.029 | 0.002 | 0.145 | 291 | 0.060 | 0.004 | 0.310 | 160 | 0.019 | 0.001 | 0.156 | 144 | 0.098 | 0.008 | 0.313 | 463 | 0.026 | 0.001 | 0.145 | 309 | 0.059 | 0.003 |
| 47407 Coral | | | | | | | | | | | | | | | | | | | | | | | | | 0.707 | 9 | 0.025 | 0.008 | 0.275 | 11 | 0.071 | 0.021 |
| DH-2-10 | | | | | | | | | | | | | | | | | | | | | | | | | 0.554 | 11 | 0.013 | 0.004 | 0.236 | 16 | 0.082 | 0.020 |
| DH-2-11 | | | | | | | | | | | | | | | | | | | | | | | | | 0.560 | 19 | 0.027 | 0.006 | 0.196 | 17 | 0.035 | 0.009 |
| DH-2-12 | | | | | | | | | | | | | | | | | | | | | | | | | 0.564 | 18 | 0.025 | 0.006 | 0.243 | 16 | 0.032 | 0.008 |
| DH-2-13 | | | | | | | | | | | | | | | | | | | | | | | | | 0.568 | 17 | 0.027 | 0.006 | 0.261 | 19 | 0.063 | 0.014 |
| DH-2 Combined | | | | | | | | | | | | | | | | | | | | | | | | | 0.562 | 65 | 0.024 | 0.003 | 0.234 | 68 | 0.058 | 0.007 |
| ETH-1 | *0.207 | 85 | 0.025 | 0.003 | *0.130 | 88 | 0.051 | 0.005 | *0.205 | 402 | 0.026 | 0.001 | *0.133 | 376 | 0.065 | 0.003 | *0.206 | 284 | 0.020 | 0.001 | *0.139 | 188 | 0.105 | 0.008 | 0.206 | 771 | 0.023 | 0.001 | 0.132 | 464 | 0.062 | 0.003 |
| ETH-2 | *0.208 | 69 | 0.020 | 0.002 | *0.131 | 73 | 0.064 | 0.008 | *0.206 | 386 | 0.027 | 0.001 | *0.133 | 366 | 0.056 | 0.003 | *0.207 | 271 | 0.024 | 0.001 | *0.156 | 204 | 0.110 | 0.008 | 0.206 | 726 | 0.025 | 0.001 | 0.132 | 439 | 0.058 | 0.003 |
| ETH-3 | *0.612 | 69 | 0.023 | 0.003 | *0.244 | 68 | 0.054 | 0.007 | *0.602 | 184 | 0.027 | 0.002 | *0.249 | 168 | 0.058 | 0.004 | *0.614 | 210 | 0.022 | 0.002 | *0.25 | 145 | 0.082 | 0.007 | 0.609 | 463 | 0.025 | 0.001 | 0.247 | 236 | 0.057 | 0.004 |
| ETH-4 | 0.455 | 64 | 0.020 | 0.003 | 0.198 | 70 | 0.059 | 0.007 | 0.441 | 191 | 0.026 | 0.002 | 0.203 | 187 | 0.058 | 0.004 | 0.445 | 208 | 0.021 | 0.001 | 0.206 | 171 | 0.106 | 0.008 | 0.445 | 463 | 0.023 | 0.001 | 0.201 | 257 | 0.058 | 0.004 |
| IAEA-C1 | | | | | | | | | 0.300 | 68 | 0.025 | 0.003 | 0.143 | 49 | 0.056 | 0.008 | 0.294 | 15 | 0.017 | 0.004 | 0.142 | 15 | 0.141 | 0.036 | 0.299 | 83 | 0.024 | 0.003 | 0.143 | 49 | 0.056 | 0.008 |
| IAEA-C2 | | | | | | | | | 0.642 | 60 | 0.025 | 0.003 | 0.273 | 59 | 0.062 | 0.008 | 0.624 | 14 | 0.021 | 0.005 | 0.236 | 13 | 0.067 | 0.018 | 0.638 | 74 | 0.025 | 0.003 | 0.273 | 59 | 0.062 | 0.008 |
| ISTB-1 | | | | | | | | | | | | | | | | | | | | | | | | | 0.663 | 15 | 0.059 | 0.015 | 0.297 | 12 | 0.047 | 0.014 |
| Mallinckrodt | | | | | | | | | | | | | | | | | 0.465 | 16 | 0.042 | 0.011 | 0.136 | 13 | 0.081 | 0.023 | 0.465 | 16 | 0.042 | 0.011 | | | | |
| Merck | | | | | | | | | 0.514 | 67 | 0.030 | 0.004 | 0.234 | 59 | 0.055 | 0.007 | 0.514 | 14 | 0.030 | 0.008 | 0.175 | 11 | 0.170 | 0.051 | 0.514 | 81 | 0.030 | 0.003 | 0.234 | 59 | 0.055 | 0.007 |
| NBS 19 | | | | | | | | | | | | | | | | | 0.316 | 8 | 0.025 | 0.009 | 0.116 | 7 | 0.073 | 0.027 | 0.316 | 8 | 0.025 | 0.009 | | | | |
| SPEL-2-8-E | | | | | | | | | | | | | | | | | | | | | | | | | 0.596 | 11 | 0.035 | 0.011 | 0.245 | 11 | 0.089 | 0.027 |
| SRM88B | | | | | | | | | | | | | | | | | 0.528 | 11 | 0.017 | 0.005 | 0.424 | 10 | 0.153 | 0.048 | 0.528 | 11 | 0.017 | 0.005 | | | | |
| TB-1 | | | | | | | | | | | | | | | | | | | | | | | | | 0.327 | 21 | 0.034 | 0.007 | 0.133 | 23 | 0.089 | 0.019 |
| TB-2 | | | | | | | | | | | | | | | | | | | | | | | | | 0.335 | 19 | 0.035 | 0.008 | 0.164 | 19 | 0.095 | 0.022 |
| TV01 | | | | | | | | | | | | | | | | | | | | | | | | | 0.619 | 22 | 0.028 | 0.006 | 0.260 | 25 | 0.077 | 0.015 |
| TV03 | 0.626 | 47 | 0.019 | 0.003 | 0.267 | 58 | 0.043 | 0.006 | | | | | | | | | 0.626 | 80 | 0.019 | 0.002 | 0.212 | 32 | 0.063 | 0.011 | 0.626 | 127 | 0.019 | 0.002 | 0.267 | 58 | 0.043 | 0.006 |
| Veinstrom | 0.636 | 102 | 0.026 | 0.003 | 0.272 | 100 | 0.066 | 0.007 | *0.634 | 322 | 0.030 | 0.002 | *0.274 | 336 | 0.059 | 0.003 | 0.632 | 304 | 0.023 | 0.001 | 0.252 | 193 | 0.079 | 0.006 | 0.633 | 728 | 0.026 | 0.001 | 0.273 | 436 | 0.061 | 0.003 |

**Table 4.** Individual instrument and longterm combined average $\Delta_{47}$ and $\Delta_{48}$ values for all samples and standards analyzed in this study. $\Delta_{48}$ values from MAT 253 (gray columns) were not included in the combined instrument average and are given for informational purposes only. Samples with an asterisk (*) were used as standards in corrections for data normalization.

| Temperature | $\Delta_{63}$ (‰) (Hill et al., 2014; Tripati et al., 2015) | $\Delta^*_{63\text{-}47}$ (‰) | $\Delta_{47\text{ I-CDES}}$ (‰) | $\Delta_{64}$ (‰) (Hill et al., 2014; Tripati et al., 2015) | $\Delta^*_{64\text{-}48}$ (‰) | $\Delta_{48\text{ CDES 90}}$ (‰) |
|---|---|---|---|---|---|---|
| 0 | 0.470 | 0.197 | 0.667 | 0.156 | 0.131 | 0.287 |
| 10 | 0.438 | 0.196 | 0.634 | 0.140 | 0.131 | 0.271 |
| 20 | 0.408 | 0.196 | 0.604 | 0.126 | 0.131 | 0.257 |
| 22 | 0.402 | 0.196 | 0.598 | 0.123 | 0.131 | 0.254 |
| 25 | 0.394 | 0.195 | 0.589 | 0.120 | 0.131 | 0.251 |
| 30 | 0.381 | 0.195 | 0.576 | 0.114 | 0.131 | 0.245 |
| 33.7 (DH-2) | 0.371 | 0.195 | 0.566 | 0.109 | 0.131 | 0.240 |
| 40 | 0.355 | 0.195 | 0.550 | 0.103 | 0.131 | 0.233 |
| 50 | 0.332 | 0.194 | 0.526 | 0.093 | 0.131 | 0.224 |
| 60 | 0.310 | 0.194 | 0.504 | 0.084 | 0.131 | 0.215 |
| 70 | 0.290 | 0.193 | 0.483 | 0.076 | 0.131 | 0.207 |
| 80 | 0.271 | 0.193 | 0.464 | 0.069 | 0.131 | 0.200 |
| 90 | 0.254 | 0.193 | 0.446 | 0.063 | 0.131 | 0.194 |
| 100 | 0.238 | 0.192 | 0.430 | 0.058 | 0.130 | 0.188 |
| 200 | 0.128 | 0.190 | 0.318 | 0.025 | 0.130 | 0.155 |
| 300 | 0.073 | 0.189 | 0.262 | 0.012 | 0.130 | 0.142 |
| 400 | 0.044 | 0.189 | 0.232 | 0.006 | 0.130 | 0.136 |
| 500 | 0.027 | 0.188 | 0.216 | 0.004 | 0.130 | 0.134 |
| 600 | 0.018 | 0.188 | 0.206 | 0.002 | 0.130 | 0.132 |
| 700 | 0.012 | 0.188 | 0.200 | 0.002 | 0.130 | 0.132 |
| 800 | 0.009 | 0.188 | 0.197 | 0.001 | 0.130 | 0.131 |
| 900 | 0.006 | 0.188 | 0.194 | 0.001 | 0.130 | 0.131 |
| 1000 | 0.005 | 0.188 | 0.192 | 0.001 | 0.130 | 0.131 |

**Table 5.** Theoretical equilibrium $\Delta_{63}$ and $\Delta_{64}$ for calcite (Hill et al., 2014; Tripati et al., 2015), acid fractionation factors (AFFs) $\Delta^*_{63\text{-}47}$ and $\Delta^*_{64\text{-}48}$ for the phosphoric acid digestion of calcite to $CO_2$, and calcite equilibrium $\Delta_{47}$ and $\Delta_{48}$ values. The AFFs were calculated using regressions determined from the difference in theoretical $\Delta_{63}$ and $\Delta_{64}$ values at 600 $^{o}$C and 33.7 $^{o}$C and samples with known precipitation temperatures, ETH-1 (600 $^{o}$C), ETH-2 (600 $^{o}$C), and Devils Hole calcite (33.7 $^{o}$C). $\Delta_{47}$ and $\Delta_{48}$ values were calculated as $\Delta_{63} + \Delta^*_{63\text{-}47} = \Delta_{47\text{ I-CDES}}$ and $\Delta_{64} + \Delta^*_{64\text{-}48} = \Delta_{48\text{ CDES 90}}$, using equations 7 and 8, respectively.

|  | Sample | Age (ka) | N | $\Delta_{47\ \text{I-CDES}}$ (‰) | $\Delta_{47\ \text{CDES 90}}$ (‰) | $\Delta_{47}$ SE | N | $\Delta_{48\ \text{CDES 90}}$ (‰) | $\Delta_{48}$ SE |
|---|---|---|---|---|---|---|---|---|---|
| **This study** | DH-2-10 | 168-176 | 11 | 0.554 |  | 0.004 | 16 | 0.236 | 0.020 |
|  | DH-2-11 | 159-167 | 19 | 0.560 |  | 0.006 | 17 | 0.196 | 0.009 |
|  | DH-2-12 | 152-162 | 18 | 0.564 |  | 0.006 | 16 | 0.243 | 0.008 |
|  | DH-2-13 | 146-156 | 17 | 0.568 |  | 0.006 | 19 | 0.261 | 0.014 |
|  | Average |  | 65 | 0.562 |  | 0.003 | 68 | 0.234 | 0.007 |
| **Bajnai et al., 2021** | DHC2-8 | 4.5-16.9 | 14 |  | 0.573 | 0.002 | 9 | 0.255 | 0.009 |
|  | DHC2-3 | 32.2-39.8 | 9 |  | 0.575 | 0.003 | N is the same as for $\Delta_{47}$ | 0.252 | 0.009 |
|  | DH-11 19.7 | 86.4-94.3 | 9 |  | 0.572 | 0.001 |  | 0.255 | 0.009 |
|  | DH-11 44.5 | 121.8-123.7 | 12 |  | 0.581 | 0.002 |  | 0.226 | 0.008 |
|  | DH-11 73.0 | 176.1-184.8 | 9 |  | 0.575 | 0.002 |  | 0.250 | 0.008 |
|  | DH-11 109.4 | 232.8-240.5 | 23 |  | 0.575 | 0.001 |  | 0.227 | 0.006 |
|  | DH-11 141.6 | 291.3-299.0 | 9 |  | 0.570 | 0.002 |  | 0.223 | 0.009 |
|  | DH-11 189.9 | 353.0-358.3 | 14 |  | 0.574 | 0.002 |  | 0.232 | 0.006 |
|  | DH-11 201.3 | 371.7-388.4 | 9 |  | 0.568 | 0.002 |  | 0.250 | 0.010 |
|  | DH-11 296.6 | 485.5-507.8 | 8 |  | 0.575 | 0.002 |  | 0.243 | 0.008 |
|  | Average |  | 116 |  | 0.574 | 0.003 | 111 | 0.239 | 0.003 |
| **Fiebig et al., 2021** | DVH-2 | 4.5-16.9 | 9 | 0.582 |  | 0.003 | N is the same as for $\Delta_{47}$ | 0.246 | 0.012 |
|  | DHC2-8 | 4.5-16.9 | 8 | 0.585 |  | 0.006 |  | 0.234 | 0.013 |
|  | DHC2-8 | 4.5-16.9 | 9 | 0.572 |  | 0.003 |  | 0.234 | 0.012 |
|  | DHC2-8 | 4.5-16.9 | 5 | 0.576 |  | 0.004 |  | 0.247 | 0.016 |
|  | Average |  | 31 | 0.580 |  | 0.002 | 31 | 0.237 | 0.008 |
| Combined average | Average |  | 212 | 0.571 |  | 0.001 | 210 | 0.238 | 0.007 |

**Table 6.** $\Delta_{47}$ and $\Delta_{48}$ data for Devils Hole cave calcite from this study, Bajnai et al. (2021), and Fiebig et al. (2021).

# Supplementary Figures

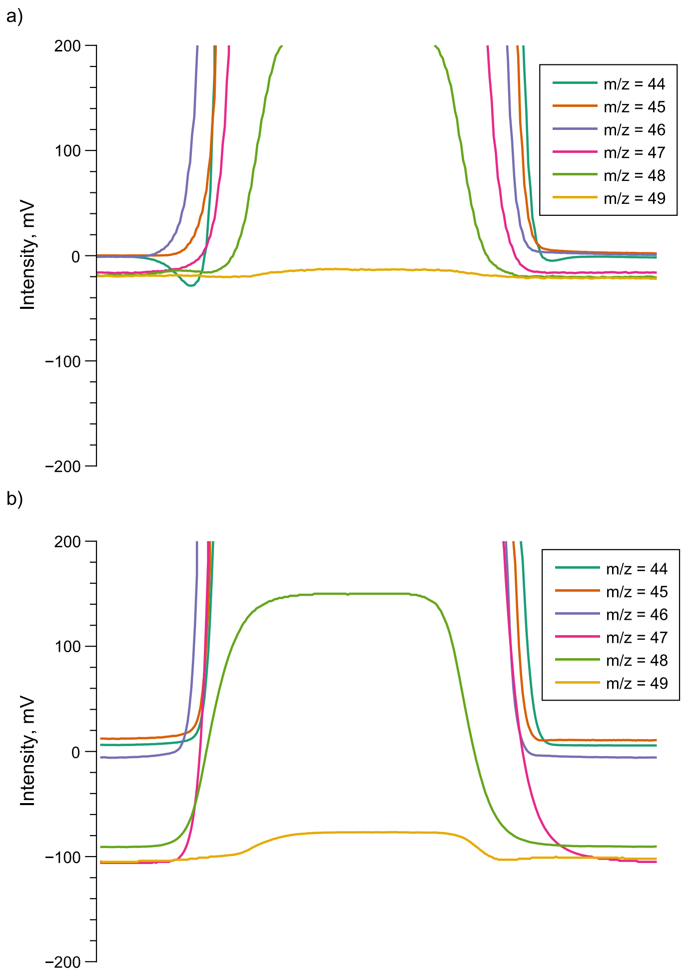

**Figure S1.** Simultaneous peakshape scans of the $CO_2$ mass peaks on a) the MAT 253, and b) the Nu Perspective-1. The Nu Perspective-1 scans have been converted to mV so that the scans are immediately comparable. The older generation MAT 253 shows negative going baselines, most readily seen on the *m/z* = 44 scan, that is not present in the Nu Perspective-1. The flatter baselines of the Nu Perspectives allow for larger and more stable intensities of the higher masses (*m/z* = 47-49) to be recorded.

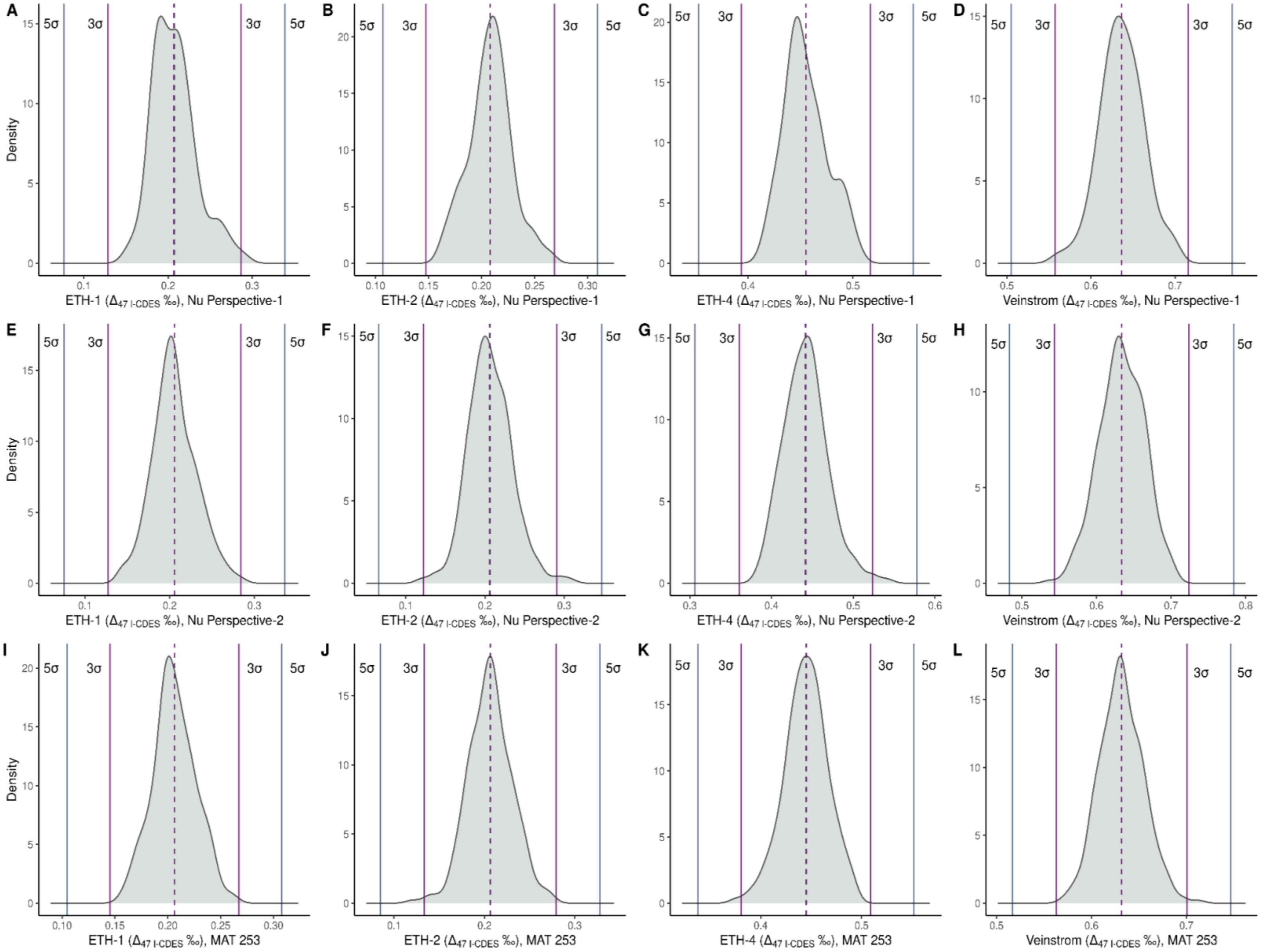
A
5σ
3σ
3σ
5σ
Density
0
5
10
15
0.1
0.2
0.3
ETH-1 ($\Delta_{47\ \text{I-CDES}}$ ‰), Nu Perspective-1
B
5σ
3σ
3σ
5σ
0
5
10
15
20
0.10
0.15
0.20
0.25
0.30
ETH-2 ($\Delta_{47\ \text{I-CDES}}$ ‰), Nu Perspective-1
C
5σ
3σ
3σ
5σ
0
5
10
15
20
0.4
0.5
ETH-4 ($\Delta_{47\ \text{I-CDES}}$ ‰), Nu Perspective-1
D
5σ
3σ
3σ
5σ
0
5
10
15
0.5
0.6
0.7
Veinstrom ($\Delta_{47\ \text{I-CDES}}$ ‰), Nu Perspective-1
E
5σ
3σ
3σ
5σ
Density
0
5
10
15
0.1
0.2
0.3
ETH-1 ($\Delta_{47\ \text{I-CDES}}$ ‰), Nu Perspective-2
F
5σ
3σ
3σ
5σ
0
5
10
15
0.1
0.2
0.3
ETH-2 ($\Delta_{47\ \text{I-CDES}}$ ‰), Nu Perspective-2
G
5σ
3σ
3σ
5σ
0
5
10
15
0.3
0.4
0.5
0.6
ETH-4 ($\Delta_{47\ \text{I-CDES}}$ ‰), Nu Perspective-2
H
5σ
3σ
3σ
5σ
0
5
10
0.5
0.6
0.7
0.8
Veinstrom ($\Delta_{47\ \text{I-CDES}}$ ‰), Nu Perspective-2
I
5σ
3σ
3σ
5σ
Density
0
5
10
15
20
0.10
0.15
0.20
0.25
0.30
ETH-1 ($\Delta_{47\ \text{I-CDES}}$ ‰), MAT 253
J
5σ
3σ
3σ
5σ
0
5
10
15
0.1
0.2
0.3
ETH-2 ($\Delta_{47\ \text{I-CDES}}$ ‰), MAT 253
K
5σ
3σ
3σ
5σ
0
5
10
15
0.4
0.5
ETH-4 ($\Delta_{47\ \text{I-CDES}}$ ‰), MAT 253
L
5σ
3σ
3σ
5σ
0
5
10
15
0.5
0.6
0.7
Veinstrom ($\Delta_{47\ \text{I-CDES}}$ ‰), MAT 253

**Figure S2.** Density curves for *Δ*$_{47}$ values measured from the anchor standards ETH-1 and ETH-2, and non-anchor standards ETH-4 and Veinstrom on Nu-Perspective-1 (**A-D)**, Nu-Perspective-2 **(E-H)**, and MAT 253 **(I-L)**. In all plots, dashed vertical lines indicate the mean using a 3σ cutoff (purple) and 5σ cutoff (blue); these lines are too close together to be visually distinguished and so the mean values are reported in text. **A)** ETH-1 on Nu-Perspective-1. If using a 3σ cutoff, final mean = 0.2066 ‰, SD = 0.025, N = 85. If using a 5σ cutoff, final mean = 0.2076 ‰, SD = 0.026, N = 86. **B)** ETH-2 on Nu-Perspective-1. Regardless of whether a 3σ or 5σ cutoff is used, final mean = 0.2081 ‰, SD = 0.020, N = 69. **C)** ETH-4 on Nu-Perspective-1. Regardless of whether a 3σ or 5σ cutoff is used, final mean = 0.4552 ‰, SD = 0.020, N = 64. **D)** Veinstrom on Nu-Perspective-1. Regardless of whether a 3σ or 5σ cutoff is used, final mean = 0.6365 ‰, SD = 0.026, N = 102. **E)** ETH-1 on Nu-Perspective-2. If using a 3σ cutoff, final mean = 0.2053 ‰, SD = 0.026, N = 402. If using a 5σ cutoff, final mean = 0.2055 ‰, SD = 0.026, N = 403. **F)** ETH-2 on Nu-Perspective-2. If using a 3σ cutoff, final mean = 0.2060 ‰, SD = 0.026, N = 386. If using a 5σ cutoff, final mean = 0.2065 ‰, SD = 0.028, N =390. **G)** ETH-4 on Nu-Perspective-2. If using a 3σ cutoff, final mean = 0.4411 ‰, SD = 0.026, N = 191. If using a 5σ cutoff, final mean = 0.4420 ‰, SD = 0.027, N = 193. **H)** Veinstrom on Nu-Perspective-2. If using a 3σ cutoff, final mean = 0.6341 ‰, SD = 0.030, N = 322. If using a 5σ cutoff, final mean = 0.6338 ‰, SD = 0.030, N = 323. **I)** ETH-1 on MAT 253. Regardless of whether a 3σ or 5σ cutoff is used, final mean = 0.2063 ‰, SD = 0.020, N = 284. **J)** ETH-2 on MAT 253. If using a 3σ cutoff, final mean = 0.2066 ‰, SD = 0.024, N = 271. If using a 5σ cutoff, final mean = 0.2063 ‰, SD =

0.024, N = 272. **K)** ETH-4 on MAT 253. If using a 3σ cutoff, final mean = 0.4451 ‰, SD = 0.021, N = 208. If using a 5σ cutoff, final mean = 0.4448 ‰, SD = 0.021, N = 209. **L)** Veinstrom on MAT 253. If using a 3σ cutoff, final mean = 0.6315 ‰, SD = 0.022, N = 304. If using a 5σ cutoff, final mean = 0.6318 ‰, SD = 0.023, N = 305.

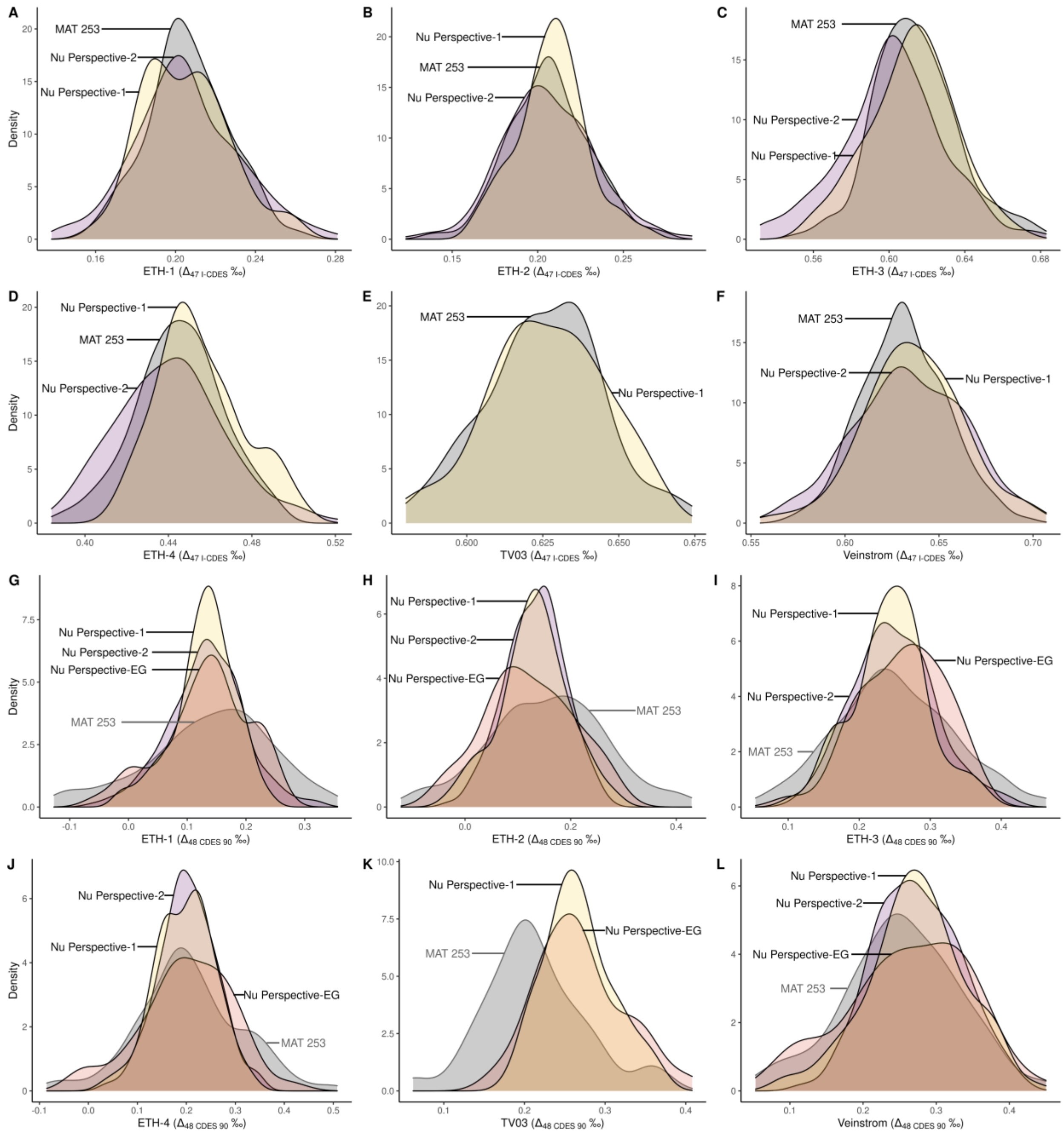
A
MAT 253
Nu Perspective-2
Nu Perspective-1
Density
ETH-1 ($\Delta_{47\ \text{I-CDES}}$ ‰)
B
Nu Perspective-1
MAT 253
Nu Perspective-2
ETH-2 ($\Delta_{47\ \text{I-CDES}}$ ‰)
C
MAT 253
Nu Perspective-2
Nu Perspective-1
ETH-3 ($\Delta_{47\ \text{I-CDES}}$ ‰)
D
Nu Perspective-1
MAT 253
Nu Perspective-2
Density
ETH-4 ($\Delta_{47\ \text{I-CDES}}$ ‰)
E
MAT 253
Nu Perspective-1
TV03 ($\Delta_{47\ \text{I-CDES}}$ ‰)
F
MAT 253
Nu Perspective-2
Nu Perspective-1
Veinstrom ($\Delta_{47\ \text{I-CDES}}$ ‰)
G
Nu Perspective-1
Nu Perspective-2
Nu Perspective-EG
MAT 253
Density
ETH-1 ($\Delta_{48\ \text{CDES}\ 90}$ ‰)
H
Nu Perspective-1
Nu Perspective-2
Nu Perspective-EG
MAT 253
ETH-2 ($\Delta_{48\ \text{CDES}\ 90}$ ‰)
I
Nu Perspective-1
Nu Perspective-EG
Nu Perspective-2
MAT 253
ETH-3 ($\Delta_{48\ \text{CDES}\ 90}$ ‰)
J
Nu Perspective-2
Nu Perspective-1
Nu Perspective-EG
MAT 253
Density
ETH-4 ($\Delta_{48\ \text{CDES}\ 90}$ ‰)
K
Nu Perspective-1
Nu Perspective-EG
MAT 253
TV03 ($\Delta_{48\ \text{CDES}\ 90}$ ‰)
L
Nu Perspective-1
Nu Perspective-2
Nu Perspective-EG
MAT 253
Veinstrom ($\Delta_{48\ \text{CDES}\ 90}$ ‰)

**Figure S3.** Final density distributions of the standards ETH-1, ETH-2, ETH-3, ETH-4, TV03, and Veinstrom, measured on multiple instrument configurations for $\Delta_{47\text{ I-CDES}}$ values **(A-F)** and $\Delta_{48}$ values **(G-L)**. We found no statistically significant differences in final values for each of the standards between any of the configurations. $\Delta_{48\text{ CDES }90}$ values from MAT 253 are provided for informational purposes only and were not included in analyses. **A)** $\Delta_{47}$ values for ETH-1 on Nu Perspective-1, Nu Perspective-2, and MAT 253. **B)** $\Delta_{47}$ values for ETH-2 on Nu Perspective-1, Nu Perspective-2, and MAT 253. **C)** $\Delta_{47}$ values for ETH-3 on Nu Perspective-1, Nu Perspective-2, and MAT 253. **D)** $\Delta_{47}$ values for ETH-4 on Nu Perspective-1, Nu Perspective-2, and MAT 253. **E)** $\Delta_{47\text{ I-CDES}}$ values for TV03 on Nu Perspective-1, and MAT 253. **F)** $\Delta_{47}$ values for Veinstrom on Nu Perspective-1, Nu Perspective-2, and MAT 253. **G)** $\Delta_{48}$ values for ETH-1 on Nu Perspective-1, Nu Perspective-2, Nu Perspective-EG and MAT 253. **H)** $\Delta_{48\text{ CDES }90}$ values for ETH-2 on Nu Perspective-1, Nu Perspective-2, Nu Perspective-EG and MAT 253. **I)** $\Delta_{48}$ values for ETH-3 on Nu Perspective-1, Nu Perspective-2, Nu Perspective-EG and MAT 253. **J)** $\Delta_{48}$ values for ETH-4 on Nu Perspective-1, Nu Perspective-2, Nu Perspective-EG and MAT 253. **K)** $\Delta_{48}$ values for TV03 on Nu Perspective-1, Nu Perspective-EG and MAT 253. **J)** $\Delta_{48}$ values for Veinstrom on Nu Perspective-1, Nu Perspective-2, Nu Perspective-EG and MAT 253.

## Appendix

Lucarelli, J., Carroll, H., Elliott, B., Coplen, T., Eagle, R., Tripati, A. Equilibrated gas and carbonate standard-derived paired clumped isotope ($\Delta_{47}$ and $\Delta_{48}$) values on the absolute reference frame, Rapid Communications in Mass Spectrometry

| Term | Definition | Abbreviation |
|---|---|---|
| Estimated marginal mean | Groupwise mean calculated from a model fit to data | EMM |
| Ordinary marginal mean | Groupwise mean calculated directly from data | OMM |
| Standard deviation | σ (sigma) | SD |
| Standard error | Standard deviation divided by the square root of the number of observations: $\frac{\sigma}{\sqrt{n}}$ | SE |

### A.1 Background of statistical methods used

For $\Delta_{47}$ and $\Delta_{48}$ quality assurance, we adapted screening criteria used in other disciplines, implementing kernel density estimation as a statistical technique for use with clumped isotope data. Kernel density estimation has a broad range of research applications, including economics[56], ecology[57], climate modeling[58], weather forecasting[59], and manufacturing controls[60], among others. We chose this approach for its relative simplicity of calculation and ability to eliminate extreme values from the dataset. Extreme values must be eliminated prior to employing a cut at 3σ because the standard deviation may be strongly affected by their presence. For each sample, we calculated a kernel density estimate using the generic S3 method ‘density’ included in base R’s stats package.[61] In quality screening of clumped isotope data, a nonparametric approach, such as kernel density estimation, is preferred because we often have no *a priori* knowledge of the statistical properties of the raw clumped isotope replicate pool. In density estimation, a weighting function, known as a kernel, is applied to the data; in the R implementation of kernel density estimation, the default is to use a normally distributed (Gaussian) kernel, *K*, applied to a variable, *u*. The normal distribution takes the form:

$$K(u) = \frac{1}{\sqrt{2\pi}} e^{\frac{-1}{2}u^2}$$

The smoothing parameter, known as bandwidth, using the default normally distributed kernel, is set to equal the standard deviation of the kernel, or weighting function, itself.[61] The kernel then becomes a curve that integrates to 1 with the statistical properties:

$$\sigma^2(K) = t^2 K(t) dt$$

For a full explanation of bandwidth selection in nonparametric probability density estimation, see Sheather & Jones[62]; for a full explanation of kernel density estimation as implemented in R, see Deng & Wickham[63].

Kernel density estimation is used to examine the underlying probability density function (PDF) for a given variable. Each clumped isotope sample value is not a single definite point, due to the uncertainty inherent in replicate measurements, but is rather a finite probable range of values. This can be visualized as a peak where the most probable values for a given variable cluster together to produce the peak's maxima; this is the probability density function. This is similar to the way in which histograms demonstrate data distributions based on counts (Figure 3A in main text). From the PDF peak for each standard, we found the nearest minima, or least probable values of the possible range, on either side of the maxima, or most probable value, and defined those minima as the initial cutpoints for exclusion (Figure 3B). In cases where the PDF revealed a double peak or a shoulder at least a third as high as the true maxima, we used the second nearest minima or left/right minima according to the shape of the density peak. We chose a cutoff of 1/3 as high as the true maxima because it produced final $\Delta_{47}$ sample mean data in good agreement with data processed using other methods (Table S2).

The PDF-based exclusion method has been included as a custom function in a publicly available R script (available on GitHub at https://github.com/Tripati-Lab/Lucarelli-et-al; all code and data will be permanently archived on Dryad upon acceptance for publication and a static link make available here), and instructions for its use are given in the script. Hereafter, we refer to this statistical technique as the “PDF method” for the sake of brevity.

Following initial screening using the PDF method, we employed a 3σ exclusion which yielded results for $\Delta_{47}$ and $\Delta_{48}$ that were consistent across instruments. A Shapiro-Wilk test was used to determine whether the resulting data were consistent with a normal distribution.

### A.1.1 Inter-instrumental comparisons and data pooling

Five mass spectrometer configurations (Table 2 in main text) were used to measure clumped isotopes in this study. To ensure it was appropriate to pool data produced using different mass spectrometer configurations, we performed statistical tests comparing individual sample mean values produced on each configuration and also the overall cumulative comparability of each configuration. To test for any differences between configurations that would preclude pooling data for analyses, we modeled final clumped isotope values by the additive effects of configuration and sample using a linear mixed effects model from package *nlme* version 3.1-152[64] after Upadhyay et al.[32] Linear mixed effects models provide a convenient extension to conventional linear models, in that they allow for both fixed effects (the independent variables) and random effects (additional variables which may affect the dependent variables, but which are not being explicitly modeled). The standard error of the final clumped isotope replicate was included as a random effect in the model. Including SE as a random effect in the model is done to capture the effect of differences in precision from measurement to measurement, and account for them in the calculation of model coefficients. Standard error is considered a random effect instead of a fixed effect (i.e., a predictor or independent variable) because it is not constant across observations in a given dataset. Standard regression models, that is, fixed effects models, are more accurate when error is relatively uniform across observations. They carry the risk of being overly sensitive to random error in the dataset when it is not uniform, which leads to bias in estimating the relationship between the independent and dependent variables. Mixed effects models account for the non-uniform random error and reduce that risk. However, mixed effects models can produce bias if the error is entirely uncorrelated with the relationship between the independent and dependent variables. In practice, this is extremely unlikely. Models did not include samples that were run rarely on these instruments, and for which we have few replicates (ISTB-1, TB-1, TB-2, CIT Carrara, DH-2-10, DH-2-11, DH-2-12, DH-2-13, TV01, 47407 Coral, Spel-2-8-E, and 102-GC-AZ01).

Pairwise differences between configurations were then assessed using contrasts with adjustment for multiple comparisons from package *emmeans* version 1.5.4.[65] Estimated marginal means, used here for inter-instrumental comparisons, are preferred to ordinary marginal means because they control for differences in the number of analyses run on individual configurations. Marginal means are defined as the mean value of a given group. For example, an ordinary mean for the standard ETH-1 would be the mean calculated from all available replicates of ETH-1, without taking the instruments which produced them into account. By contrast, ordinary marginal means would consist of a separate mean value for ETH-1 for each of the mass spectrometers on which it was measured. These are reported throughout the manuscript wherever a mass spectrometer configuration is specified. Estimated marginal means, used here for inter-instrumental comparisons, are based on a model fit to the data, rather than the raw data. This has the effect of controlling for unequal numbers of observations per group, such that the final value for a given sample produced by an instrument which has an N = 50 is not downweighted relative to an instrument which has an N = 150. This is useful when comparing the values produced by one instrument to another, as unequal numbers of observations violate the assumptions of most parametric statistical tests and may lead to erroneous conclusions. As the estimated marginal means differ slightly from the more commonly reported ordinary marginal means, we use them strictly for inter-instrumental comparisons, and report ordinary marginal means throughout the rest of the manuscript. Data were pooled for further analyses only if there was no evidence of a statistically significant difference between configurations across any of the samples reported herein.

### A.1.2 Statistical method implementation

This section contains step-by-step instructions with examples for working with the custom R script available at https://github.com/Tripati-Lab/Lucarelli-et-al. Note that the subset of data present here is unusually noisy for demonstration purposes, and more replicates are removed than what is typically observed in a real dataset. We chose this subset so that users would be able to clearly follow our descriptions and visualize changes in the data distribution.

Samples or standards with multiple aliquots should be grouped. For example, many labs will utilize ETH-1. Aliquots included in this study are 1-4. If these are coded by aliquot number, such as ETH-1-1, ETH-1-2, etc., these should be grouped together and named ETH-1. As an example:

```
unique(data$Easotope_Name)
##  [1] "TV03"          "Veinstrom"      "Carmel Chalk"   "ETH-1-1"
##  [5] "ETH-2-1"       "ETH-3-1"        "ETH-4-1"        "Carrara Marble"
##  [9] "ETH-2-2"       "ETH-3-3"        "ETH-4-2"        "ETH-1-2"
## [13] "ETH-1-3"       "ETH-2-3"
```

We have multiple aliquots of ETH-1, ETH-2, ETH-3, and ETH-4. The rest of the samples/standareds are not given aliquot numbers. We only need to group the ETH standards. We use partial string matching for this purpose:

```
library(dplyr)


data <- data %>%
  mutate(Standard = case_when(
    !grepl("ETH", Easotope_Name) ~ Easotope_Name,
    grepl("ETH-1", Easotope_Name) ~ "ETH-1",
    grepl("ETH-2", Easotope_Name) ~ "ETH-2",
    grepl("ETH-3", Easotope_Name) ~ "ETH-3",
    grepl("ETH-4", Easotope_Name) ~ "ETH-4"
```

```
   )
  )
```

We now have standardized names as follows. Note that the original name is not overwritten - we add a new column and preserve the original designations.

```
unique(data$Standard)
## [1] "TV03"          "Veinstrom"      "Carmel Chalk"   "ETH-1"
## [5] "ETH-2"          "ETH-3"          "ETH-4"          "Carrara Marble"
```

### Finding initial cutpoints

Kernel density estimation is used to find initial cutpoints.

When there is a singular peak, the findCutpoints function is employed as follows:

```
ETH2_cuts <- findCutpoints(data$D48CDES_Final[data$Standard == "ETH-2"])
```

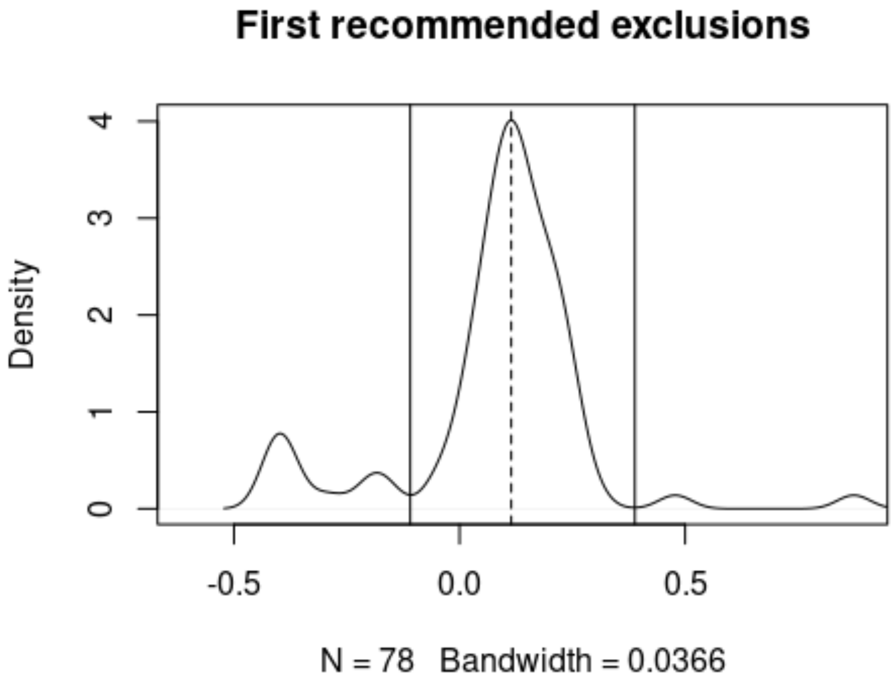

The recommended cuts (nearest minima on either side of the maxima) are marked in solid black vertical lines. In this case, recommended cuts are:

```
ETH2_cuts[1]

## [1] -0.1093086

ETH2_cuts[2]

## [1] 0.3886321
```

*Note that the functions do not round values, as we wish to avoid accumulating rounding error.*

Those suggested cuts are stored in the object **ETH2_cuts**, then applied to the raw data as follows:

```
ETH2_firstcut <- data$D48CDES_Final[data$Standard == "ETH-2" &
                                    data$D48CDES_Final >= ETH2_cuts[1] &
                                    data$D48CDES_Final <= ETH2_cuts[2] ]
```

Following the exclusion of extreme values, our data are as follows:

```
mean(ETH2_firstcut)

## [1] 0.1275455

sd(ETH2_firstcut)

## [1] 0.07563763

length(ETH2_firstcut)

## [1] 66
```

**Final exclusions**

A visual representation of options for the final exclusion:

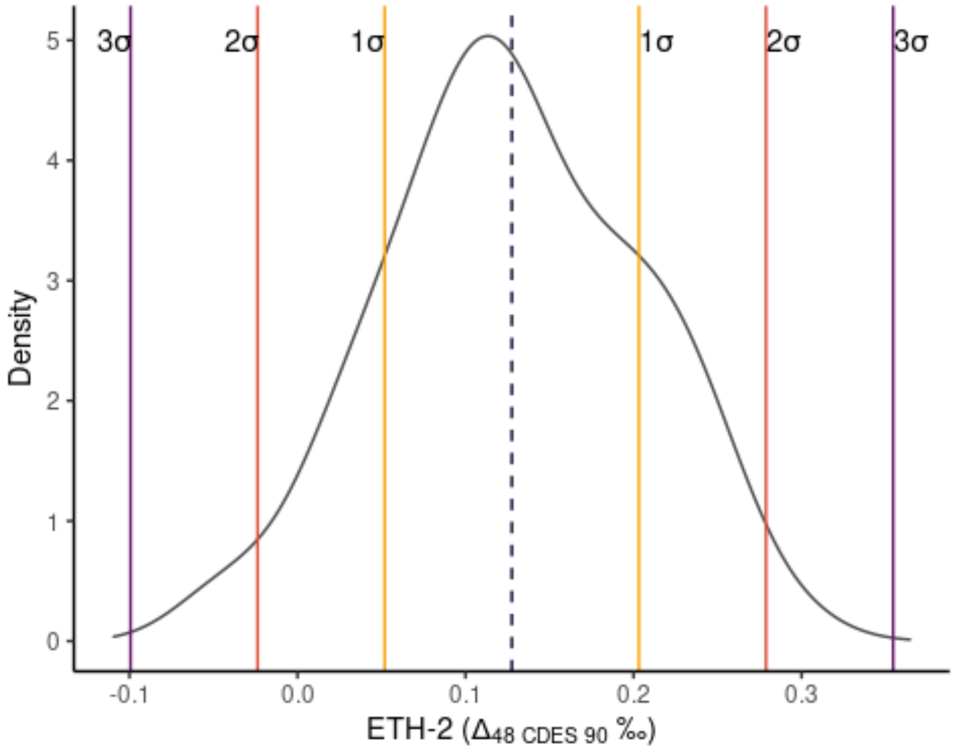

We then employ a 3σ exclusion (outermost pair of solid vertical lines in purple) to complete the quality control process:

```
ETH2_secondcut <- ETH2_firstcut[ETH2_firstcut >= (mean(ETH2_firstcut)-
(3*sd(ETH2_firstcut))) &
                              ETH2_firstcut <= (mean(ETH2_firstcut)+(3*sd(ETH2_firstcut)))]


mean(ETH2_secondcut)
## [1] 0.1275455
```

```
sd(ETH2_secondcut)

## [1] 0.07563763

length(ETH2_secondcut)

## [1] 66
```

These final cuts are then applied to the full dataset:

```
ETH2_final <- data[data$Standard == "ETH-2" &

                data$D48CDES_Final >= range(ETH2_secondcut)[1] &

                data$D48CDES_Final <= range(ETH2_secondcut)[2],]
```

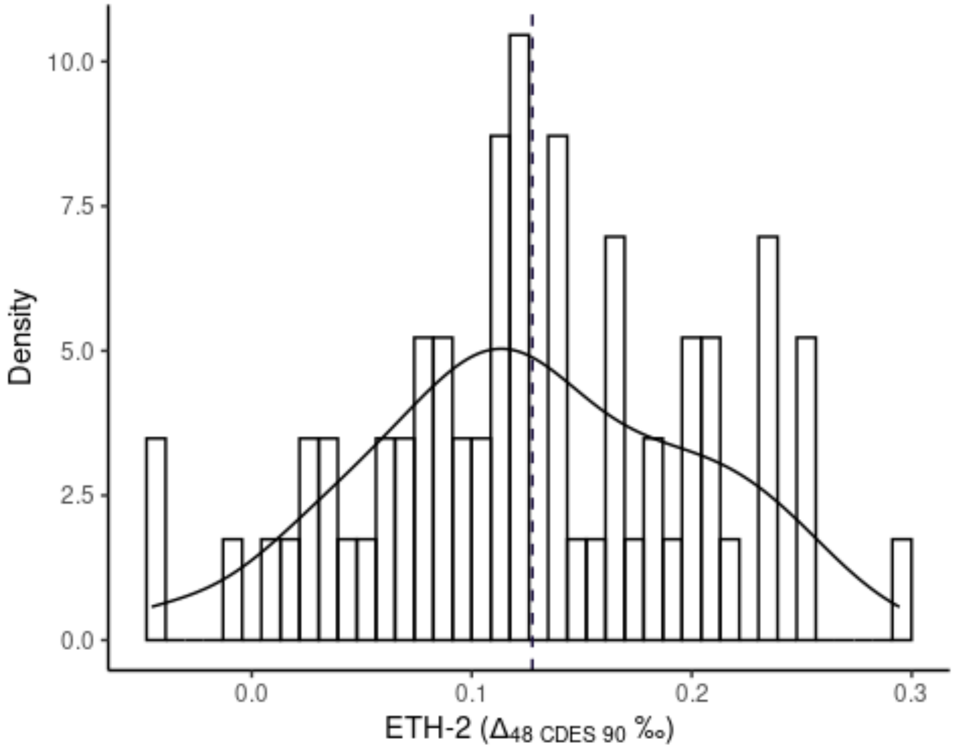

We test for normality of the final dataset as follows:

```
shapiro.test(ETH2_final$D48CDES_Final)

##

##  Shapiro-Wilk normality test
```

```
##
## data:  ETH2_final$D48CDES_Final
## W = 0.98847, p-value = 0.8011
```

The final data are normally distributed, so we are satisfied with the 3σ exclusion.

### Data screening when there are double peaks or shoulders

We provide an additional set of functions to address more complex situations. For double or shouldered peaks, the nearest minima will be inaccurate. Where a second peak or shoulder is approximately a third as high as the highest peak, these data should be included in the initial cut. This is most likely to occur when replicate pools are relatively small or when older instrumentation, such as a Thermo Finnigan MAT 253, is used to measure $\Delta_{48}$.

An example where the second peak is on the left hand side of the maxima:

```
findCutpoints(data2$D47CDES_90[data2$Standard == "IAEA-C2"])
```

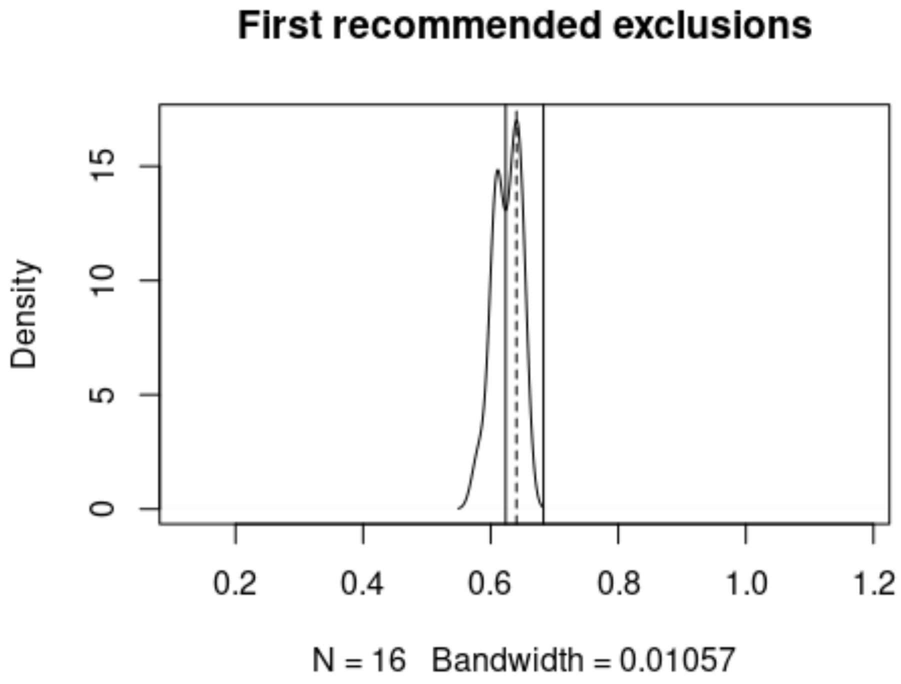

This will require the function findCutpointsLeftShoulder:

```
findCutpointsLeftShoulder(data2$D47CDES_90[data2$Standard == "IAEA-C2"])
```

The findCutpointsRightShoulder function is provided for cases such as the example below:

```
findCutpointsRightShoulder(data2$D47CDES_Final[data2$Standard == "102-GC-AZ01"])
```

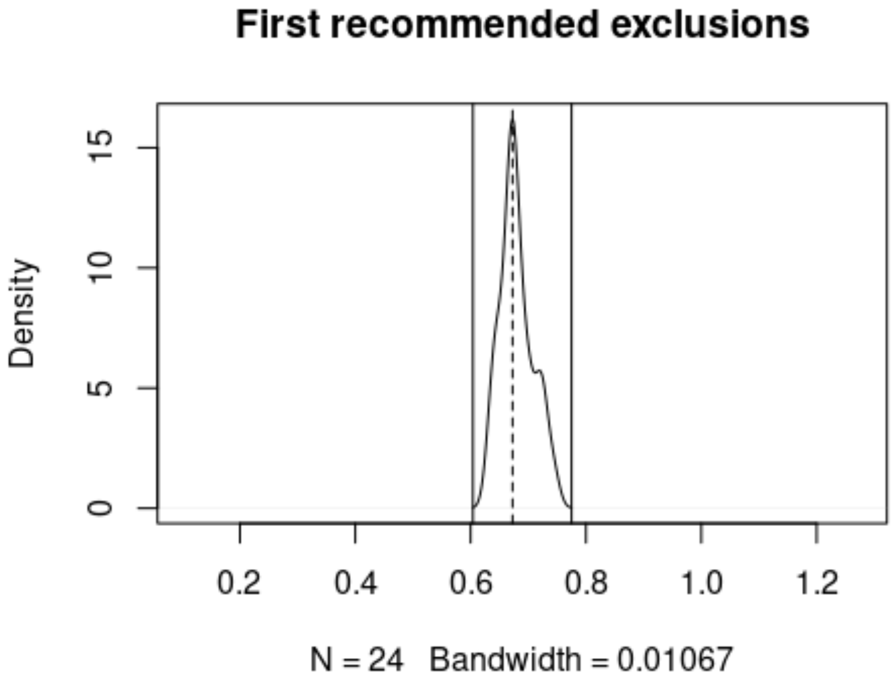

We provide the function findCutpointsDouble for peaks with shoulders on both sides:

```
findCutpointsDouble(data3$D48CDES_Final[data3$Standard == "ETH-1"])
```

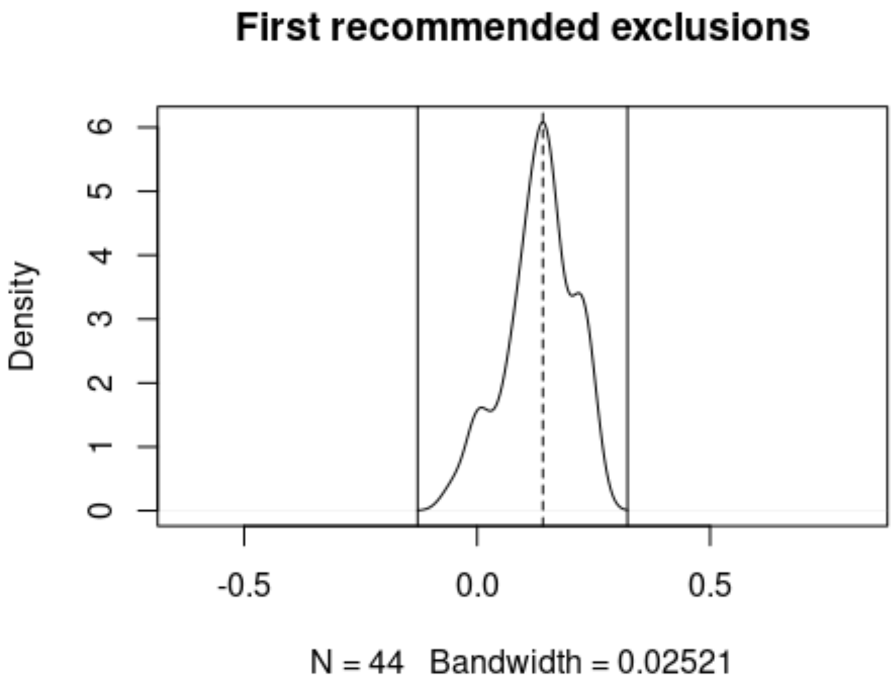

Following the initial exclusions, we then proceed with the final exclusions as described above.

### A.2 Regression-form acid digestion fractionation factors, $\Delta^*_{63\text{-}47}$ and $\Delta^*_{64\text{-}48}$

Model calculations from Guo et al.[3] predicted that acid digestion fractionation factors (AFFs) for when calcite mineral is digested in phosphoric acid, $\Delta^*_{63\text{-}47}$ and $\Delta^*_{64\text{-}48}$, should depend on the $\Delta_{63}$ and $\Delta_{64}$ values of the reactant carbonate, respectively. Here, to calculate this dependence, nonlinear regressions of the theoretical model equilibrium $\Delta_{63}$ or $\Delta_{64}$ and temperature[4,5] were used to determine theoretical equilibrium

$\Delta_{63}$ and $\Delta_{64}$ values for the precipitation temperature of Devils Hole calcite at 33.7 $^{o}$C[34] ($\Delta_{63} \approx 0.3707$ ‰; $\Delta_{64} \approx 0.1092$ ‰) and ETH-1 and ETH-2 at 600 $^{o}$C[43] ($\Delta_{63} \approx 0.0179$ ‰; $\Delta_{64} \approx 0.0022$ ‰). The experimentally determined $\Delta_{47}$ and $\Delta_{48}$ values for DH-2 average and the pooled average of ETH-1 and ETH-2 were subtracted from the theoretical equilibrium $\Delta_{63}$ and $\Delta_{64}$ values, respectively, to yield AFFs for calcite at 33.7 $^{o}$C ($\Delta^{*}_{63\text{-}47}$ = 0.1949 ‰; $\Delta^{*}_{64\text{-}48}$ = 0.1308 ‰) and 600 $^{o}$C ($\Delta^{*}_{63\text{-}47}$ = 0.1881 ‰; $\Delta^{*}_{64\text{-}48}$ = 0.1300 ‰) using Equations A1 and A2

$$\Delta^{*}_{63\text{-}47} = \Delta_{47\ \text{I-CDES}} - \Delta_{63} \qquad \text{Equation A1}$$

$$\Delta^{*}_{63\text{-}47} = \Delta_{48\ \text{CDES 90}} - \Delta_{64} \qquad \text{Equation A2}$$

where $\Delta^{*}_{63\text{-}47}$ and $\Delta^{*}_{63\text{-}47}$ are the AFFs. Devils Hole calcite was used in construction of the coupled carbonate clumped isotope relationship because it is assumed to have precipitated near isotopic equilibrium due to extremely slow precipitation rate (0.1-0.8 μm year-1), low calcite saturation index (0.16-0.21) and a stable temperature of 33.7 (±0.8) $^{o}$C throughout the Holocene.[34,35,66] The pooled average of ETH-1 and ETH-2 was used because their $\Delta_{47}$ and $\Delta_{48}$ values were statistically indistinguishable, and both have a known equilibration temperature of 600 $^{o}$C.[43] Additionally, samples equilibrated at high temperatures are much less likely to have detectable kinetic biases due to faster exchange of isotopes among isotopologues and decreased time to reach isotopic equilibrium.

Linear regressions were made for $\Delta^*_{63\text{-}47}$ versus $\Delta_{63}$, and $\Delta^*_{64\text{-}48}$ versus $\Delta_{64}$ for 33.7 °C and 600 °C (Figure A1). The slope and intercept from these regressions were used to calculate $\Delta^*_{63\text{-}47}$ and $\Delta^*_{64\text{-}48}$ for 0-1000 °C (Table 8), using Equations 13 and 14.

$$\Delta^*_{63\text{-}47} = 0.0193 \times \Delta_{63} + 0.1878 \qquad \text{Equation A3}$$

$$\Delta^*_{64\text{-}48} = 0.0077 \times \Delta_{64} + 0.1300 \qquad \text{Equation A4}$$

The relationship between precipitation temperature and $\Delta^*_{63\text{-}47}$ from 0-600 °C (Figure A1c) is represented by equation A4 ($r^2$ =1). The relationship between precipitation temperature and $\Delta^*_{64\text{-}48}$ was split into two ranges to acquire a more accurate fit, with 0-300 °C (Figure A1d) represented by equation A5 ($r^2$ = 1), and 300-1000 °C (Figure A1e) represented by Equation A6 ($r^2$ = 1). Equations 15-17 use temperature in degrees Celsius.

Equation A5

$$\Delta^*_{63\text{-}47} = [0.1968 \pm (1.805 \times 10^{-5})] - [(6.111 \times 10^{-5}) \pm (5.894 \times 10^{-7})]T + [(1.922 \times 10^{-7}) \pm (4.733 \times 10^{-9})]T^2 - [(2.965 \times 10^{-10}) \pm (1.304 \times 10^{-11})]T^3 + [(1.762 \times 10^{-13}) \pm (1.126 \times 10^{-14})]T^4$$

Equation A6

$$\mathit{\Delta}^*_{64\text{-}48} = [0.1312 \pm (7.348 \times 10^{-7})] - [(1.266 \times 10^{-5}) \pm (4.736 \times 10^{-8})]T + [(6.890 \times 10^{-8}) \pm (8.299 \text{ x } 10^{-10})]T^2 - [(2.029 \times 10^{-10}) \pm (4{,}756 \times 10^{-12})]T^3 + [(2.428 \times 10^{-13}) \pm (8.335 \times 10^{-15})]T^4$$

Equation A7

$$\mathit{\Delta}^*_{64\text{-}48} = [0.1305 \pm (2.101 \times 10^{-5})] - [(2.165 \text{ x } 10^{-6}) \pm (1.516 \times 10^{-7})]T + [(4.011 \times 10^{-9}) \pm (3.858 \times 10^{-10})]T^2 - [(3.377 \times 10^{-12}) \pm (4.135 \times 10^{-13})]T^3 + [(1.072 \times 10^{-15}) \pm (1.587 \times 10^{-16})]T^4$$

The relationship between $\mathit{\Delta}^*_{63\text{-}47}$ and $\mathit{\Delta}^*_{64\text{-}48}$ is represented by equation A8.

Equation A8

$$\mathit{\Delta}^*_{64\text{-}48} = (0.3964 \pm 0.0033) + (-2.898 \pm 0.0340)\, \mathit{\Delta}^*_{63\text{-}47} + (7.88 \pm 0.0887)\, \mathit{\Delta}^*_{63\text{-}47}{}^2$$

For samples with unknown precipitation temperature, $\mathit{\Delta}^*_{63\text{-}47}$ and $\mathit{\Delta}^*_{64\text{-}48}$ can be calculated using equations A9 and A10 (Figure A1a, b).

$$\mathit{\Delta}^*_{63\text{-}47} = 0.0190 \times \mathit{\Delta}_{47 \text{ I-CDES}} + 0.1842 \qquad \text{Equation A9}$$

$$\mathit{\Delta}^*_{64\text{-}48} = 0.0077 \times \mathit{\Delta}_{48 \text{ CDES } 90} + 0.1290 \qquad \text{Equation A10}$$

Equations A11 and A12 may be used to calculate $\Delta_{63}$ and $\Delta_{64}$ from $\Delta_{47}$ and $\Delta_{48}$ values (Figure A1c, d).

Equation A11

$$\Delta_{63} = (-0.1845 \pm 0.0007) + (0.9839 \pm 0.0078)\Delta_{47\ \text{I-CDES}} + (-0.0121 \pm 0.0299)\Delta_{47\ \text{I-CDES}}^{2} + (0.0207 \pm 0.0483)\ \Delta_{47\ \text{I-CDES}}^{3} + (-0.0125 \pm 0.0281)\Delta_{47\ \text{I-CDES}}^{4}$$

Equation A12

$$\Delta_{64} = (-0.1377 \pm 0.0048) + (1.166 \pm 0.0981)\Delta_{48\ \text{CDES 90}} + (-1.267 \pm 0.7306)\Delta_{488\ \text{CDES 90}}^{2} + (4.007 \pm 2.363)\Delta_{48\ \text{CDES 90}}^{3} + (-4.645 \pm 2.807)\Delta_{488\ \text{CDES 90}}^{4}$$

The $\Delta^{*}_{63\text{-}47}$ versus $\Delta_{63}$ slope of 0.0193 determined here (Figure A1a) differs by -0.0112 ‰ from the model predicted slope from Guo et al.[3] of 0.0305. The model calculated the dependence based on carbonates with $\delta^{13}$C = 0 and $\delta^{18}$O = 0, however, this may not be the source of the offset because the slope is only predicted to change by ~0.002 ‰ and ~-0.0005 ‰ for a 50 ‰ increase in $\delta^{13}$C and $\delta^{18}$O, respectively.[3] The slope offset may in-part arise from approximations made in the model calculations for isotopologues containing $^{17}$O, and uncertainty in the slope determined in this study from the use of only two temperatures.

Fiebig et al.[7] used a similar method to determine AFFs at 600 °C. Our 600 °C $\Delta^{*}_{63\text{-}47}$ and $\Delta^{*}_{64\text{-}48}$ values differed by 0.008 ‰ and 0.006 ‰, respectively, from their values of 0.196 ‰ and 0.136 ‰. Because the calculation of AFFs relies on the long term ETH-1 and ETH-2 $\Delta_{47}$ and $\Delta_{48}$ values, the difference in AFFs is equivalent to the difference in the long term pooled average ETH-1 and ETH-2 $\Delta_{47}$ and $\Delta_{48}$ values from this study (pooled average ETH-1 and ETH-2 $\Delta_{47\ \text{I-CDES}} = 0.206 \pm 0.0006$ ‰, n = 1497; $\Delta_{48\ \text{CDES 90}} = 0.132 \pm 0.002$ ‰, n = 903) versus Fiebig et al.[7] (pooled average ETH-1 and ETH-2 $\Delta_{47\ \text{I-CDES}} = 0.214 \pm 0.005$ ‰, n = 37; $\Delta_{48\ \text{CDES 90}} = 0.138 \pm 0.015$ ‰, n = 37).

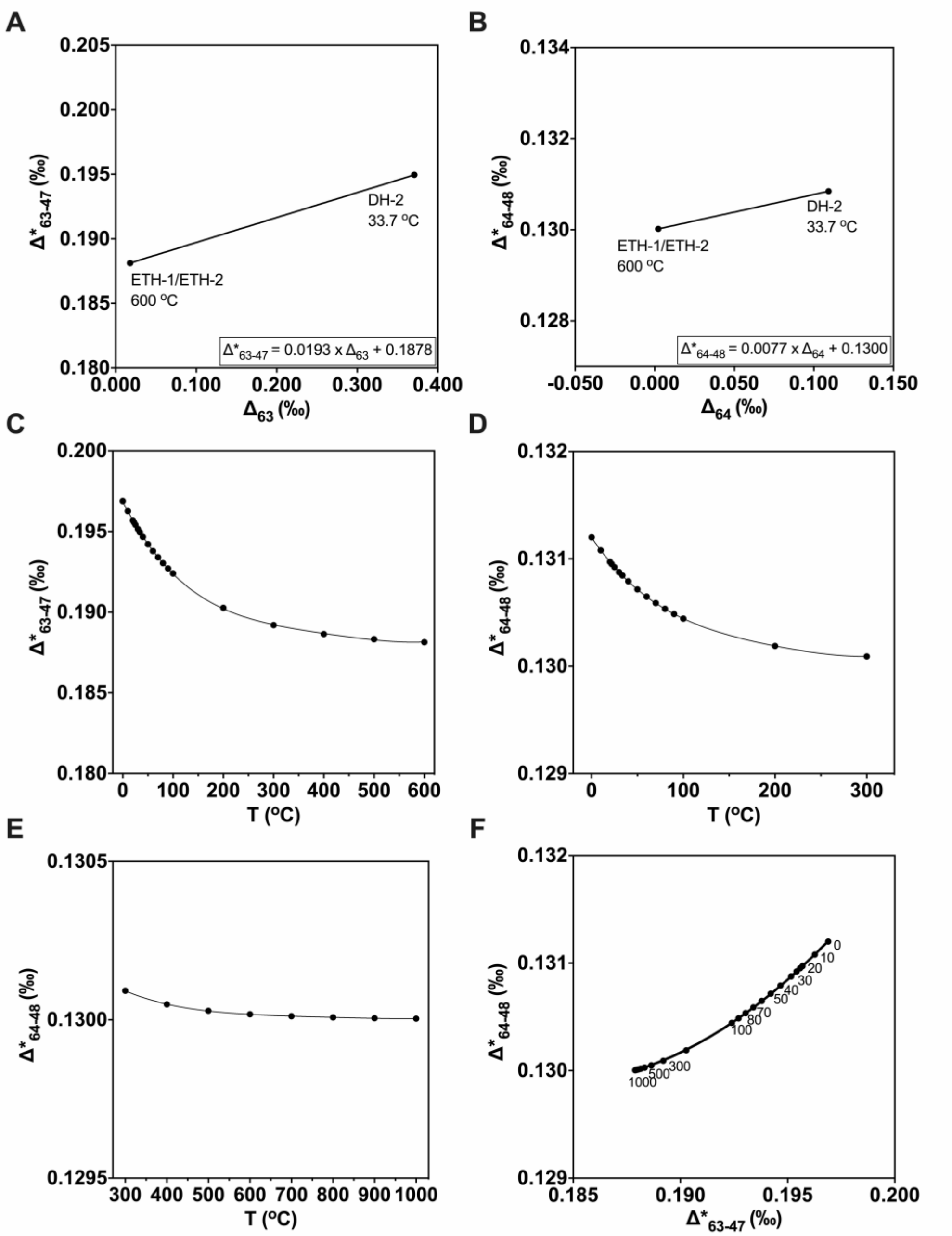

**Figure A1.** Constraints on acid digestion fractionation factors. **A)** Regression for the acid digestion fractionation factor, $\Delta^*_{63\text{-}47}$, versus theoretical $\Delta_{63}$[4,5]. **B)** Regression for the acid digestion fractionation factor, $\Delta^*_{64\text{-}48}$ versus theoretical $\Delta_{64}$[4,5]. **C)** Regression for acid digestion fractionation factor, $\Delta^*_{63\text{-}47}$, versus precipitation temperature (°C), where $r^2 = 0.99$. **D)** Regression for the acid digestion fractionation factor, $\Delta^*_{64\text{-}48}$ versus precipitation temperature from 0-300 °C ($r^2 = 1$) **E)** and from 300-1000 °C ($r^2 = 0.9998$).

**F)** Regression for acid digestion fractionation factors, $\Delta^*_{64\text{-}48}$ versus $\Delta^*_{63\text{-}47}$ ($r^2 = 1$).

Numbers on regression indicate temperature in Celsius.

## References

1. Ghosh, P. *et al.* 13C–18O bonds in carbonate minerals: A new kind of paleothermometer. *Geochimica et Cosmochimica Acta* **70**, 1439–1456 (2006).
2. Schauble, E. A., Ghosh, P. & Eiler, J. M. Preferential formation of 13C–18O bonds in carbonate minerals, estimated using first-principles lattice dynamics. *Geochimica et Cosmochimica Acta* **70**, 2510–2529 (2006).
3. Guo, W., Mosenfelder, J. L., Goddard, W. A. & Eiler, J. M. Isotopic fractionations associated with phosphoric acid digestion of carbonate minerals: Insights from first-principles theoretical modeling and clumped isotope measurements. *Geochimica et Cosmochimica Acta* **73**, 7203–7225 (2009).
4. Hill, P. S., Tripati, A. K. & Schauble, E. A. Theoretical constraints on the effects of pH, salinity, and temperature on clumped isotope signatures of dissolved inorganic carbon species and precipitating carbonate minerals. *Geochimica et Cosmochimica Acta* **125**, 610–652 (2014).
5. Tripati, A. K. *et al.* Beyond temperature: Clumped isotope signatures in dissolved inorganic carbon species and the influence of solution chemistry on carbonate mineral composition. *Geochimica et Cosmochimica Acta* **166**, 344–371 (2015).
6. Guo, Y., Deng, W. & Wei, G. Kinetic effects during the experimental transition of aragonite to calcite in aqueous solution: Insights from clumped and oxygen isotope signatures. *Geochimica et Cosmochimica Acta* **248**, 210–230 (2019).
7. Fiebig, J. *et al.* Combined high-precision $\Delta 48$ and $\Delta 47$ analysis of carbonates. *Chemical Geology* **522**, 186–191 (2019).

8. Bajnai, D. *et al.* Dual clumped isotope thermometry resolves kinetic biases in carbonate formation temperatures. *Nat Commun* **11**, 4005 (2020).
9. Swart, P. K. *et al.* A calibration equation between $\Delta_{48}$ values of carbonate and temperature. *Rapid Commun Mass Spectrom* **35**, (2021).
10. Fiebig, J. *et al.* Calibration of the dual clumped isotope thermometer for carbonates. *Geochimica et Cosmochimica Acta* S0016703721004208 (2021) doi:10.1016/j.gca.2021.07.012.
11. Eiler, J. M. & Schauble, E. 18O13C16O in Earth's atmosphere. *Geochimica et Cosmochimica Acta* **68**, 4767–4777 (2004).
12. Eiler, J. M. "Clumped-isotope" geochemistry—The study of naturally-occurring, multiply-substituted isotopologues. *Earth and Planetary Science Letters* **262**, 309–327 (2007).
13. Urey, H. C. The thermodynamic properties of isotopic substances. *J. Chem. Soc.* 562 (1947) doi:10.1039/jr9470000562.
14. Passey, B. H. & Henkes, G. A. Carbonate clumped isotope bond reordering and geospeedometry. *Earth and Planetary Science Letters* **351–352**, 223–236 (2012).
15. Henkes, G. A. *et al.* Temperature evolution and the oxygen isotope composition of Phanerozoic oceans from carbonate clumped isotope thermometry. *Earth and Planetary Science Letters* **490**, 40–50 (2018).
16. Huntington, K. W., Wernicke, B. P. & Eiler, J. M. Influence of climate change and uplift on Colorado Plateau paleotemperatures from carbonate clumped isotope thermometry. *Tectonics* **29**, 2009TC002449 (2010).

17. Lechler, A. R., Niemi, N. A., Hren, M. T. & Lohmann, K. C. Paleoelevation estimates for the northern and central proto-Basin and Range from carbonate clumped isotope thermometry: $\Delta_{47}$ PALEOALTIMETRY OF BASIN AND RANGE. *Tectonics* **32**, 295–316 (2013).
18. Eagle, R. A. *et al.* Body temperatures of modern and extinct vertebrates from 13C-18O bond abundances in bioapatite. *Proceedings of the National Academy of Sciences* **107**, 10377–10382 (2010).
19. Affek, H. P., Bar-Matthews, M., Ayalon, A., Matthews, A. & Eiler, J. M. Glacial/interglacial temperature variations in Soreq cave speleothems as recorded by ‘clumped isotope’ thermometry. *Geochimica et Cosmochimica Acta* **72**, 5351–5360 (2008).
20. Daëron, M. *et al.* 13C18O clumping in speleothems: Observations from natural caves and precipitation experiments. *Geochimica et Cosmochimica Acta* **75**, 3303–3317 (2011).
21. Thiagarajan, N., Adkins, J. & Eiler, J. Carbonate clumped isotope thermometry of deep-sea corals and implications for vital effects. *Geochimica et Cosmochimica Acta* **75**, 4416–4425 (2011).
22. Kimball, J., Eagle, R. & Dunbar, R. Carbonate “clumped” isotope signatures in aragonitic scleractinian and calcitic gorgonian deep-sea corals. *Biogeosciences* **13**, 6487–6505 (2016).
23. Saenger, C. *et al.* Carbonate clumped isotope variability in shallow water corals: Temperature dependence and growth-related vital effects. *Geochimica et Cosmochimica Acta* **99**, 224–242 (2012).

24. Guo, W. Kinetic clumped isotope fractionation in the DIC-H2O-CO2 system: Patterns, controls, and implications. *Geochimica et Cosmochimica Acta* **268**, 230–257 (2020).
25. Hill, P. S., Schauble, E. A. & Tripati, A. Theoretical constraints on the effects of added cations on clumped, oxygen, and carbon isotope signatures of dissolved inorganic carbon species and minerals. *Geochimica et Cosmochimica Acta* **269**, 496–539 (2020).
26. Dennis, K. J., Affek, H. P., Passey, B. H., Schrag, D. P. & Eiler, J. M. Defining an absolute reference frame for 'clumped' isotope studies of CO2. *Geochimica et Cosmochimica Acta* **75**, 7117–7131 (2011).
27. Bernasconi, S. M. *et al.* InterCarb: A Community Effort to Improve Interlaboratory Standardization of the Carbonate Clumped Isotope Thermometer Using Carbonate Standards. *Geochem Geophys Geosyst* **22**, (2021).
28. Zaarur, S., Affek, H. P. & Brandon, M. T. A revised calibration of the clumped isotope thermometer. *Earth and Planetary Science Letters* **382**, 47–57 (2013).
29. Burgener, L. *et al.* Variations in soil carbonate formation and seasonal bias over >4 km of relief in the western Andes (30°S) revealed by clumped isotope thermometry. *Earth and Planetary Science Letters* **441**, 188–199 (2016).
30. Peral, M. *et al.* Updated calibration of the clumped isotope thermometer in planktonic and benthic foraminifera. *Geochimica et Cosmochimica Acta* **239**, 1–16 (2018).
31. Meckler, A. N., Ziegler, M., Millán, M. I., Breitenbach, S. F. M. & Bernasconi, S. M. Long-term performance of the Kiel carbonate device with a new correction scheme

for clumped isotope measurements: Performance and correction of Kiel clumped isotope measurements. *Rapid Commun. Mass Spectrom.* **28**, 1705–1715 (2014).

32. Upadhyay, D. *et al.* Carbonate clumped isotope analysis ($\Delta_{47}$) of 21 carbonate standards determined via gas-source isotope-ratio mass spectrometry on four instrumental configurations using carbonate-based standardization and multiyear data sets. *Rapid Commun Mass Spectrom* **35**, (2021).
33. Tripati, A. K. *et al.* 13C–18O isotope signatures and 'clumped isotope' thermometry in foraminifera and coccoliths. *Geochimica et Cosmochimica Acta* **74**, 5697–5717 (2010).
34. Winograd, I. J. *et al.* Continuous 500,000-Year Climate Record from Vein Calcite in Devils Hole, Nevada. *Science* **258**, 255–260 (1992).
35. Coplen, T. B. Calibration of the calcite–water oxygen-isotope geothermometer at Devils Hole, Nevada, a natural laboratory. *Geochimica et Cosmochimica Acta* **71**, 3948–3957 (2007).
36. Kluge, T., Affek, H. P., Dublyansky, Y. & Spötl, C. Devils Hole paleotemperatures and implications for oxygen isotope equilibrium fractionation. *Earth and Planetary Science Letters* **400**, 251–260 (2014).
37. Winograd, I. J., Coplen, T. B., Szabo, B. J. & Riggs, A. C. A 250,000-Year Climatic Record from Great Basin Vein Calcite: Implications for Milankovitch Theory. *Science* **242**, 1275–1280 (1988).
38. Passey, B. H., Levin, N. E., Cerling, T. E., Brown, F. H. & Eiler, J. M. High-temperature environments of human evolution in East Africa based on bond

ordering in paleosol carbonates. *Proceedings of the National Academy of Sciences* **107**, 11245–11249 (2010).

39. John, C. M. & Bowen, D. Community software for challenging isotope analysis: First applications of 'Easotope' to clumped isotopes: Community software for challenging isotope analysis. *Rapid Commun. Mass Spectrom.* **30**, 2285–2300 (2016).
40. Brand, W. A., Assonov, S. S. & Coplen, T. B. Correction for the 17O interference in δ(13C) measurements when analyzing CO2 with stable isotope mass spectrometry (IUPAC Technical Report). *Pure and Applied Chemistry* **82**, 1719–1733 (2010).
41. Daëron, M., Blamart, D., Peral, M. & Affek, H. P. Absolute isotopic abundance ratios and the accuracy of Δ47 measurements. *Chemical Geology* **442**, 83–96 (2016).
42. Wang, Z., Schauble, E. A. & Eiler, J. M. Equilibrium thermodynamics of multiply substituted isotopologues of molecular gases. *Geochimica et Cosmochimica Acta* **68**, 4779–4797 (2004).
43. Bernasconi, S. M. *et al.* Reducing Uncertainties in Carbonate Clumped Isotope Analysis Through Consistent Carbonate-Based Standardization. *Geochem. Geophys. Geosyst.* **19**, 2895–2914 (2018).
44. Bajnai, D. *et al.* Devils Hole Calcite Was Precipitated at ±1°C Stable Aquifer Temperatures During the Last Half Million Years. *Geophys Res Lett* **48**, (2021).
45. Daëron, M. Full Propagation of Analytical Uncertainties in $\Delta_{47}$ Measurements. *Geochem Geophys Geosyst* **22**, (2021).
46. Kocken, I. J., Müller, I. A. & Ziegler, M. Optimizing the Use of Carbonate Standards to Minimize Uncertainties in Clumped Isotope Data. *Geochem. Geophys. Geosyst.* **20**, 5565–5577 (2019).

47. Müller, I. A. *et al.* Clumped isotope fractionation during phosphoric acid digestion of carbonates at 70 °C. *Chemical Geology* **449**, 1–14 (2017).

48. Daëron, M. *et al.* Most Earth-surface calcites precipitate out of isotopic equilibrium. *Nat Commun* **10**, 429 (2019).

49. Miller, R. Miller, Robert Rush. "The cyprinodont fishes of the Death Valley system of eastern California and southwestern Nevada. *Miscellaneous Publications Museum of Zoology, University of Michigan* **68**, (1948).

50. Dudley, W. & Larson, J. D. *Effect of irrigation pumping on desert pupfish habitats in the Ash Meadows, Nye County, Nevada*. (1976).

51. Hoffman, R. *Chronology of diving activities and underground surveys in Devils Hole and Devils Hole Cave, Nye County, Nevada, 1950-86*. (1988).

52. Plummer, L. N., Busenberg, E. & Riggs, A. C. In-situ Growth of Calcite at Devils Hole, Nevada: Comparison of Field and Laboratory Rates to a 500,000 Year Record of Near-Equilibrium Calcite Growth. *Aquatic Geochemistry* **6**, 257–274 (2000).

53. Kluge, T. & Affek, H. P. Quantifying kinetic fractionation in Bunker Cave speleothems using Δ47. *Quaternary Science Reviews* **49**, 82–94 (2012).

54. Affek, H. P. & Zaarur, S. Kinetic isotope effect in CO2 degassing: Insight from clumped and oxygen isotopes in laboratory precipitation experiments. *Geochimica et Cosmochimica Acta* **143**, 319–330 (2014).

55. Guo, W. & Zhou, C. Patterns and controls of disequilibrium isotope effects in speleothems: Insights from an isotope-enabled diffusion-reaction model and implications for quantitative thermometry. *Geochimica et Cosmochimica Acta* **267**, 196–226 (2019).

56. Correa-Quezada, R., Cueva-Rodríguez, L., Álvarez-García, J. & del Río-Rama, M. de la C. Application of the Kernel Density Function for the Analysis of Regional Growth and Convergence in the Service Sector through Productivity. *Mathematics* **8**, 1234 (2020).
57. Seaman, D. E. & Powell, R. A. An Evaluation of the Accuracy of Kernel Density Estimators for Home Range Analysis. *Ecology* **77**, 2075–2085 (1996).
58. Pulkkinen, S. Nonlinear kernel density principal component analysis with application to climate data. *Stat Comput* **26**, 471–492 (2016).
59. Wahiduzzaman, M. & Yeasmin, A. A kernel density estimation approach of North Indian Ocean tropical cyclone formation and the association with convective available potential energy and equivalent potential temperature. *Meteorol Atmos Phys* **132**, 603–612 (2020).
60. Lee, W. J., Mendis, G. P., Triebe, M. J. & Sutherland, J. W. Monitoring of a machining process using kernel principal component analysis and kernel density estimation. *J Intell Manuf* **31**, 1175–1189 (2020).
61. R Core Team. R: A language and environment for statistical computing. (2021).
62. Sheather, S. J. & Jones, M. C. A Reliable Data-Based Bandwidth Selection Method for Kernel Density Estimation. *Journal of the Royal Statistical Society: Series B (Methodological)* **53**, 683–690 (1991).
63. Deng, H. & Wickham, H. Density estimation in R. (2011).
64. J Pinheiro, Bates, D., DebRoy, S., Sarkar, D. & R Core Team. nlme: Linear and nonlinear mixed effects models. (2021).

65. Lenth, R. V. emmeans: Estimated marginal means, aka least-squares means. (2021).
66. Winograd, I. J. *et al.* Devils Hole, Nevada, $\delta^{18}$O record extended to the mid-Holocene. *Quat. res.* **66**, 202–212 (2006).

# CHAPTER 2

# Paired $\Delta_{47}$ and $\Delta_{48}$ analyses and model calculations constrain equilibrium, experimentally-manipulated kinetic isotope effects, and mixing effects in calcite

Jamie Lucarelli[1], Bettina Purgstaller[2], Zeeshan Parvez[1], James M. Watkins[3], Robert A. Eagle[1], Martin Dietzel[2], Aradhna Tripati[1]

[1]Department of Earth, Planetary, and Space Sciences, Department of Atmospheric and Oceanic Sciences, Institute of the Environment and Sustainability, Center for Diverse Leadership in Science, UCLA, Los Angeles, CA 90095 USA.
[2]Institute of Applied Geosciences, Graz University of Technology, 8010 Graz, Austria
[3]Department of Earth Science, University of Oregon, Eugene, OR 97403 USA
Correspondence to: jklucarelli@gmail.com and atripati@g.ucla.edu

## Abstract

The high-precision analysis of the abundance of the dominant *m/z* 47 $CO_2$ isotopologue derived from acid digestion of carbonate minerals ($^{13}C^{18}O^{16}O$; denoted by $\Delta_{47}$) forms the basis for carbonate clumped isotope thermometry. Since the first measurements were published 16 years ago, considerable effort has gone into characterizing the relationship between $\Delta_{47}$ and carbonate precipitation temperature, and in identifying carbonates that do not achieve isotopic equilibrium. Mass

spectrometry is now capable of the paired measurement of the primary *m/z* 47 and *m/z* 48-isotopologues ($\Delta_{47}$ and $\Delta_{48}$; $^{12}C^{18}O_2$ is denoted by $\Delta_{48}$), which has the potential to place additional constraints on kinetic isotope effects in carbonate minerals and trace distinct reaction pathways. Here, we explored factors that contribute to calcite mineral equilibrium and disequilibrium in $\Delta_{47}$ and $\Delta_{48}$ using a combination of experiments and theoretical calculations with three types of models. We precipitated calcite at pH 8.3 with carbonic anhydrase (CA) to approach quasi-isotopic equilibrium in the dissolved inorganic carbon pool and report values for $\Delta_{47}$, $\Delta_{48}$, and oxygen isotopes ($\delta^{18}O$) for calcite grown over a temperature range from 5 to 25 $^{o}$C and compare our findings to predictions from an ion-by-ion model that support equilibrium precipitation. We also compare results to the Devils Hole slow-growing cave calcite, and other published temperature calibration data. We report the following combined equilibrium calibration relationships: $\Delta_{48\ \mathrm{CDES\ 90}} = (0.429 \pm 0.010)\ \Delta_{47\ \mathrm{CDES\ 90}} - (0.006 \pm 0.006)$; $r^2 = 0.98$; $\Delta_{47\ \mathrm{I\text{-}CDES}} = (0.037 \pm 0.001) \times 10^6 T^{-2} + (0.178 \pm 0.009)$; $r^2 = 0.99$; $\Delta_{48\ \mathrm{CDES\ 90}} = (0.015 \pm 0.0005) \times 10^6 T^{-2} + (0.078 \pm 0.006)$; $r^2 = 0.98$. We used paired measurements of $\Delta_{47}$ and $\Delta_{48}$ to constrain kinetic isotope effects in calcite precipitated at pH ranging from 8.3-11 and temperatures from 5 to 25 $^{o}$C, with and without CA present, and observe kinetic enrichments in $\Delta_{47}$, negative (hyperstochastic) values for $\Delta_{48}$, and depleted values of $\delta^{18}O$, compared to equilibrium values. Experimentally constrained kinetic trajectories, when compared with an ion-by-ion model and IsoDIC theoretical predictions, are consistent with $CO_2$ hydration/hydroxylation. Mixing drives elevated $\Delta_{47}$ and $\Delta_{48}$ values and was assessed using mixing experiments with endmembers of varying isotopic compositions and compared to a $\Delta_{47}$ and $\Delta_{48}$ mixing model that constrains nonlinear mixing trajectories for calcite. While mixing may induce artifacts in two-component mixtures when endmember bulk compositions differ by more than 7 ‰, or if endmember $\Delta_{47}$ and $\Delta_{48}$ differ by more than 0.03 ‰, this should be detectable and potentially correctible using paired clumped isotope measurements and is unlikely to be important for some materials.

## 1. Introduction

Carbonate clumped isotope thermometry is based on the frequency with which rare, heavy isotopes of carbon ($^{13}$C) or oxygen ($^{18}$O) in carbonate minerals are bonded to each other relative to a stochastic (random) distribution (Wang et al., 2004; Eiler and Schauble, 2004; Ghosh et al., 2006; Schauble et al., 2006). The dominant clumped isotopologue measured in carbonate minerals from phosphoric acid digestion of carbonates is $^{13}C^{18}O^{16}O$ and has a mass of 47 amu ($\Delta_{47}$), while $^{12}C^{18}O^{18}O$ is the dominant mass-48 isotopologue ($\Delta_{48}$). The use of $\Delta_{47}$ and $\Delta_{48}$ as paleothermometers rely on equilibrium clumped isotope fractionation in the carbonate mineral lattice. However, recent theoretical and experimental work has shown that some biogenic and abiogenic carbonates yield disequilibrium $\Delta_{47}$ (Ghosh et al., 2006; Daëron et al., 2011, Saenger et al, 2012, Tang et al., 2014; Tripati et al., 2015; Guo et al., 2019; Daeron et al., 2019) and $\Delta_{48}$ values (Tripati et al., 2015; Guo, 2020; Bajnai et al., 2020; Lucarelli et al., 2021; Fiebig et al., 2021).

The paired measurement of $\Delta_{47}$ and $\Delta_{48}$ has been theoretically (Hill et al., 2014; Tripati et al., 2015; Guo, 2020; Hill et al., 2020) and experimentally (Fiebig et al., 2019; Bajnai et al., 2020; Swart et al., 2021; Lucarelli et al., 2021; Fiebig et al., 2021) shown to have a characteristic equilibrium relationship. The equilibrium $\Delta_{47}$-$\Delta_{48}$ relationship along with constrained boundaries of disequilibrium trajectories in dissolved inorganic carbon (DIC) pools and in carbonate minerals may be used to identify the origin of kinetic isotope effects (Tripati et al., 2015; Bajnai et al., 2020; Guo, 2020) and used to correct for such effects and derive expected equilibrium clumped isotope values from samples (Bajnai et al., 2020; Guo, 2020).

Through comparison of theoretical predictions with experimental data, a robust framework can be developed to advance the paired carbonate clumped isotope approach as a potential tool for constraining kinetic isotope effects (KIEs), including vital effects in biogenic carbonates. Currently, the paired $\Delta_{47}$ and $\Delta_{48}$ trajectory of kinetic isotope effects (KIEs) in carbonates is limited to theory with calculations for a DIC pool at equilibrium (Hill et al., 2014; Tripati et al., 2015), hydration/hydroxylation (Guo, 2020), and for growth from a solution of DIC with cations present (Hill et al., 2020). Theory has been used to explain some measurements of disequilibrium $\Delta_{47}$ values in corals, speleothems, and high pH travertines (Guo, 2020), and disequilibrium $\Delta_{47}$ and $\Delta_{48}$ values in speleothems, stalagmites, and corals (Bajnai et al., 2020).

Here, we adapted experimental approaches used in Tang et al. (2014) and Tripati et al. (2015) to constrain KIEs in $\Delta_{47}$, $\Delta_{48}$, and $\delta^{18}O$ in calcite precipitated under controlled conditions at different pH and temperatures, with and without the addition of the enzyme carbonic anhydrase (CA). We compared data from calcite grown under isotopic disequilibrium conditions at varying pH to calcite formed at quasi-equilibrium conditions. We measured samples to further constrain equilibrium and kinetically governed relationships for clumped isotopes, including $\Delta_{47}$-$\Delta_{48}$, $\Delta_{47}$ and $T$, $\Delta_{48}$ and $T$, and bulk $\delta^{18}$O and $\delta^{13}$C and clumped isotopes, and compared experimental results to model calculations. We constructed and used a numerical mixing model and predicted nonlinear effects in $\Delta_{47}$ and $\Delta_{48}$ and compared results to experimental data.

## 2. Background

### 2.1 Carbonate clumped isotopes and notation

Historically, carbonate clumped isotope thermometry used the deviations in the abundance of the *m/z* 47 $CO_2$ isotopologue, $^{16}$O-$^{13}$C-$^{18}$O, which is liberated from the phosphoric acid digestion of the most abundant (67 ppm) *m/z* 63 carbonate isotopologue, $^{13}$C-$^{16}$O-$^{16}$O-$^{18}$O, relative to a stochastic distribution of isotopologues (Ghosh et al., 2006). Recent developments in mass spectrometry precision, such as the use of secondary electron suppression and $10^{13}$ Ω resistors, has enabled the accurate measurement of the lower abundance *m/z* 48 $CO_2$ isotopologue, $^{18}$O-$^{12}$C-$^{18}$O, which is liberated from the phosphoric acid digestion of the most abundant (12 ppm) *m/z* 64 carbonate isotopologue, $^{12}$C-$^{16}$O-$^{18}$O-$^{18}$O (Ghosh et al., 2006). The thermodynamic equilibrium relationship between *m/z* 63 and *m/z* 64 isotopologues with precipitation temperature is governed by the equilibrium constant, $K$, in Reactions 1 and 2 (Wang et al., 2004; Ghosh et al., 2006).

$^{13}\mathrm{C}^{16}\mathrm{O}^{16}\mathrm{O}^{16}\mathrm{O}^{2-} + {}^{12}\mathrm{C}^{18}\mathrm{O}^{16}\mathrm{O}^{16}\mathrm{O}^{2-} \rightleftharpoons {}^{13}\mathrm{C}^{18}\mathrm{O}^{16}\mathrm{O}^{16}\mathrm{O}^{2-} + {}^{12}\mathrm{C}^{16}\mathrm{O}^{16}\mathrm{O}^{16}\mathrm{O}^{2-}$ Reaction 1

Reaction 2

$^{12}\mathrm{C}^{18}\mathrm{O}^{16}\mathrm{O}^{16}\mathrm{O}^{2-}$ + ($^{12}\mathrm{C}^{16}\mathrm{O}^{18}\mathrm{O}^{16}\mathrm{O}^{2-}$ or $^{12}\mathrm{C}^{16}\mathrm{O}^{16}\mathrm{O}^{18}\mathrm{O}^{2-}$) $\rightleftharpoons$ ($^{12}\mathrm{C}^{18}\mathrm{O}^{18}\mathrm{O}^{16}\mathrm{O}^{2-}$ or $^{12}\mathrm{C}^{18}\mathrm{O}^{16}\mathrm{O}^{18}\mathrm{O}^{2-}$ or $^{12}\mathrm{C}^{16}\mathrm{O}^{18}\mathrm{O}^{18}\mathrm{O}^{2-}$) +$^{12}\mathrm{C}^{16}\mathrm{O}^{16}\mathrm{O}^{16}\mathrm{O}^{2-}$

When *m/z* 63 and 64 carbonate isotopologues are digested in phosphoric acid, one oxygen is cleaved, and the resulting excess *m/z* 47 and 48 $CO_2$, respectively, is measured on an isotope ratio mass spectrometer and described as

$$\Delta_{47} = (R47_{\mathrm{sample}}/R47_{\mathrm{stochastic}} - 1) \tag{1}$$

$$\Delta_{48} = (R48_{\mathrm{sample}}/R48_{\mathrm{stochastic}} - 1) \tag{2}$$

where $Ri$ is the ratio of $i$/44 $CO_2$ isotopologues, and $\Delta_{47}$ and $\Delta_{48}$ are given in parts per thousand (‰) (Ghosh et al., 2006; Eiler et al., 2007).

### 2.2 Disequilibrium processes in carbonates

$\Delta_{47}$ data for some abiotic and biogenic carbonates have been shown to record precipitation out of isotopic equilibrium (Affek et al., 2008; Daeron et al., 2011; Saenger et al., 2012; Tang et al., 2014; Tripati et al., 2015; Kimball et al., 2016; Daëron et al., 2019; Bajnai et al., 2020). This can be correlated with $\delta^{18}$O disequilibria and observed in experiments at elevated pH (e.g., Tang et al., 2014). Multiple coral species are known to significantly elevate the pH of their calcifying fluid (Ghosh et al., 2006; Affek et al., 2008; Trotter et al., 2011; Anagnostou et al., 2012; Adkins et al., 2003; Saenger et al., 2012; Kimball et al., 2016; Spooner et al., 2016). Strongly alkaline abiotic carbonate precipitation occurs in surface and subsurface aqueous systems, such as alkaline springs with pH > 11 (Christensen et al., 2021).

Multiple mechanisms have been proposed to explain $\Delta_{47}$ isotope disequilibrium mineral compositions. They have been observed experimentally at elevated pH (Tang et al., 2014). Clumped isotopic disequilibrium can arise from mineral growth from a DIC pool that is at equilibrium with DIC from speciation effects (e.g., Hill et al., 2014; Tripati et al., 2015; Watkins and Hunt, 2015; Hill et al., 2020). Carbonate mineral precipitation can occur before isotopic equilibration of dissolved inorganic carbon (DIC) (Beck et al. 2005; Tripati et al., 2015; Staudigal and Swart, 2018). $CO_2$ hydration and hydroxylation reactions are another potential source of isotopic disequilibrium (Staudigal and Swart, 2018; Guo, 2020; Boettger and Kubicki, 2021), as are dehydration and dehydroxylation reactions, and these can arise from $CO_2$ absorption and degassing processes (Daeron et al., 2011; Guo, 2020). Aqueous ion and $CO_2$ gas diffusion (Thiagarajan et al., 2011), and organism-specific vital effects from enzymatic activity and metabolism have also been hypothesized to give rise to clumped isotope disequilibrium. Clumped isotopic disequilibrium in the DIC pool has been hypothesized to be modulated by carbonate precipitation rate (Tripati et al., 2015), as with other geochemical systems such as oxygen isotopes (Dietzel et al., 2009; Watkins et al., 2014).

When carbonate minerals precipitate under isotopic disequilibrium conditions, KIEs originating from differing reaction rates of heavy versus light isotopologues can result in clumped isotope values that are higher or lower than equilibrium mineral clumped isotope values, which in turn can yield an over- or underestimation of precipitation temperature. Depending on carbonate mineral growth conditions, there are different trajectories for possible KIEs, and these can potentially be used to identify the process(es) involved through measurement of paired $\Delta_{47}$ and $\Delta_{48}$, and bulk isotope values. However, these trajectories are not yet well constrained and are limited to only a few studies. DIC speciation effects that could get recorded in a growing mineral were explored in Tripati et al. (2015). Recent modeling predictions from Guo (2020) has aimed to constrain KIEs in the $\Delta_{47}$, $\Delta_{48}$ and $\delta^{18}O$ of the $HCO_3^-$ endmember in hydration and hydroxylation reactions occurring during $CO_2$ absorption, degassing, and DIC-$H_2O$ exchange. Bajnai et al. (2020) and Fiebig et al. (2021) constructed $\Delta_{47}$ and $\Delta_{48}$ slopes relative to an equilibrium regression to remove kinetic biases from warm and cold-water coral, brachiopod, belemnite, stalagmite, and speleothem samples.

### *2.2.1 $CO_2$ hydration and hydroxylation*

$CO_2$ hydration (Reaction 3) and hydroxylation (Reaction 4) reactions are responsible for $^{18}O/^{16}O$ equilibration, as they are the only direct route for the exchange of O atoms between $H_2O$ and DIC (Zeebe and Wolf-Gladrow, 2001). Clumped and oxygen isotope equilibration of DIC in an aqueous solution are also controlled by three additional key reactions (Reactions 5-7) (Guo, 2020).

$CO_2 + H_2O \leftrightharpoons HCO_3^- + H^+$ (Reaction 3)

$CO_2 + OH^- \leftrightharpoons HCO_3^-$ (Reaction 4)

$HCO_3^- \leftrightharpoons CO_3^{2-} + H^+$ (Reaction 5)

$HCO_3^- + OH^- \leftrightharpoons CO_3^{2-} + H_2O$ (Reaction 6)

$H_2O \leftrightharpoons H^+ + OH^-$ (Reaction 7)

Equilibrium isotopic compositions are obtained when DIC and $H_2O$ have had sufficient time to isotopically equilibrate. When DIC and $H_2O$ have not been equilibrated, KIEs and disequilibrium isotopic compositions can arise. The parameters governing the time to reach isotopic equilibrium are the forward and reverse $CO_2$ hydration and hydroxylation kinetic rate constants, which depend on temperature (Zeebe and Wolf-Gladrow, 2001), and DIC speciation, which is function of temperature and pH (Uchikawa and Zeebe, 2012; Tripati et al., 2015). The rate constant for hydration is not sensitive to ionic strength (Johnson, 1982; Miller et al., 1971; Knocke 1980; Zeebe and Wolf-Gladrow, 2001), whereas a subtle dependency has been documented for the hydroxylation rate constant (Johnson, 1982). Higher temperature results in faster reaction kinetics and thus faster isotopic equilibration of the DIC pool. A higher pH causes much longer isotopic equilibration times induced by extreme low molar fraction of aqueous $CO_2$ in DIC, leading $CO_2$ to be mostly unavailable for isotope exchange in Reactions 3 and 4 (Beck et al., 2005; Weise and Kluge, 2020). For example, at 25 $^{o}$C at pH of 8.7, $^{18}$O equilibration is reached at ~17 hours, whereas at pH 12, $^{18}$O equilibration is reached at ~35 days (Beck et al., 2005). At 40 $^{o}$C and a pH of 12, $^{18}$O equilibration time is reduced to ~10 days (Beck et al., 2005).

### *2.2.2 Carbonic anhydrase*

The addition of the enzyme carbonic anhydrase (CA) catalyzes the forward and reverse hydration reaction and thus significantly decreases the time to reach isotopic equilibrium. The uncatalyzed hydration reaction rate at 25 $^{o}$C and pH 7.4 is ~$10^{-1}$ $s^{-1}$, while the CA catalyzed rate can reach ~$10^{6}$ $s^{-1}$ depending on [CA] (Kernohan, 1964), where highest catalyzation effects are achieved at pH > 8 (Berg et al., 2002). Many marine calcifiers used for climate reconstructions are thought to have CA within their calcifying space, including coccolithophores (Nimer et al., 1994; Soto et al., 2006) and other phytoplankton (Rost et al., 2003), oysters (Miyamoto et al., 1996; Yu et al., 2006), scleractinian coral (Al-Horani et al., 2003; Moya et al., 2008; Bertucci et al, 2011), and benthic foraminifera (de Goeyse et al., 2019). The role that CA plays in calcification is not completely known, including the effectiveness of CA at reducing clumped and bulk KIEs at high pH and varying temperatures.

### *2.2.3 Mixing effects*

Numerical models and experimentation have shown that while $\delta^{13}C$, $\delta^{18}O$, $\delta^{45}$, $\delta^{46}$, and $\delta^{47}$ mix linearly, $\Delta_{47}$ mixes non-linearly (Eiler and Schauble, 2004; Defliese and Lohmann, 2015). Thus, in addition to KIEs, mixing effects from the homogenization of isotopically heterogeneous samples can result in measured $\Delta_{47}$ values that do not accurately reflect precipitation temperature (Defliese and Lohmann, 2015). Some samples that are commonly used for $\Delta_{47}$-based temperature reconstructions display isotopic heterogeneity in isotopically distinct growth bands or multiple cementation stages (Jones et al., 2015), and thus sampling that integrates over growth increments or cements has the potential to give rise to mixing effects.

## 3. Methods

### 3.1 Calcite precipitation experiments

Calcite was precipitated under controlled conditions at pH 8.3, 9.0, 9.5, 10.0, 10.5, and 11.0 at 5 °C, 10 °C, 15 °C, and 25 °C, with and without the addition of CA (molecular weight 29,000 g/mol). CA has been shown to be active in catalyzing $CO_2$

hydration at all pH values used in our experiment (Kernohan, 1964). Experimental conditions are given in Table 7. Calcite was precipitated by using a method adapted from Dietzel et al. (2004). A schematic of the precipitation apparatus is shown in Figure 9. In all experiments, a 0.5 L bottle that is 2 mm thick polyethylene is filled with 0.83 M $NaHCO_3$ and 2 M HCl and placed inside a 5 L outer container filled with 4.9 L Milli Q water, 10 mM $CaCl_2$, 0.01 mM $SrCl_2$, 50 mM NaCl, and no DIC. All chemicals are reagent grade from Merck.

The $pCO_2$ gradient between the inner and outer containers causes $CO_2$ gas to diffuse through the polyethylene membrane into the outer container solution where the $CO_2$ reacts to form carbonate ions that precipitate as $CaCO_3$. The outer solution was constantly stirred with a large floating stir bar by placing the containers on top of a stir plate at 200 rpm. A piece of Styrofoam was placed in between the stir plate and solution to prevent temperature changes. The pH of the outer container solution was held constant by a Schott TitroLine alpha plus titrator (± 0.03 accuracy) with 2 M NaOH. The entire precipitation apparatus was placed inside an Aqualytic Thermostatic Cabinet (± 0.5 $^{o}$C accuracy) to hold the precipitation temperature constant. In experiments with CA, 0.25 μM CA is added to the outer solution. A concentration of 0.25 μM CA should be sufficient to maintain oxygen isotopic equilibrium among DIC species up to at least pH = 9.3 (Watkins et al., 2014). Each experiment yielded 30-40 mg of precipitate. The mineralogy of the precipitate was determined by X-ray powder diffraction (XRD) PANalytical X'Pert PRO diffractometer. The mineral phase was determined using PANalytical X'Pert HighSchore Plus software.

Every 2-3 days a 2 ml sample of the solution was removed from the outer solution via a syringe that was inserted into an airtight port through the lid of the apparatus. The solution was filtered through a 0.2 μm cellulose acetate membrane to remove any precipitate and subsequently analyzed for trace elements on a Perkin Elmer Optime 4300DV Inductively Coupled Plasma - Optical Emission Spectrometer (ICP-OES). This analysis yielded the [Ca], allowing for the estimation of the precipitation rate by ($[Ca]_{final}$ - $[Ca]_{initial}$) / ($t_{final}$ - $t_{initial}$), which was converted to mol $s^{-1}$ $m^{-2}$ using the specific surface area of 0.27 $m^2$/g (Tang et al., 2008). Oxygen isotopes of the precipitation solution were measured at the start and end of most experiments by wavelength-scanned cavity ring-down spectroscopy (WS-CRDS) using a Picarro L2140-i system. Typical analytical precision (1 σ) was ±0.05 ‰ for $\delta^{18}O_{water}$, where the values are referenced relative to the Vienna Standard Mean Ocean Water (VSMOW).

### 3.2 Mixing experiments

Two internal carbonate standards, CM Tile and Mallinckrodt, were used as isotopic endmembers to constrain $\Delta_{48}$ mixing effects. These standards were selected as endmembers because they have greatly varying bulk and clumped isotope values (see Table 11), with a ~20 ‰ difference in $\delta^{18}O$, ~38 ‰ difference in $\delta^{13}C$, 0.164 ‰ difference in $\Delta_{47}$, and 0.062 ‰ difference in $\Delta_{48}$. Endmembers with large differences in isotopic values have been shown to have a greater magnitude of mixing effects than endmembers with smaller isotopic differences (Defliese et al., 2015).

The two endmembers were combined into three mixes with varying contributions from each endmember. Mix 1 was 75 % Mallinckrodt and 25 % CM Tile, Mix 2 was 50 % Mallinckrodt and 50 % CM Tile, and Mix 3 was 25 % Mallinckrodt and 75 % CM Tile. The mixes were created by weighing out the carbonate powder from each sample and pouring them into a glass vial, where they were first stirred with a spatula, then shaken by hand for several minutes. The mixtures were then crushed in a mortar and pestle to equalize grain size, then remixed with a spatula and shaken in a glass vial. Each endmember and mix were analyzed for $\Delta_{47}$, $\Delta_{48}$, $\delta^{13}C$, $\delta^{18}O$. The observed change in $\Delta_{47}$ and $\Delta_{48}$ values due to mixing effects is referred to as $\Gamma$, described in Equation 3:

$$\Gamma_i = \Delta_{i\ \mathrm{endmember}} - \Delta_{\mathrm{i\ mix}} \tag{3}$$

where $\Delta_{i\ \mathrm{endmember}}$ is the $\Delta_{47}$ or $\Delta_{48}$ of the endmember with the highest value. It represents clumped isotope enrichment beyond what would be observed in linear mixing.

### 3.3 Clumped isotope instrumentation

Standards and samples were analyzed on three isotope ratio mass spectrometers (IRMS) during 2018-2021. The instruments used in this work were a Thermo Fisher MAT 253, and two Nu Instruments Perspective mass spectrometers, with both Nu Instruments having multiple configurations (Table 8). All instrumental configurations used here have been shown to produce statistically indistinguishable $\Delta_{47}$

(Upadhyay et al., 2021; Lucarelli et al., 2021) and the Nu Instruments produce statistically indistinguishable $\Delta_{48}$ data (Lucarelli et al, 2021). Only data from the Nu Instruments are used in the $\Delta_{48}$ analyses reported here.

A typical daily run on all instruments consists of five samples and five standards, with standards bracketing the samples. Raw data was processed and corrected in Easotope 64-bit version from release 20201231 (John and Bowen, 2016) using the IUPAC parameter set (Brand et al., 2010; Daëron et al., 2016). $\Delta_{47}$ data are presented relative to international standards ETH-1, ETH-2, ETH-3 in the I-CDES reference frame (Bernasconi et al., 2021) at 90 $^{o}$C, $\Delta_{47\ \text{I-CDES}}$. $\Delta_{48}$ data are presented relative to the same carbonate standards, with the addition of the in-house carbonate standard, Veinstrom (Upadhyay et al., 2021; Lucarelli et al., 2021), in the 90 $^{o}$C reference frame, $\Delta_{48\ \text{CDES}\ 90}$.

The Thermo Fisher MAT 253 used an autosampler similar to what is described in Passey and Henkes (2010) with a 105 weight % phosphoric acid bath held at 90 $^{o}$C. After carbonate samples of 4-7 mg are digested, $CO_2$ (g) is cryogenically purified through traps containing dry ice-cooled ethanol and liquid nitrogen, which remove low vapor pressure gases such as $H_2O$ (g). The $CO_2$ passed through elemental silver wool (Sigma Aldrich), followed by a -20 $^{o}$C gas chromatograph (GC) that contains Porapak Type-Q$^{TM}$ 50/80 mesh column pack material with He carrier gas. The *m/z* 44 beam intensity is 16000 mV. There are a total of 80-90 cycles of sample-standard comparison with a total integration time of 720 s.

Nu Instruments Perspective configurations 1a, 1b, and 1c (Table 8) consist of the same mass spectrometer with differences in the reaction and digestion system. Thus, the sample purification method, acid digestion temperature, and acid digestion method differ. All configurations on this instrument used a sample size of 0.4-0.6 mg with a total of 60 cycles of sample-standard comparison with a total integration time of 1200 s. This instrument is equipped with two curved plates with a voltage difference in front of the Faraday collectors for *m/z* 47-49 to perform secondary electron suppression, which makes the linearity correction an order of magnitude smaller than on the Thermo Fisher MAT 253. Nu Instruments Perspective configuration 1a used the same autosampler setup as the MAT 253 with an acid digestion temperature of 90 $^{o}$C, common acid bath, GC, He carrier gas, and cryogenic purification traps. New Instruments Perspective 1b is identical to 1a, except for the sample purification method, which used a relatively short GC column called an adsorption trap that is under vacuum (no carrier gas) and contains Poropak Type Q$^{TM}$. New Instruments Perceptive 1c used an acid digestion temperature of 70 $^{o}$C with individual glass reaction vials and an adsorption trap. Nu Instruments Perspective 2a and 2b use the same mass spectrometer with differences in the acid digestion temperature and method. Nu Instruments Perspective 2a used a 90 $^{o}$C acid digestion temperature, common acid bath, and adsorption trap. Nu Instruments Perspective Config. 1b used 70 $^{o}$C acid digestion, individual glass sample vials, and an adsorption trap. Both configurations used samples from 0.4-0.6 mg, and had 60 cycles of sample-standard comparison with a total integration time of 1200 s.

### 3.4 Converting $\Delta_{47}$ and $\Delta_{48}$ to $\Delta_{63}$ and $\Delta_{64}$

Measured $\Delta_{47}$ and $\Delta_{48}$ were converted to theoretical calcite mineral $\Delta_{63}$ and $\Delta_{64}$, respectively, for direct comparison to model predictions for kinetic and equilibrium relationships between bulk and clumped isotopes. This conversion was carried out using equations from Lucarelli et al. (2021). In summary, regressions were determined for compositionally dependent acid digestion fractionation factors (AFFs), $\Delta^*_{63\text{-}47}$ and $\Delta^*_{64\text{-}48}$, by using model predicted $\Delta_{63}$ and $\Delta_{64}$ values for calcite precipitated at 600 °C and 33.7 °C (Hill et al., 2014; Tripati et al., 2015). The difference was calculated between the model-predicted $\Delta_{63}$ and $\Delta_{64}$ and experimentally determined $\Delta_{47}$ and $\Delta_{48}$ for ETH-1 and ETH-2, calcite standards equilibrated at 600 °C (Bernasconi et al., 2018), and Devils Hole, a cave vein calcite precipitated near isotopic equilibrium at 33.7 °C (Winograd et al., 1988, 1992; Coplen, 2007). These values were used as the AFFs, $\Delta^*_{63\text{-}47}$ and $\Delta^*_{64\text{-}48}$, for 600 °C and 33.7 °C. Regressions were made for $\Delta^*_{63\text{-}47}$ and $\Delta_{47}$ and $\Delta^*_{64\text{-}48}$ and $\Delta_{48}$. These regressions (Equations 4 and 5) can be used to calculate acid digestion fractionation factors for unknown samples (Lucarelli et al., 2021), and then applied in Equations 6 and 7 to calculate $\Delta_{63}$ and $\Delta_{64}$.

$$\Delta^*_{63\text{-}47} = 0.0190 \times \Delta_{47\ \text{I-CDES}} + 0.1842 \tag{4}$$

$$\Delta^*_{64\text{-}48} = 0.0077 \times \Delta_{48\ \text{CDES 90}} + 0.1290 \tag{5}$$

$$\Delta_{63} = \Delta_{47\ \text{I-CDES}} - \Delta^*_{63\text{-}47} \tag{6}$$

$$\Delta_{64} = \Delta_{48\ \text{CDES 90}} - \Delta^*_{64\text{-}48} \tag{7}$$

### 3.5 $\Delta_{48}$ mixing model

For this study, a numerical model was built to estimate $\Delta_{48}$ mixing effects in $CaCO_3$ and was compared to experimental data for two carbonate reference materials, Mallinckrodt and CM Tile, which are used as isotopic endmembers. The model was constructed based on methods detailed in Defliese and Lohmann et al. (2015), with the addition of $\delta^{48}$ and $\Delta_{48}$ in this study. In the model, $\Delta_{47}$, $\Delta_{48}$, $\delta^{18}O$, and $\delta^{13}C$ values are assigned to each endmember. $\delta^{18}O$ and $\delta^{13}C$ values are also given to a hypothetical working gas (WG). The slope and intercept for an empirical transfer function (ETF) are entered into the model. All isotopic values for model samples and the working gas, as well as the transfer function values, were based on experimental data taken from the Nu Perspective instruments. No acid fractionation factor was used, and model calculations were based on values determined in the I-CDES (Bernasconi et al., 2021) reference frame at 90 $^{o}$C. The model calculates $\delta^{45}$, $\delta^{46}$, $\delta^{47}$, $\delta^{48}$, $\delta^{18}O$, and $\delta^{13}C$ values of $CO_2$ gas produced by phosphoric acid digestion of carbonate relative to a working gas (WG). The ratio of each endmember is entered into the model and the isotopic values of the mix are calculated. The full set of equations and parameters used and a link to a Github site where the model can be downloaded are detailed in the Appendix (section S.1).

### 3.6 Parameters used for IsoDIC modelling

To estimate the evolution of the isotopic composition of $HCO_3^-$ and $CO_3^{2-}$ endmembers during $CO_2$ absorption in an aqueous solution at pH 10.5, in conditions similar to our experiments, we used the IsoDIC model (Guo, 2020). This numerical modeling software predicts kinetic clumped isotope fractionations in the DIC-$H_2O$-$CO_2$ system. The model simulates five key reactions (Reactions 3-7) that control isotope fractionation, and all related isotopologue reactions involving $^{12}C$, $^{13}C$, $^{16}O$, $^{17}O$, and $^{18}O$, for a total of 155 reactions. The forward and reverse rate constants were estimated using equation 8,

$$k^{*} = \alpha_{KIE} \times k \tag{8}$$

where $k^{*}$ is the rate constant of the isotopically substituted reaction, $k$ is the rate constant of the isotopically non-substituted reactions, and $\alpha_{KIE}$ is the kinetic isotope fractionation factor for the isotopically substituted reaction. Isotopic equilibrium was assumed between $HCO_3^-$ and $CO_3^{2-}$ and $H_2O$ and $OH^-$ due to rapid equilibration via Reactions 5-7 relative to the reaction rate of hydration (Reaction 1) and hydroxylation (Reaction 2). Therefore, the only reactions that contribute to isotopic fractionation in the IsoDIC model are the forward and reverse $CO_2$ hydration and hydroxylation reactions (Guo, 2020).

To use the IsoDIC model in the $CO_2$ absorption regime, we assumed the model default values for $\delta^{13}C$ of the $CO_2$ in air of -10 ‰, $\delta^{18}O_{VSMOW}$ of water to be 0 ‰, and $\Delta'^{17}O_{VSMOW}$ of water to be 0 ‰ (Guo, 2020). The initial oxygen and clumped isotope values of DIC and air were set to be in equilibrium with water. We set the solution temperature to be 5°C in the first simulation and 25°C in the second simulation, both with a solution pH of 10.5. The model has a total evolution time of 12 hours. The full set of equations used are available in Guo (2020).

### 3.7 Box model for kinetic isotope effects in $\Delta_{47}$, $\Delta_{48}$, and $\delta^{18}O$

To predict kinetic isotope effects in calcite during $CO_2$ absorption for $\Delta_{47}$, $\Delta_{48}$, and $\delta^{18}O$, we used a box model built on the ExClump38 framework (Chen et al., 2018; Uchikawa et al., 2021; Watkins and Devriendt, 2021). The model tracks the isotopic composition of DIC species in a homogeneous (i.e., well-stirred) solution from an initial unequilibrated state. In the box model, the isotopic composition of DIC is affected by two additional fluxes: (1) a specified $CO_2$ influx and (2) a calculated $CaCO_3$ outflux that is based on the following reactions:

$Ca^{2+} + HCO_3^- \rightleftharpoons CaCO_3 + H^+$ Reaction 8

$Ca^{2+} + CO_3^{2-} \rightleftharpoons CaCO_3$ Reaction 9

These reactions affect the isotopic composition of DIC in two ways: (1) the rate constants for Reactions 8 and 9 are mass dependent and can therefore influence the isotopic composition of residual DIC (Watkins and Hunt, 2015) and (2) the rate of calcite precipitation affects the degree of hydration/hydroxylation reaction reversibility at steady state and the extent to which the kinetic isotope effects attending these reactions are expressed in solution.

In the model, we begin with [$Ca^{2+}$] = 10 mM and enough DIC to bring the initial degree of supersaturation to 7, as estimated from Dietzel et al. (2009) for spontaneous nucleation of calcite;

$$\Omega = \frac{[CO_3^{2-}][Ca^{2+}]}{K_{sp\ (calcite)}} \sim 7 \tag{9}$$

where Ω is the saturation state and $K_{sp}$ is the solubility product for calcite. The DIC is initially isotopically equilibrated. As $CO_2$ fluxes into solution it gets converted to isotopically lighter-than-equilibrium $HCO_3^-$ and $CO_3^{2-}$ by hydration (Reaction 3) and hydroxylation (Reaction 4). The rate of calcite growth depends on [$Ca^{2+}$] and [$CO_3^{2-}$], which is updated at each time step. Each simulated experiment lasts 1000 hours, which is far longer than the time required to reach steady state, and outputs the steady state composition of each DIC species and calcite. In the default scenario, we treat the reaction rate constants as “known” and the ion-by-ion model as “correct” to assess how well the model predicts the trends observed in the data. This leaves the $CO_2$ flux ($F_{CO2}$) as the only adjustable parameter in the default scenario, but even $F_{CO2}$ (which is equal to $F_{CaCO3}$ at steady state) is constrained by the data. A description of all equations and parameters used are provided in Appendix (S.2) that also contains a link to a Github site with the parameters utilized and code used.

The steady state $\Delta_{47}$, $\Delta_{48}$, and 1000ln$\alpha_{carb-water}$ at variable pH from 8.3 to 11, at temperatures of 5 °C and 25 °C, and variable FCO2 (related to calcite growth rate) ranging from typical experimental rates to those from extremely slow calcite growth. The oxygen fractionation factor between carbonate and water, $\alpha_{carb-water}$, is expressed by the equation:

$$\alpha_{carb-water} = \frac{^{18}R_{carb}}{^{18}R_{water}} = \frac{\delta^{18}O_{carb}+1000}{\delta^{18}O_{water}+1000} \quad (10)$$

where $^{18}R$ is the ratio of $^{18}O$ to $^{16}O$ in the carbonate and water.

We repeated the same model calculations, but simulated the impact of the addition of 0.25 μM CA.  All model calculations had 0 ‰ salinity, while experiments had a starting ionic strength of ~0.045 mol/L. This should have a negligible effect on our model calculations given that the reaction rate constants will not be affected by the ionic strength. We compared the results of the model calculations (with and without CA) to our experimental data (with and without CA) and to experimental data from Tang et al. (2014), where calcite was precipitated at pH 8.3, 8.5, 9.0, 10.0, and 10.5 at 5 $^{o}$C, and pH 8.3 at 25 $^{o}$C (no enzyme was utilized in their experiments).

## 4. Results

### 4.1 Calcite precipitated with and without carbonic anhydrase

#### *4.1.1 $\delta^{13}C$ and $\delta^{18}O$*

Calcite, verified by XRD, precipitated at increasing pH had an increasing amount of $\delta^{18}$O depletion (Figure 10A-D, Table 9). The largest $\delta^{18}$O depletion relative to the near equilibrium sample (precipitated at the same temperature at pH 8.3 with CA) was observed in the samples with the lowest temperature and highest pH, at 5 $^{o}$C and pH 10.5 and 11.0, with depletions of 17.7 ‰ and 18.8 ‰, respectively. All samples precipitated with and without CA at pH 8.3 had statistically identical $\delta^{18}$O. At 5 $^{o}$C, depletions in $\delta^{18}$O were observed at pH > 9. Calcite precipitated without CA had depleted $\delta^{13}$C when compared to samples precipitated with CA for all temperatures and pHs (Figure 10E-H, Table 9).

### ***4.1.2 $\Delta_{47}$ and $\Delta_{48}$***

For a given temperature, calcite precipitated with and without CA at pH 8.3 had statistically identical $\Delta_{47}$ and $\Delta_{48}$. Samples precipitated without CA at pH ≥ 9.5 had enriched $\Delta_{47}$ and depleted $\Delta_{48}$ values relative to calcite precipitated with CA, and these samples also had negative $\Delta_{48}$ values (i.e., $^{12}$C$^{18}$O$^{18}$O occurring less frequently than predicted due to random chance) (Figure 11, Table 9). The enrichment of $\Delta_{47}$ and depletion of $\Delta_{48}$ increased with increasing pH. The largest $\Delta_{47}$ enrichment was 0.198 ‰ at 5 $^{o}$C and pH 10.5. The largest $\Delta_{48}$ depletion was -0.628 ‰ at 5 $^{o}$C and pH 11.0. Despite the relatively large depletions in $\Delta_{48}$ compared to enrichments in $\Delta_{47}$, CA appears to be more effective at returning $\Delta_{48}$ values to near-equilibrium values than for $\Delta_{47}$.

Kinetic slopes for $\Delta_{47}$ and $\delta^{18}$O, $\Delta_{48}$ and $\delta^{18}$O, and $\Delta_{48}$ and $\Delta_{47}$ were determined (Table 12). Kinetic slopes for $\Delta_{47}$ and $\delta^{18}$O (Figure 12A-D) at 5 °C, 10 °C, 15 °C, and 25 °C were -0.011 ± 0.001, -0.013 ± 0.0001, -0.012 ± 0.0002, and -0.020 ± 0.001, respectively. Kinetic slopes for $\Delta_{48}$ and $\delta^{18}$O (Figure 12E-H) at 5 °C, 10 °C, 15 °C, and 25 °C were 0.033 ± 0.001, 0.038 ± 0.0004, 0.034, and 0.048 ± 0.002, respectively. Kinetic slopes for $\Delta_{48}$ and $\Delta_{47}$ (Figure 13) at 5 °C, 10 °C, 15 °C, and 25 °C were -2.989 ± 0.125, -3.071 ± 0.011, -2.976 ± 0.034, and -2.455 ± 0.024, respectively.

Equilibrium regressions were made for $\Delta_{47}$ and $\Delta_{48}$ relative to precipitation temperature in Kelvin (Figure 14A-B), $\Delta_{47}$ and $\Delta_{48}$ relative to $\delta^{18}$O (Figure 14C-D), and $\Delta_{48}$ and $\Delta_{47}$ (Figure 14E), for calcite precipitated at 5 °C, 10 °C, 15 °C, and 25 °C with CA at pH 8.3, which are expected to achieve quasi-isotopic equilibrium. Devils Hole core DH-2 data previously analyzed in Lucarelli et al. (2021) was included in the equilibrium regressions for $\Delta_{48}$ and $\Delta_{47}$, $\Delta_{47}$ and precipitation temperature, and $\Delta_{48}$ and precipitation temperature. Devils Hole has been shown to be near isotopic equilibrium (Winograd et al., 1998; Coplen, 2007) and has a very precisely known precipitation temperature of 33.7 ± 0.2 °C (Plummer et al., 2000). The experimental $\Delta_i$ and $T$ relationships were determined to be

$$\Delta_{47\ \mathrm{I\text{-}CDES}} = (0.037 \pm 0.002) \times 10^6 T^{-2} + (0.175 \pm 0.026);\ r^2 = 0.99 \tag{10}$$

$$\Delta_{48\ \mathrm{CDES\ 90}} = (0.013 \pm 0.001) \times 10^6 T^{-2} + (0.100 \pm 0.012);\ r^2 = 0.98 \tag{11}$$

where $T$ is the precipitation temperature in Kelvin. The $\Delta_{48}$ and $\Delta_{47}$ relationship is represented by equation 12.

$\Delta_{48\ \mathrm{CDES}\ 90} = (0.355 \pm 0.030)\ \Delta_{47\ \mathrm{I\text{-}CDES}} + (0.039 \pm 0.018);\ r^2 = 0.98$ (12)

The equilibrium relationships for $\Delta_{47}$ and $\Delta_{48}$ and $\delta^{18}O$ (Figure 14C-D) are represented by equations 13 and 14.

$\Delta_{47\ \mathrm{I\text{-}CDES}} = (0.013 \pm 0.001)\ \delta^{18}O_{\mathrm{VPDB}} + (0.743 \pm 0.006);\ r^2 = 0.99$ (13)

$\Delta_{48\ \mathrm{CDES}\ 90} = (0.004 \pm 0.001)\ \delta^{18}O_{\mathrm{VPDB}} + (0.303 \pm 0.005);\ r^2 = 0.97$ (14)

### *4.1.3 Measured and modeled $\Delta_{47}$, $\Delta_{48}$, $\alpha_{carb\text{-}water}$, and growth rate effects*

We compare our calcite isotopic values to those we predicted using the IsoDIC model (Guo, 2020) for different temperatures and pH in Figure 15. We used the model to quantify the temporal evolution of disequilibrium $\Delta_{63}$ and $\Delta_{64}$ in bicarbonate and carbonate ion endmembers during $CO_2$ absorption in an aqueous solution at pH 10.5 at 5 °C and 25 °C. The experimental kinetic slope for our samples precipitated at 5 °C and pH ≥ 9.5 was $m$ = -3.127 ± 0.302 and for samples precipitated at 25 °C at pH 10.5, $m$ = -2.485 ± 0.025 (Figure 15). The model trajectories agree with titration data indicating that in experiments with pH ≥ 9.5 at 5 °C and 25 °C, calcite precipitation began during the first day. At both temperatures, the calcite precipitated at pH 10.5 exceeded the model predictions for maximum enrichment of $\Delta_{63}$, and conversely, did not achieve the maximum amount of depletion for $\Delta_{64}$ predicted by the model, that could indicate the influence of another factor, such as growth rate.

We compare our experimentally constrained mineral isotopic compositions to box model calculations that factor into account modulation of isotopic fractionation by growth rate (Figure 16). We used the model to predict 1000ln($\alpha_{carb\text{-}water}$), $\Delta_{47}$, and $\Delta_{48}$ with and without CA and compared simulated values to our experimental results. We also compared our results to experimental data from Tang et al. (2014) (Figure 16). Tang et al. (2014) performed calcite precipitation experiments at pH 8.3, 8.5, 9.0, 9.5, 10.0, and 10.5 at 5 $^{o}$C, and pH 8.3 at 25 $^{o}$C, with precipitation rates ranging from -5.99 to -7.38. Our precipitation rates are given as the log of *R* (mol $s^{-1}$ $m^{-2}$) for direct comparability to previous modeling and measurements (Table 7). The precipitation rates measured here range from -7.02 to -7.48, which are typical growth rates for calcite precipitation experiments or for corals, which range from ~-4.8 to ~-7.6 (Dietzel et al., 2009; Ghosh et al., 2006; Saenger et al., 2012).

The default model for 1000ln($\alpha_{carb\text{-}water}$) at 5 $^{o}$C and 25 $^{o}$C underestimates the observed experimental fractionations at high pH, even at the fastest precipitation rate. The largest difference between the model and experimental values is at 5 $^{o}$C and pH 10.5, with a model predicted 1000ln($\alpha_{carb\text{-}water}$) value of 22.0, and experimental values of 14.8 and 13.1 for this study and Tang et al. (2014), respectively. The default model-predicted values for $\Delta_{47}$ and $\Delta_{48}$ had overall good agreement with experimental values at high and low pH. Model calculations that consider the addition of 0.25 μM CA had better agreement with experimental data at pH ≥ 10 at 5 $^{o}$C and 25 $^{o}$C.

Calcite precipitated at high pH with CA (hollow data points in Figures 12, 13, 15, and 13) followed a different trajectory with a shallower $\Delta_{47}$ versus $\Delta_{48}$ slope (*m* = -0.371 ± 0.107 at 5 $^{o}$C; *m* = -0.443 at 25 $^{o}$C) (Figure 13). The shallower slope may be more representative for organisms that have CA in their calcifying fluid. Increased disequilibrium was observed in $\Delta_{47}$ relative to $\Delta_{48}$ in samples at pH ≥ 9.5 with CA indicating that CA may be better at equilibrating *m/z* 64 isotopologues than *m/z* 63 isotopologues. Since *m/z* 63 isotopologues contain both $^{13}$C and $^{18}$O it likely takes longer to equilibrate than *m/z* 64 isotopologues, which contain 2 $^{18}$O atoms and no $^{13}$C, due to CA catalyzing O isotope exchange. It has been shown experimentally that CA discriminates against $CO_2$ and $HCO_3$ that contain $^{13}$C due to slower rates of diffusion to the enzyme (Paneth and O'Leary, 1985).

### 4.2 $\Delta_{47}$ and $\Delta_{48}$ mixing experiment and model results

Two internal carbonate standards, CM Tile and Mallinckrodt, were used as endmembers to constrain clumped isotope mixing effects because they have large differences in their bulk and clumped isotope values. Mix 1 (75 % Mallinckrodt, 25 % CM Tile) had $\Gamma_{47}$ = 0.106 ‰ and $\Gamma_{48}$ = 0.039 ‰, Mix 2 (50 % Mallinckrodt, 50 % CM Tile) had $\Gamma_{47}$ = 0.107 and $\Gamma_{48}$ = 0.042, Mix 3 (25 % Mallinckrodt, 75 % CM Tile) had $\Gamma_{47}$ = 0.014 ‰ and $\Gamma_{48}$ = 0.007 ‰ (Figure 17A, Table 11). The measured $\Delta_{47}$ and $\Delta_{48}$ were within error of model predicted values, validating the robustness of the model. Table 12 lists all model parameters.

Figure 17B shows $\Delta_{47}$ and $\Delta_{48}$ model predictions for modeled calcite formation with differing clumped and bulk isotopes, differing clumped isotopes and identical bulk isotopes, and identical clumped isotopes with differing bulk isotopes. The model with a difference of 0.141‰ for $\Delta_{47}$ and 0.064 ‰ for $\Delta_{48}$, and 20 ‰ difference in $\delta^{18}$O and $\delta^{13}$C between endmember 1 (E1) and endmember 2 (E2), had $\Gamma_{47}$ = 0.029 ‰ and $\Gamma_{48}$ = 0.039 ‰. These $\Gamma_{47}$ and $\Gamma_{48}$ values were smaller than for the endmembers with the same clumped isotope values and a 20 ‰ difference in $\delta^{18}$O and $\delta^{13}$C, where $\Gamma_{47}$ = 0.086 and $\Gamma_{48}$ = 0.073. The endmembers with differing clumped isotope values and the same bulk isotope values mix linearly. For endmembers with identical clumped isotope values and differing bulk isotope values (Figure 17C-D), the largest $\Gamma_{47}$ and $\Gamma_{48}$ were 0.769 ‰ and 0.660 ‰, respectively, for endmembers with a 30 ‰ difference in $\delta^{18}$O and $\delta^{13}$C. The smallest $\Gamma_{47}$ and $\Gamma_{48}$ predicted were 0.021 ‰ and 0.018 ‰, respectively, for endmembers with a 10 ‰ difference in $\delta^{18}$O and $\delta^{13}$C.

## 5. Discussion

### 5.1 Comparison of kinetic effects observed in isotopic data with theory

#### *5.1.1 $\delta^{18}$O and $\delta^{13}$C*

There are multiple factors that may contribute to the observed clumped and bulk kinetic isotope effects in this study, including $CO_2$ hydration and hydroxylation, pH dependent DIC speciation, growth rate effects, diffusive isotope effects, and precipitation occurring before temperature and pH dependent equilibrium is achieved in the DIC pool. Modeling predicts that hydration should discriminate against $^{18}$O by 14-15 ‰ and $^{13}$C by 19-23 ‰ at 25 $^{o}$C, while hydroxylation would discriminate against $^{18}$O by

27-30 ‰ and $^{13}C$ by 26-31 ‰ at 25 $^{o}C$ (Boettger and Kubicki, 2021). At a pH > ~8.4 hydroxylation starts to dominate, and at a pH of 10, hydroxylation represents 95% of reactions (McConnaughey, 1989). Additionally, at equilibrium, $\delta^{18}O$ decreases in DIC species in the following order: $CO_2 > H_2CO_3 > HCO_3^- > CO_3^{2-}$ (Usdowski et al., 1991; Beck et al., 2005), and at pH > 10, $CO_3^{2-}$ dominates the DIC composition (Hill et al., 2014; Tripati et al., 2015). This is consistent with what we experimentally observed, with increasing depletion in oxygen isotopes starting in samples precipitated at pH > 9 without CA (Table 9, Figure 10).

The trend observed in $\delta^{13}C$ also indicates subtle depletion starting at pH ≥ 9.5 for samples precipitated without CA (Figure 10). For calcite precipitated with CA, there was depletion starting at pH ≥ 9. When calcite precipitated with and without CA at the same pH and temperature were directly compared, there was an offset observed in $\delta^{13}C$, including for samples precipitated at pH 8.3 (Table 9, Figure 11). This offset may be due to diffusion and the effects of CA on the $CO_2$ gradient between the inner and outer solutions. The enzyme CA makes the hydration reaction more reversible, and thus, the $[CO_2]$ in the outer solution could be higher in experiments with CA. If so, this would decrease the $CO_2$ gradient between the inner and outer chambers and lead to less diffusive isotopic fractionation. For samples precipitated without CA in the outer solutions, the $CO_2$ diffusing into the outer chamber would be isotopically lighter, which is consistent with observations. The offset in $\delta^{13}C$ between experiments with and without CA decreases with increasing pH, consistent with the decreasing influence of the CA-catalyzed hydration reaction with increasing pH.

This same effect is not evident in $\delta^{18}O$, with catalyzed and uncatalyzed reactions precipitated at pH 8.3 and the same temperature having statistically indistinguishable $\delta^{18}O$ values (Figure 10). Since CA catalyzes the pathway for O exchange among DIC to a nearly instantaneous reaction, does not exchange C among DIC species, and changes the transition state to a more hydroxylation-type reaction, this potentially explains why the use of CA may alter the $\delta^{13}C$, but not the $\delta^{18}O$, of inorganically precipitated carbonates.

### *5.1.2 Paired clumped isotopes ($\Delta_{47}$-$\Delta_{48}$ and $\Delta_{63}$-$\Delta_{64}$) and clumped isotopes with $\delta^{18}O$*

Samples grown at elevated pH without CA exhibit enriched $\Delta_{47}$ and depleted $\delta^{18}O$ (Figure 12) consistent with $CO_2$ hydrolysis (Tripati et al., 2015; Guo, 2020). These samples also exhibit "hyperstochastic" values for $\Delta_{48}$ that we hypothesized resulted from a depletion in $^{12}C^{18}O^{18}O$ produced by the relative rate kinetics for different $CO_2$ isotopologues during hydration and hydroxylation, which we test by comparing experimental data to model calculations. Our experimental data yield slopes that range between -2.455 to -3.071 for $\Delta_{47}$ and $\Delta_{48}$ (Figure 13), and -2.485 to -3.127 for $\Delta_{63}$ and $\Delta_{64}$. These experimental data at high pH fall between model-predicted slopes for $CO_2$ absorption and high pH travertines (Figure 18). The IsoDIC model (Guo, 2020) yields predicted slopes for $\Delta_{63}$ and $\Delta_{64}$ of $HCO_3^-$ produced from hydration and hydroxylation reactions during $CO_2$ absorption, $CO_2$ outgassing, DIC speciation, DIC diffusion, thermodynamic equilibrium, and in pH 11.5 travertines. We calculated model-predicted slopes using the clumped isotope composition of the bicarbonate endmember for times ranging from 0-5 minutes after the initial reaction occurs. The model predicted slope for $\Delta_{63}$ and $\Delta_{64}$ during $CO_2$ absorption at a pH 9 was -1.72, while the predicted slope for pH 11.5 travertines was -8.33.

We were able to simulate observed hyperstochastic $\Delta_{64}$ values that are consistent with our experimental observations of $\Delta_{48}$. Our measured kinetic slopes at 25 °C for $\Delta_{47}$ and $\delta^{18}$O of -0.020 ± 0.001, and $\Delta_{48}$ and $\delta^{18}$O of 0.048 ± 0.002 (Figure 13, Table 10) are in good agreement with model predicted slopes for hydration/hydroxylation during $CO_2$ absorption of -0.024 for $\Delta_{47}$ and $\delta^{18}$O and 0.041 for $\Delta_{48}$ and $\delta^{18}$O (Guo, 2020). This agreement indicates that hydration and hydroxylation KIEs occurring following $CO_2$ absorption are likely the most significant KIEs observed in our samples precipitated at elevated pH.

In our 5 °C sample at pH 9, there was a depletion in $\delta^{18}$O of 4 ‰ relative to the calcite precipitated with CA under the same conditions, and no statistically significant change in $\Delta_{47}$ (Table 9). This may indicate that carbonates precipitated at pH ≤ 9 are more likely to exhibit a decoupling of disequilibrium in $\delta^{18}$O and $\Delta_{47}$, but calcite precipitated at pH ≥ 9.5 exhibit disequilibrium in $\delta^{18}$O and $\Delta_{47}$ values. It should also be noted that our 5 °C sample at pH 9 had a depletion of 0.042 ‰ relative to expected equilibrium in $\Delta_{48}$, possibly indicating a greater sensitivity to pH and non-equilibrium oxygen isotope values than for $\Delta_{47}$, potentially due to the presence of two $^{18}$O substitutions in *m/z* 64 isotopologues. It is possible this may represent the same type of decoupling between oxygen isotopes and $\Delta_{47}$ that were observed in deep-sea corals (Thiagarajan et al., 2011).

### *5.1.3 The effect of precipitation rate on bulk and clumped isotopes*

KIEs resulting in non-equilibrium clumped isotope compositions of DIC species have the potential to be recorded in carbonate minerals, modulated by growth rate (Tripati et al., 2015; Watkins and Hunt, 2015). It has been suggested that at rapid growth rates, a kinetic limit may be reached while at slow growth, an equilibrium limit may be attained (e.g., DePaolo, 2011; Tripati et al., 2015; Watkins and Hunt, 2015). For samples precipitated at pH 8-9 in a solution with a fully equilibrated DIC pool at 25 $^oC$, Watkins and Hunt (2015) used an ion-by-ion growth model to predict that the $\Delta_{63}$ of calcite precipitated at typical experimental growth rates ($\log_{10}R$ = -5 to -7 mol/m$^2$/s) should be at or near the kinetic limit, and that given equilibrium isotopic compositions for DIC endmembers (Hill et al., 2014; Tripati et al, 2015), calcite $\Delta_{63}$ would be ~0.01 ‰ higher than expected equilibrium value at 25 $^oC$, while for samples precipitated at pH > 10, calcite would be ~0.01 ‰ to ~0.02 ‰ lower than expected equilibrium $\Delta_{63}$ values. The kinetic limit should be substantially different if the DIC pool has not achieved equilibrium (Tripati et al., 2015; Guo, 2020), and we find that our measured $\Delta_{47}$ values for samples precipitated at pH 10.5 have $\Delta_{47}$ that are elevated by 0.168-0.198 from expected mineral equilibrium values (Figure 11). While these observations are consistent with relatively large kinetic effects associated with $CO_2$ absorption, including hydration, hydroxylation, and a DIC pool that is not equilibrated, it is also likely they include a kinetic contribution to the isotopic signatures from growth rate effects.

For samples from this study and most from Tang et al. (2014) at pH 8.3, we find that $\Delta_{47}$ and $\Delta_{48}$ values are indistinguishable from equilibrium values irrespective of precipitation rate. This is the case for calcite precipitation at temperatures of 5 °C and 25 °C, both with and without CA. This suggests that the intrinsic kinetic fractionation factor for clumped isotopes is close to unity (Guo, 2020) and that accurate temperatures can be retrieved even when there are large kinetic oxygen isotope effects.

At higher pH, over the growth rates observed here, modeling and experimental data suggests that mineral disequilibrium occurs. Specifically, our calculations (Figure 16) suggest that samples precipitated at the same pH and temperature but at different growth rates, in a system where $CO_2$ absorption is dominant, and a DIC pool that has not reached equilibrium, may yield calcite with mineral disequilibrium of up to ~8.4 for 1000ln(carb-water), ~0.23 ‰ for $\Delta_{47}$, and ~0.51 ‰ for $\Delta_{48}$. These effects are the largest for calcite growing at pH ≥ 9.5 and low temperature.

We note this model underestimates oxygen isotope fractionations observed in the experimental samples synthesized in both this study and Tang et al. (2014) at multiple temperature and pH. This may reflect the presence of an additional KIE influencing oxygen isotopes in DIC. In both this work and in Tang et al. (2014), $CO_2$ diffused through a polyethylene membrane, which may enrich the solution in $^{12}C$ and $^{16}O$. Thus, results may reflect a kinetic oxygen isotope effect from membrane diffusion, as Tang et al. (2014) hypothesized in their work. Since the time to reach isotopic equilibrium is much longer at high pH and low temperature (Beck et al., 2005), a diffusive signal in oxygen isotopes would be more apparent in samples precipitated at high pH and low temperature, which is what we observe. The other possibility is that the hydroxylation KFFs from the literature are underestimated. When the hydroxylation KFF for oxygen is increased to match the 1000ln($\alpha_{\text{carb-water}}$) data (Figure 16Q-X), however, there is significantly less agreement between measured and modeled $\Delta_{48}$. This suggests either that diffusion is responsible for the low 1000ln($\alpha_{\text{carb-water}}$) values or that the model is over-predicting the sensitivity of $\Delta_{48}$ to kinetic oxygen isotope fractionations. Additionally, the model may underestimate the catalytic ability of CA to equilibrate $\Delta_{47}$ and $\Delta_{48}$ for calcite formed at fast growth rates and at high pH.

However, no such signal is observed for clumped isotopes, with all measured sample $\Delta_{47}$ and $\Delta_{48}$ values residing within the model predicted range, with the exception of one calcite sample precipitated with CA at pH 11 at 25°C. It may be possible that a diffusive signal, which is expected to lower $\delta^{18}$O and increase $\Delta_{47}$ (Thagarajan et al., 2011), is smaller or absent in the experimental $\Delta_{47}$ and $\Delta_{48}$. Currently, we are unable to resolve the diffusive contribution to our experimental isotope signatures, but an upper bound of a 22 ‰ decrease for $\delta^{18}$O and 0.5 ‰ increase for $\Delta_{47}$ for Knudsen diffusion was calculated by Eiler and Schauble (2004). An additional possibility is that the oxygen isotope kinetic fractionation factors used in the model calculations are underestimated. However, when oxygen isotope kinetic fractionation factors are increased to match experimental oxygen isotope data (Figure 16Q-X) the agreement between model and experimental $\Delta_{48}$ is decreased. This may indicate than another kinetic effect is the source of the mismatch between modeled and measured 1000ln($\alpha_{carb\text{-}water}$) or that $\Delta_{48}$ is less sensitive to oxygen isotope fractionation factors than is predicted by the model.

Future work could further constrain growth rate effects by precipitating calcite under controlled conditions over an even broader range of growth rates than what was done in this work and in Tang et al. (2014). This would allow for experimental data to be compared to model predictions for the slow and fast growth limits. Diffusion effects could also be explored by precipitating calcite at fast growth rates from $CO_2$ diffused at different rates through membranes of varying pore sizes.

### 5.2 Paired clumped isotope data: Near equilibrium mineral compositions

Samples grown at pH 8.3 and at variable temperatures with CA yield $\Delta_{47}$ and $\Delta_{48}$ values that are consistent with mineral equilibrium as constrained using multiple independent approaches. The calcite growth rates achieved are ones that our modeling indicates should attain the equilibrium limit, and experimental data and model calculations converge (Figure 16). Theory from Hill et al. (2014) and Tripati et al. (2015) combined with experimental AFF values (Lucarelli et al., 2021) show that measured $\Delta_{47}$ and $\Delta_{48}$ from this work are consistent with calcite equilibrium (Figure 19A-C).

These results lend further support to experimental and field-derived calibration datasets being in near equilibrium. An F test (performed in PRISM 7) was used for a statistical comparison between experimentally determined regressions for $\Delta_{47}$ and $\Delta_{48}$ values for near-equilibrium samples with known precipitation temperatures from Swart et al. (2021), Fiebig et al. (2021), with results from this study (Table 13). The test determined that the regressions were not statistically different ($p$ = 0.99, Table 14) and a combined regression is represented by equation 15 (Figure 19).

$$\Delta_{48\ \mathrm{CDES\ 90}} = (0.407 \pm 0.016)\ \Delta_{47\ \mathrm{CDES\ 90}} + (0.006 \pm 0.009);\ r^2 = 0.98 \qquad (15)$$

The data from Fiebig et al. (2021) includes lake and cave calcites, inorganic precipitations, and samples equilibrated at high temperatures, with samples having crystallization temperatures from 7.9 °C to 1100 °C. Sample data from Swart et al. (2021) includes 7 inorganic calcite precipitations from 5 °C to 65 °C. The experimentally determined regressions from Swart et al. (2021), Fiebig et al. (2021), and this study are bracketed by regressions from Bajnai et al. (2020) and Lucarelli et al. (2021) determined using a combination of theory from Hill et al. (2014) and Tripati et al. (2015) and experimental AFF values. These regressions are statistically indistinguishable from the experimental regressions ($p = 0.99$).

It was also determined that the experimental regressions based on samples with known precipitation temperatures from Swart et al. (2021), Fiebig et al. (2021), and this study are statistically indistinguishable ($p > 0.99$) from the $\Delta_{47}$ and $\Delta_{48}$ regression from Lucarelli et al. (2021) based on measurements of 20 carbonates, most of which are used as standards and had unknown precipitation temperatures but were shown to have clumped isotope values near clumped isotopic equilibrium. The combined regression for these experimental datasets is represented by equation 16.

$$\Delta_{48\ \mathrm{CDES}\ 90} = (0.429 \pm 0.010)\ \Delta_{47\ \mathrm{CDES}\ 90} - (0.006 \pm 0.006);\ r^2 = 0.98 \qquad (16)$$

An F test was used to test for statistical differences between experimentally determined regressions for $\Delta_{47}$ and $10^6T^{-2}$ and $\Delta_{48}$ and $10^6T^{-2}$ from Swart et al. (2021), Fiebig et al. (2021), and this study (Figure 19). It was determined that these regressions were not statistically different ($p$ = 0.99 for $\Delta_{47}$ and $10^6T^{-2}$; $p$ = 0.99 for $\Delta_{48}$ and $10^6T^{-2}$). The combined experimentally based regressions are presented in equations 17 and 18 with temperature in Kelvin.

$$\Delta_{47\ \text{I-CDES}} = (0.037 \pm 0.001) \times 10^6T^{-2} + (0.178 \pm 0.009);\ r^2 = 0.99 \tag{17}$$

$$\Delta_{48\ \text{CDES 90}} = (0.015 \pm 0.0005) \times 10^6T^{-2} + (0.078 \pm 0.006);\ r^2 = 0.98 \tag{18}$$

The experimental regressions were also determined to be statistically indistinguishable from the regressions based on theory and experimental AFFs from Bajnai et al. (2020) and Lucarelli et al. (2021) ($p$ = 0.99).

Offsets in $\Delta_{48}$ are likely from differences in standardization. This study and Lucarelli et al. (2021) used carbonate-based standardization, Swart et al. (2021) used gas-based standardization, and Bajnai et al. (2020) and Fiebig et al. (2021) used a combination of carbonate and gas-based standardization. For $\Delta_{47}$, this study and Fiebig et al. (2021) use the I-CDES reference frame, while Bajnai et al. (2020) and Fiebig et al. (2021) use the CDES 90 reference frame. While I-CDES and CDES 90 are very similar reference frames being that they are both present data at 90 $^{o}$C, the main difference is that the I-CDES reference frame uses multi-lab determined values presented in Bernasconi et al. (2021) for the carbonate standards ETH-1, ETH-2, and ETH-3 for standardization, while CDES 90 may use slightly different values these carbonate standards and other carbonate standards or may also present data relative to equilibrated gas standards. All data reported thus far use the CDES 90 reference frame for $\Delta_{48}$, however, differences in values used for carbonate standards and the use of carbonate and/or gas-based standardization vary between labs, as discussed in Lucarelli et al. (2021). Additionally, $\Delta_{48}$ is relatively sensitive compared to $\Delta_{47}$ to subtle changes in transfer functions and nonlinearity slopes used in data corrections. For example, a shift of ~0.05 in the slope of the $\Delta_{48}$ transfer function can shift $\Delta_{48}$ values by ~0.029 ‰, while the same magnitude shift in the $\Delta_{47}$ transfer function will shift $\Delta_{47}$ values by ~0.013 ‰ (Supplementary Table S5).

### 5.3 Mixing effects in paired clumped isotopes

Biominerals and abiotic natural systems often have fluxes of isotopically distinct fluids associated with carbonate mineral precipitation, which in turn can yield products with distinct bulk isotopic compositions. This can occur from the precipitation processes themselves, or arise from temperature fluctuations over the course of precipitation, or be associated with the integration of seawater into calcifying spaces. Additionally, diagenetic processes can give rise to multiple phases of carbonates being present, which in turn can be sampled. Thus, it is possible that carbonates with different bulk isotopic compositions, and clumped isotope compositions, can be mixed physically within a single clumped isotope sample. Mixing effects have been explored for $\Delta_{47}$ in $CO_2$ (Eiler and Schauble, 2004) and in carbonate minerals (Defliese and Lohmann, 2015). For carbonate minerals, this can potentially lead to the underestimation of temperature from enriched $\Delta_{47}$ values (Defliese and Lohmann, 2015).

Both experimental data and theoretical calculations from our non-linear mixing model indicate that artifacts in both $\Delta_{47}$ and $\Delta_{48}$ can arise from mixing (Figures 17-18;

Table 12). Values for $\Delta_{47}$ and $\Delta_{48}$ in mixtures are enriched compared to equilibrium values. The trajectories for $\Delta_{47}$ and $\Delta_{48}$ mixing effects in this study have slopes that vary depending on endmember compositions and the fraction of the mixture. Values for slopes range from 0.397-0.872.

For the calculations performed here, the minimum non-linear mixing-related biases occur when calcite endmembers have the same clumped isotope compositions but a 10 ‰ difference in $\delta^{18}$O and $\delta^{13}$C. This could represent several scenarios, such as correspond to mixing of carbonate from growth bands in a coral that formed at the same temperature but with variable bulk compositions, or mixing of different mollusk specimens that formed at similar temperatures and are within the same sediment sample, or of adjacent foraminiferal samples during times when temperatures were relatively similar.

Maximum mixing-related biases are predicted when calcites with the same clumped isotope values is mixed that has a 60 ‰ difference in $\delta^{18}$O and $\delta^{13}$C (Figure 17C-D). This type of difference is likely to rarely be important for most natural settings, though this suggests that caution should be taken when working with methane-derived carbonates, or when sampling rocks containing cements formed from brine and freshwater settings.

Mixing of samples with different clumped and bulk isotope endmember values predicted from our model fall between the minimum and maximum trajectories (Figure 17A-B). Our measured values from mixing experiments fall in this category and agree with model predictions. The minimum trajectory observed here is slightly higher than the equilibrium slope for $\Delta_{47}$ and $\Delta_{48}$.

If endmembers vary by less than 5 ‰ in $\delta^{13}C$ and $\delta^{18}O$, mixing effects of 0.005 ‰ could be observed in $\Delta_{47}$ and 0.004 ‰ in $\Delta_{48}$, which are within the range of instrumental precision. Thus, mixing could introduce ~1.9 $^{o}C$ of potential bias in $\Delta_{47}$-derived temperatures (as has previously been discussed in Defliese and Lohmann, 2015), and ~3.5 $^{o}C$ in $\Delta_{48}$ -derived temperatures, at Earth surface temperatures. If endmembers have the same bulk composition but varying $\Delta_{47}$ and $\Delta_{48}$, the clumped isotope values mix linearly as a weighted sum of the contribution of each endmember. Additionally, $\Delta_{47}$ values below equilibrium values are predicted when an endmember has $\delta^{18}O$ that is higher and $\delta^{13}C$ that is lower than the other endmember. For example, if two endmembers have identical $\Delta_{47}$, and one end member has a $\delta^{18}O$ of 5 ‰ higher and $\delta^{13}C$ of 5 ‰ lower than the other endmember, the resultant $\Delta_{47}$ value will be 0.005 ‰ below the $\Delta_{47}$ value of each individual endmember. In this scenario, the $\Delta_{47}$ value continues to decrease with increasing $\delta^{18}O$ and decreasing $\delta^{13}C$.

This work indicates that paired clumped isotopes ($\Delta_{47}$ and $\Delta_{48}$) could be used to identify mixing effects that would otherwise bias paleothermometry, but also suggests that endmember compositions in clumped or bulk compositions, or both, would need to be substantially different for biases to be expressed. $\Delta_{47}$ and $\Delta_{48}$ values for unknown calcite samples that do not conform to temperature-dependent equilibrium $\Delta_{47}$ - $\Delta_{48}$ relationship (Figure 19), or kinetically governed disequilibrium mineral signatures (Figure 18), but that do fall within the mixing effect bounds shown in Figure 18 for calcite samples, could be indicative of enriched clumped isotope values from non-linear mixing effects. If mixing fractions and endmembers could be constrained, paired $\Delta_{47}$ and $\Delta_{48}$ data could potentially be used to correct for artifacts and extract primary temperatures.

## 6. Conclusions

Utilizing a combination of experimental data and multiple modeling frameworks, we show that paired $\Delta_{47}$ and $\Delta_{48}$ can be used to identify when disequilibrium effects are negligible, and in cases where disequilibrium is non-negligible, constrain kinetic isotope effects and mixing effects. By precipitating calcite at five temperatures at pH 8.3 with the enzyme carbonic anhydrase (CA), we reduce kinetic isotope effects in the DIC pool, with $\Delta_{47}$ and $\Delta_{48}$ values consistent with model predictions for equilibrium precipitation. Experimental data provide an independent set of constraints on the equilibrium relationship between $\Delta_{47}$ and $\Delta_{48}$, $\Delta_{47}$ and $T$, $\Delta_{48}$ and $T$, $\Delta_{47}$ and $\delta^{18}$O, and $\Delta_{48}$ and $\delta^{18}$O. The experimentally determined $\Delta_{47}$ and $\Delta_{48}$ relationship from this study is statistically indistinguishable from published regressions. We report a new combined regression fit through all experimental data from Swart et al. (2021), Fiebig et al. (2021), Lucarelli et al. (2021), and this study:

$$\Delta_{48\ \mathrm{CDES}\ 90} = (0.429 \pm 0.010)\ \Delta_{47\ \mathrm{CDES}\ 90} - (0.006 \pm 0.006);\ r^2 = 0.98$$

which further constrains the equilibrium relationships between $\Delta_{47}$ and $\Delta_{48}$. We also report combined temperature dependent relationships using data from Swart et al. (2021), Fiebig et al. (2021), and this study:

$$\Delta_{47\ \mathrm{I\text{-}CDES}} = (0.037 \pm 0.001) \times 10^6 T^{-2} + (0.178 \pm 0.009);\ r^2 = 0.99$$

$$\Delta_{48\ \mathrm{CDES}\ 90} = (0.015 \pm 0.0005) \times 10^6 T^{-2} + (0.078 \pm 0.006);\ r^2 = 0.98$$

which further constrains equilibrium relationships between $\Delta_{47}$ and $T$, and $\Delta_{48}$ and $T$.

At elevated pH, we observe $\Delta_{47}$ values that are enriched relative to expected isotope equilibrium, while $\Delta_{48}$, $\delta^{18}$O, and $\delta^{13}$C are depleted. The largest enrichment relative to quasi-equilibrium observed here for $\Delta_{47}$ was 0.198 ‰ at pH 10.5 and 5 $^{o}$C. The largest depletion relative to quasi-equilibrium for $\Delta_{48}$ was -0.628 ‰ at pH 11 and 5 $^{o}$C. All calcite precipitated here with pH ≥ 9.5 had $\Delta_{48}$ values less than 0 ‰, indicating values below a stochastic distribution. Calcite precipitated with CA in the solution returned to $\Delta_{47}$ and $\Delta_{48}$ values expected at quasi-equilibrium, where CA was more successful at catalyzing $\Delta_{48}$ than $\Delta_{47}$.

The kinetic slopes for hydration and hydroxylation for paired $\Delta_{47}$ and $\Delta_{48}$ measurements determined here may be used to return calcite samples to near equilibrium clumped isotope values. Calcite precipitated at pH ≥ 9.5 followed a steep kinetic slope, while calcite precipitated at pH ≥ 9.5 with CA followed a shallower kinetic slope. Calcite precipitated at pH ≤ 9.0 had negligible clumped isotope kinetic effects, while kinetic oxygen isotope effects may have been present.

Samples grown at pH 8.3 and with growth rates of $\log_{10}R$ that are -7.3 to 7.5 mol/m$^2$/s have $\Delta_{47}$ and $\Delta_{48}$ values that overlap the equilibrium limit, while samples at higher pH have clumped isotope compositions that record kinetic isotope effects. The observed paired clumped isotope values in calcite samples grown at elevated pH without CA can be explained by hydration/hydroxylation during $CO_2$ absorption. Calcite precipitated at fast growth rates may inherit larger kinetic isotopic effects from $CO_2$

hydration/hydroxylation and a disequilibrium DIC pool compared to calcite precipitated at slower growth rates. Kinetic isotope effects associated with fast growth rate and $CO_2$ hydration/hydroxylation may be as large as ~0.23 ‰ for $\Delta_{47}$ and ~0.51 ‰ for $\Delta_{48}$.

Mixing experiments and non-linear mixing model calculations show that mixing results in enrichments in both $\Delta_{47}$ and $\Delta_{48}$ compared to equilibrium values. There are a range of characteristic trajectories for mixing effects in $\Delta_{47}$ and $\Delta_{48}$ for calcites with varying bulk and clumped isotopes. Paired measurements of $\Delta_{47}$ and $\Delta_{48}$ may provide a mechanism by which mixing effects can be identified in biological and abiogenic carbonate samples. Such effects are likely to be $\geq$ 0.009 ‰ for $\Delta_{47}$ if there is more than 30 % of a secondary component in a two-component system if bulk compositions vary by more than 7 ‰, or if $\Delta_{47}$ and $\Delta_{48}$ vary by more than 0.03 ‰.

## Acknowledgments

We thank lab members past and present for their work running standards, efforts in data entry, and contributions to discussions, NAWI Graz Central Lab for Water, Minerals and Rocks for experimental and analytical support, and Albrecht Leis (JR-AquaConSol, Graz) for support on liquid isotope analyses. This work was funded by DOE BES grant DE-FG02-83613ER16402 to Aradhna Tripati. Jamie Lucarelli and Zeeshan Parvez also acknowledge support from fellowships granted by The Center for Diverse Leadership in Science supported by the Packard Foundation, Sloan Foundation, Silicon Valley Community Foundation, and NSF (ICER- 2039462 for Veterans in Green STEM). Jamie Lucarelli received support from Cota Robles and Dissertation Year Fellowships from the University of California, Los Angeles, and Zeeshan Parvez received support as a

Tillman Scholar. We thank Ben Elliot and members of the Tripati lab for their technical support in mass spectrometry.

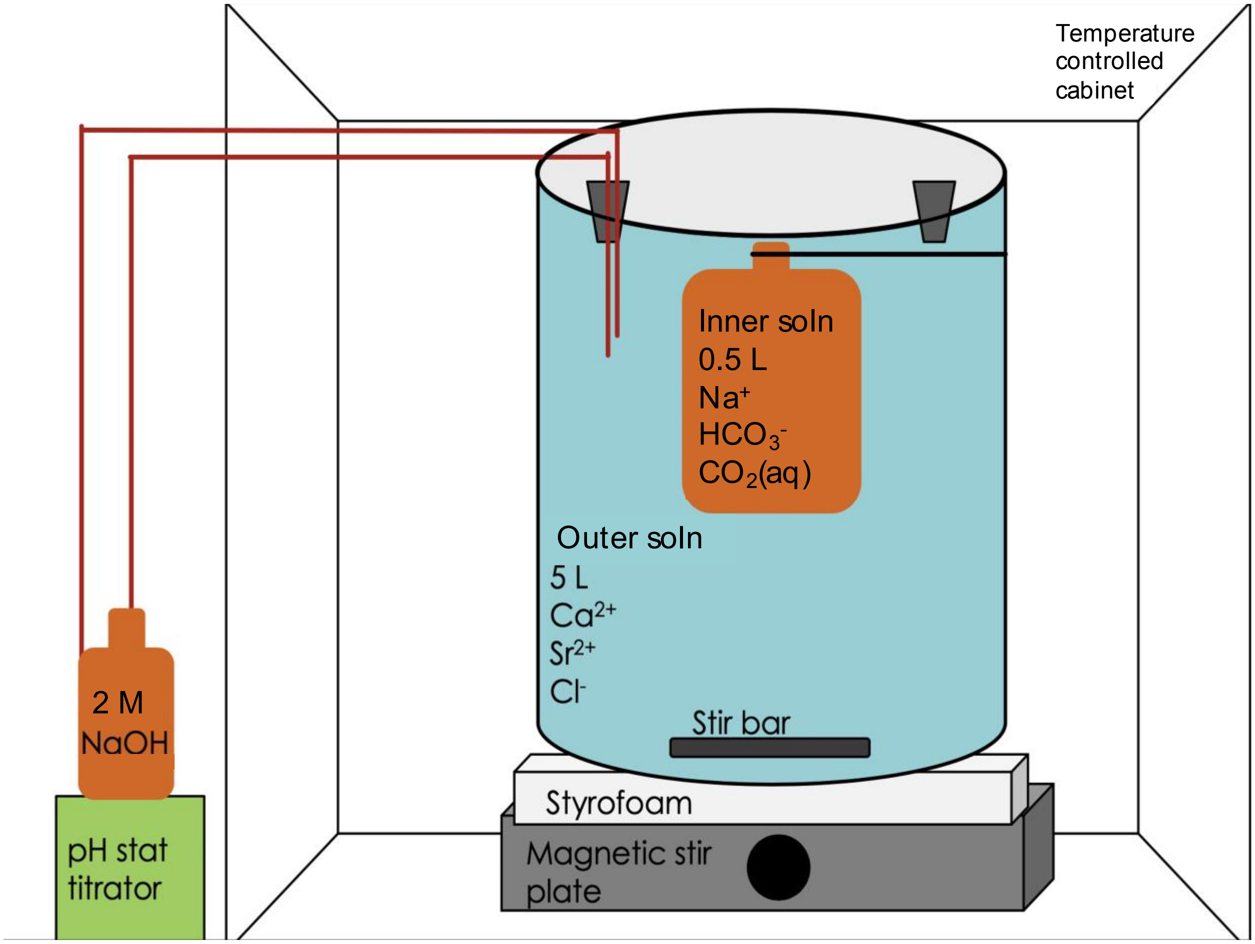

**Figure 9.** Schematic of the precipitation apparatus used for this work. The inner bottle is a 0.5 L, 2 mm thick polyethylene bottle that serves as a membrane through which $CO_2$ diffuses into the outer solution. The outer solution is inside a 5 L container that contains $Ca^{2+}$ from CaCl. A pH-stat titrator holds the pH of the outer solution constant by titrating NaOH. The temperature is held constant by placing the entire apparatus inside a temperature-controlled cabinet. Adapted from Dietzel and Usdowski (1996), Dietzel et al. (2004), Tang et al., (2008), and Tang et al. (2014).

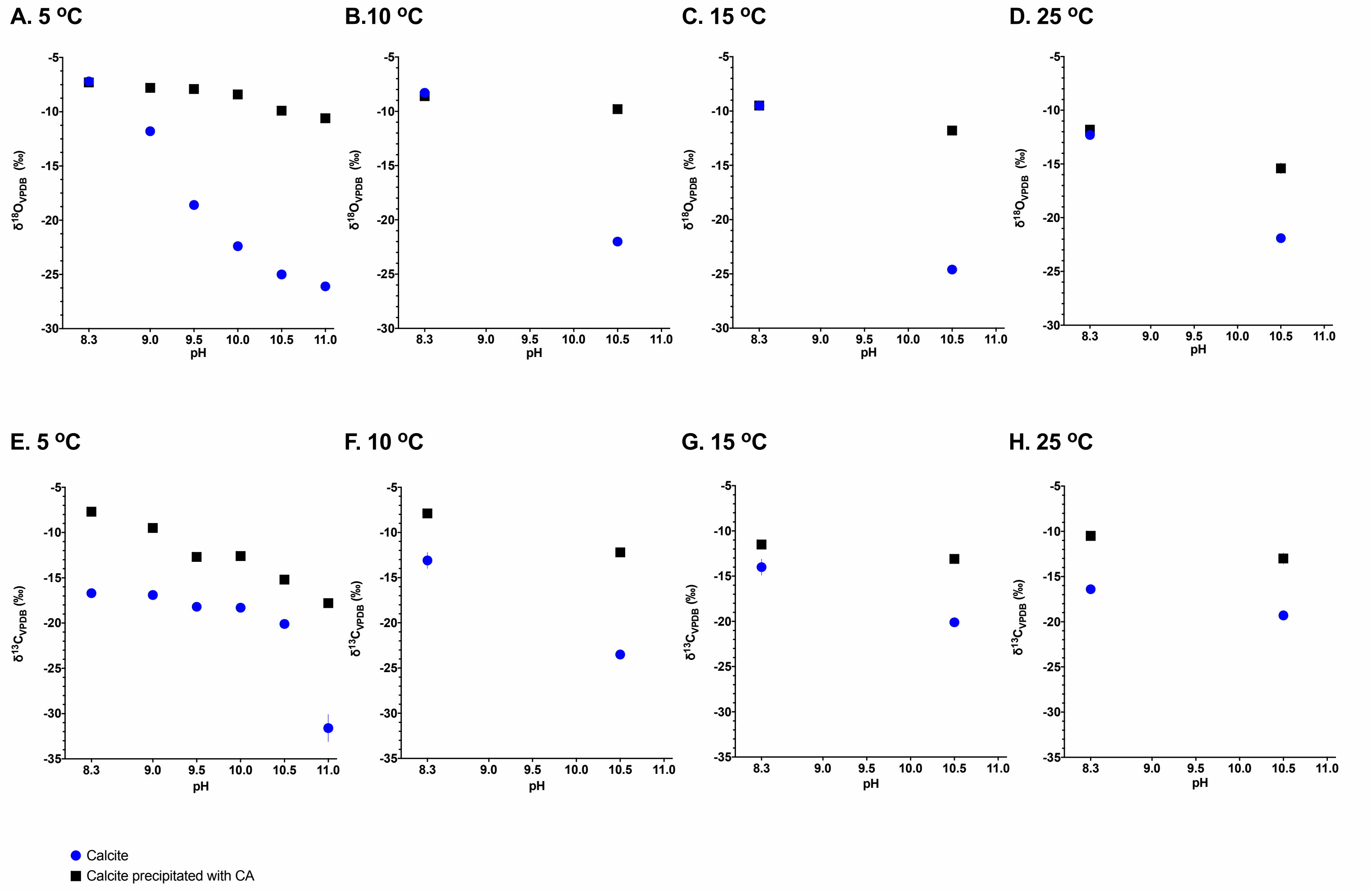

**Figure 10.** $\delta^{18}O$ and $\delta^{13}C$ with precipitation pH for calcite precipitated with and without carbonic anhydrase (CA) at variable temperature. $\delta^{18}O$ versus precipitation pH for A) 5 °C, B) 10 °C, C) 15 °C, and D) 25 °C. $\delta^{13}C$ versus precipitation pH for E) 5 °C, F) 10 °C, G) 15 °C, and H) 25 °C.

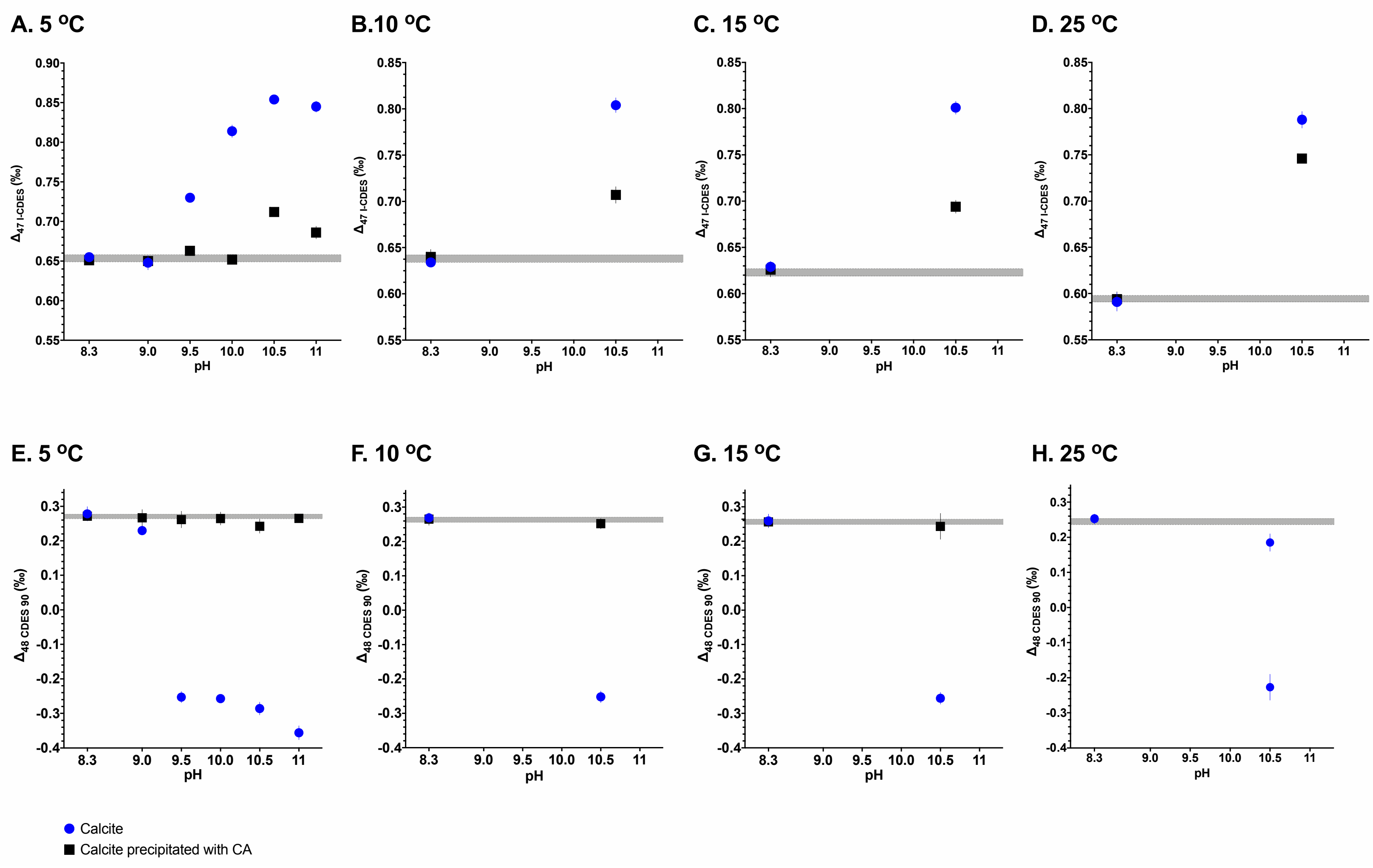
A. 5 °C
B.10 °C
C. 15 °C
D. 25 °C
Δ47 I-CDES (‰)
0.90
0.85
0.80
0.75
0.70
0.65
0.60
0.55
8.3
9.0
9.5
10.0
10.5
11
pH
E. 5 °C
F. 10 °C
G. 15 °C
H. 25 °C
Δ48 CDES 90 (‰)
0.3
0.2
0.1
0.0
-0.1
-0.2
-0.3
-0.4
● Calcite
■ Calcite precipitated with CA

**Figure 11.** $\Delta_{47}$ relative to pH at variable temperature for for calcite precipitated with and without carbonic anhydrase (CA). A) 5 °C, B) 10 °C, C) 15 °C, and D) 25 °C, and $\Delta_{48}$ relative to pH at E) 5 °C, F) 10 °C, G) 15 °C, and H) 25 °C.

Enrichments in $\Delta_{47}$ and depletions in $\Delta_{48}$ in samples precipitated at pH > 9.5. The gray bar is the range of expected equilibrium values derived from Swart et al. (2021), Fiebig et al. (2021), Lucarelli et al. (2021), and this study.

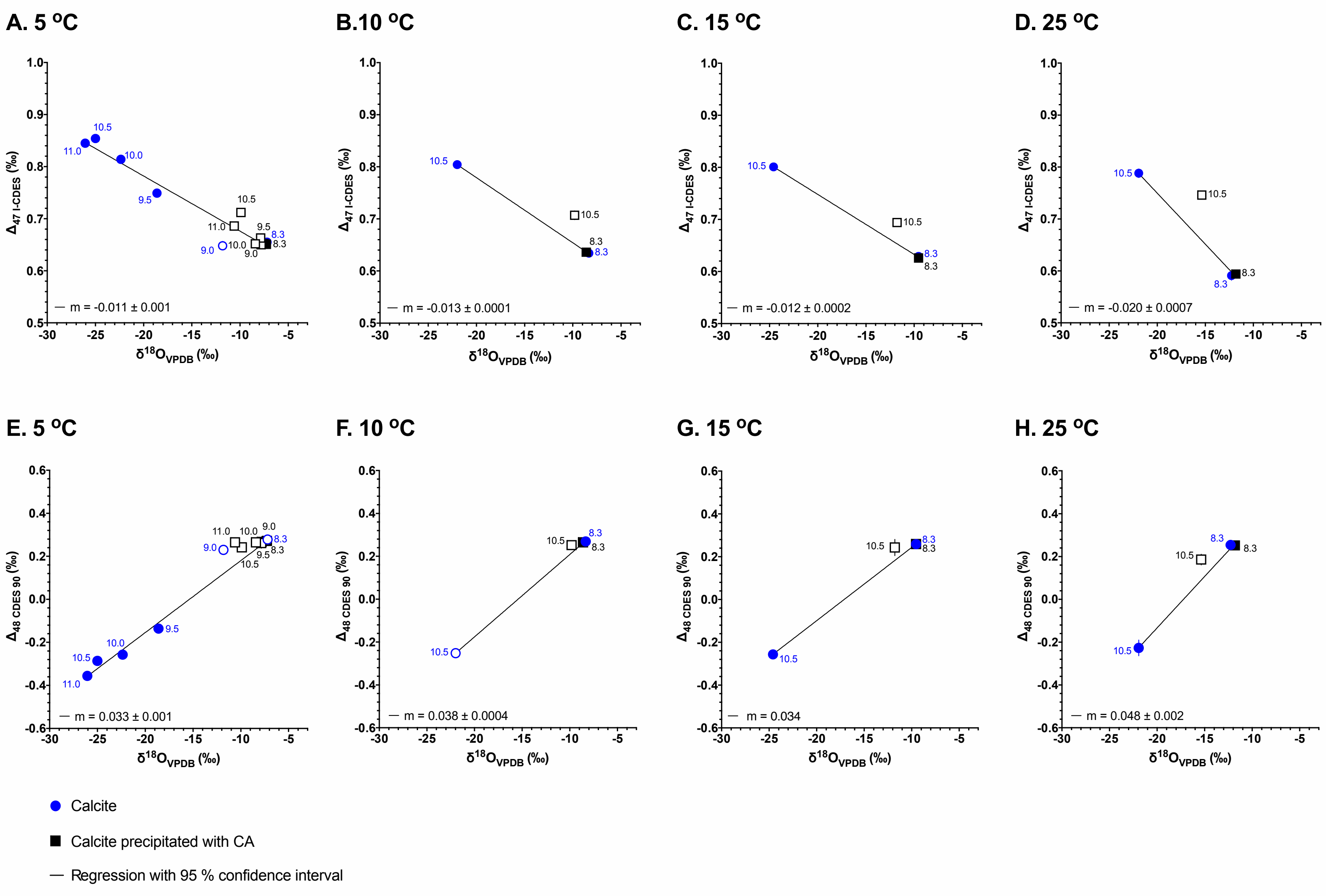

A. 5 °C
B.10 °C
C. 15 °C
D. 25 °C
E. 5 °C
F. 10 °C
G. 15 °C
H. 25 °C
Δ47 I-CDES (‰)
Δ48 CDES 90 (‰)
δ18OVPDB (‰)
m = -0.011 ± 0.001
m = -0.013 ± 0.0001
m = -0.012 ± 0.0002
m = -0.020 ± 0.0007
m = 0.033 ± 0.001
m = 0.038 ± 0.0004
m = 0.034
m = 0.048 ± 0.002
11.0
10.5
10.0
9.5
9.0
8.3
1.0
0.9
0.8
0.7
0.6
0.5
0.4
0.2
0.0
-0.2
-0.4
-0.6
-30
-25
-20
-15
-10
-5
● Calcite
■ Calcite precipitated with CA
— Regression with 95 % confidence interval

**Figure 12.** $\Delta_{47}$ and $\delta^{18}O$ at variable temperature for calcite precipitated with and without carbonic anhydrase (CA). A) 5 °C ($r^2 = 0.96$), B) 10 °C ($r^2 = 0.99$), C) 15 °C ($r^2 = 0.99$), and D) 25 °C ($r^2 = 0.99$), and $\Delta_{48}$ and $\delta^{18}O$ at E) 5 °C ($r^2 = 0.99$), F) 10 °C ($r^2 = 0.99$), G) 15 °C ($r^2 = 0.99$), and H) 25 °C ($r^2 = 0.99$). Numbers next to each data point indicate precipitation pH. Samples at elevated pH are depleted in $\delta^{18}O$ and $\Delta_{47}$, and enriched in $\Delta_{48}$ relative to expected equilibrium values. Regressions are between quasi-equilibrium samples synthesized at pH 8.3 and samples synthesized at elevated pHs without CA, with negative slopes for $\Delta_{47}$ relative to $\delta^{18}O$, and positive slopes for $\Delta_{48}$ relative to $\delta^{18}O$. Data with open symbols are not included in regression.

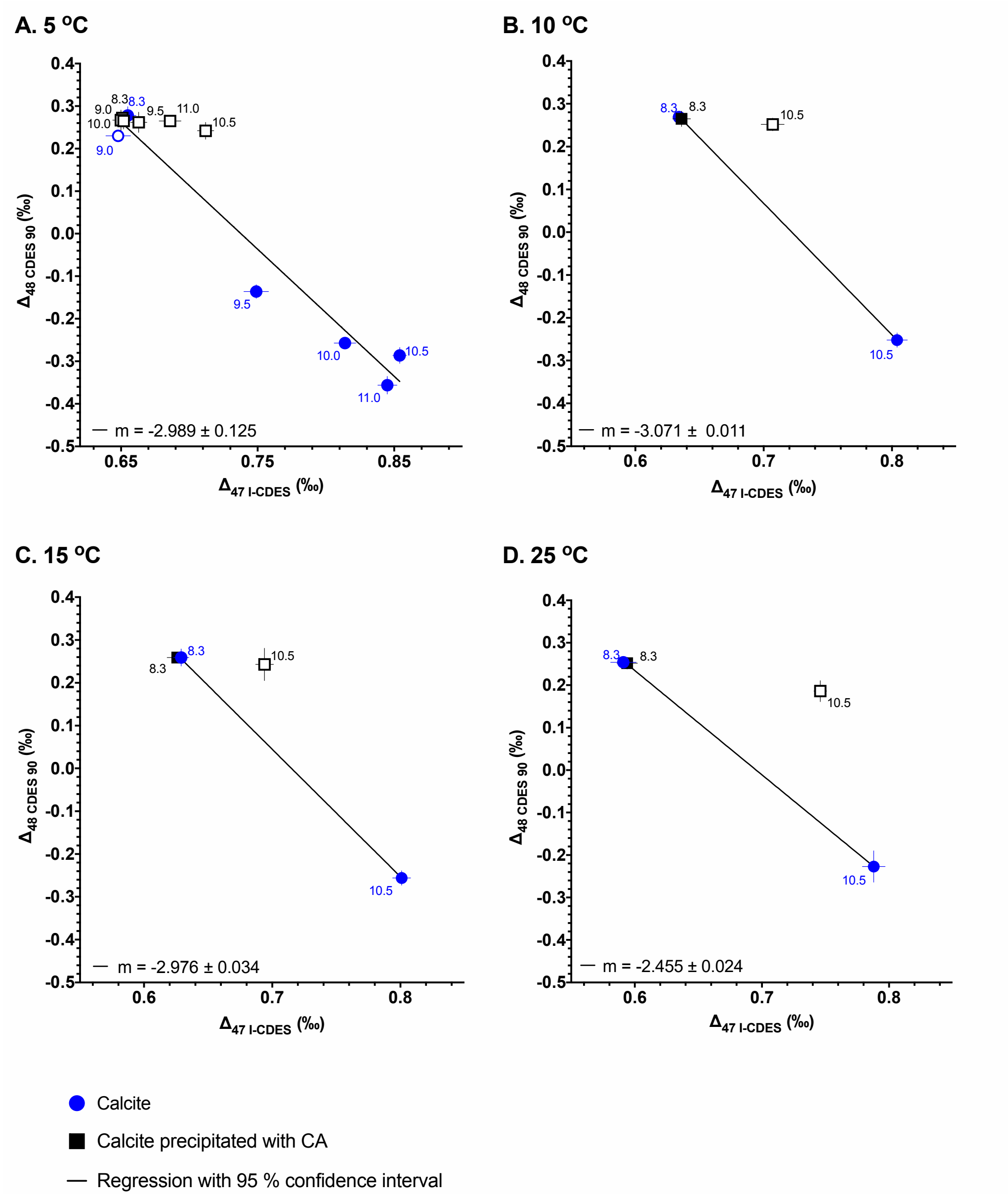

**Figure 13.** *Δ*47 and *Δ*48 for calcite synthesized at variable pH with and without CA at different temperatures. A) 5 °C ($r^2$ = 0.95), B) 10 °C ($r^2$ = 0.99), C) 15 °C ($r^2$ = 0.99), and D) 25 °C ($r^2$ = 0.99). Numbers next to each data point indicate precipitation pH. Regressions are between quasi-equilibrium samples synthesized at pH 8.3 and samples synthesized at elevated pHs without CA, with negative slopes observed for all experiments. Data with open symbols are not included in the regressions.

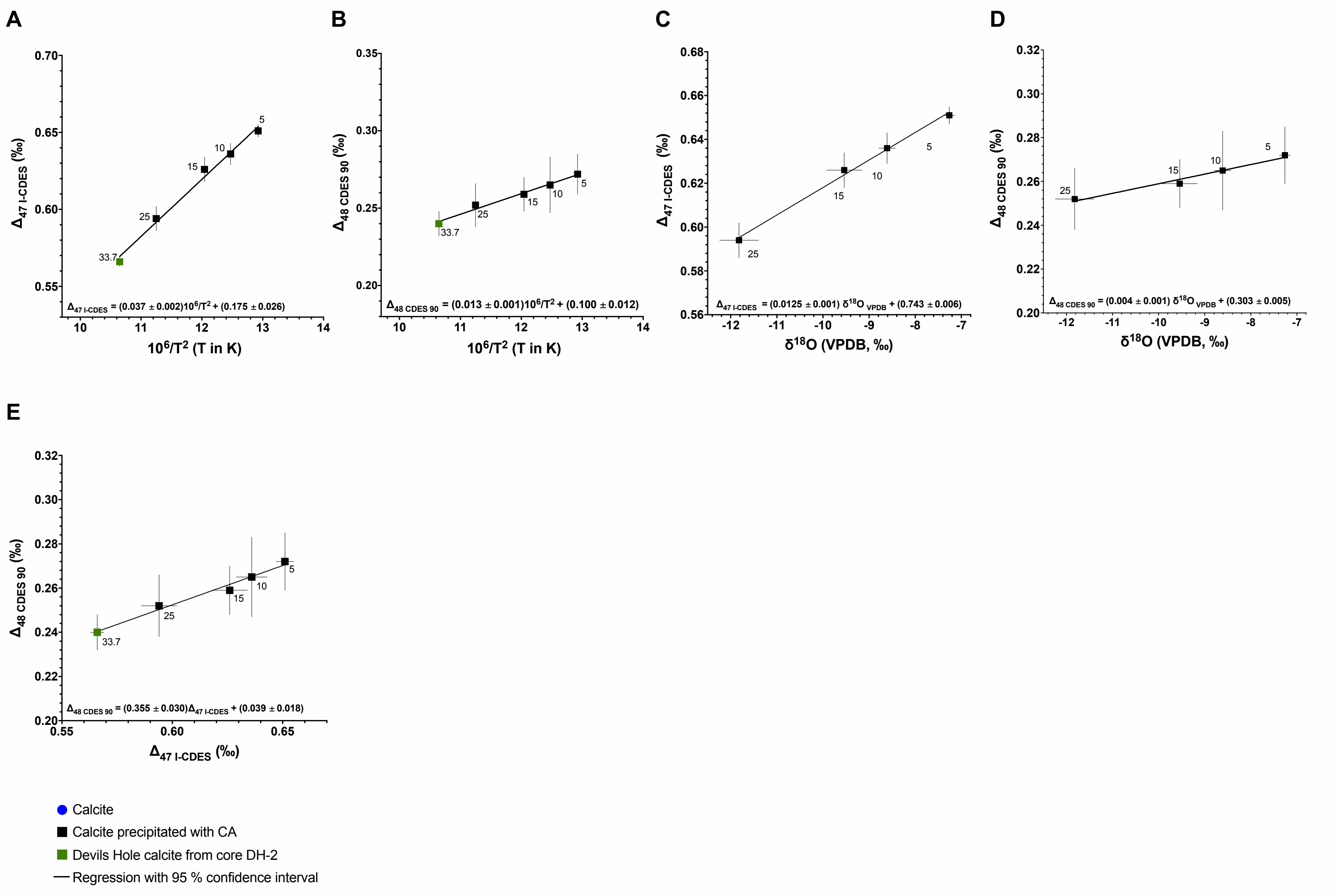
A
Δ47 I-CDES (‰)
0.70
0.65
0.60
0.55
10
11
12
13
14
10^6/T^2 (T in K)
5
10
15
25
33.7
Δ47 I-CDES = (0.037 ± 0.002)10^6/T^2 + (0.175 ± 0.026)
B
Δ48 CDES 90 (‰)
0.35
0.30
0.25
0.20
10
11
12
13
14
10^6/T^2 (T in K)
5
10
15
25
33.7
Δ48 CDES 90 = (0.013 ± 0.001)10^6/T^2 + (0.100 ± 0.012)
C
Δ47 I-CDES (‰)
0.68
0.66
0.64
0.62
0.60
0.58
0.56
-12
-11
-10
-9
-8
-7
δ18O (VPDB, ‰)
5
10
15
25
Δ47 I-CDES = (0.0125 ± 0.001) δ18O VPDB + (0.743 ± 0.006)
D
Δ48 CDES 90 (‰)
0.32
0.30
0.28
0.26
0.24
0.22
0.20
-12
-11
-10
-9
-8
-7
δ18O (VPDB, ‰)
5
10
15
25
Δ48 CDES 90 = (0.004 ± 0.001) δ18O VPDB + (0.303 ± 0.005)
E
Δ48 CDES 90 (‰)
0.32
0.30
0.28
0.26
0.24
0.22
0.20
0.55
0.60
0.65
Δ47 I-CDES (‰)
5
10
15
25
33.7
Δ48 CDES 90 = (0.355 ± 0.030)Δ47 I-CDES + (0.039 ± 0.018)
● Calcite
■ Calcite precipitated with CA
🟩 Devils Hole calcite from core DH-2
— Regression with 95 % confidence interval

**Figure 14.** Quasi-equilibrium regressions for clumped isotope data and precipitation temperature, A) $\Delta_{47}$ and $10^6T^{-2}$ ($r^2 = 0.99$) and B) $\Delta_{48}$ and $10^6T^{-2}$ ($r^2 = 0.98$) with temperature in Kelvin. Quasi-equilibrium regressions for C) $\Delta_{47}$ and $\delta^{18}O$ ($r^2 = 0.99$) and D) $\Delta_{48}$ and $\delta^{18}O$ ($r^2 = 0.97$). Quasi-equilibrium regression for $\Delta_{47}$ and $\Delta_{48}$ ($r^2 = 0.98$). Data on all panels is for samples precipitated at pH 8.3 with CA and for Devils Hole calcite (DH-2), which is thought to have formed in near isotopic equilibrium at a temperature of 33.7 $^{o}$C (Winograd et al., 1988; Winograd et al., 1992; Coplen, 2007; Kluge et al., 2014; Tripati et al., 2015; Daëron et al., 2019; Bajani et al., 2021).

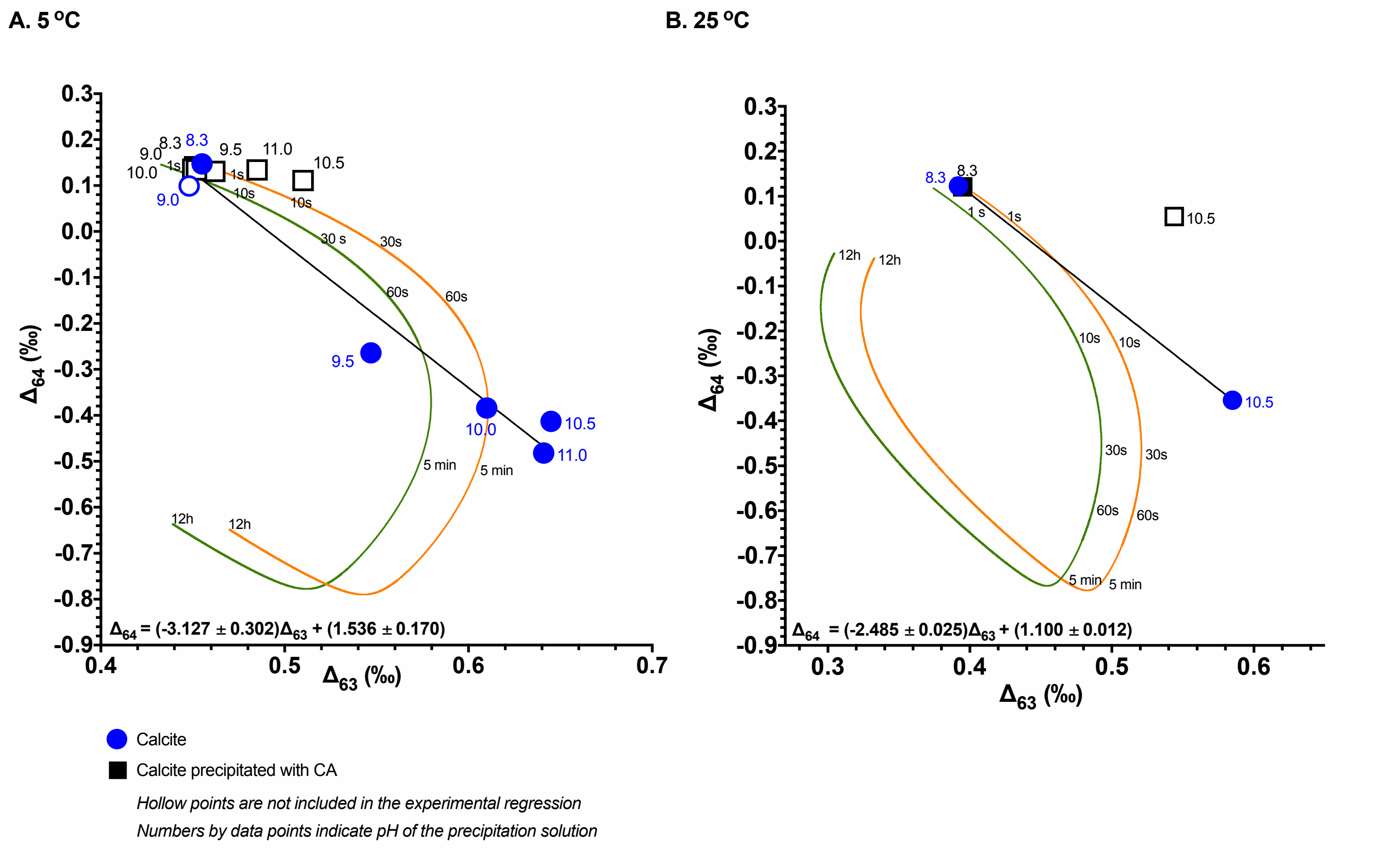

**Figure 15.** Experimental results compared to IsoDIC model predictions for the evolution of $HCO_3^-$ and $CO_3^{2-}$ isotopic composition at different temperatures and as a function of time. Experimental data are for calcite precipitated with (blue circles) and without CA (black squares) at varying pH. Numbers by data points indicate pH of precipitation solution. Regression through data (black line) and 95% confidence interval also shown. Calculations are for end member compositions at A) 5 °C and pH 10.5 and B) 25 °C and pH 10.5. Green trajectory shows modelled values for $CO_3^{2-}$ and orange trajectory shows modelled values for $HCO_3^-$. Numbers on model trajectories indicate evolution time after the start of calcite precipitation. IsoDIC model software we used for our calculations was from Guo (2020).

Default model

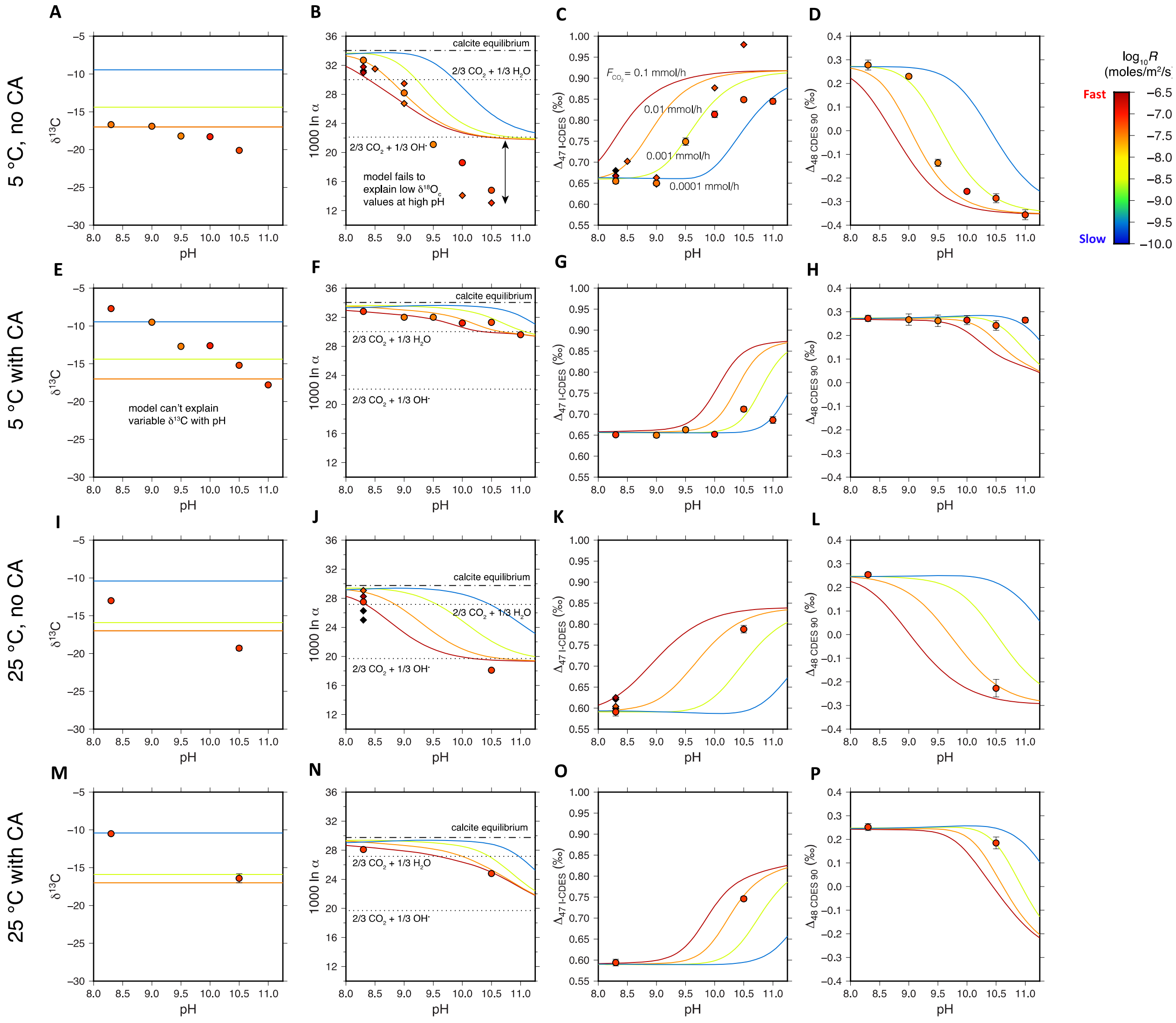

Model with larger hydroxylation KFF for oxygen

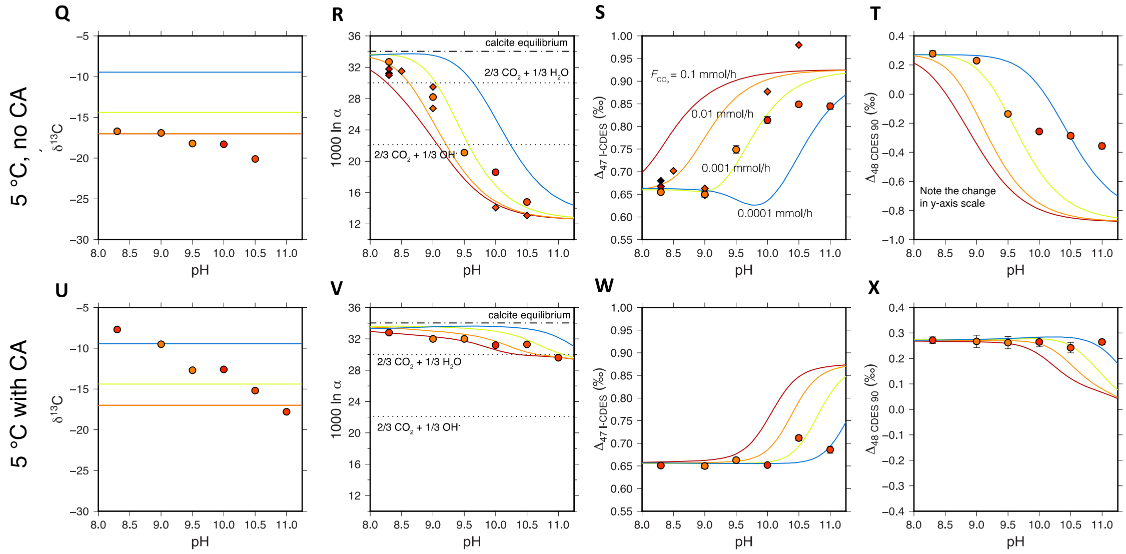

**Figure 16.** Experimental results from this work compared to data from Tang et al. (2014) and box model predictions. Symbol color indicates precipitation rate with color scale shown. Black points have precipitation faster than a log R (mol/m$^2$/s) value of -6.5. Colored curves show $\alpha_{\text{carb-water}}$, $\Delta_{47}$, and $\Delta_{48}$ of calcite predicted by box model for different precipitation rates, with kinetic limit reflecting $CO_2$ hydration and hydroxylation and presence or absence of carbonic anhydrase (CA; calculations utilize values of 0 or 0.25 µM CA). Panels A-P show default model conditions with and with and without CA, and panels Q-X show the model with larger KFFs for oxygen. Clumped isotopic compositions of calcite are predicted to be sensitive to temperature, growth rate, and pH (Watkins and Hunt, 2015; Tripati et al., 2015, Guo, 2020; Uchikawa et al., 2021).

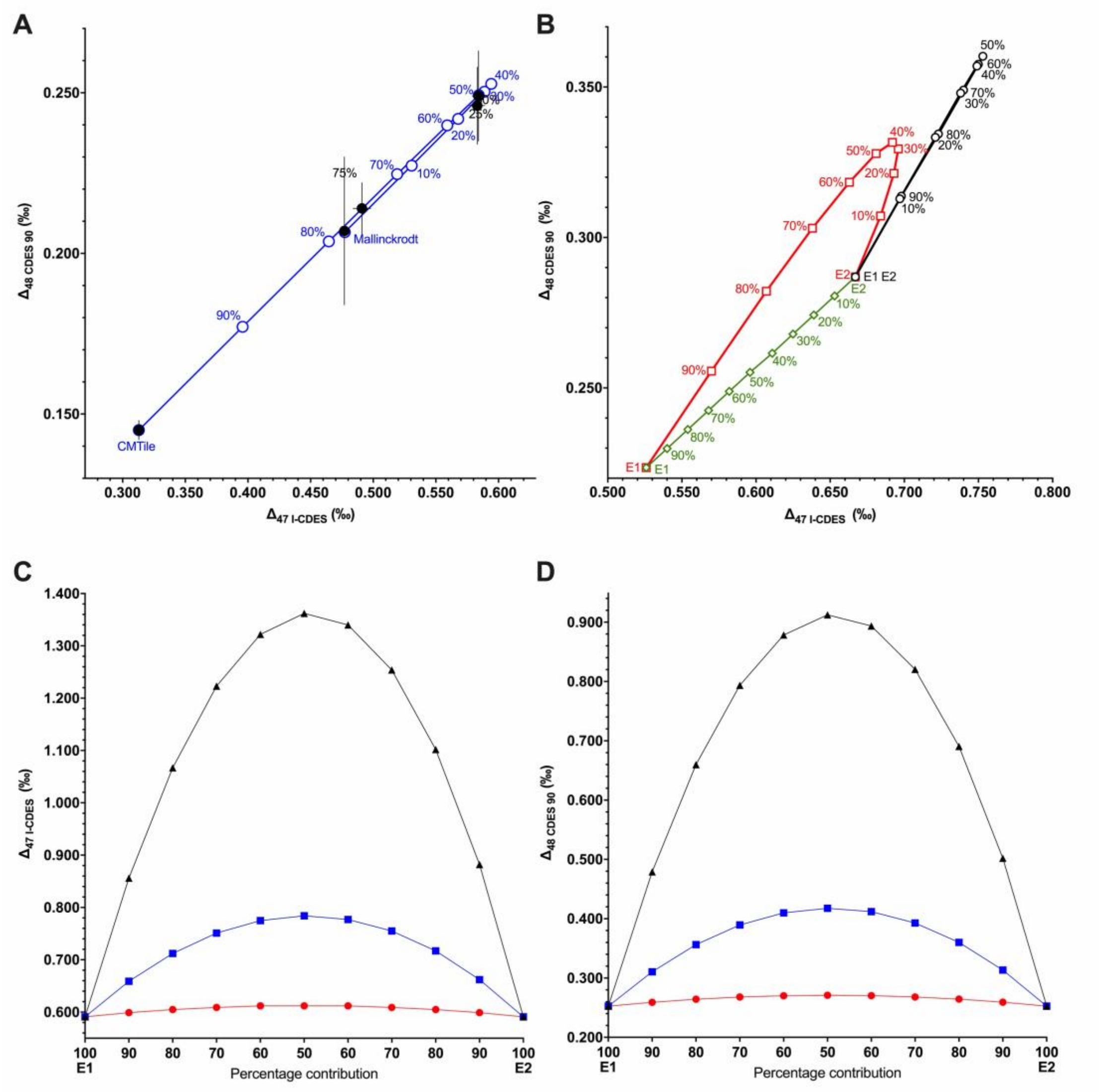

**Figure 17.** Predicted and observed clumped isotope composition for mixing experiments. A) *Δ*47 and *Δ*48 for non-linear mixing model predictions compared to experimental results. Two internal standards, CM Tile and Mallinckrodt, were used as endmembers. B) Mixing model predictions with different endmembers. Red line is for end members with a 0.141‰ and 0.063 ‰ difference in *Δ*47 and *Δ*48, and a 20 ‰ difference in $\delta^{18}$O and $\delta^{13}$C. Green line endmembers with a 0.141‰ and 0.063 ‰ difference in *Δ*47 and *Δ*48, and identical $\delta^{18}$O and $\delta^{13}$C. The difference in the clumped isotope values of the endmembers in the green and red lines is approximately equivalent to a 50 °C temperature difference. Black line endmembers with identical

clumped isotope values and a 20 ‰ difference in $\delta^{18}O$ and $\delta^{13}C$. C) $\Delta_{47}$ and percentage contribution of each endmember for mixing model predictions where the endmembers have identical $\Delta_{47}$ values and a 60 ‰ difference in $\delta^{18}O$ and $\delta^{13}C$ (black line), 30 ‰ difference in $\delta^{18}O$ and $\delta^{13}C$ (blue line), and 10 ‰ difference in $\delta^{18}O$ and $\delta^{13}C$ (red line). D) $\Delta_{48}$ and percentage contribution of each endmember for mixing model predictions where the endmembers have identical $\Delta_{48}$ values and a 60 ‰ difference in $\delta^{18}O$ and $\delta^{13}C$ (black line), 30 ‰ difference in $\delta^{18}O$ and $\delta^{13}C$ (blue line), and 10 ‰ difference in $\delta^{18}O$ and $\delta^{13}C$ (red line).

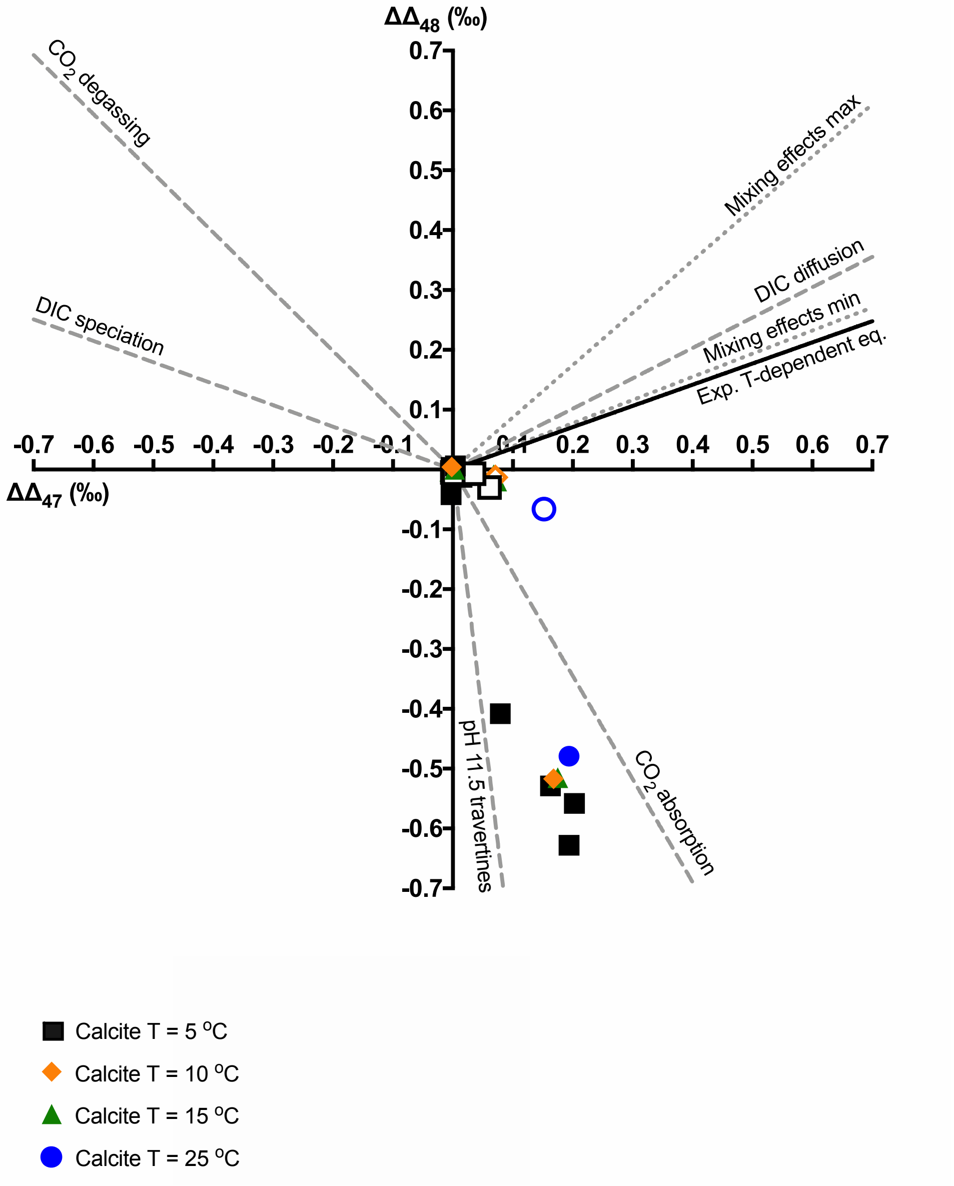

**Figure 18.** $\Delta\Delta_{47}$ and $\Delta\Delta_{48}$ data from experiments compared to theoretical predictions. Colored symbols are for calcite from this study synthesized at different temperatures. Open symbols are for samples grown with carbonic anhydrase (CA). Kinetic slopes include $\Delta_{63}$ and $\Delta_{64}$ values for $HCO_3^-$ endmembers produced through varying processes (Guo, 2020) that we use to predict $\Delta_{47}$ and $\Delta_{48}$, and mixing model predictions for calcite (this study). Experimental $T$-dependent equilibrium slope = 0.387. Slopes published in Guo (2020) using IsoDIC modeling software and our

mixing model predicted non-equilibrium slopes for different processes. DIC speciation =- -0.358; DIC diffusion = 0.506, $CO_2$ degassing at pH 8 = -0.990; $CO_2$ absorption at pH 9 = -1.72; travertine precipitation at pH 11.5 = -8.33; mixing values = 0.387 to 0.872.

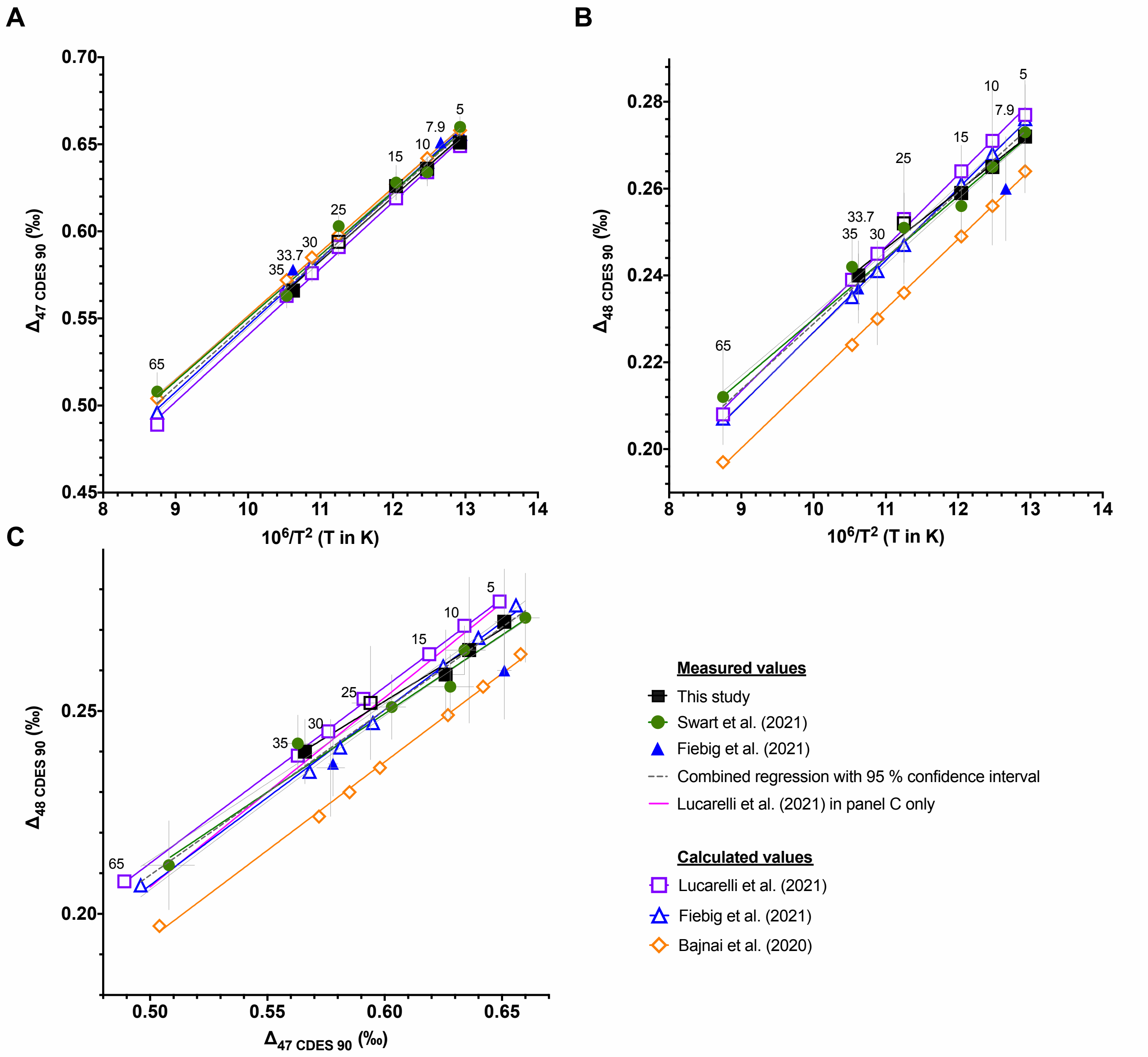

**Figure 19.** Comparison of $\Delta_{47}$ and $\Delta_{48}$ regressions from this work to published results. A) $\Delta_{47}$ and $10^6$ $T^{-2}$ with T in K, B) $\Delta_{48}$ and $10^6$ $T^{-2}$ with T in K, and C) is $\Delta_{47}$ and $\Delta_{48}$. Results for samples grown at pH 8.3 with carbonic anhydrase (CA) from this work are compared to experimentally-based regressions (Swart et al., 2021; Fiebig et al., 2021; Bajnai et al., 2020; Lucarelli et al., 2021). Bajnai et al. (2020) and Lucarelli et al. (2021) are based on theory from Hill et al. (2014) and Tripati et al. (2015) with experimental AFFs. All regressions were determined to be statistically

indistinguishable, and a combined regression was determined for the experimentally based regressions. Numbers by symbols indicate precipitation temperature in Celsius.

| Temperature of precipitation (°C) | pH of precipitation solution | CA (yes or no) | Time from beginning of experiment until start of precipitation (days) | Total experiment time (days) | Precipitation rate ($\log_{10}R$ with R in mol $s^{-1}$ $m^{-2}$) | Initial water $\delta^{18}O_{VSMOW}$ (‰) | FInal water $\delta^{18}O_{VSMOW}$ (‰) | Calcite (weight %) | Vaterite (weight %) | Aragonite (weight %) |
|---|---|---|---|---|---|---|---|---|---|---|
| 5 | 8.3 | Y | 23 | 34 | -7.11 | n/a | -9.52 | 100 | | |
| 5 | 8.3 | N | 29 | 52 | -7.43 | n/a | -9.44 | 100 | | |
| 5 | 9.0 | Y | 3 | 27 | -7.45 | -9.22 | -9.14 | 100 | | |
| 5 | 9.0 | N | 5 | 27 | -7.41 | -9.40 | -9.31 | 100 | | |
| 5 | 9.5 | Y | 1 | 26 | -7.47 | -9.37 | -9.26 | 100 | | |
| 5 | 9.5 | N | <1 | 26 | -7.48 | -9.44 | -9.33 | 100 | | |
| 5 | 10.0 | Y | <1 | 9 | -7.02 | -9.47 | -9.13 | 100 | | |
| 5 | 10.0 | N | <1 | 9 | -7.02 | -9.64 | -9.56 | 100 | | |
| 5 | 10.5 | Y | <1 | 14 | -7.21 | n/a | -9.07 | 100 | | |
| 5 | 10.5 | N | <1 | 14 | -7.21 | -9.37 | -9.25 | 100 | | |
| 5 | 11.0 | Y | <1 | 12 | -7.15 | n/a | -9.44 | 100 | | |
| 5 | 11.0 | N | <1 | 12 | -7.15 | n/a | n/a | 100 | | |
| 10 | 8.3 | Y | 14 | 26 | -7.15 | -9.26 | -9.40 | 100 | | |
| 10 | 8.3 | N | 10 | 26 | -7.27 | -9.18 | -9.35 | 100 | | |
| 10 | 10.5 | Y | 1 | 15 | -7.21 | -8.83 | -8.86 | 21 | 75 | 4 |
| 10 | 10.5 | N | 1 | 15 | -7.21 | -8.96 | -9.01 | 100 | | |
| 15 | 8.3 | Y | 9 | 20 | -7.11 | -9.03 | -9.15 | 100 | | |
| 15 | 8.3 | N | 9 | 20 | -7.11 | -9.16 | -9.10 | 100 | | |
| 15 | 10.5 | Y | <1 | 14 | -7.21 | -9.22 | -9.02 | 54 | 43 | 3 |
| 15 | 10.5 | N | <1 | 14 | -7.21 | -9.34 | -9.06 | 100 | | |
| 25 | 8.3 | Y | 2 | 14 | -7.15 | -9.30 | -9.29 | 100 | | |
| 25 | 8.3 | N | 3 | 14 | -7.11 | -9.32 | -9.33 | 100 | | |
| 25 | 10.5 | Y | <1 | 12 | -7.15 | -9.53 | -9.38 | 72 | 2 | 26 |
| 25 | 10.5 | N | <1 | 12 | -7.15 | -9.33 | -9.29 | 60 | | 40 |

**Table 7.** Experimental conditions for precipitation experiments with and without carbonic anhydrase (CA). Mineralogy as determined by XRD indicated.

| Mass Spectrometer | Acid digestion T (°C) | Acid digestion method | Sample size (mg) | GC column with He carrier gas | Adsorption trap | m/z 44 ion beam intensity | Integration time (s) |
|---|---|---|---|---|---|---|---|
| Thermo Fisher MAT 253 | 90 | common acid bath | 5 | x | | 16 V | 720 |
| Nu Instruments Perspective-1a | 90 | common acid bath | 0.5 | x | | 80-30 nA | 1600 |
| Nu Instruments Perspective -1b | 70 | individual vials | 0.5 | | x | 80-30 nA | 1600 |
| Nu Instruments Perspective-1c | 90 | common acid bath | 0.5 | | x | 80-30 nA | 1600 |
| Nu Instruments Perspective-2a | 70 | individual vials | 0.5 | | x | 80-30 nA | 1200 |
| Nu Instruments Perspective-2b | 90 | common acid bath | 0.5 | | x | 80-30 nA | 1200 |

**Table 8.** Mass spectrometer configurations used in this study.

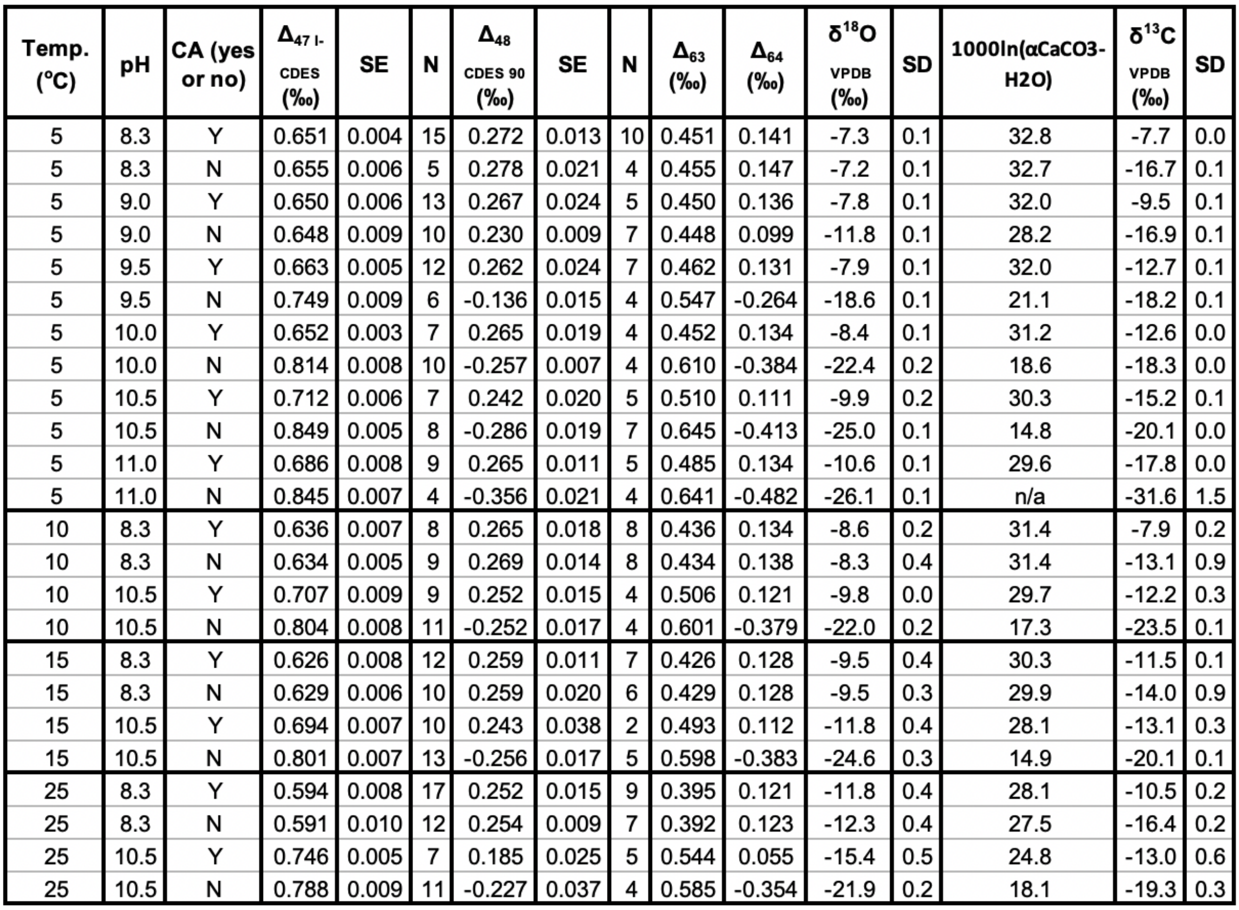

| Temp. (°C) | pH | CA (yes or no) | $\Delta_{47}$ I-CDES (‰) | SE | N | $\Delta_{48}$ CDES 90 (‰) | SE | N | $\Delta_{63}$ (‰) | $\Delta_{64}$ (‰) | $\delta^{18}O$ VPDB (‰) | SD | 1000ln(αCaCO3-H2O) | $\delta^{13}C$ VPDB (‰) | SD |
|---|---|---|---|---|---|---|---|---|---|---|---|---|---|---|---|
| 5 | 8.3 | Y | 0.651 | 0.004 | 15 | 0.272 | 0.013 | 10 | 0.451 | 0.141 | -7.3 | 0.1 | 32.8 | -7.7 | 0.0 |
| 5 | 8.3 | N | 0.655 | 0.006 | 5 | 0.278 | 0.021 | 4 | 0.455 | 0.147 | -7.2 | 0.1 | 32.7 | -16.7 | 0.1 |
| 5 | 9.0 | Y | 0.650 | 0.006 | 13 | 0.267 | 0.024 | 5 | 0.450 | 0.136 | -7.8 | 0.1 | 32.0 | -9.5 | 0.1 |
| 5 | 9.0 | N | 0.648 | 0.009 | 10 | 0.230 | 0.009 | 7 | 0.448 | 0.099 | -11.8 | 0.1 | 28.2 | -16.9 | 0.1 |
| 5 | 9.5 | Y | 0.663 | 0.005 | 12 | 0.262 | 0.024 | 7 | 0.462 | 0.131 | -7.9 | 0.1 | 32.0 | -12.7 | 0.1 |
| 5 | 9.5 | N | 0.749 | 0.009 | 6 | -0.136 | 0.015 | 4 | 0.547 | -0.264 | -18.6 | 0.1 | 21.1 | -18.2 | 0.1 |
| 5 | 10.0 | Y | 0.652 | 0.003 | 7 | 0.265 | 0.019 | 4 | 0.452 | 0.134 | -8.4 | 0.1 | 31.2 | -12.6 | 0.0 |
| 5 | 10.0 | N | 0.814 | 0.008 | 10 | -0.257 | 0.007 | 4 | 0.610 | -0.384 | -22.4 | 0.2 | 18.6 | -18.3 | 0.0 |
| 5 | 10.5 | Y | 0.712 | 0.006 | 7 | 0.242 | 0.020 | 5 | 0.510 | 0.111 | -9.9 | 0.2 | 30.3 | -15.2 | 0.1 |
| 5 | 10.5 | N | 0.849 | 0.005 | 8 | -0.286 | 0.019 | 7 | 0.645 | -0.413 | -25.0 | 0.1 | 14.8 | -20.1 | 0.0 |
| 5 | 11.0 | Y | 0.686 | 0.008 | 9 | 0.265 | 0.011 | 5 | 0.485 | 0.134 | -10.6 | 0.1 | 29.6 | -17.8 | 0.0 |
| 5 | 11.0 | N | 0.845 | 0.007 | 4 | -0.356 | 0.021 | 4 | 0.641 | -0.482 | -26.1 | 0.1 | n/a | -31.6 | 1.5 |
| 10 | 8.3 | Y | 0.636 | 0.007 | 8 | 0.265 | 0.018 | 8 | 0.436 | 0.134 | -8.6 | 0.2 | 31.4 | -7.9 | 0.2 |
| 10 | 8.3 | N | 0.634 | 0.005 | 9 | 0.269 | 0.014 | 8 | 0.434 | 0.138 | -8.3 | 0.4 | 31.4 | -13.1 | 0.9 |
| 10 | 10.5 | Y | 0.707 | 0.009 | 9 | 0.252 | 0.015 | 4 | 0.506 | 0.121 | -9.8 | 0.0 | 29.7 | -12.2 | 0.3 |
| 10 | 10.5 | N | 0.804 | 0.008 | 11 | -0.252 | 0.017 | 4 | 0.601 | -0.379 | -22.0 | 0.2 | 17.3 | -23.5 | 0.1 |
| 15 | 8.3 | Y | 0.626 | 0.008 | 12 | 0.259 | 0.011 | 7 | 0.426 | 0.128 | -9.5 | 0.4 | 30.3 | -11.5 | 0.1 |
| 15 | 8.3 | N | 0.629 | 0.006 | 10 | 0.259 | 0.020 | 6 | 0.429 | 0.128 | -9.5 | 0.3 | 29.9 | -14.0 | 0.9 |
| 15 | 10.5 | Y | 0.694 | 0.007 | 10 | 0.243 | 0.038 | 2 | 0.493 | 0.112 | -11.8 | 0.4 | 28.1 | -13.1 | 0.3 |
| 15 | 10.5 | N | 0.801 | 0.007 | 13 | -0.256 | 0.017 | 5 | 0.598 | -0.383 | -24.6 | 0.3 | 14.9 | -20.1 | 0.1 |
| 25 | 8.3 | Y | 0.594 | 0.008 | 17 | 0.252 | 0.015 | 9 | 0.395 | 0.121 | -11.8 | 0.4 | 28.1 | -10.5 | 0.2 |
| 25 | 8.3 | N | 0.591 | 0.010 | 12 | 0.254 | 0.009 | 7 | 0.392 | 0.123 | -12.3 | 0.4 | 27.5 | -16.4 | 0.2 |
| 25 | 10.5 | Y | 0.746 | 0.005 | 7 | 0.185 | 0.025 | 5 | 0.544 | 0.055 | -15.4 | 0.5 | 24.8 | -13.0 | 0.6 |
| 25 | 10.5 | N | 0.788 | 0.009 | 11 | -0.227 | 0.037 | 4 | 0.585 | -0.354 | -21.9 | 0.2 | 18.1 | -19.3 | 0.3 |

**Table 9.** Clumped and stable isotope data for all samples measured in this study. Calcite mineral $\Delta_{63}$ and $\Delta_{64}$ was calculated using equations from Lucarelli et al. (2021), which were based on theory from Hill et al. (2014) and Tripati et al. (2015) and experimentally determined acid digestions fractionation factors (AFFs).

| Temp. ($^{o}$C) | Quasi-equilibrium or kinetic | Slope: $\Delta_{47\ \text{I-CDES}}$ versus $\delta^{18}O_{VPDB}$ | SE | Slope: $\Delta_{48\ \text{CDES 90}}$ versus $\delta^{18}O_{VPDB}$ | SE | Slope: $\Delta_{47\ \text{I-CDES}}$ versus $\Delta_{48\ \text{CDES 90}}$ | SE | Slope: $\Delta_{64}$ versus $\Delta_{63}$ |
|---|---|---|---|---|---|---|---|---|
| 5 to 25 | quasi-equilibrium | 0.013 | 0.001 | 0.004 | 0.001 | 0.355 | 0.030 | 0.373 |
| 5 | kinetic | -0.011 | 0.001 | -0.033 | 0.001 | -2.989 | 0.125 | -3.127 |
| 10 | kinetic | -0.013 | 0.000 | -0.038 | 0.000 | -3.071 | 0.011 | -3.102 |
| 15 | kinetic | -0.012 | 0.000 | -0.034 | n/a | -2.976 | 0.034 | -2.996 |
| 25 | kinetic | -0.020 | 0.001 | -0.048 | 0.002 | -2.455 | 0.024 | -2.485 |

**Table 10.** Equilibrium and kinetic trajectories for clumped and bulk isotopes for calcite precipitated with varying temperature and pH with and without CA. Near equilibrium slopes were determined by precipitating calcite at pH 8.3 with CA at 5 $^{o}$C, 10 $^{o}$C, 15 $^{o}$C, and 25 $^{o}$C. Kinetic slopes at 5 $^{o}$C were determined with a regression through samples precipitated at pH 8.3 with and without CA, and 9.5, 10.0, 10.5, and 11.0 without CA. Kinetic slopes at 10 $^{o}$C, 15 $^{o}$C, and 25 $^{o}$C were determined by regressions through samples precipitated at pH 8.3 with and without CA, and at pH 10.5 without CA. Calcite mineral $\Delta_{63}$ and $\Delta_{64}$ were calculated using equations from Lucarelli et al. (2021), which use theory from Hill et al. (2014) and Tripati et al. (2015) with experimentally-determined compositionally-dependent acid digestion fractionation factors.

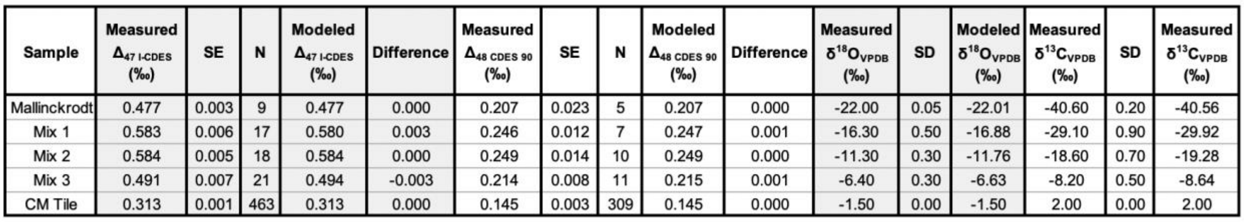

| Sample | Measured $\Delta_{47\ \text{I-CDES}}$ (‰) | SE | N | Modeled $\Delta_{47\ \text{I-CDES}}$ (‰) | Difference | Measured $\Delta_{48\ \text{CDES}\ 90}$ (‰) | SE | N | Modeled $\Delta_{48\ \text{CDES}\ 90}$ (‰) | Difference | Measured $\delta^{18}O_{VPDB}$ (‰) | SD | Modeled $\delta^{18}O_{VPDB}$ (‰) | Measured $\delta^{13}C_{VPDB}$ (‰) | SD | Measured $\delta^{13}C_{VPDB}$ (‰) |
|---|---|---|---|---|---|---|---|---|---|---|---|---|---|---|---|---|
| Mallinckrodt | 0.477 | 0.003 | 9 | 0.477 | 0.000 | 0.207 | 0.023 | 5 | 0.207 | 0.000 | -22.00 | 0.05 | -22.01 | -40.60 | 0.20 | -40.56 |
| Mix 1 | 0.583 | 0.006 | 17 | 0.580 | 0.003 | 0.246 | 0.012 | 7 | 0.247 | 0.001 | -16.30 | 0.50 | -16.88 | -29.10 | 0.90 | -29.92 |
| Mix 2 | 0.584 | 0.005 | 18 | 0.584 | 0.000 | 0.249 | 0.014 | 10 | 0.249 | 0.000 | -11.30 | 0.30 | -11.76 | -18.60 | 0.70 | -19.28 |
| Mix 3 | 0.491 | 0.007 | 21 | 0.494 | -0.003 | 0.214 | 0.008 | 11 | 0.215 | 0.001 | -6.40 | 0.30 | -6.63 | -8.20 | 0.50 | -8.64 |
| CM Tile | 0.313 | 0.001 | 463 | 0.313 | 0.000 | 0.145 | 0.003 | 309 | 0.145 | 0.000 | -1.50 | 0.00 | -1.50 | 2.00 | 0.00 | 2.00 |

**Table 11.** Measured and model predicted clumped and bulk isotope values from a mixing experiment using two endmembers with varying clumped and bulk isotope compositions. Mix 1 is 75% Mallinckrodt and 25 % CM Tile. Mix 2 is 50 % Mallinckrodt and 50 % CM Tile. Mix 3 is 25 % Mallinckrodt and 75 % CM Tile.

| Figure | Line color, symbol | Endmember | Initial $\Delta_{47}$ I-CDES (‰) | Initial $\Delta_{48}$ CDES 90 (‰) | Initial $\delta^{18}O$ VPDB (‰) | Initial $\delta^{13}C$ VPDB (‰) | $\Gamma_{47}$ (‰) | $\Gamma_{48}$ (‰) |
|---|---|---|---|---|---|---|---|---|
| 9A | blue, circle | Mallinckrodt | 0.477 | 0.202 | -21.9 | -40.5 | 0.117 | 0.045 |
| | | CM Tile | 0.313 | 0.576 | -1.5 | 2.0 | | |
| 9B | red, square | E1 | 0.667 | 0.287 | -10.0 | -10.0 | 0.029 | 0.045 |
| | | E2 | 0.526 | 0.223 | 10.0 | 10.0 | | |
| | black, circle | E1 | 0.667 | 0.287 | -10.0 | -10.0 | 0.086 | 0.073 |
| | | E2 | 0.667 | 0.287 | 10.0 | 10.0 | | |
| | green, diamond | E1 | 0.667 | 0.287 | 1.0 | 1.0 | 0.000 | 0.000 |
| | | E2 | 0.526 | 0.223 | 1.0 | 1.0 | | |
| 9C | black, triangle | E1 | 0.591 | 0.253 | -30.0 | -30.0 | 0.769 | |
| | | E2 | 0.591 | 0.253 | 30.0 | 30.0 | | |
| | blue, square | E1 | 0.591 | 0.253 | -15.0 | -15.0 | 0.193 | |
| | | E2 | 0.591 | 0.253 | 15.0 | 15.0 | | |
| | red, circle | E1 | 0.591 | 0.253 | -5.0 | -5.0 | 0.021 | |
| | | E2 | 0.591 | 0.253 | 5.0 | 5.0 | | |
| 9D | black, triangle | E1 | 0.591 | 0.253 | -30.0 | -30.0 | | 0.660 |
| | | E2 | 0.591 | 0.253 | 30.0 | 30.0 | | |
| | blue, square | E1 | 0.591 | 0.253 | -15.0 | -15.0 | | 0.164 |
| | | E2 | 0.591 | 0.253 | 15.0 | 15.0 | | |
| | red, circle | E1 | 0.591 | 0.253 | -5.0 | -5.0 | | 0.018 |
| | | E2 | 0.591 | 0.253 | 5.0 | 5.0 | | |

**Table 12.** Mixing model conditions for model data plotted in Figure 9, including experimental data using the internal carbonate standards Mallinckrodt and CM Tile as endmembers, and modeled endmembers with varying clumped and bulk isotope compositions. For the experimental data in Figure 9a, the largest $\Gamma_{47}$ and $\Gamma_{48}$ were observed when the mix contained 60% Mallinckrodt and 40 % CM Tile, where $\Gamma_i = \Delta_{i\ \mathrm{endmember}} - \Delta_{i\ \mathrm{mix}}$.

| | Measured values | | | | Calculated values | | | Measured values | | | | Calculated values | | |
|---|---|---|---|---|---|---|---|---|---|---|---|---|---|---|
| Temp. (°C) | $\Delta_{47\ \text{I-CDES}}$ (this study) (‰) | SE | $\Delta_{47\ \text{CDES 90}}$ (Swart et al., 2021) (‰) | SE | $\Delta_{47\ \text{I-CDES}}$ (Lucarelli et al., 2021) (‰) | $\Delta_{47\ \text{CDES 90}}$ (Bajnai et al., 2020) (‰) | $\Delta_{47\ \text{CDES 90}}$ (Fiebig et al., 2021) (‰) | $\Delta_{48\ \text{CDES 90}}$ (this study) (‰) | SE | $\Delta_{48\ \text{CDES 90}}$ (Swart et al., 2021) (‰) | SE | $\Delta_{48\ \text{CDES 90}}$ (Lucarelli et al., 2021) (‰) | $\Delta_{48\ \text{CDES 90}}$ (Bajnai et al., 2020) (‰) | $\Delta_{48\ \text{CDES 90}}$ (Fiebig et al., 2021) (‰) |
| 5 | 0.651 | 0.004 | 0.660 | 0.006 | 0.649 | 0.658 | 0.656 | 0.272 | 0.013 | 0.273 | 0.011 | 0.277 | 0.264 | 0.276 |
| 10 | 0.636 | 0.007 | 0.634 | 0.008 | 0.634 | 0.642 | 0.640 | 0.265 | 0.018 | 0.265 | 0.006 | 0.271 | 0.256 | 0.268 |
| 15 | 0.626 | 0.008 | 0.628 | 0.01 | 0.619 | 0.627 | 0.625 | 0.259 | 0.011 | 0.256 | 0.008 | 0.264 | 0.249 | 0.261 |
| 25 | 0.594 | 0.008 | 0.603 | 0.006 | 0.591 | 0.598 | 0.595 | 0.252 | 0.014 | 0.251 | 0.008 | 0.253 | 0.236 | 0.247 |
| 30 | | | 0.577 | 0.006 | 0.576 | 0.585 | 0.581 | | | 0.236 | 0.012 | 0.245 | 0.230 | 0.241 |
| 35 | | | 0.563 | 0.007 | 0.563 | 0.572 | 0.568 | | | 0.242 | 0.007 | 0.239 | 0.224 | 0.235 |
| 65 | | | 0.508 | 0.011 | 0.489 | 0.504 | 0.496 | | | 0.212 | 0.011 | 0.208 | 0.197 | 0.207 |

**Table 13.** Comparison of measured and calculated $\Delta_{47}$ and $\Delta_{48}$ values. Experimental data from Swart et al. (2021) is from inorganic calcite precipitations. Fiebig et al. (2021) calculated values are based on a regression determined from experimental measurments of carbonates, including lake and cave calcite, inorganic precipitations, and samples equilibrated at high temperature, with samples having crystallization temperatrues from 7.9 °C to 1100 °C. Lucareli et al. (2021) and Bajnai et al. (2020) calculated values are based on regressions determined using a combination of theory from Hill et al. (2014) and Tripati et al. (2015) with experimentally determined acid digestion fractionation factors.

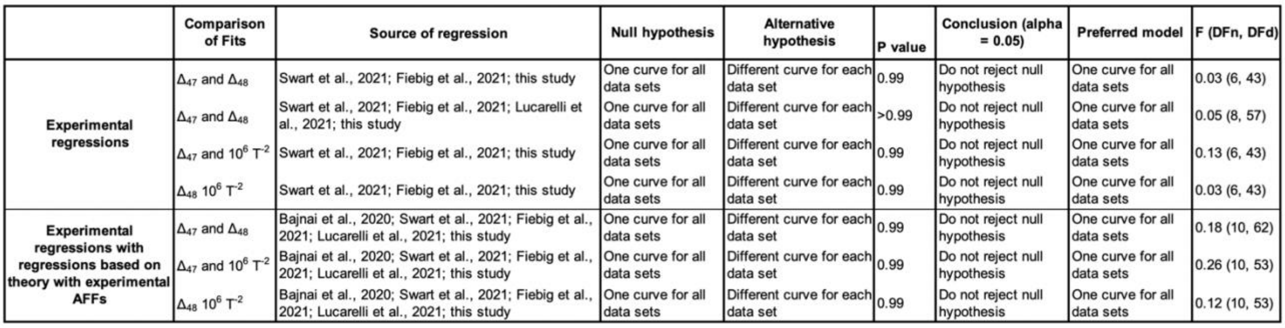

| | Comparison of Fits | Source of regression | Null hypothesis | Alternative hypothesis | P value | Conclusion (alpha = 0.05) | Preferred model | F (DFn, DFd) |
|---|---|---|---|---|---|---|---|---|
| **Experimental regressions** | $\Delta_{47}$ and $\Delta_{48}$ | Swart et al., 2021; Fiebig et al., 2021; this study | One curve for all data sets | Different curve for each data set | 0.99 | Do not reject null hypothesis | One curve for all data sets | 0.03 (6, 43) |
| | $\Delta_{47}$ and $\Delta_{48}$ | Swart et al., 2021; Fiebig et al., 2021; Lucarelli et al., 2021; this study | One curve for all data sets | Different curve for each data set | >0.99 | Do not reject null hypothesis | One curve for all data sets | 0.05 (8, 57) |
| | $\Delta_{47}$ and $10^6$ $T^{-2}$ | Swart et al., 2021; Fiebig et al., 2021; this study | One curve for all data sets | Different curve for each data set | 0.99 | Do not reject null hypothesis | One curve for all data sets | 0.13 (6, 43) |
| | $\Delta_{48}$ $10^6$ $T^{-2}$ | Swart et al., 2021; Fiebig et al., 2021; this study | One curve for all data sets | Different curve for each data set | 0.99 | Do not reject null hypothesis | One curve for all data sets | 0.03 (6, 43) |
| **Experimental regressions with regressions based on theory with experimental AFFs** | $\Delta_{47}$ and $\Delta_{48}$ | Bajnai et al., 2020; Swart et al., 2021; Fiebig et al., 2021; Lucarelli et al., 2021; this study | One curve for all data sets | Different curve for each data set | 0.99 | Do not reject null hypothesis | One curve for all data sets | 0.18 (10, 62) |
| | $\Delta_{47}$ and $10^6$ $T^{-2}$ | Bajnai et al., 2020; Swart et al., 2021; Fiebig et al., 2021; Lucarelli et al., 2021; this study | One curve for all data sets | Different curve for each data set | 0.99 | Do not reject null hypothesis | One curve for all data sets | 0.26 (10, 53) |
| | $\Delta_{48}$ $10^6$ $T^{-2}$ | Bajnai et al., 2020; Swart et al., 2021; Fiebig et al., 2021; Lucarelli et al., 2021; this study | One curve for all data sets | Different curve for each data set | 0.99 | Do not reject null hypothesis | One curve for all data sets | 0.12 (10, 53) |

**Table 14.** Extra-sum-of-squares F test results which determines if regressions have significant differences between them and if all datasets can be represented by one combined regression. Experimental regressions for samples with known precipitation temperature were used from Swart et al. (2021), Fiebig et al. (2021), and this study. An additional comparison was performed using an experimental $\Delta_{47}$ and $\Delta_{48}$ regression with samples of unknown precipitation temperature, including standards, from Lucarelli et al. (2021). The regressions from Bajnai et al. (2020) and Lucarelli et al. (2021) based on theory from Hill et al. (2014) and Tripati et al. (2015) with experimental AFFs were then compared to the experimental regressions.

# Appendix

The equations used in the mixing model (A.1) and box model (A.2) are detailed here. The models with the parameters used are available on the Github site for this manuscript: https://github.com/Tripati-Lab/ Lucarelli-et-al-D48exp2022.

## A.1 Mixing model equations

The mixing model calculates $\delta^{45}$, $\delta^{46}$, $\delta^{47}$, $\delta^{48}$, $\delta^{18}$O, $\delta^{13}$C, $\Delta_{47}$, and $\Delta_{48}$ values of $CO_2$ gas produced by phosphoric acid digestion of carbonate relative to a working gas (WG) for two endmembers and the mix of the endmembers. The equations used here for calculation of $\delta^{45}$, $\delta^{46}$, $\delta^{47}$, $\delta^{48}$, $\delta^{18}$O, $\delta^{13}$C, $\Delta_{47}$ are based on equations from Defliese and Lohmann (2015). Here, we add the calculation of $\Delta_{48}$ to the model. We have updated the model to use the IUPAC absolute abundance ratios from Brand et al. (2014) to calculate the endmember $R^{13}$ and $R^{18}$ in equations A1 and A2.

$$R^{13} = (\delta^{13}\mathrm{C}/1000 + 1) \times 0.01118 \qquad \text{(A1)}$$

$$R^{18} = (\delta^{18}\mathrm{O}/1000 + 1) \times 0.0020052 \qquad \text{(A2)}$$

$$R^{17} = (R^{18}/0.0020052)^{0.528} \times 0.00038475 \qquad \text{(A3)}$$

$R$ values were then used to calculate the absolute abundance of each isotope in equations A4-A8.

$$[^{12}\mathrm{C}] = 1/(1 + R^{13}) \qquad \text{(A4)}$$

$[^{13}C] = R^{13}/(1 + R^{13})$ (A5)

$[^{16}O] = 1/(1 + R^{17} + R^{18})$ (A6)

$[^{17}O] = R^{17}/(1 + R^{17} + R^{18})$ (A7)

$[^{18}O] = R^{18}/(1 + R^{17} = R^{18})$ (A8)

The C and O isotopic abundances were used to calculate the stochastic distribution of model sample and working gas $CO_2$ isotopes, $R^*$ and $R^*_{WG}$, by equations A9-A12.

$R^{45*} =( [^{13}C] [^{16}O]^2 + 2[^{12}C] [^{16}O] [^{17}O]) / [^{12}C] [^{16}O]^2$ (A9)

$R^{46*} = (2[^{13}C] [^{16}O] [^{18}O] + [^{12}C] [^{17}O]^2 + 2[^{13}C] [^{16}O] [^{17}O]) / [^{12}C] [^{16}O]^2$ (A10)

$R^{47*} = (2[^{13}C] [^{16}O] [^{18}O] + [^{12}C] [^{17}O]^2 + 2[^{12}C] [^{18}O] [^{17}O]) / [^{12}C] [^{16}O]^2$ (A11)

$R^{48*} = ([^{12}C] [^{18}O]^2 + 2[C^{13}] [^{17}O] [^{18}O]) / [^{12}C] [^{16}O]^2$ (A12)

The endmember $\delta^{45}$ and $\delta^{46}$ were calculated by equations A13 and A14.

$\delta^{45} = (R^{45*}/R^{45*}_{WG} - 1) \times 1000$ (A13)

$\delta^{46} = (R^{46*}/R^{46*}_{WG} - 1) \times 1000$ (A14)

The $\delta^{47}$ values were calculated using equations A15 and A16.

$$\delta^{47} = [\Delta_{47\ SC} + 1000) \times R^{47*} - 1000 \times R^{47*}{}_{WG}] / (R^{47*}{}_{WG} - SC \times R^{47*}) \tag{A15}$$

$$\Delta_{47\ SC} = (\Delta_{47\ CDES90} - \mathrm{ETF}_{\mathrm{Intercept}}) / \mathrm{ETF}_{\mathrm{Slope}} \tag{A16}$$

where $\Delta_{47\ SC}$ is the non-linearity slope corrected $\Delta_{47}$ value, $\Delta_{47\ CDES90}$ is the $\Delta_{47}$ value projected into the absolute CDES 90 (Bernasconi et al., 2021) reference frame, *SC* is non-linearity slope correction, and $\mathrm{ETF}_{\mathrm{slope}}$ and $\mathrm{ETF}_{\mathrm{intercept}}$ are the empirical transfer function slope and intercept (Dennis et al., 2011; Defliese and Lohmann, 2015).

$\delta^{48}$ and $\Delta_{48}$ were calculated similarly using equations A17 and A18.

$$\delta^{48} = [\Delta_{48\ SC} + 1000) \times R^{48*} - 1000 \times R^{48*}{}_{WG}] / (R^{48*}{}_{WG} - SC \times R^{48*}) \tag{A17}$$

$$\Delta_{48\ SC} = (\Delta_{48\ CDES\ 90} - \mathrm{ETF}_{\mathrm{Intercept}}) / \mathrm{ETF}_{\mathrm{Slope}} \tag{A18}$$

$\Delta_{48\ SC}$ is the non-linearity corrected $\Delta_{48}$ value, $\Delta_{48\ CDES\ 90}$ is the $\Delta_{48}$ value projected into the CDES 90 absolute reference frame, and $\mathrm{ETF}_{\mathrm{slope}}$ and $\mathrm{ETF}_{\mathrm{intercept}}$ are the slope and intercept of the empirical transfer function.

$\delta^{13}$C, $\delta^{18}$O, $\delta^{45}$, $\delta^{46}$, $\delta^{47}$, and $\delta^{48}$ were assumed to have linear mixing and are calculated by equation A19.

$$\delta \mathrm{i}_{\mathrm{mix}} = x_1\delta i_1 + x_2\delta i_2 \ldots + x_n\delta i_n \tag{A19}$$

where $\delta$i is a linearly mixed component, $x$ is the fractional contribution of each endmember ($\Sigma_x = 1$), and n represents the endmember composition. The stochastic distribution of isotopes in the endmember mix, $R^{45*}_{mix}$, $R^{46*}_{mix}$, $R^{47*}_{mix}$, and $R^{48*}_{mix}$, were calculated using $\delta^{13}C_{mix}$ and $\delta^{18}O_{mix}$ in equation S19. The isotopic ratios of the mix were calculated using:

$$R^{i}_{mix} = [(\delta i_{mix} / 1000) + 1] \times R^{i*}_{WG} \tag{A20}$$

where $i$ represents $CO_2$ with $m/z$ of 45, 46, 47, and 48. $\Delta_{47\ CDES90\ mix}$ and $\Delta_{48\ CDES90\ mix}$ were calculated using equations A21-A26.

$$\Delta_{47[SGvsWG]\ mix} = [(R^{47}{}_{mix}/R^{47*}{}_{mix} - 1) - (R^{46}{}_{mix}/R^{46*}{}_{mix} - 1) - (R^{45}{}_{mix}/R^{45*}{}_{mix} - 1)] \times 1000 \tag{A21}$$

$$\Delta_{47\ SC} = \Delta_{47[SGvsWG]mix} - \delta^{47}{}_{mix} \times SC \tag{A22}$$

$$\Delta_{47\ CDES\ 90\ mix} = \Delta_{47\ SC}\ \mathrm{x}\ \mathrm{ETF}_{slope} + \mathrm{ETF}_{intercept} \tag{A23}$$

$$\Delta_{48[SGvsWG]\ mix} = [(R^{48}{}_{mix}/R^{48*}{}_{mix} - 1) - 2(R^{46}{}_{mix}/R^{46*}{}_{mix} - 1)] \times 1000 \tag{A24}$$

$$\Delta_{48\ SC} = \Delta_{48[SGvsWG]mix} - \delta^{48}{}_{mix} \times SC \tag{A25}$$

$$\Delta_{48\ CDES\ 90\ mix} = \Delta_{48\ SC} \times \mathrm{ETF}_{slope} + \mathrm{ETF}_{intercept} \tag{A26}$$

## A2. Box model

This box model tracks the isotopic composition of DIC species in a homogeneous (well-stirred) solution into and out of which there are two fluxes: (1) a $CO_2$ influx, and (2) a $CaCO_3$ outflux. The incoming $CO_2$ has a fixed isotopic composition that is assumed to be in equilibrium with water. The $CaCO_3$ flux depends on the degree of supersaturation as well as the $Ca^{2+}$:$CO_3^{2-}$ ratio according to the ion-by-ion model (Wolthers et al., 2012). The box model used here is based on the framework of Chen et al. (2018) for $\delta^{18}O$ and $\delta^{13}C$. The oxygen isotope mass balance was updated by Christensen et al. (2021). The calculation of $\Delta_{47}$ was added to the model by Uchikawa et al. (2021) in the ExClump38 model. Kinetic effects associated with growth rate are calculated with equations from Watkins and Hunt (2015) and Watkins and Devriendt (2021). The calculation of $\Delta_{48}$ was added by Watkins and Devriendt (2021).

As $CO_2$ enters solution, it gets converted to $HCO_3^-$ and $CO_3^{2-}$. The carbon and oxygen isotope exchange reactions for (de)hydration and (de)hydroxylation of $CO_2$ involve six isotopically distinct DIC species (note that $^{12}C$ = 2, $^{13}C$ = 3, $^{16}O$ = 6, $^{18}O$ = 8, and superscripts on charged ionic species have been dropped):

$$266 + H_26 \underset{k_{-1}}{\overset{k_{+1}}{\leftrightarrows}} H2666 + H \tag{A27}$$

$$266 + 6H \underset{k_{-4}}{\overset{k_{+4}}{\leftrightarrows}} H2666 \tag{A28}$$

$$366 + H_26 \underset{c_{-1}}{\overset{c_{+1}}{\leftrightarrows}} H3666 + H \tag{A29}$$

$$366 + 6H \underset{c_{-4}}{\overset{c_{+4}}{\leftrightarrows}} H3666 \tag{A30}$$

266 + $H_2$8 $\underset{1/3a_{-1}}{\overset{a_{+1}}{\leftrightharpoons}}$ H2866 + H (A31)

286 + $H_2$6 $\underset{2/3b_{-1}}{\overset{b_{+1}}{\leftrightharpoons}}$ H2866 + H (A32)

266 + 8H $\underset{1/3a_{-4}}{\overset{a_{+4}}{\leftrightharpoons}}$ H2866 (A33)

286 + 6H $\underset{2/3b_{-4}}{\overset{b_{+4}}{\leftrightharpoons}}$ H2866 (A34)

These reactions are tracked through a system of ordinary differential equations (ODEs) where $HCO_3^-$ and $CO_3^{2-}$ are written together as equilibrated inorganic carbon, EIC (Chen et al., 2018). For example, H2666 + 2666 = E2666. It is assumed the [266] ≈ [$CO_2$], [H2666] ≈ [$HCO_3^-$], [6H] ≈ [$OH^-$], and [$H_2$6] ≈ [$H_2O$] = 1. It is also assumed that $HCO_3^-$ and $CO_3^{2-}$ achieve instantaneous isotopic equilibrium, as the protonation and deprotonation reactions proceed at much faster rates than hydration and hydroxylation and their reverse reactions.

$$\begin{aligned}\frac{d[266]}{dt} &= -\,k_{+1}[266] + k_{-1}[E2666]\chi[H] \\ &\quad - k_{+4}[266][6H] + k_{-4}[E2666]\chi\end{aligned} \tag{A35}$$

$$\begin{aligned}\frac{d[E2666]}{dt} &= k_{+1}[266] - k_{-1}[E2666]\chi[H] \\ &\quad + k_{+4}[266][6H] - k_{-4}[E2666]\chi\end{aligned} \tag{A36}$$

$$\frac{d[366]}{dt} = -\, c_{+1}[366] + c_{-1}[E3666]^{13}\chi[H] \qquad \text{(A37)}$$

$$-c_{+4}[366][6H] + c_{-4}[E3666]^{13}\chi$$

$$\frac{d[E3666]}{dt} = c_{+1}[366] - c_{-1}[E3666]^{13}\chi[H] \qquad \text{(A38)}$$

$$+\, c_{+4}[366][6H] - \; c_{-4}[E3666]^{13}\chi$$

$$\frac{d[286]}{dt} = -b_{+1}[286] + \frac{2}{3}b_{-1}[E2866]^{18}\chi[H] \qquad \text{(A39)}$$

$$-b_{+4}[286][6H] + \frac{2}{3}b_{-4}[E2866]^{18}\chi$$

$$\frac{d[E2866]}{dt} = a_{+1}[266]r_w - \frac{1}{3}a_{-1}[E2866]^{18}\chi[H] \qquad \text{(A40)}$$

$$+a_{+4}[266][8H] - \frac{1}{3}a_{-4}[E2866]^{18}\chi$$

$$+\, b_{+1}[286] - \frac{2}{3}b_{-1}[E2866]^{18}\chi[H]$$

$$+\, b_{+4}[286][6H] - \frac{2}{3}b_{-4}[E2866]^{18}\chi$$

The $\chi$ term is the fraction of $HCO_3^-$ in EIC (Chen et al., 2018).

$$\chi = \frac{[H2666]}{[H2666]+[2666]} = \frac{1}{1+\frac{K_2}{[H]}} \qquad \text{(A41)}$$

$$^{13}\chi = \frac{[H3666]}{[H3666]+[3666]} = \frac{1}{1+\frac{K_2\cdot {}^{13}\alpha^{eq}_{CO_3^{2-}-HCO_3^-}}{[H^+]}} \tag{A42}$$

$$^{18}\chi = \frac{[H3666]}{[H3666]+[3666]} = \frac{1}{1+\frac{K_2\cdot {}^{13}\alpha^{eq}_{CO_3^{2-}-HCO_3^-}}{[H^+]}} \tag{A43}$$

The term $\alpha^{eq}_{CO_3^{2-}\,-\,HCO_3^-}$ is the equilibrium fractionation factor between $CO_3^{2-}$ and $HCO_3^-$. K2 is the equilibrium constant for the dissociation of $HCO_3^-$ to $CO_3^{2-}$ and H+, which are related to the kinetic rate constants, $k_{+2}$ and $k_{-2}$.

$$HCO_3^- \underset{k_{-2}}{\overset{k_{+2}}{\rightleftharpoons}} CO_3^{2-} + H^+ \tag{A44}$$

$$K_2 = \frac{[H^+][CO_3^{2-}]}{[HCO_3^-]} = \frac{k_{+2}}{k_{-2}} \tag{A45}$$

Other equilibrium constants are as follows:

$$K_1 = \frac{[H][H2666]}{[266]} = \frac{k_{+1}}{k_{-1}} \tag{A46}$$

$$K_w = [H][OH]\ . \tag{A47}$$

The kinetic fractionation factors (KFFs) for carbon and oxygen isotope fractionation are directly related to the forward rate constants, with the numerator of the left-hand side of the equation being the singly heavy isotope substituted isotopologue and the denominator being the most abundant isotopologue. For the hydration reactions, the KFFs are:

$$\frac{c_{+1}}{k_{+1}} = {}^{13}\alpha_{c_{+1}}^{KFF} \tag{A48}$$

$$\frac{a_{+1}}{k_{+1}} = {}^{18}\alpha_{a_{+1}}^{KFF} \tag{A49}$$

$$\frac{b_{+1}}{k_{+1}} = {}^{18}\alpha_{b_{+1}}^{KFF} \quad . \tag{A50}$$

For hydroxylation reactions, the KFFs are:

$$\frac{c_{+4}}{k_{+4}} = {}^{13}\alpha_{c_{+4}}^{KFF} \tag{A51}$$

$$\frac{a_{+4}}{k_{+4}} = {}^{18}\alpha_{a_{+4}}^{KFF} \tag{A52}$$

$$\frac{b_{+4}}{k_{+4}} = {}^{18}\alpha_{b_{+4}}^{KFF} \quad . \tag{A53}$$

After combining the equilibrium constant and rearranging, forward and backward kinetic rate constants satisfy equilibrium, which results in the following relationships:

$$k_{+1}[266][H_26] = k_{-1}[H2666][H] \tag{A54}$$

$$c_{+1}[366][H_26] = c_{-1}[H3666][H] \tag{A55}$$

$$a_{+1}[266][H_28] = \frac{1}{3}a_{-1}[H2866][H] \tag{A56}$$

$b_{+1}[286][H_26] = \frac{2}{3}b_{-1}[H2866][H]$ (A57)

$k_{+4}[266][6H] = k_{-4}[H2666]$ (A58)

$c_{+4}[366][6H] = c_{-4}[H3666]$ (A59)

$a_{+4}[266][8H] = \frac{1}{3}a_{-4}[H2866]$ (A60)

$b_{+4}[286][6H] = \frac{2}{3}b_{-4}[H2866]$ . (A61)

To add carbonate clumped isotopes, $\Delta_{47}$ and $\Delta_{48}$, to the model, equations from Uchikawa et al. (2021) were used for $\Delta_{47}$ and new equations from this study were used for $\Delta_{48}$. Clumping in $CO_2$ is based on the following reactions and equilibrium constants for the internal equilibrium of $^{13}C–^{18}O–^{16}O$ and $^{12}C–^{18}O–^{18}O$:

$$366 + 286 \leftrightharpoons 386 + 266 \quad \text{(A62)}$$

$$286 + 286 \leftrightharpoons 288 + 266 \quad \text{(A63)}$$

$$^{47}K_{CO_2} = \frac{[386][266]}{[366][286]} \quad \text{(A64)}$$

$$^{48}K_{CO_2} = \frac{[288][266]}{[286][286]} \ . \quad \text{(A65)}$$

The abundance of m/z 47 and m/z 48 $CO_2$ isotopologues are defined by equations A66 and A67, respectively,

$$\Delta_{47} = \left(\frac{^{47}R}{^{47}R^{*}} - 1\right) \tag{A66}$$

$$\Delta_{48} = \left(\frac{^{48}R}{^{48}R^{*}} - 1\right) \tag{A67}$$

$$^{47}\mathrm{R} = \frac{[386]}{[266]} \tag{A68}$$

$$^{48}\mathrm{R} = \frac{[288]}{[266]} \tag{A69}$$

where R is the ratio of heavy isotope substituted isotopologue to the most abundant isotopologue, and $R^{*}$ is the stochastic ratio. It is customary to present $\Delta_{47}$ and $\Delta_{48}$ in parts per thousand (‰), and a factor of 1000 is multiplied by equations A66 and A67. The stochastic ratios are related to the equilibrium constants by the following equations (Watkins and Hunt, 2015; Uchikawa et al., 2021; Watkins and Devriendt, 2021):

$$^{47}K_{CO_2} = \left(\frac{^{47}R}{^{47}R^{*}}\right)_{CO_2}^{eq} = \left(\frac{\Delta_{47,CO_2}^{eq}}{1000} + 1\right) \tag{A70}$$

$$^{48}K_{CO_2} = \frac{1}{4}\left(\frac{^{48}R}{^{48}R^{*}}\right)_{CO_2}^{eq} = \frac{1}{4}\left(\frac{\Delta_{48,CO_2}^{eq}}{1000} + 1\right). \tag{A71}$$

Similarly, expressions relating the equilibrium constants and isotope ratios can be written for $HCO_3^-$ and $CO_3^{2-}$:

$$^{63}K_{HCO_3^-} = \left(\frac{^{63}R}{^{63}R^*}\right)_{HCO_3^-}^{eq} = \left(\frac{\Delta_{63,HCO_3^-}^{eq}}{1000} + 1\right) \tag{A72}$$

$$^{64}K_{HCO_3^-} = \frac{1}{3}\left(\frac{^{64}R}{^{64}R^*}\right)_{HCO_3^-}^{eq} = \frac{1}{3}\left(\frac{\Delta_{64,HCO_3^-}^{eq}}{1000} + 1\right) \tag{A73}$$

$$^{63}K_{CO_3^{2-}} = \left(\frac{^{63}R}{^{63}R^*}\right)_{CO_3^{2-}}^{eq} = \left(\frac{\Delta_{63,CO_3^{2-}}^{eq}}{1000} + 1\right) \tag{A74}$$

$$^{64}K_{CO_3^{2-}} = \frac{1}{3}\left(\frac{^{64}R}{^{64}R^*}\right)_{CO_3^{2-}}^{eq} = \frac{1}{3}\left(\frac{\Delta_{64,CO_3^{2-}}^{eq}}{1000} + 1\right) \tag{A75}$$

The model includes the following reactions that result in the formation $^{13}C$–$^{18}O$–$^{16}O$ and $^{12}C$–$^{18}O$–$^{18}O$ species in $HCO_3^-$ and $CO_3^{2-}$, where reactions that form a clumped isotopologue from singly substituted reactants is “primary”, denoted *p*, and the others are secondary, denoted *s* (Guo, 2020):

$$366 + H_28 \underset{1/3p_{-1}}{\overset{p_{+1}}{\leftrightharpoons}} H3866 + H \tag{A76}$$

$$386 + H_26 \underset{2/3s_{-1}}{\overset{s_{+1}}{\leftrightharpoons}} H3866 + H \tag{A77}$$

$$366 + 8H \underset{1/3p_{-4}}{\overset{p_{+4}}{\leftrightharpoons}} H3866 \tag{A78}$$

$$386 + 6H \underset{2/3s_{-4}}{\overset{s_{+4}}{\leftrightharpoons}} H3866 \tag{A79}$$

$$286 + H_2 8 \underset{2/3p'_{-1}}{\overset{p'_{+1}}{\leftrightharpoons}} H2886 + H \tag{A80}$$

$$288 + H_2 6 \underset{1/3s'_{-1}}{\overset{s'_{+1}}{\leftrightharpoons}} H2886 + H \tag{A81}$$

$$286 + 8H \underset{2/3p'_{-4}}{\overset{p'_{+4}}{\leftrightharpoons}} H2886 \tag{A82}$$

$$288 + 6H \underset{1/3s'_{-4}}{\overset{s'_{+4}}{\leftrightharpoons}} H2886 \tag{A83}$$

From these reactions, the following ODEs are obtained (Uchikawa et al., 2021; Watkins and Devriendt, 2021)):

$$\frac{d[386]}{dt} = -p_{+1}[386] + \frac{1}{3}p_{-1}[E3866]^{63}\chi[H] \tag{A84}$$

$$-s_{+4}[386][6H] + \frac{2}{3}s_{-4}[E3866]^{63}\chi$$

$$\frac{d[E3866]}{dt} = p_{+1}[366]r_w - \frac{1}{3}p_{-1}[E3866]^{63}\chi[H] \tag{A85}$$

$$+p_{+4}[266][8H] - \frac{1}{3}p_{-4}[E3866]^{63}\chi$$

$$+ s_{+1}[386] - \frac{2}{3}s_{-1}[E3866]^{63}\chi[H]$$

$$+ s_{+4}[386][6H] - \frac{2}{3} s_{-4}[E3866]^{63}\chi$$

$$\frac{d[288]}{dt} = -s'_{+1}[288] + \frac{1}{3} s'_{-1}[E2886]^{64}\chi[H]$$ (A86)

$$-s'_{+4}[288][6H] + \frac{1}{3} s'_{-4}[E3866]^{64}\chi$$

$$\frac{d[E2886]}{dt} = p'_{+1}[286]r_w - \frac{2}{3} p'_{-1}[E2886]^{64}\chi[H]$$ (A87)

$$+p'_{+4}[266][8H] - \frac{2}{3} p'_{-1}[E2886]^{64}\chi$$

$$+ s'_{+1}[288] - \frac{1}{3} s'_{-1}[E2886]^{64}\chi[H]$$

$$+ s'_{+4}[288][6H] - \frac{1}{3} s'_{-4}[E2886]^{64}\chi$$

The terms ${}^{63}\chi$ and ${}^{64}\chi$ take the same form and ${}^{13}\chi$ and ${}^{18}\chi$ because the fraction of EIC that is $HCO_3^-$ has the same pH dependence for clumped, oxygen, and carbon isotopes (Hill et al., 2014).

$${}^{63}\chi = \frac{1}{1+\frac{{}^{63}K_2}{[H^+]}}$$ (A88)

$${}^{64}\chi = \frac{1}{1+\frac{{}^{64}K_2}{[H^+]}}$$ (A89)

$${}^{63}K_2 = \frac{[3866][H]}{[H3866]}$$

(A90)

$$^{64}K_2 = \frac{[2886][H]}{[H2886]} \quad \text{(A91)}$$

The model assumes that the kinetic clumped isotope effects ($^{47}$KIE and $^{48}$KIE) for hydration and hydroxylation are a combination of kinetic effects in carbon and oxygen isotopes, $^{13}\alpha^{KIF}$, $^{18}\alpha^{KIF}$, with an additional fractionation specific to clumped isotope species, ($^{47}\alpha^{KIF}$ and $^{48}\alpha^{KIF}$) (Watkins and Hunt, 2015; Guo, 2020). For the forward reactions, the relationships are as follows:

$$^{47}KIE_{p_1} = \frac{^{47}\alpha_{p_{+1}}}{^{13}\alpha^{KIF}_{c_{+1}} \cdot {}^{18}\alpha^{KIF}_{a_{+1}}} = \frac{p_{+1} \cdot k_{+1}}{c_{+1} \cdot a_{+1}} \quad \text{(A92)}$$

$$^{47}KIE_{s_1} = \frac{^{47}\alpha_{s_{+1}}}{^{13}\alpha^{KIF}_{c_{+1}} \cdot {}^{18}\alpha^{KIF}_{b_{+1}}} = \frac{s_{+1} \cdot k_{+1}}{c_{+1} \cdot b_{+1}} \quad \text{(A93)}$$

$$^{47}KIE_{p_4} = \frac{^{47}\alpha_{p_{+4}}}{^{13}\alpha^{KIF}_{c_{+4}} \cdot {}^{18}\alpha^{KIF}_{a_{+4}}} = \frac{p_{+4} \cdot k_{+4}}{c_{+4} \cdot a_{+4}} \quad \text{(A94)}$$

$$^{47}KIE_{s_4} = \frac{^{47}\alpha_{s_{+4}}}{^{13}\alpha^{KIF}_{c_{+4}} \cdot {}^{18}\alpha^{KIF}_{b_{+4}}} = \frac{s_{+4} \cdot k_{+4}}{c_{+4} \cdot b_{+4}} \quad \text{(A95)}$$

$$^{48}KIE_{p'_1} = \frac{^{48}\alpha_{p'_{+1}}}{^{18}\alpha^{KIF}_{a_{+1}} \cdot {}^{18}\alpha^{KIF}_{b_{+1}}} = \frac{p'_{+1} \cdot k_{+1}}{a_{+1} \cdot b_{+1}} \quad \text{(A96)}$$

$$^{48}KIE_{s'_1} = \frac{^{48}\alpha_{s'_{+1}}}{^{18}\alpha^{KIF}_{b_{+1}} \cdot {}^{18}\alpha^{KIF}_{b_{+1}}} = \frac{s'_{+1} \cdot k_{+1}}{b_{+1} \cdot b_{+1}} \quad \text{(A97)}$$

$$^{48}KIE_{p'_4} = \frac{^{48}\alpha_{p'_{+4}}}{^{18}\alpha^{KIF}_{a_{+4}} \cdot {}^{18}\alpha^{KIF}_{b_{+4}}} = \frac{p'_{+4} \cdot k_{+4}}{a_{+4} \cdot b_{+4}} \quad \text{(A98)}$$

$$^{48}KIE_{s'_4} = \frac{^{48}\alpha_{s'_{+4}}}{^{18}\alpha^{KIF}_{b_{+4}} \cdot {}^{18}\alpha^{KIF}_{b_{+4}}} = \frac{s'_{+4} \cdot k_{+4}}{b_{+4} \cdot b_{+4}} \, . \tag{A99}$$

The reverse reaction rate constants can be calculated via the following relationships (Uchikawa et al., 2021):

$$\frac{p_{+1}}{p_{-1}} = \left(\frac{^{63}R}{^{63}R^*}\right)^{eq}_{HCO_3^-} \cdot \, K_1 \, \cdot \, {}^{13}\alpha^{eq}_{HCO_3^- - CO_2} \, \cdot {}^{18}\alpha^{eq}_{HCO_3^- - H_2O} \tag{A100}$$

$$\frac{s_{+1}}{s_{-1}} = \frac{\left(\frac{^{63}R}{^{63}R^*}\right)^{eq}_{HCO_3^-} \cdot K_1 \cdot {}^{13}\alpha^{eq}_{HCO_3^- - CO_2} \cdot {}^{18}\alpha^{eq}_{HCO_3^- - H_2O}}{\left(\frac{^{47}R}{^{47}R^*}\right)^{eq}_{CO_2}} \tag{A101}$$

$$\frac{p_{+4}}{p_{-4}} = \left(\frac{^{63}R}{^{63}R^*}\right)^{eq}_{HCO_3^-} \cdot \, \frac{K_1}{K_w} \cdot \, {}^{13}\alpha^{eq}_{HCO_3^- - CO_2} \, \cdot {}^{18}\alpha^{eq}_{HCO_3^- - OH^-} \tag{A102}$$

$$\frac{s_{+4}}{s_{-4}} = \frac{\left(\frac{^{63}R}{^{63}R^*}\right)^{eq}_{HCO_3^-} \cdot \frac{K_1}{K_w} \cdot {}^{13}\alpha^{eq}_{HCO_3^- - CO_2} \cdot {}^{18}\alpha^{eq}_{HCO_3^- - H_2O}}{\left(\frac{^{47}R}{^{47}R^*}\right)^{eq}_{CO_2}} \tag{A103}$$

$$\frac{p'_{+1}}{p'_{-1}} = \left(\frac{^{64}R}{^{64}R^*}\right)^{eq}_{HCO_3^-} \cdot \, K_1 \, \cdot \, {}^{18}\alpha^{eq}_{HCO_3^- - CO_2} \, \cdot {}^{18}\alpha^{eq}_{HCO_3^- - H_2O} \tag{A104}$$

$$\frac{s'_{+1}}{s'_{-1}} = \frac{\left(\frac{{}^{64}R}{{}^{64}R^{*}}\right)^{eq}_{HCO_3^-} \cdot K_1 \cdot {}^{18}\alpha^{eq}_{HCO_3^- - CO_2} \cdot {}^{18}\alpha^{eq}_{HCO_3^- - CO_2}}{\left(\frac{{}^{48}R}{{}^{48}R^{*}}\right)^{eq}_{CO_2}} \tag{A105}$$

$$\frac{p'_{+4}}{p'_{-4}} = \left(\frac{{}^{64}R}{{}^{64}R^{*}}\right)^{eq}_{HCO_3^-} \cdot \frac{K_1}{K_w} \cdot {}^{18}\alpha^{eq}_{HCO_3^- - CO_2} \cdot {}^{18}\alpha^{eq}_{HCO_3^- - OH^-} \tag{A106}$$

$$\frac{s'_{+4}}{s'_{-4}} = \frac{\left(\frac{{}^{64}R}{{}^{64}R^{*}}\right)^{eq}_{HCO_3^-} \cdot \frac{K_1}{K_w} \cdot {}^{18}\alpha^{eq}_{HCO_3^- - CO_2} \cdot {}^{18}\alpha^{eq}_{HCO_3^- - CO_2}}{\left(\frac{{}^{47}R}{{}^{47}R^{*}}\right)^{eq}_{CO_2}}\,. \tag{A107}$$

To account for kinetic effects from carbonate precipitation, we use the ion-by-ion model from Watkins and Hunt (2015). The model describes crystal growth ($\Omega > 1$) through the attachment and detachment rates of $HCO_3^-$ and $CO_3^{2-}$ isotopologues to a calcite crystal, which affects the isotopic composition of residual EIC. The $CO_2$ flux in the modelled solution reacts via hydration and hydroxylation reactions to form $HCO_3^-$ and $CO_3^{2-}$, and the calcite growth rate depends on the [$Ca^{2+}$] and [$CO_3^{2-}$].

$$Ca^{2+} + HCO_3^- \underset{\nu_{B_2}}{\overset{k_{B_2}}{\rightleftharpoons}} CaCO_3 + H^+ \tag{A108}$$

$$Ca^{2+} + CO_3^{2-} \underset{\nu_{B_1}}{\overset{k_{B_1}}{\rightleftharpoons}} CaCO_3 \tag{A109}$$

The rate constants in equations A108 and A109 are mass dependent and using notation from Wolthers et al. (2012). The effect of $CaCO_3$ precipitation on the clumped isotope composition of residual EIC is calculated by equation A110:

$$\frac{d([3866])_{CaCO_3}}{dt} = -\frac{d[3866])_{DIC}}{dt} \tag{A110}$$

The equations solved in the ion-by-ion model are:

$$\frac{d[266]}{dt} = \{rxn\ terms, Eq. S34\} + \frac{F_{CO_2}}{V} \tag{A111}$$

$$\frac{d[2666]}{dt} = \{rxn\ terms, Eq. S35\} - \frac{F_{CaCO_3}}{V} \tag{A112}$$

$$\frac{d[366]}{dt} = \{rxn\ terms, Eq. S36\} + \frac{F_{CO_2} \cdot {}^{13}R_{CO_2}}{V} \tag{A113}$$

$$\frac{d[3666]}{dt} = \{rxn\ terms, Eq. S37\} - \frac{F_{CaCO_3}}{V} \cdot \frac{[E3666]}{[E2666]} \cdot {}^{13}\alpha_{CaCO_3\ -EIC} \tag{A114}$$

$$\frac{d[286]}{dt} = \{rxn\ terms, Eq. S38\} + \frac{F_{CO_2} \cdot {}^{18}R_{CO_2}}{V} \tag{A115}$$

$$\frac{d[2866]}{dt} = \{rxn\ terms, Eq. S39\} - \frac{F_{CaCO_3}}{V} \cdot \frac{[E2866]}{[E2666]} \cdot {}^{18}\alpha_{CaCO_3\ -EIC} \tag{A116}$$

$$\frac{d[386]}{dt} = \{rxn\ terms, Eq. S83\} + \frac{F_{CO_2} \cdot {}^{47}R_{CO_2}}{V} \tag{A117}$$

(A118)

$$\frac{d[3866]}{dt} = \{rxn\ terms, Eq. S84\} - \frac{F_{CaCO_3}}{V} \cdot \frac{[E3866]}{[E2666]} \cdot {}^{63}\alpha_{CaCO_3\ -EIC} \cdot {}^{13}\alpha_{CaCO_3\ -EIC} \cdot$$

$${}^{18}\alpha_{CaCO_3\ -EIC}$$

$$\frac{d[Ca^{2+}]}{dt} = -\frac{F_{CaCO_3}}{V} \tag{A119}$$

In the model, we begin with $[Ca^{2+}]$ = 10 mM and enough DIC to bring the degree of supersaturation to unity. Hence, the amount of initial DIC depends on the specified pH. Since $\Omega = 1$, the precipitation flux of $CaCO_3$ = 0 initially but then monotonically increases until it exactly balances with the incoming constant $CO_2$ flux. Depending on the rate of $CO_2$ flux, the system will eventually reach steady state that is not in equilibrium. The flux of $CaCO_3$ was calculated by multiplying the growth rate by an average reactive surface area of 0.1 $m^2$, as estimated to be representative of the experiments.

The addition of carbonic anhydrase increases the hydration rate constant according to (Uchikawa and Zeebe, 2012):

$$k_{+1}{}^{*} = k_{+1} + \frac{k_{\mathrm{cat}}}{K_{\mathrm{M}}} \cdot [\mathrm{CA}], \tag{A120}$$

where [CA] is in moles/L, $k_{\mathrm{cat}}$ is the turnover number and $K_{\mathrm{M}}$ is the Michaelis-Menten constant. Uchikawa and Zeebe (2012) determined $k_{\mathrm{cat}}/K_{\mathrm{M}} = 2.7 \times 10^7\ M^{-1}\ s^{-1}$ for the same type of CA that we used in our experiments.

| Symbol | Expression or value at 25°C | Reference |
|---|---|---|
| $K_1$ | $\frac{[H][H2666]}{[266]}$ | - |
| $K_2$ | $\frac{[H][H2666]}{[H2666]}$ | - |
| $K_w$ | [6H][H] | - |
| $k_{+1}$ | $\ln k_{+1} = 1246.98 - \frac{61900}{T_K} - 183.0 ln T_k$ | Uchikawa and Zeebe (2012) |
| $k_{-1}$ | $k_{-1} = k_{+1}/K_1$ | - |
| $k_{+4}$ | $ln\ k_{+4} = 17.67 - \frac{2790.47}{T_K}$ | Uchikawa and Zeebe (2012) |
| $k_{-4}$ | $k_{-4} = k_{+4}\frac{K_w}{K_1}$ | - |
| $\chi$ | $\chi = \frac{1}{1+\frac{K_2}{[H^+]}}$ | - |
| **Carbon isotope parameters** | | |

|  |  |  |
|---|---|---|
| ${}^{13}\alpha^{eq}_{HCO_3^- - CO_2}$ | $-9.866 T^{-1} + 1.02412$ | Zhang et al. (1995) |
| ${}^{13}\alpha^{eq}_{HCO_3^- - CO_2}$ | $-0.867\ T^{-1} + 1.00252$ | Zhang et al. (1995) |
| ${}^{13}\alpha^{KFF}_{c_{+1}}$ | 0.9872 | Yumol et al. (2020) |
| ${}^{13}\alpha^{KFF}_{c_{+4}}$ | 0.9814 | Christensen et al. (2021) |
| $c_{+1}$ | $c_{+1} = {}^{13}\alpha^{KFF}_{c_{+1}} \cdot k_{+1}$ | - |
| $c_{-1}$ | $c_{-1} = c_{+1} / \left(K_1 \cdot {}^{13}\alpha^{eq}_{HCO_3^- - CO_2}\right)$ | - |
| $c_{+4}$ | $c_{+4} = {}^{13}\alpha^{KFF}_{c_{+4}} \cdot k_{+4}$ | - |
| $c_{-4}$ | $c_{-4} = c_{+4} / \left(\frac{K_1}{K_w} \cdot {}^{13}\alpha^{eq}_{HCO_3^- - CO_2}\right)$ | - |
| ${}^{13}\chi$ | ${}^{13}\chi = \frac{1}{1+\frac{K_2 \cdot {}^{13}\alpha^{eq}_{HCO_3^- - CO_3}}{[H^+]}}$ | - |
| **Oxygen isotope parameters** |  |  |
| ${}^{18}\alpha^{eq}_{CO_2 - H_2O}$ | $\exp(2520\ T_K^{-2} + 0.01212$ | Beck et al. (2005) |
| ${}^{18}\alpha^{eq}_{HCO_3^- - H_2O}$ | $\exp(2590\ T_K^{-2} + 0.00189$ | Beck et al. (2005) |
| ${}^{18}\alpha^{eq}_{CO_3^{2-} - H_2O}$ | $\exp(2390\ T_K^{-2} - 0.00270$ | Beck et al. (2005) |
| ${}^{18}\alpha^{eq}_{OH^- - H_2O}$ | $5.6676 \times 10^{-5}\ T_K + 0.9622$ | Zeebe (2020) |
| ${}^{18}\alpha^{KFF}_{a_{+1}}$ | 1.0000 | Yumol et al. (2020) |
| ${}^{18}\alpha^{KFF}_{b_{+1}}$ | 0.9812 | Yumol et al. (2020) |
| ${}^{18}\alpha^{KFF}_{a_{+4}}$ | 0.9988 | Christensen et al. (2021) |
| ${}^{18}\alpha^{KFF}_{b_{+4}}$ | 1.0000 | Christensen et al. (2021) |
| $a_{+1}$ | $a_{+1} = {}^{18}\alpha^{KFF}_{a_{+1}} \cdot k_{+1}$ | - |
| $b_{+1}$ | $b_{+1} = {}^{18}\alpha^{KFF}_{b_{+1}} \cdot k_{+1}$ | - |
| $a_{-1}$ | $a_{-1} = a_{+1} / (K_1 \cdot {}^{18}\alpha_{HCO_3^- - H_2O})$ | - |
| $b_{-1}$ | $b_{-1} = b_{+1} / (K_1 \cdot {}^{18}\alpha_{HCO_3^- - CO_2})$ | - |
| $a_{+4}$ | $a_{+4} = {}^{18}\alpha^{KFF}_{a_{+4}} \cdot k_{+4}$ | - |
| $b_{+4}$ | $b_{+4} = {}^{18}\alpha^{KFF}_{b_{+4}} \cdot k_{+4}$ | - |
| $a_{-4}$ | $a_{-4} = a_{+4} / \left(\frac{K_1}{K_w} \cdot \frac{{}^{18}\alpha_{HCO_3^- - H_2O}}{{}^{18}\alpha^{eq}_{OH^- - H_2O}}\right)$ | - |
| $b_{-4}$ | $b_{-4} = b_{+4} / \left(\frac{K_1}{K_w} \cdot {}^{18}\alpha_{HCO_3^- - CO_2}\right)$ | - |
| ${}^{18}\chi$ | ${}^{18}\chi = \frac{1}{1 + \frac{K_2 \cdot {}^{13}\alpha^{eq}_{CO_3 - HCO_3^-}}{[H^+]}}$ | - |
| **$\Delta_{47}$ parameters** |  |  |
| $\left(\frac{{}^{47}R}{{}^{47}R^*}\right)^{eq}_{CO_2}$ | $(\Delta^{eq}_{47,CO_2}/1000) + 1$ | Hill et al. (2020) |
| $\left(\frac{{}^{63}R}{{}^{63}R^*}\right)^{eq}_{HCO_3^-}$ | $(\Delta^{eq}_{63,HCO_3^-}/1000) + 1$ | Hill et al. (2020); Tripati et al. (2015) |
| $\left(\frac{{}^{63}R}{{}^{63}R^*}\right)^{eq}_{CO_3^{2-}}$ | $(\Delta^{eq}_{63,CO_3^{2-}}/1000) + 1$ | Hill et al. (2020); Tripati et al. (2015) |

|  |  |  |
|---|---|---|
| ${}^{63}\alpha^{eq}_{CO_3^{2-}-HCO_3}$ | $\left(\frac{{}^{63}R}{{}^{63}R^*}\right)^{eq}_{CO_3^{2-}} / \left(\frac{{}^{63}R}{{}^{63}R^*}\right)^{eq}_{HCO_3^-}$ | - |
| ${}^{63}K_2$ | ${}^{63}\alpha^{KFF}_{CO_3^{2-}-HCO_3^-} \cdot {}^{13}\alpha^{eq}_{HCO_3^--CO_3} \cdot {}^{18}\alpha^{eq}_{CO_3^{2-}-HCO_3^-} \cdot K_2$ | - |
| ${}^{63}\chi$ | $\frac{1}{1+\frac{{}^{63}K_2 \cdot {}^{63}\alpha^{eq}_{CO_3{}_-HCO_3^-}}{[H^+]}}$ | - |
| ${}^{13-18}KIE_{p+1}$ | 1-0.146/1000 | Guo (2020) |
| ${}^{13-18}KIE_{s+1}$ | 1-0.219/1000 | Guo (2020) |
| ${}^{13-18}KIE_{p+4}$ | 1-0.016/1000 | Guo (2020) |
| ${}^{13-18}KIE_{s+1}$ | 1-0.175/1000 | Guo (2020) |
| $p_{+1}$ | $\frac{c_{+1} \cdot a_{+1}}{k_{+1} \cdot {}^{47}KIE_{p_1}}$ | Uchikawa et al. (2021) |
| $s_{+1}$ | $\frac{c_{+1} \cdot b_{+1}}{k_{+1} \cdot {}^{47}KIE_{s_1}}$ | Uchikawa et al. (2021) |
| $p_{-1}$ |  | - |
| $s_{-1}$ |  | - |
| $p_{+4}$ | $\frac{c_{+4} \cdot a_{+4}}{k_{+4} \cdot {}^{13-18}KIE_{p4}}$ | Uchikawa et al. (2021) |
| $s_{+4}$ | $\frac{c_{+4} \cdot b_{+4}}{k_{+4} \cdot {}^{47}KIE_{s4}}$ | Uchikawa et al. (2021) |
| $p_{-4}$ | $p_{+4} / \left[\left(\frac{{}^{63}R}{{}^{63}R^*}\right)^{eq}_{HCO_3^-} \cdot \frac{K_1}{K_w} \cdot {}^{13}\alpha^{eq}_{HCO_3^--CO_2} \cdot {}^{18}\alpha^{eq}_{HCO_3^--OH^-}\right]$ | - |
| $s_{-4}$ | $s_{+4} \cdot \left[\left(\frac{{}^{47}R}{{}^{47}R^*}\right)^{eq}_{CO_2} / \left(\frac{{}^{63}R}{{}^{63}R^*}\right)^{eq}_{HCO_3^-} \cdot \frac{K_1}{K_w} \cdot {}^{13}\alpha^{eq}_{HCO_3^--CO_2} \cdot {}^{18}\alpha^{eq}_{HCO_3^--CO_2}\right]$ | - |
| ***Δ*₄₈ parameters** |  |  |
| $\left(\frac{{}^{64}R}{{}^{64}R^*}\right)^{eq}_{CO_2}$ | $(\Delta^{eq}_{48,CO_2}/1000)\ +1$ | Hill et al. (2020) |
| $\left(\frac{{}^{64}R}{{}^{64}R^*}\right)^{eq}_{HCO_3^-}$ | $(\Delta^{eq}_{64,HCO_3^-}/1000)\ +1$ | Hill et al. (2020) |
| $\left(\frac{{}^{64}R}{{}^{64}R^*}\right)^{eq}_{CO_3^{2-}}$ | $(\Delta^{eq}_{64,CO_3^{2-}}/1000)\ +1$ | Hill et al. (2020) |
| ${}^{64}\alpha^{eq}_{CO_3^{2-}-HCO_3}$ | $\left(\frac{{}^{64}R}{{}^{64}R^*}\right)^{eq}_{CO_3^{2-}} / \left(\frac{{}^{64}R}{{}^{64}R^*}\right)^{eq}_{HCO_3^-}$ | - |
| ${}^{64}K_2$ | ${}^{64}\alpha^{KFF}_{CO_3^{2-}-HCO_3^-} \cdot {}^{18}\alpha^{eq}_{CO_3^{2-}-HCO_3^-} {}^{18}\alpha^{eq}_{CO_3^{2-}-HCO_3^-} \cdot K_2$ | - |
| ${}^{64}\chi$ | $\frac{1}{1+\frac{{}^{64}K_2 \cdot {}^{64}\alpha^{eq}_{CO_3{}_-HCO_3^-}}{[H^+]}}$ | - |
| ${}^{18-18}KIE_{p'_{+1}}$ | 1+0.049/1000 | Guo (2020) |
| ${}^{18-18}KIE_{s'_{+1}}$ | 1-0.146/1000 | Guo (2020) |
| ${}^{18-18}KIE_{p'_{+4}}$ | 1-0.144/1000 | Guo (2020) |
| ${}^{18-18}KIE_{s'_{+4}}$ | 1-0.086/1000 | Guo (2020) |
| $p'_{+1}$ | $\frac{a_{+1} \cdot b_{+1}}{{}^{48}KIE_{p'_1} \cdot k_{+1}}$ | - |
| $s'_{+1}$ | $\frac{b_{+1} \cdot b_{+1}}{{}^{48}KIE_{s'_1} \cdot k_{+1}}$ | - |
| $p'_{-1}$ |  | - |
| $s'_{-1}$ |  | - |

| | | |
|---|---|---|
| $p'_{+4}$ | $\frac{a_{+4} \cdot b_{+4}}{^{48}KIE_{p'_4} \cdot k_{+4}}$ | - |
| $s'_{+4}$ | $\frac{b_{+4} \cdot b_{+4}}{^{48}KIE_{s'_4} \cdot k_{+4}}$ | - |
| $p'_{-4}$ | $p'_{+4} \,/ \left[ \left( \frac{^{64}R}{^{64}R^*} \right)^{eq}_{HCO_3^-} \cdot \frac{K_1}{K_w} \cdot {}^{18}\alpha^{eq}_{HCO_3^- - CO_2} \cdot {}^{18}\alpha^{eq}_{HCO_3^- - OH^-} \right]$ | - |
| $s'_{-4}$ | $s'_{+4} \cdot \left[ \left( \frac{^{48}R}{^{48}R^*} \right)^{eq}_{CO_2} \Big/ \left( \frac{^{64}R}{^{64}R^*} \right)^{eq}_{HCO_3^-} \cdot \frac{K_1}{K_w} \cdot {}^{18}\alpha^{eq}_{HCO_3^- - CO_2} \cdot {}^{18}\alpha^{eq}_{HCO_3^- - CO_2} \right]$ | - |

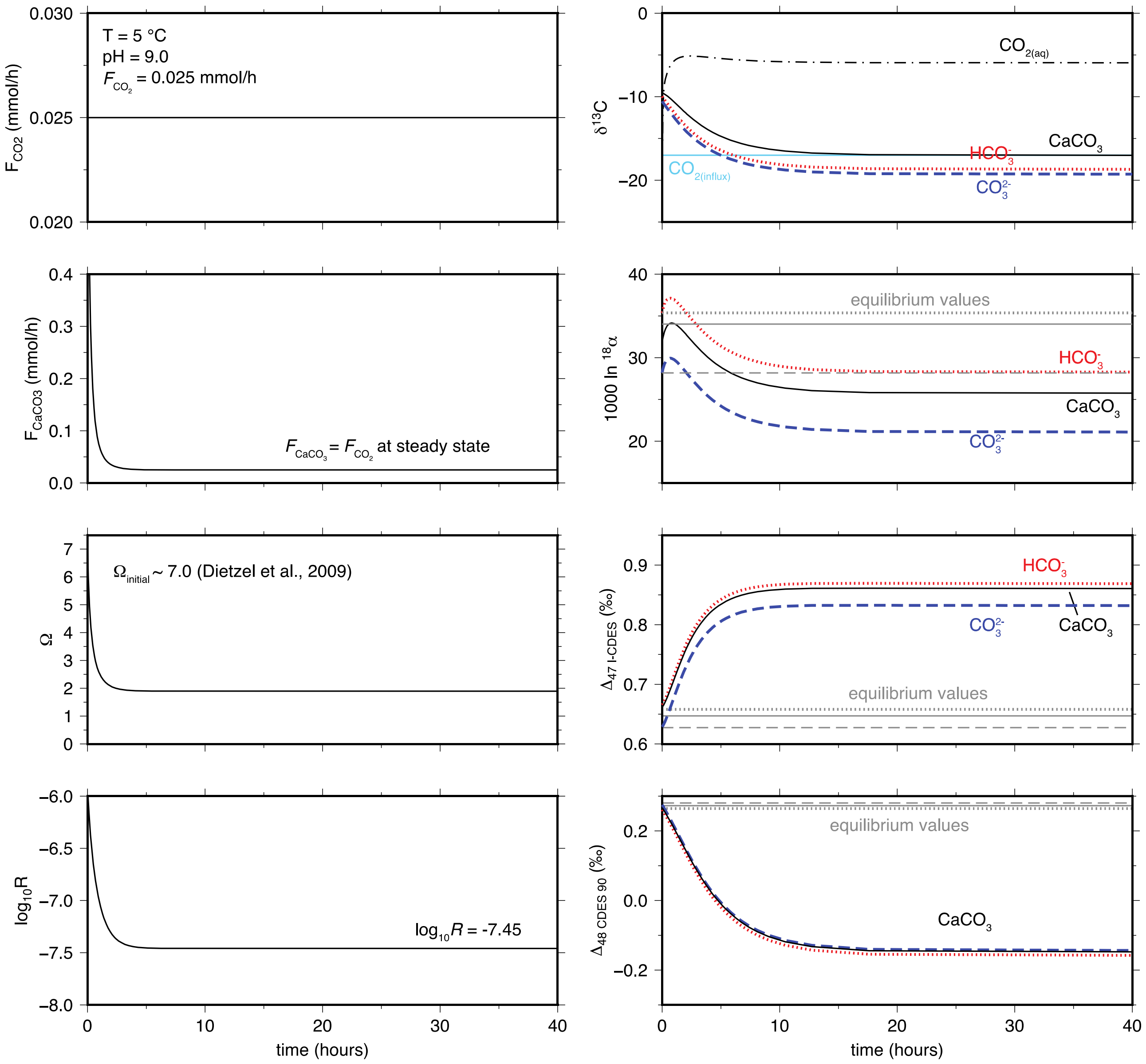

**Figure A2.** Example showing the time evolution to steady-state for bulk and clumped isotopes. The time to reach steady state depends on $F_{CO2}$, with lower $F_{CO2}$ taking longer to reach steady state.

## References

Adkins, J.F., Boyle, E.A., Curry, W.B. and Lutringer, A., 2003. Stable isotopes in deep-sea corals and a new mechanism for “vital effects”. *Geochimica et Cosmochimica Acta*, *67*(6), pp.1129-1143. https://doi.org/10.1016/S0016-7037(02)01203-6

Affek, H.P., Bar-Matthews, M., Ayalon, A., Matthews, A., Eiler, J.M., 2008. Glacial/interglacial temperature variations in Soreq cave speleothems as recorded by ‘clumped isotope’ thermometry. *Geochimica et Cosmochimica Acta 72*, 5351–5360. https://doi.org/10.1016/j.gca.2008.06.031

Al-Horani, F.A., Al-Moghrabi, S.M., de Beer, D., 2003. Microsensor study of photosynthesis and calcification in the scleractinian coral, Galaxea fascicularis: active internal carbon cycle. *Journal of Experimental Marine Biology and Ecology 288*, 1–15. https://doi.org/10.1016/S0022-0981(02)00578-6

Anagnostou, E., K-F. Huang, C-F. You, E. L. Sikes, and R. M. Sherrell. "Evaluation of boron isotope ratio as a pH proxy in the deep sea coral *Desmophyllum dianthus*: Evidence of physiological pH adjustment." *Earth and Planetary Science Letters 349* (2012): 251-260. https://doi.org/10.1016/j.epsl.2012.07.006

Bajnai, D., Guo, W., Spötl, C., Coplen, T.B., Methner, K., Löffler, N., Krsnik, E., Gischler, E., Hansen, M., Henkel, D. and Price, G.D., 2020. Dual clumped isotope thermometry resolves kinetic biases in carbonate formation temperatures. *Nature communications*, *11*(1), pp.1-9. https://doi.org/10.1038/s41467-020-17501-0

Beck, W.C., Grossman, E.L., Morse, J.W., 2005. Experimental studies of oxygen isotope fractionation in the carbonic acid system at 15°, 25°, and 40°C.

*Geochimica et Cosmochimica Acta 69,* 3493–3503. https://doi.org/10.1016/j.gca.2005.02.003

Berg, J., Tymoczko, J., Stryer, L., 2002. Biochemistry, 5th ed. W H Freeman, New York.

Bernasconi, S.M., Daëron, M., Bergmann, K.D., Bonifacie, M., Meckler, A.N., Affek, H.P., Anderson, N., Bajnai, D., Barkan, E., Beverly, E. and Blamart, D., 2021. InterCarb: A community effort to improve interlaboratory standardization of the carbonate clumped isotope thermometer using carbonate standards. *Geochemistry, Geophysics, Geosystems, 22*(5), p.e2020GC009588. https://doi.org/10.1029/2020GC009588

Bernasconi, S.M., Müller, I.A., Bergmann, K.D., Breitenbach, S.F., Fernandez, A., Hodell, D.A., Jaggi, M., Meckler, A.N., Millan, I. and Ziegler, M., 2018. Reducing uncertainties in carbonate clumped isotope analysis through consistent carbonate-based standardization. *Geochemistry, Geophysics, Geosystems, 19*(9), pp.2895-2914. https://doi.org/10.1029/2017GC007385

Bertucci, A., Innocenti, A., Scozzafava, A., Tambutté, S., Zoccola, D., Supuran, C.T., 2011. Carbonic anhydrase inhibitors. Inhibition studies with anions and sulfonamides of a new cytosolic enzyme from the scleractinian coral Stylophora pistillata. *Bioorganic & Medicinal Chemistry Letters 21*, 710–714. https://doi.org/10.1016/j.bmcl.2010.11.124

Boettger, J.D., Kubicki, J.D., 2021. Equilibrium and kinetic isotopic fractionation in the CO2 hydration and hydroxylation reactions: Analysis of the role of hydrogen-bonding via quantum mechanical calculations. *Geochimica et Cosmochimica Acta 292*, 37–63. https://doi.org/10.1016/j.gca.2020.09.019

Brand, W.A., Assonov, S.S., Coplen, T.B., 2010. Correction for the 17O interference in δ(13C) measurements when analyzing CO2 with stable isotope mass spectrometry (IUPAC Technical Report). *Pure and Applied Chemistry 82*, 1719–1733. https://doi.org/10.1351/PAC-REP-09-01-05

Christensen, J.N., Watkins, J.M., Devriendt, L.S., DePaolo, D.J., Conrad, M.E., Voltolini, M., Yang, W., Dong, W., 2021. Isotopic fractionation accompanying CO2 hydroxylation and carbonate precipitation from high pH waters at The Cedars, California, USA. *Geochimica et Cosmochimica Acta 301*, 91–115. https://doi.org/10.1016/j.gca.2021.01.003

Coplen, T.B., 2007. Calibration of the calcite–water oxygen-isotope geothermometer at Devils Hole, Nevada, a natural laboratory. *Geochimica et Cosmochimica Acta 71*, 3948–3957. https://doi.org/10.1016/j.gca.2007.05.028

Daëron, M., Blamart, D., Peral, M., Affek, H.P., 2016. Absolute isotopic abundance ratios and the accuracy of Δ47 measurements. Chemical Geology 442, 83–96. https://doi.org/10.1016/j.chemgeo.2016.08.014

Daëron, M., Drysdale, R.N., Peral, M., Huyghe, D., Blamart, D., Coplen, T.B., Lartaud, F. and Zanchetta, G., 2019. Most Earth-surface calcites precipitate out of isotopic equilibrium. *Nature communications*, *10*(1), pp.1-7. https://doi.org/10.1038/s41467-019-08336-5

Daëron, M., Guo, W., Eiler, J., Genty, D., Blamart, D., Boch, R., Drysdale, R., Maire, R., Wainer, K., Zanchetta, G., 2011. 13C18O clumping in speleothems: Observations from natural caves and precipitation experiments. *Geochimica et Cosmochimica Acta 75*, 3303–3317. https://doi.org/10.1016/j.gca.2010.10.032

de Goeyse, S., Webb, A.E., Reichart, G.-J., de Nooijer, L.J., 2021. Carbonic anhydrase is involved in calcification by the benthic foraminifer *Amphistegina lessonii*; *Biogeosciences 18*, 393–401. https://doi.org/10.5194/bg-18-393-2021

Defliese, W.F., Lohmann, K.C., 2015. Non-linear mixing effects on mass-47 CO $_2$ clumped isotope thermometry: Patterns and implications: Non-linear mixing effects on mass-47 clumped isotopes. Rapid Commun. Mass Spectrom. 29, 901–909. https://doi.org/10.1002/rcm.7175

Dennis, K.J., Affek, H.P., Passey, B.H., Schrag, D.P., Eiler, J.M., 2011. Defining an absolute reference frame for 'clumped' isotope studies of CO2. *Geochimica et Cosmochimica Acta 75*, 7117–7131. https://doi.org/10.1016/j.gca.2011.09.025

Dietzel, M., Gussone, N., Eisenhauer, A., 2004. Co-precipitation of Sr2+ and Ba2+ with aragonite by membrane diffusion of CO2 between 10 and 50 °C. *Chemical Geology 203*, 139–151. https://doi.org/10.1016/j.chemgeo.2003.09.008

Dietzel, M., Tang, J., Leis, A., & Köhler, S. J., 2009. Oxygen isotopic fractionation during inorganic calcite precipitation—Effects of temperature, precipitation rate and pH. *Chemical Geology 268*, 107-115. https://doi.org/10.1016/j.chemgeo.2009.07.015

Eiler, J.M., Schauble, E., 2004. 18O13C16O in Earth's atmosphere. *Geochimica et Cosmochimica Acta 68*, 4767–4777. https://doi.org/10.1016/j.gca.2004.05.035

Fiebig, J., Bajnai, D., Löffler, N., Methner, K., Krsnik, E., Mulch, A., Hofmann, S., 2019. Combined high-precision ∆48 and ∆47 analysis of carbonates. *Chemical Geology 522*, 186–191. https://doi.org/10.1016/j.chemgeo.2019.05.019

Fiebig, J., Daëron, M., Bernecker, M., Guo, W., Schneider, G., Boch, R., Bernasconi, S.M., Jautzy, J., Dietzel, M., 2021. Calibration of the dual clumped isotope thermometer for carbonates. *Geochimica et Cosmochimica Acta S0016703721004208*. https://doi.org/10.1016/j.gca.2021.07.012

Ghosh, P., Adkins, J., Affek, H., Balta, B., Guo, W., Schauble, E.A., Schrag, D., Eiler, J.M., 2006. 13C–18O bonds in carbonate minerals: A new kind of paleothermometer. *Geochimica et Cosmochimica Acta 70*, 1439–1456. https://doi.org/10.1016/j.gca.2005.11.014

Gonfiantini, R., Stichler, W., Rozanski, K., 1995. Standards and intercomparison materials distributed by the International Atomic Energy Agency for stable isotope measurements (No. IAEA-TECDOC--825).

Guo, W., Mosenfelder, J.L., Goddard, W.A., Eiler, J.M., 2009. Isotopic fractionations associated with phosphoric acid digestion of carbonate minerals: Insights from first-principles theoretical modeling and clumped isotope measurements. *Geochimica et Cosmochimica Acta 73*, 7203–7225. https://doi.org/10.1016/j.gca.2009.05.071

Guo, W., 2020. Kinetic clumped isotope fractionation in the DIC-H2O-CO2 system: patterns, controls, and implications. *Geochimica et Cosmochimica Acta*, *268*, pp.230-257. https://doi.org/10.1016/j.gca.2019.07.055

Hill, P.S., Schauble, E.A., Tripati, A., 2014. Theoretical constraints on the effects of pH, salinity, and temperature on clumped isotope signatures of dissolved inorganic carbon species and precipitating carbonate minerals. Geochimica et Cosmochimica Acta 125, 610–652. https://doi.org/10.1016/j.gca.2013.06.018 Hill, P.S., Schauble, E.A. and Tripati, A., 2020. Theoretical constraints on the effects of added cations on clumped, oxygen, and carbon isotope signatures of dissolved inorganic carbon species and minerals. Geochimica et Cosmochimica Acta, 269, pp.496-539. https://doi.org/10.1016/j.gca.2019.10.016

Johnson, K.S., 1982. Carbon dioxide hydration and dehydration kinetics in seawater1: CO $_2$ reaction kinetics. Limnol. Oceanogr. 27, 849–855. https://doi.org/10.4319/lo.1982.27.5.0849

Jones, J.P., Carricart-Ganivet, J.P., Prieto, R.I., Enríquez, S., Ackerson, M. and Gabitov, R.I., 2015. Microstructural variation in oxygen isotopes and elemental calcium ratios in the coral skeleton of Orbicella annularis. *Chemical Geology*, 419, pp.192-199. https://doi.org/10.1016/j.chemgeo.2015.10.044

Kernohan, J.C., 1964. The activity of bovine carbonic anhydrase in imidazole buffers. *Biochimica et Biophysica Acta (BBA) - Specialized Section on Enzymological Subjects 81*, 346–356. https://doi.org/10.1016/0926-6569(64)90050-1

Kimball, J., Eagle, R., Dunbar, R., 2016. Carbonate “clumped” isotope signatures in aragonitic scleractinian and calcitic gorgonian deep-sea corals. *Biogeosciences 13*, 6487–6505. https://doi.org/10.5194/bg-13-6487-2016

Knoche, W., 1980. Chemical Reactions of CO2 in Water, in: Bauer, C., Gros, G., Bartels, H. (Eds.), Biophysics and Physiology of Carbon Dioxide, *Proceedings in Life Sciences*. Springer Berlin Heidelberg, Berlin, Heidelberg, pp. 3–11. https://doi.org/10.1007/978-3-642-67572-0_1

Lindskog, S., 1997. Structure and mechanism of carbonic anhydrase. *Pharmacology & Therapeutics 74*, 1–20. https://doi.org/10.1016/S0163-7258(96)00198-2

Lucarelli, J., Carroll, H., Elliott, B., Eagle, R., Tripati, A., 2021. Equilibrated gas and carbonate standard-derived paired clumped isotope (Δ47 and Δ48) values on the absolute reference frame (preprint). Physical Sciences and Mathematics. https://doi.org/10.31223/X5T318

McConnaughey, T., 1989. 13C and 18O isotopic disequilibrium in biological carbonates: II. In vitro simulation of kinetic isotope effects. *Geochimica et Cosmochimica Acta 53*, 163–171. https://doi.org/10.1016/0016-7037(89)90283-4

Miller, R.F., Berkshire, D.C., Kelley, J.J. and Hood, D.W., 1971. Method for determination of reaction rates of carbon dioxide with water and hydroxyl ion in seawater. *Environmental Science & Technology*, *5*(2), pp.127-133. https://doi.org/10.1021/es60049a006

Miyamoto, H., Miyashita, T., Okushima, M., Nakano, S., Morita, T., Matsushiro, A., 1996. A carbonic anhydrase from the nacreous layer in oyster pearls. *Proceedings of the National Academy of Sciences 93*, 9657–9660. https://doi.org/10.1073/pnas.93.18.9657

Moya, A., Tambutté, S., Bertucci, A., Tambutté, E., Lotto, S., Vullo, D., Supuran, C.T., Allemand, D., Zoccola, D., 2008. Carbonic Anhydrase in the Scleractinian Coral Stylophora pistillata. *Journal of Biological Chemistry 283*, 25475–25484. https://doi.org/10.1074/jbc.M804726200

Nimer, N.A., Guan, Q., Merrett, M.J., 1994. Extra- and intra-cellular carbonic anhydrase in relation to culture age in a high-calcifying strain of Emiliania huxleyi Lohmann. *New Phytologist 126*, 601–607. https://doi.org/10.1111/j.1469-8137.1994.tb02954.x

Passey, B.H., Henkes, G.A., 2012. Carbonate clumped isotope bond reordering and geospeedometry. *Earth and Planetary Science Letters 351–352*, 223–236. https://doi.org/10.1016/j.epsl.2012.07.021

Rost, B., Riebesell, U., Burkhardt, S. and Sültemeyer, D., 2003. Carbon acquisition of bloom-forming marine phytoplankton. *Limnology and oceanography*, *48*(1), pp.55-67. https://doi.org/10.4319/lo.2003.48.1.0055

Saenger, C., Affek, H.P., Felis, T., Thiagarajan, N., Lough, J.M., Holcomb, M., 2012. Carbonate clumped isotope variability in shallow water corals: Temperature dependence and growth-related vital effects. *Geochimica et Cosmochimica Acta 99*, 224–242. https://doi.org/10.1016/j.gca.2012.09.035

Schauble, E.A., Ghosh, P., Eiler, J.M., 2006. Preferential formation of 13C–18O bonds in carbonate minerals, estimated using first-principles lattice dynamics. *Geochimica et Cosmochimica Acta 70*, 2510–2529. https://doi.org/10.1016/j.gca.2006.02.011

Spooner, Peter T., Weifu Guo, Laura F. Robinson, Nivedita Thiagarajan, Katharine R. Hendry, Brad E. Rosenheim, and Melanie J. Leng. "Clumped isotope composition of cold-water corals: A role for vital effects?." *Geochimica et Cosmochimica Acta 179* (2016): 123-141. https://doi.org/10.1016/j.gca.2016.01.023

Staudigel, P.T. and Swart, P.K., 2018. A kinetic difference between 12C-and 13C-bound oxygen exchange rates results in decoupled δ18O and Δ47 values of equilibrating DIC solutions. *Geochemistry, Geophysics, Geosystems, 19*(8), pp.2371-2383. https://doi.org/10.1029/2018GC007500

Swart, Peter K., Chaojin Lu, Evan W. Moore, Megan E. Smith, Sean T. Murray, and Philip T. Staudigel. "A calibration equation between Δ48 values of carbonate and temperature." *Rapid Communications in Mass Spectrometry 35*, no. 17 (2021): e9147. https://doi.org/10.1002/rcm.9147

Tang, J., Dietzel, M., Böhm, F., Köhler, S.J. and Eisenhauer, A., 2008. Sr2+/Ca2+ and 44Ca/40Ca fractionation during inorganic calcite formation: II. Ca isotopes. *Geochimica et Cosmochimica Acta, 72(15),* pp.3733-3745. https://doi.org/10.1016/j.gca.2008.05.033

Tang, J., Dietzel, M., Fernandez, A., Tripati, A.K., Rosenheim, B.E., 2014. Evaluation of kinetic effects on clumped isotope fractionation (Δ47) during inorganic calcite precipitation. *Geochimica et Cosmochimica Acta 134*, 120–136. https://doi.org/10.1016/j.gca.2014.03.005

Thiagarajan, N., Adkins, J., Eiler, J., 2011. Carbonate clumped isotope thermometry of deep-sea corals and implications for vital effects. *Geochimica et Cosmochimica Acta 75*, 4416–4425. https://doi.org/10.1016/j.gca.2011.05.004

Tripati, A.K., Hill, P.S., Eagle, R.A., Mosenfelder, J.L., Tang, J., Schauble, E.A., Eiler, J.M., Zeebe, R.E., Uchikawa, J., Coplen, T.B., Ries, J.B., Henry, D., 2015.

Beyond temperature: Clumped isotope signatures in dissolved inorganic carbon species and the influence of solution chemistry on carbonate mineral composition. *Geochimica et Cosmochimica Acta 166*, 344–371. https://doi.org/10.1016/j.gca.2015.06.021

Trotter, J., Montagna, P., McCulloch, M., Silenzi, S., Reynaud, S., Mortimer, G., Martin, S., Ferrier-Pagès, C., Gattuso, J.-P., Rodolfo-Metalpa, R., 2011. Quantifying the pH ‘vital effect’ in the temperate zooxanthellate coral Cladocora caespitosa: Validation of the boron seawater pH proxy. *Earth and Planetary Science Letters 303*, 163–173. https://doi.org/10.1016/j.epsl.2011.01.030

Uchikawa, J., Zeebe, R.E., 2012. The effect of carbonic anhydrase on the kinetics and equilibrium of the oxygen isotope exchange in the CO2–H2O system: Implications for δ18O vital effects in biogenic carbonates. *Geochimica et Cosmochimica Acta 95*, 15–34. https://doi.org/10.1016/j.gca.2012.07.022

Uchikawa, J., Chen, S., Eiler, J.M., Adkins, J.F. and Zeebe, R.E., 2021. Trajectory and timescale of oxygen and clumped isotope equilibration in the dissolved carbonate system under normal and enzymatically-catalyzed conditions at 25° C. *Geochimica et Cosmochimica Acta*, *314*, pp.313-333. https://doi.org/10.1016/j.gca.2021.08.014

Upadhyay, D., Lucarelli, J., Arnold, A., Flores, R., Bricker, H., Ulrich, R.N., Jesmok, G., Santi, L., Defliese, W., Eagle, R.A. and Carroll, H.M., 2021. Carbonate clumped isotope analysis (Δ47) of 21 carbonate standards determined via gas-source isotope-ratio mass spectrometry on four instrumental configurations using carbonate-based standardization and multiyear data sets. *Rapid Communications in Mass Spectrometry*, *35*(17), p.e9143.https://doi.org/10.1002/rcm.9143

Usdowski, E., Michaelis, J., Boettcher, M., Hoefs, J., 1991. Factors for the oxygen isotope equilibrium fractionation between aqueous and gaseous CO2, carbonic acid, bicarbonate, carbonate, and water (19°C). *Zeitschrift fur physikalische chemie-international journal of research in physical chemistry & Chemical Physics 237–249*.

Wang, Z., Schauble, E.A., Eiler, J.M., 2004. Equilibrium thermodynamics of multiply substituted isotopologues of molecular gases. *Geochimica et Cosmochimica Acta 68*, 4779–4797. https://doi.org/10.1016/j.gca.2004.05.039

Watkins, J.M., Hunt, J.D., Ryerson, F.J., DePaolo, D.J., 2014. The influence of temperature, pH, and growth rate on the δ18O composition of inorganically precipitated calcite. *Earth and Planetary Science Letters 404*, 332–343. https://doi.org/10.1016/j.epsl.2014.07.036

Watkins, J.M. and Hunt, J.D., 2015. A process-based model for non-equilibrium clumped isotope effects in carbonates. *Earth and Planetary Science Letters*, *432*, pp.152-165. https://doi.org/10.1016/j.epsl.2015.09.042

Weise, A. and Kluge, T., 2020. Isotope exchange rates in dissolved inorganic carbon between 40° C and 90° C. *Geochimica et Cosmochimica Acta*, *268*, pp.56-72. https://doi.org/10.1016/j.gca.2019.09.032

Winograd, I.J., Coplen, T.B., Landwehr, J.M., Riggs, A.C., Ludwig, K.R., Szabo, B.J., Kolesar, P.T., Revesz, K.M., 1992. Continuous 500,000-Year Climate Record from Vein Calcite in Devils Hole, Nevada. *Science 258*, 255–260. https://doi.org/10.1126/science.258.5080.255

Winograd, I.J., Coplen, T.B., Szabo, B.J., Riggs, A.C., 1988. A 250,000-Year Climatic Record from Great Basin Vein Calcite: Implications for Milankovitch Theory. *Science 242*, 1275–1280. https://doi.org/10.1126/science.242.4883.1275

Wolthers, M., Nehrke, G., Gustafsson, J.P. and Van Cappellen, P., 2012. Calcite growth kinetics: Modeling the effect of solution stoichiometry. *Geochimica et Cosmochimica Acta*, *77*, pp.121-134. https://doi.org/10.1016/j.gca.2011.11.003

Yu, Z., Xie, L., Lee, S., Zhang, R., 2006. A novel carbonic anhydrase from the mantle of the pearl oyster (Pinctada fucata). *Comparative Biochemistry and Physiology Part B: Biochemistry and Molecular Biology 143*, 190–194. https://doi.org/10.1016/j.cbpb.2005.11.006

Zeebe, R.E., Wolf-Gladrow, D.A., 2001. $CO_2$ in seawater: equilibrium, kinetics, isotopes, *Elsevier oceanography series*. Elsevier, Amsterdam; New York.

Zeebe, R.E., 2020. Oxygen isotope fractionation between water and the aqueous hydroxide ion. *Geochimica et Cosmochimica Acta*, *289*, pp.182-195. https://doi.org/10.1016/j.gca.2020.08.025

Zeebe, R.E., 2014. Kinetic fractionation of carbon and oxygen isotopes during hydration of carbon dioxide. *Geochimica et Cosmochimica Acta*, *139*, pp.540-552. https://doi.org/10.1016/j.gca.2014.05.005

# CHAPTER 3

# Dual clumped isotope data for amorphous carbonates and transformation products reveal novel mechanisms for nonequilibrium effects

Jamie K. Lucarelli[1,*], Bettina Purgstaller[2,*], Robert N. Ulrich[1], Zeeshan Parvez[1], Albrecht Leis[2], Katja E. Goetschl[2], Robert A. Eagle[1], Aradhna Tripati[1]

[1]Department of Earth, Planetary, and Space Sciences, Institute of the Environment and Sustainability, Department of Atmospheric and Oceanic Sciences, Center for Diverse Leadership in Science, University of California - Los Angeles, USA
[2]Graz University of Technology, Institute of Applied Geosciences, Graz, Austria

*JL and BP contributed equally to this work and are listed based on alphabetical ordering.
+ MD and AT are joint senior authors.
Correspondence to: Jamie Lucarelli at jklucarelli@gmail.com, Martin Dietzel at martin.dietzel@tugraz.at, or Aradhna Tripati at atripati@g.ucla.edu

## ABSTRACT

Transient amorphous precursors to minerals have been observed in a range of laboratory materials and in nature including across diverse phyla. These metastable phases can allow for the incorporation of cations at higher concentrations than classical crystallization pathways. Thus their chemistry and behavior have implications in an array of disciplines across the geosciences and chemical, health, and material sciences. However, there are major knowledge gaps in characterization of the isotopic composition of the anion in amorphous carbonates and behavior during transformation. Here, we examined the evolution of the isotopic composition of amorphous carbonates and transformation products to constrain reaction mechanisms and potential origins of non-equilibrium isotopic compositions in carbonate minerals. We measured dual clumped isotopes ($^{13}C^{18}O^{16}O$ - $\Delta_{47}$; $^{12}C^{18}O^{18}O$ - $\Delta_{48}$), bulk stable isotope ratios ($\delta^{13}C$, $\delta^{18}O$), and chemical and structural data before, during, and after the transformation of an amorphous calcium magnesium carbonate (ACMC) precursor into high Mg-calcite (HMC) over 1 year, with crystallization occurring in solutions at different temperatures (10 to 60 °C). ACMC synthesized from an unequilibrated dissolved inorganic carbon (DIC) pool at 10 °C had lower $\Delta_{47}$ and higher $\Delta_{48}$ than equilibrium HMC. At all temperatures, $\Delta_{47}$, $\Delta_{48}$, and $\delta^{18}O$ evolved considerably during transformation of ACMC to HMC. $\Delta_{47}$ and $\Delta_{48}$ values achieved a non-equilibrium steady-state, while $\delta^{18}O$ continued to evolve after crystallization. Observations and modeling simulations were consistent with the dissolution of ACMC altering the chemistry of the solution and driving disequilibrium in the DIC pool, which was then recorded during subsequent crystallization of HMC. Clumped isotope results may also reflect mixing effects due to ACMC progressively dissolving and reprecipitating over time while the DIC pool has an evolving isotopic composition. These results have implications for applied studies as they demonstrate new mechanisms where nonequilibrium isotope effects could be produced in minerals formed from amorphous precursors, but with expression of the effects dependent on the conditions during transformation.

## SIGNIFICANCE

Transient amorphous carbonates and their crystalline products are of broad interest including in biomineralization, ocean acidification, carbon sequestration, paleoclimate, ecology, environmental science, Earth history, material science, physical chemistry, and medicine. However, the characterization of isotopic signatures in amorphous precursors and their evolution during transformation to crystalline carbonates is poorly understood. Here we report state-of-the-art measurements constraining the evolution of dual clumped isotopes in amorphous carbonates and transformation products. Data reveal the amorphous precursor has isotopic compositions distinct from products. A major factor affecting the isotopic signatures of the crystal is disequilibrium in the dissolved inorganic carbon pool during transformation from dissolution of the amorphous precursor. Dual clumped isotope measurements have the potential to provide a window into reaction pathways and isotope effects in metastable carbonates and products.

## INTRODUCTION

Many calcitic and aragonitic minerals begin as an amorphous, metastable precursor (Addadi et al., 2003; De Yoreo et al., 2015; Weiss et al., 2002). For example, amorphous calcium carbonate (ACC) has been observed in caves (Demény et al., 2016), and high-Mg amorphous carbonate precursor phases span phyla and have been observed in taxa as wide-ranging as coralline alga (Raz et al., 2000), sea urchin (Politi et al., 2004), corals (Mass et al., 2017), mollusks (Weiss et al., 2002), and foraminifera (Jacob et al., 2017). The ubiquity of amorphous carbonates and use of transformation products in a breadth of disciplines, including the application of isotope geochemistry of carbonate minerals to study ocean acidification, ecological and environmental change, paleoclimate, and material science, highlight the importance of understanding these precursors.

In the laboratory, amorphous precursors allow the synthesis of carbonate minerals of compositions impossible to reach via classical crystal growth, such as high-Mg carbonate minerals found in biominerals (e.g., Wang et al., 2012). In nature, most amorphous carbonates form in the presence of Mg ions, resulting in the formation of amorphous calcium magnesium carbonate (ACMC) (Albéric et al., 2018; Purgstaller et al., 2019). ACMC precursors result in increased Mg ion incorporation into the calcite crystal lattice (Loste et al., 2003; Purgstaller et al., 2016, 2019, 2021). To date, the inorganic precipitation of high-Mg calcite (HMC; defined as calcite with > 4 mol% Mg) with >20 mol% Mg from classical crystallization pathways at ambient conditions has not been successful, as high Mg/Ca ratios in solution favor aragonite (Berner, 1975; Fernandez-Diaz et al., 1996; Goetschl et al., 2019). Additionally, aqueous $Mg^{2+}$ inhibits the formation of calcite due to the strong affinity of $Mg^{2+}$ for the aqueous solvent, which is evidenced by its high hydration Gibbs free energy (Markham et al., 1996) and slow exchange of water molecules in its hydration sphere (Bleuzen et al., 1997; Schott et al., 2009; Aufort et al., 2022), resulting in a rate-limiting step of dehydrating $Mg^{2+}$ at the lattice growth site and thus inhibiting calcite growth (Purgstaller et al., 2021).

Experimental syntheses have demonstrated that the mechanism of transformation undergone by amorphous carbonates is dependent on ambient conditions, primarily water content (Konrad et al., 2016). The stability of amorphous carbonates as a phase is dependent on both the composition of the particle itself, such as Mg content, as well as the availability of water (Konrad et al., 2016; Koishi et al., 2018; Purgstaller et al., 2019). Further, there is evidence that amorphous carbonate transformation through dissolution-reprecipitation does not purely record the chemistry of the surrounding solution at the time of transformation (Guiffre et al., 2015; Purgstaller et al., 2021). Instead, the dissolution of an amorphous carbonate particle alters the composition of the solution immediately surrounding the particle, resulting in chemical and isotopic values of the transformation product that reflect both the amorphous carbonate and solution (Guiffre et al., 2015).

The few studies reporting isotopic ratio determinations on cations ($Ca^{2+}$, $Mg^{2+}$) in amorphous carbonates and transformation products show the potential for utilizing isotopic signatures to elucidate the processes involved in transformation. Isotope tracer studies using $^{43}Ca/^{40}Ca$ and $^{25}Mg/^{24}Mg$ in both amorphous phases and the resultant minerals show that the cation signals recorded in amorphous carbonates contrast those in the final carbonate minerals (Guiffre et al., 2015). Mg isotopic compositions of amorphous carbonates are also distinct from classically precipitated carbonates (Mavromatis et al., 2017). ACC modestly fractionates (-1.0 ‰) $^{26}Mg$ relative to the reactant solution, but this fractionation is hypothesized to be further augmented during transformation via dissolution-reprecipitation (-3.0 to -3.6 ‰), and significantly alters the [Mg] of the reactant solution (Mavromatis et al., 2017; Purgstaller et al., 2021). In contrast, classical calcite mineral precipitation via ion-by-ion growth does not alter the [Mg] of the reactant solution, and the extent of Mg isotope fractionation is significantly lower (Mavromatis et al., 2017). It has also been argued that the recorded Ca and Mg isotope signals in calcite reflect mixing of the dissolved ACC and the surrounding solution isotopic compositions (Guiffre et al., 2015).

Little is known about the isotopic composition of the anion in amorphous precursors and transformation products. The use of isotopic signatures of the anion in carbonate minerals for paleoenvironmental reconstructions assumes that biogenic and inorganic carbonates form in quasi-equilibrium and record the isotopic signatures of the environment at the time of formation. The origin of disequilibrium isotope values are not well understood but some work has shown the potential for the use of dual clumped isotopes to study processes influencing dissolved inorganic carbon transformation in carbonate minerals (Tripati et al., 2015; Guo, 2020; Bajnai et al., 2020). Previous studies have found disequilibrium clumped isotope values in biogenic carbonate from organisms that have been shown to produce ACC or ACMC, including warm and cold-water corals (Saenger et al., 2012; Atasoy, 2015; Spooner et al., 2016; Kimball et al., 2016), cephalopods (Dennis et al., 2013), mollusks (Eagle et al., 2013; Henkes et al., 2013) and brachiopods (Bajnai et al., 2018). It has also been shown that Mg incorporation in calcite can significantly affect the degree of oxygen isotope fractionation between the mineral and solution, with $^{18}O$ concentrating in Mg-calcite relative to pure calcite precipitated under the same conditions by 0.06 ‰ for each mol-percent of Mg in calcite (Tarutani et al., 1969; Mavromatis et al., 2012). To date, the sole work we are aware of is from Dietzel et al. (2020) that examined the oxygen ($\delta^{18}O$) and clumped isotope ($\Delta_{47}$) composition of transformation products of ACMC to HMC at 25 $^{o}$C and pH 8.3. ACMC was transformed to HMC at the same temperature it formed, and then analyzed. There was an increase of ~2 ‰ for $\delta^{18}O$ while $\Delta_{47}$ was invariant through the experiment.

Here, we examined the isotopic compositions of synthesized ACMC and transformation products using the dual clumped isotope approach ($\Delta_{47}$ and $\Delta_{48}$) and traditional oxygen and carbon isotopes ($\delta^{18}O$, $\delta^{13}C$) to obtain a complete set of anion isotopic data. We characterized the composition of ACMC and then studied its isotopic evolution at multiple timesteps during the transformation of ACMC to HMC at four different temperatures. We also used modeling to explore the effects of the dissolution of ACMC during transformation on the isotopic composition of the surrounding solution. The results suggest new mechanisms for the nonequilibrium isotope values observed in carbonate minerals derived from amorphous precursors.

## RESULTS AND DISCUSSION

To assess the evolution of oxygen, carbon, and clumped isotope signatures during the transformation of ACMC to fully crystallized HMC, one sample of ACMC was quasi-instantaneously precipitated at 10 °C from a solution that had a dissolved inorganic carbon (DIC) pool that had not achieved isotopic equilibrium with water. The initial ACMC sample was characterized with chemical, isotopic, and structural analyses. Subsamples of the ACMC precursor were placed into $MgCl_2$-$NaHCO_3$ solutions with equilibrium DIC compositions and transformed at 10, 20, 40, and 60 °C, with chemical, isotopic, and structural analyses determined over one year. This experimental design enabled the tracking of isotopic trajectories towards equilibrium by creating large differences in the starting ACMC oxygen and clumped isotopic values compared to equilibrium values for HMC. We also compared measured data to model simulations to examine potential clumped and oxygen isotope disequilibrium in DIC from the dissolution of ACMC. A mixing model was used to study the progressive mixing of initial ACMC and HMC isotopic values.

### Temporal evolution of the solid phase

The transformation of ACMC with near dolomite stoichiometry (47.9 ± 1.5 mol% Mg) into HMC in solution was tracked by sample analysis at multiple time steps during the experimental runs, with the mineralogy of solids characterized using scanning electron microscope (SEM) imaging and X-ray diffraction (XRD) patterns (also see Purgstaller et al., 2021). The XRD pattern of ACMC was characterized by a broad hump between 25° and 45° 2ϴ (Rodriguez-Blanco et al., 2008). This pattern was shown for all solids collected at a reaction time of 5 minutes (Fig. 1A). SEM imaging of the synthesized ACMC (Fig. 1B) showed spherical particles (<100 nm) that were consistent with previously reported imaging of ACMC (Long et al., 2011; Konrad et al., 2016; Blue and Dove, 2015).

As indicated by SEM images, ACMC progressively dissolved and transformed between 5 to 61 minutes of reaction time, resulting in ACMC and HMC solids being concurrently present during transformation (Fig. 1C). As ACMC transformed into HMC at >5 minutes, crystalline peaks appeared in the XRD patterns of the collected solids. XRD patterns and SEM imaging indicated that ACMC was the sole phase for 11 minutes at 10 $^{o}$C, and 5 minutes for experiments at ≥20 $^{o}$C. At 21 minutes of reaction time, a large amount of ACMC remained in experiments performed at ≤20 $^{o}$C, whereas experiments performed at ≥40 $^{o}$C consisted mainly of HMC (Fig. 1A, C). ACMC was absent from solids collected at ≥32 minutes in experiments ≥40 $^{o}$C, and at ≥61 minutes at 10 and 20 $^{o}$C (Fig. 1D).

XRD indicated that after transformation at all temperatures, HMC was ≥90 wt% of the reaction product, with traces of aragonite and hydromagnesite (Table S1); however, the aragonite was not found in SEM images. The final HMC solid at ≤20 $^{o}$C was composed of spindle-shaped assemblages of nanocrystals, and at ≥40 $^{o}$C there were spheroidal aggregates, consistent with previous morphologies of HMC precipitated from amorphous precursors (Schmidt et al., 2005; Zhang et al., 2010; Purgstaller et al., 2016, 2017; Blue et al., 2017). At 10 $^{o}$C, star-shaped aggregates were observed in SEM images, which likely corresponded to the second HMC detected in the XRD pattern at ≥61 minutes (Fig. 1A, E). Trace amounts of a star-shaped aggregate were also observed in final solids at 20 $^{o}$C and 40 $^{o}$C (Fig. 1E).

The Mg content of the final HMC (determined by XRD pattern shift) accounted for 40.9 mol% at 60°C, 29.6 mol% at 40°C and 18 mol% at 20°C, thus increasing with temperature (Table S1). In the experiment at 10 °C, two Mg-calcites with 6.3 mol% Mg (~53 wt%, HMC_I) and 15.9 mol% Mg (~43 wt%, HMC_II) were detected (Table S1, Fig. 1A,C).

## Temporal evolution of Ca and Mg in the solids and solutions

Mg was preferentially dissolved in experiments at lower temperatures. From 0 to 21 minutes of reaction time, the [Mg] of the solutions indicated ~1.6 times more Mg was released at 10 °C than at 60 °C (at 21 minutes, [Mg] = 110.1 mmol/L for 10 °C; [Mg] = 67.1 mmol/L for 60 °C) (Table S1, Fig. 2B). The solutions at 10 and 20 °C continued to have measured increases in [Mg] between 21 to 61 minutes of reaction time, while the solutions at 40 and 60 °C reached their measured maximum [Mg] at 21 minutes, likely due to the higher solubility of ACMC at lower temperatures (Fig. S1) and more extensive uptake of Mg during crystallization at higher temperatures (Purgstaller et al., 2021). This resulted in the [Mg] of the final HMC, $[Mg]_S$, being positively correlated to temperature, similar to what was reported in Purgstaller et al. (2021) for a subset of the samples reported here. The final $[Mg]_S$ of the bulk solid was 16.6, 24.6, 40.9, and 47.3 mol% for 10, 20, 40, and 60 °C, respectively (Table S1).

The introduction of ACMC into the solution resulted in an increase in the [Ca] of the solution, $[Ca]_L$, from 0 to 5 minutes for all temperatures, with ~5.3 times more [Ca] released at 10 °C than at 60 °C (at 5 minutes, [Ca] = 35.1 mmol/L for 10 °C; [Ca] = 6.6 mmol/L for 60 °C) (Table S1, Fig. 2A). This was also likely related to the increased solubility of ACMC at lower temperatures (Fig. S1) (Purgstaller et al., 2021). The solution at 10 °C continued to have a measured increase in $[Ca]_L$

between 5 to 11 minutes of reaction time, while the samples at 20, 40, and 60 °C showed a decrease in $[Ca]_L$ between 5 to 11 minutes, likely from the earlier transformation to HMC as indicated by XRD and SEM (Fig. 1).

Chemical data revealed that after the transformation of ACMC into HMC ($t \leq$ 61 minutes), the solutions were still supersaturated or saturated with respect to calcite, with $SI_{calcite}$ values of 1.76, 1.54, 0.91, and 0.72 at 10, 20, 40, and 60 °C, respectively (Fig. S2), which lead to the continuous growth of HMC and other carbonate minerals (aragonite and hydromagnesite). Between 1 week and 1 year of reaction time, the $SI_{calcite}$ values were quasi-constant at all temperatures indicating chemical equilibrium conditions. For experiments at 10, 20, and 40 °C, the average $SI_{calcite}$ between 1 week and 1 year of reaction time was 0.3. The 60 °C had an average $SI_{calcite}$ of -0.03 (minimum = -0.08, maximum = 0.06) from 1 week to 1 year of reaction time, indicating that there may have been a small amount of dissolution during this period (Fig. S2).

## Disequilibrium isotopic composition of ACMC

The initial ACMC was precipitated under conditions that would lead to disequilibrium in the dissolved inorganic carbon solution that it formed from, with the goal of facilitating the observation of isotopic trajectories during transformation. The initial ACMC used in all experiments had a $\delta^{18}O_{carb}$ value of 24.0 ± 0.2 ‰, and a $\delta^{13}C_{carb}$ value of -2.8 ± 0.0 ‰ (Fig. 3B-C; Table 1). The $\delta^{18}O_{carb}$ value of the ACMC was significantly higher than the equilibrium value for HMC (Mavromatis et al., 2012), as indicated by the apparent oxygen isotope fractionation factor between the ACMC and water of the solution ($\alpha_{carb\text{-}water}$), with a $1000\ln(\alpha_{carb\text{-}water})$ value of 71.7 (Fig. 2D).

The initial ACMC also had disequilibrium clumped isotope values for both $\Delta_{47}$ and $\Delta_{48}$. The ACMC was precipitated at 10 °C and had an initial $\Delta_{47}$ value of 0.499 ±0.010 ‰ (Table 1). This value was significantly lower than the HMC or calcite clumped isotope equilibrium value at 10, 20, and 40 °C, and within the range of equilibrium values for HMC (Hill et al., 2020) and calcite (Fiebig et al., 2021) for 60 °C (Fig. 4). The initial ACMC $\Delta_{48}$ value of 0.552 ±0.056 ‰ was significantly higher than HMC (Hill et al., 2021) or calcite (Fiebig et al., 2021) equilibrium values at all temperatures (Table 1, Fig. 4).

## Temporal evolution of $\delta^{18}O_{water}$, $\delta^{18}O_{carb}$, $\delta^{13}C_{carb}$, and $\alpha_{carb\text{-}water}$

The bulk isotopic composition of the solids evolved during all experimental phases (Table 1; Fig. 3). The temporal evolution of the measured values is divided into three stages: 1) solely ACMC in the solids, 2) the solids contained a mix of ACMC and HMC indicating transformation of ACMC into HMC was occurring, 3) solids contained only crystalline mineral phases. We note although XRD patterns showed no crystalline peaks for the samples collected at 5 minutes, traces of HMC aggregates were observed in the SEM images of experiments at 40°C and 60°C (Fig. 1B).

After the ACMC was added into the solution, the solution showed an increase to isotopically enriched $\delta^{18}O_{water}$ values during the ACMC and transformation stage, which was more pronounced when the temperature of the solution was lower (Fig. 3A). The initial $\delta^{18}O_{water}$ value of the solution was -46.8 ± 0.06 ‰, and reached a maximum of -40.4, -42.2, and -43.4 ‰ at 10, 20, and ≥40 °C, respectively, after 1 day. After 1 week, all experiments yielded similar $\delta^{18}O_{water}$ values of -43.3 ±0.3 ‰, which remained quasi-constant over the remaining experimental run time (Fig. 3A).

The $\delta^{18}O_{carb}$ values of ACMC solids exhibited a slight depletion before transformation (Fig. 3B), whereas the $\delta^{13}C_{carb}$ values remained quasi-constant at -2.8 ± 0.1 ‰ (Fig. 3C). During transformation, $\delta^{18}O_{carb}$ values decreased significantly, the magnitude of which increased with temperature. From the final $\delta^{18}O_{carb}$ value of ACMC (t = 5 minutes) to the $\delta^{18}O_{carb}$ value of the first fully crystallized HMC sample (t = 61 minutes), there was a -9.4, -10.9, -18.0, -28.9 ‰ decrease in $\delta^{18}O_{carb}$ values at 10, 20, 40, and 60 °C, respectively (Fig. 3B). The $\delta^{18}O_{carb}$ values continued to decrease slightly in the HMC phase over the remaining time of the experimental runs (t = 61 minutes to 1 year). In contrast, the $\delta^{13}C_{carb}$ values increased during and subsequent to ACMC transformation (Fig. 3C). At a reaction time of 1 day, the measured $\delta^{13}C_{carb}$ values of the solids were slightly enriched at lower temperatures ($\delta^{13}C_{carb}$ = -1.6 ‰ at 10°C) relative to higher temperatures ($\delta^{13}C_{carb}$ = -2.2 ‰ at 60°C).

After 1 year of reaction time, none of the HMC solids achieved predicted oxygen isotope equilibrium with water, as was indicated by our measurements constraining the evolution of $1000\ln(\alpha_{carb\text{-}water})$ in Fig. 3D. The extent of oxygen isotope disequilibrium was negatively correlated with reaction temperature. The final HMC sample $1000\ln(\alpha_{carb\text{-}water})$ values were 52.5, 46.3, 37.6, and 29.4, at 10, 20, 40, and 60 °C, respectively, while the equilibrium values for HMC were calculated to be 35.5, 33.9, 30.6, and 26.4 for 10, 20, 40, and 60 °C, respectively, using equations from Mavromatis et al. (2012).

### Temporal evolution of $\Delta_{47}$ and $\Delta_{48}$

The quasi-constant $\Delta_{47}$ and $\Delta_{48}$ values during the ACMC precursor phase of all experiments indicated that the clumped isotope values of ACMC did not measurably evolve after its addition into the solution (Fig. 4), despite the evolution of δ$^{18}$O$_{carb}$ (Fig. 3). During transformation, the $\Delta_{47}$ values increased, with larger increases at lower solution temperatures. The total measured increase in $\Delta_{47}$ during the transformation (calculated as the average HMC $\Delta_{47}$ value − the average ACMC $\Delta_{47}$ value, not including the initial ACMC $\Delta_{47}$ value) for 10, 20, 40, and 60 °C was 0.154, 0.157, 0.139, and 0.079 ‰, respectively. Between 61 minutes and 1 year, the $\Delta_{47}$ values of HMC remained quasi-constant at 0.648 ±0.011, 0.652 ±0.025, 0.627 ±0.017 and 0.571 ±0.014 at 10, 20, 40, and 60 °C, respectively, but did not achieve equilibrium values for HMC (Hill et al., 2020) or calcite (Fiebig et al., 2021).

For $\Delta_{48}$, the transformation from ACMC to HMC resulted in $\Delta_{48}$ depletion, with larger depletions associated with increasing solution temperature (Table 1; Fig. 4). In all experiments, this trend was the opposite of what was observed for $\Delta_{47}$. The total depletion in $\Delta_{48}$ values during the transformation (calculated similarly to that for $\Delta_{47}$) for 10, 20, 40, and 60 °C was -0.219, -0.211, -0.229, and -0.265, respectively. The $\Delta_{48}$ values were quasi-constant between 60 minutes and 1 year of reaction time, with values of 0.280 ±0.023, 0.286 ±0.024, 0.292 ±0.023 and 0.281 ±0.020 at 10, 20, 40 and 60 °C, and did not achieve equilibrium values for HMC (Hill et al., 2020) or calcite (Fiebig et al., 2021).

While it is known that in carbonate minerals, each isotopologue reacts at different rates, leading to well-documented fractionations during acid digestion (e.g., Guo et al., 2009), it is unknown whether kinetic fractionations can be introduced due to dissolution of amorphous carbonates. We note that these data do not provide support for incongruent dissolution of ACMC, and are suggestive that for amorphous carbonates, dissolution is a congruent process.

### δ$^{18}$O exchange between ACMC and solution

During the ACMC phase of each experiment, the pH of the solution was adjusted to 7.6 by HCl titration, and the ACMC partially dissolved to maintain saturation between the solution and the respective solid (see also Purgstaller et al., 2021). The obtained data indicated that the increase of the $\delta^{18}O_{water}$ values of 1.8 to 2.9 ‰ (Fig. 3A) at 0 to 5 minutes of reaction time was likely from the addition of the HCl solution ($\delta^{18}O$ = -9 ‰ VSMOW). At lower temperatures, ACMC is more soluble (Fig. S1), which resulted in more $CO_3$ ions being released into the solution, thus, the maximum added amount of HCl was 3.8 mL in the experiment at 10 °C at 4.1 minutes. This resulted in a calculated $\delta^{18}O_{water}$ enrichment of 2.9 ‰, considering linear mixing, which is consistent with the measured enrichment of 2.9 ‰ between 0 to 5 minutes at 10 °C. The enrichment of $\delta^{18}O_{water}$ values may also have been subtly affected by the release of structurally bound $H_2O$ and $CO_3$ ions from the relatively isotopically enriched ACMC solid ($\delta^{18}O_{carb}$= 24.0 ‰, Table 1) into the isotopically depleted solution (initial $\delta^{18}O_{water}$= -46.9 ‰, Table 1). The effect of structural water on the isotopic composition of the solution was expected to be negligibly small (0.26 ‰, considering linear mixing) as the amount of $H_2O$ released into the solution corresponded to only 0.15 mL if all the ACMC (1.5 g) would be completely dissolved, while the volume of the reactive solution was 50 mL. Therefore, it can be reasonably assumed that the enrichment of $\delta^{18}O_{water}$ values during the ACMC experimental phase (t = 0 to 5 minutes) was predominantly caused by the addition of HCl.

The collected ACMC solids showed a slight depletion in $\delta^{18}O_{carb}$ values from 0 to 5 minutes of reaction time, where the depletion was more pronounced at higher temperatures (Table 1, Fig. 3B). These findings indicated that there was oxygen isotope exchange between the ACMC solid and the surrounding solution, in particular at higher temperatures. This was congruent with previous findings that demonstrated that the inclusion of Mg in amorphous carbonates increased solid-state diffusivity and surface exchange rates (Koishi et al., 2018; Lammers and Koishi, 2021).

## Isotopic evolution during the transformation of ACMC into HMC

As ACMC transformed into HMC, results revealed significant evolution of $\delta^{13}C_{carb}$, $\delta^{18}O_{carb}$, $\delta^{18}O_{water}$, $\Delta_{47}$, and $\Delta_{48}$, consistent with inferences of a dissolution-reprecipitation mechanism from other types of observations (Schmidt et al., 2005; Giuffre et al., 2015; Mavromatis et al., 2017; Dietzel et al., 2020; Lammers et al., 2021). During transformation, $\delta^{18}O_{carb}$ values rapidly depleted, while $\delta^{18}O_{water}$ values enriched, likely from the dissolution of the ACMC (Fig. 3A, B), resulting in the $\alpha_{carb-water}$ values significantly decreasing between 5 and 61 minutes of reaction time (Fig. 3D). The first fully crystallized HMC (t = 61 minutes) had $\delta^{18}O_{carb}$ values (Table 1) that probably reflected the extent of isotopic disequilibrium in the transformation solution DIC pool that was caused by dissolution of ACMC (Fig. 5), thus, the $\alpha_{carb-water}$ values for all experiments were enriched relative to isotopic equilibrium (Fig. 3).

The $\delta^{13}C_{carb}$ values evolved during transformation to yield higher $\delta^{13}C_{carb}$ values, despite the $MgCl_2$-$NaHCO_3$ solution having a depleted $\delta^{13}C$ value (-5.18 ±0.2 ‰, VPDB) relative to the solid (Table 1). Additionally, the $\delta^{13}C_{carb}$ values continued to enrich slightly between 1 day and 1 year during the HMC phase. The changes in $\delta^{13}C_{carb}$ may be explained by continuous precipitation of HMC (and other minerals), and small amounts of degassing that in principle, could have occurred when the solution was sampled. If degassing did occur, it likely had a negligible effect on the clumped isotopic signatures, as the predicted slope for $CO_2$ degassing (Guo, 2020) has an opposite sign relative to measured values (Fig. 6I).

Contrary to oxygen and carbon isotopic evolution, $\Delta_{47}$ and $\Delta_{48}$ values only measurably evolved during transformation. Both $\Delta_{47}$ and $\Delta_{48}$ values evolved towards equilibrium and had final HMC values that were enriched relative to predicted equilibrium; however, their trajectories differed substantially (Fig. 4). The initial $\Delta_{47}$ value of ACMC was depleted relative to HMC equilibrium values (Hill et al., 2020) for all temperatures except in the 60 $^{o}$C experiment. During transformation, for all experiments, the $\Delta_{47}$ values significantly enriched and yielded HMC values that exceeded the predicted equilibrium value for 10, 20, 40, and 60 $^{o}$C. For $\Delta_{48}$, the initial ACMC value was enriched relative to HMC equilibrium at all temperatures. During transformation, the $\Delta_{48}$ values evolved towards equilibrium, but the HMC values remained enriched relative to equilibrium in all experiments. As discussed below, these markedly different trajectories towards equilibrium likely resulted from a combination of temperature-dependent disequilibrium in the DIC pool during the transformation time interval (Fig. 5), in combination with mixing effects (Fig. 6).

## Disequilibrium in the DIC pool from the dissolution of ACMC

We hypothesize that the largest contributing factor to the disequilibrium clumped and oxygen isotope values in HMC is the dissolution of ACMC resulting in a DIC pool comprised of mixing of DIC from newly dissolved ACMC and the surrounding solution. Uchikawa et al. (2021) used modeling to show that at a pH of 8.9 at 25 $^{o}$C, where the $\delta^{18}O_{HCO3\,+\,CO3}$ is higher than the equilibrium value (similar to the experimental conditions here), there would be an "overshoot" in the $\Delta_{47\ HCO3\,+\,CO3}$ value beyond equilibrium values for ~900 minutes. Here, we used the IsoDIC model (Guo, 2020) to test our hypothesis. The model was initiated with water that was isotopically equilibrated at either 10, 20, 40, and 60 $^{o}$C. We calculated the evolution of $\delta^{18}O_{HCO3}$, $\Delta_{63\ HCO3}$, and $\Delta_{64\ HCO3}$ when unequilibrated $NaHCO_3$ was introduced. Due to constraints built into the model, the model results likely underestimate the extent of disequilibrium from the dissolution of ACMC, modestly for $\Delta_{63\ HCO3}$ and more extensively for $\delta^{18}O_{HCO3}$ and $\Delta_{64\ HCO3}$.

We test if the congruent dissolution of ACMC, which had an initial $\delta^{18}O_{carb}$ value higher than the equilibrium value for HMC, would cause similar isotopic disequilibrium in the DIC pool (Fig. 5). However, model results should be interpreted as estimates of the direction of the isotopic trajectories but not the magnitudes. Model calculations support the hypothesis that the DIC pool would not achieve equilibrium oxygen and dual clumped isotope compositions in the majority of the transformation experiments. The extent of clumped and oxygen isotope disequilibrium in the DIC pool that would occur from the dissolution of ACMC varied with reaction temperature, and the isotopic values of HMC were likely obtained during the transformation interval (Fig. 5).

During the transformation time interval (5 to 61 minutes at ≤20 °C; 5 to 32 minutes at ≥40 °C), the $\Delta_{63\ HCO3-}$ values were modeled to have maximum enrichments of 0.033, 0.153 and 0.167 ‰ at 20, 40, 60 °C, respectively, relative to expected equilibrium values (Hill et al., 2020) (Fig. 5F-H). At a transformation temperature of 10 °C, no enrichments relative to equilibrium were predicted within the transformation interval (Fig. 5E). Conversely, a maximum depletion of $\Delta_{64\ HCO3-}$ values relative to equilibrium of -0.015, -0.049, -0.046, -0.116 ‰ was predicted for 10, 20, 40 and 60 °C, respectively, during the transformation intervals (Fig. 5I-L). Modeled equilibrium $\Delta_{63\ HCO3-}$ values were achieved after ~74, ~26, and ~4 hours, for 10, 20 and 40 °C, respectively, and ~57 minutes at 60 °C. Modeled equilibrium $\Delta_{64\ HCO3-}$ values were achieved after ~51, ~17, and ~3, hours for 10, 20 and 40 °C, respectively, and ~41 minutes at 60 °C. Additionally, the model predicted that at lower solution temperatures, oxygen isotope equilibrium would not be obtained during the transformation time interval, with equilibrium achieved at ~62, ~23, and 4 hours for 10, 20, and 40 °C, respectively (Fig. 5A-C). At 60 °C, oxygen isotope equilibrium was predicted to be achieved before transformation was complete, with equilibrium reached at 54 minutes (Fig. 5D).

The differences between the model parameters and those corresponding to actual experimental conditions are likely the cause of the underestimation of disequilibrium by the model. The initial modeled $\delta^{18}O_{water}$ was unchangeable and set to 0 ‰, and the maximum allowable input for $\delta^{18}O_{HCO3}$ was 50 ‰, yielding initial $\Delta\delta^{18}O_{HCO3}$ values of 14.5, 16.8, 20.8, and 24.3 ‰ for 10, 20, 40, and 60 °C, respectively. The initial experimental $\Delta\delta^{18}O_{carb}$ values were 30.2, 33.1, 38.7, and 42.1 ‰ for 10, 20, 40, and 60 °C, respectively. Additionally, for the calculations of $\Delta_{64\ HCO3}$, the initial simulated $\Delta_{64\ HCO3}$ value was set to the highest allowable value within the model, ~0.141 ‰, yielding $\Delta\Delta_{64\ HCO3}$ values of 0.015, 0.028, 0.042, and 0.067 ‰ for 10, 20, 40, and 60 °C, respectively. The initial experimental $\Delta\Delta_{48}$ values were 0.286, 0.303, 0.329, 0.350 ‰ for 10, 20, 40, and 60 °C, respectively. Finally, the initial modeled $\delta^{13}C$ of the solution was unchangeable at 0 ‰, meaning it had no initial DIC. The experimental solution contained $NaHCO_3$ with an initial $\delta^{13}C$ value of -5.18 ±0.2 ‰.

Despite these differences, the model was useful to discern the isotopic trajectories towards equilibrium due to similarities in the model and experimental conditions. The modeled pH was 7.6, consistent with the pH of 7.6 for all experiments. For simulations of $\Delta_{63\ HCO3}$, the modeled $NaHCO_3$ had an initial $\Delta_{63\ HCO3}$ of 0.308 ‰. This was consistent with the experimental ACMC $\Delta_{47}$ value of 0.499 ±0.010, which yielded a $\Delta_{63\ HCO3}$ of ~0.305 ‰ (Hill et al., 2020). The initial modeled $\Delta_{64\ HCO3}$ value was higher than the expected equilibrium value, which was consistent with the initial $\Delta_{48}$ values for ACMC that were higher than equilibrium values for HMC. The initial modeled $\delta^{18}O_{HCO3}$ was higher than the expected equilibrium value, which was consistent with experimental $\delta^{18}O$ values for ACMC that were higher than equilibrium values for HMC. The initial modeled $\delta^{13}C_{DIC}$ of $NaHCO_3$ was -2.8 ‰, which was consistent with the experimental $\delta^{13}C_{carb}$ value for ACMC of -2.8 ‰.

These calculations suggest that the dissolution of ACMC caused oxygen and clumped isotopic disequilibrium in the transformation solution DIC, with a trajectory that was temperature-dependent and would produce an overshoot in both clumped isotope systems (Fig. 5). When compared to the model, the experimental results suggest the isotopic signatures of HMC were obtained during transformation; therefore, the extent of DIC disequilibria during transformation was recorded in the crystal.

For oxygen isotopes, the extent of disequilibrium in DIC during the transformation time interval (Fig. 5A-D) (5 to 61 minutes at ≤20 °C; 5 to 32 minutes at ≥40 °C) decreased with increasing temperature, which was consistent with experimental results (Fig. 3D). Only the 60 °C model simulation was predicted to achieve equilibrium values within the transformation time interval. This was consistent with experimental results, where measured $\delta^{18}O_{carb}$ values for HMC formed at 60 °C (Fig. 3D) were within ~3.0 ‰ of equilibrium, while $\delta^{18}O_{carb}$ values for HMC formed at 10 °C were ~14.8 ‰ from equilibrium (Mavromatis et al., 2012).

For $\Delta_{63\ HCO3}$, the model predicted that the extent of disequilibrium during transformation would increase with temperature due to faster rates of enrichment of $\Delta_{63\ HCO3}$ values at higher temperature (Fig. 5E-H). This was consistent with measured $\Delta_{47}$ values, where the HMC formed at 10 °C was within 0.020 ‰ of the equilibrium value, while the HMC formed at 60 °C was 0.098 ‰ from the equilibrium value (Hill et al., 2020) (Fig. 4A, D).

For $\Delta_{64\ \mathrm{HCO3}}$, the model predicted that the extent of disequilibrium during transformation increased with temperature due to faster rates of depletion of $\Delta_{64\ \mathrm{HCO3}}$ values occurring at higher temperatures (Fig. 5I-L). The experimental values were consistent with the trajectory that the model predicted; however, none of the $\Delta_{48}$ values for HMC were below equilibrium, as predicted for modeled $\Delta_{64\ \mathrm{HCO3}}$ values during the transformation time interval at ≥20 $^{o}$C. This may be because the modeled versus measured initial $\Delta\Delta_{64\ \mathrm{HCO3}}/\Delta\Delta_{48}$ values had different magnitudes, as discussed above, or it may be due to mixing effects or other kinetic effects contributing to the measured $\Delta_{48}$ values, which we explore using a mixing model.

## Mixing effects in clumped and bulk isotopes

We used a non-linear dual clumped isotope mixing model (Lucarelli et al., 2022) to conduct calculations where the mixing end members were isotopic values for the initial ACMC sample and fully crystallized HMC samples at each respective transformation temperature. Mixing models results indicated progressive mixing of isotopic values during all experimental phases, with differential mixing observed in $\delta^{13}C_{carb}$, $\delta^{18}O_{carb}$, and clumped isotope values (Fig. 6). The measured mixing was not consistent with mixing model calculations between an ACMC endmember and an equilibrium HMC endmember.

The measured isotopic evolution in all experiments was consistent with the mixing of DIC from the dissolution of ACMC and the surrounding solution altering the solution isotopic composition resulting in disequilibrium, which was subsequently recorded in HMC (Fig. 6). The mixing model (Defliese and Lohmann, 2015; Lucarelli et al., 2022) assumes linear mixing between endmembers for $\delta^{18}O_{carb}$ and $\delta^{13}C_{carb}$; however, this was not observed in the experiments here. For $\delta^{18}O_{carb}$ and $\delta^{13}C_{carb}$ to mix linearly, the ratio of the [DIC] in the DIC pool from the dissolved ACMC and surrounding solution needs to equal 1 (Zheng and Hoefs, 1991). The curvature observed in the $\delta^{13}C_{carb}$ versus $\delta^{18}O_{carb}$ relationship is consistent with mixing of two DIC pools with unequal [DIC] (Zheng and Hoefs, 1991). Similar curved mixing relationships for $\delta^{18}O_{carb}$ versus $\delta^{13}C_{carb}$ from mixing of DIC pools have been observed in mollusks (Fry, 2002; McConnaughey and Gillikin, 2008) and hydrothermal calcites (Zheng and Hoefs, 1993). Mixing of the DIC pools may occur more extensively at higher temperatures due to faster diffusion of DIC through the solution (Guo and Zhou, 2019), resulting in increased deviation from a linear mixing relationship. It is also possible that DIC diffusion contributes to the clumped isotope signatures, as it is predicted to enrich both $\Delta_{47}$ and $\Delta_{48}$ values of calcite relative to equilibrium (Eiler and Schauble, 2004; Thiagarajan et al., 2011; Guo, 2020).

Further, given that the IsoDIC model indicates rapid evolution of the DIC oxygen and clumped isotope compositions during transformation at higher temperatures (Fig. 5), and SEM and XRD analyses suggest successive formation of HMC (Fig. 1), a heterogeneous bulk HMC isotopic composition is possible. This is supported by mixing calculations that indicated the samples that contained a mix of ACMC and HMC (t = 21 minutes) have between a ~30-60% mix of the endmember $\delta^{13}C_{carb}$ and $\delta^{18}O_{carb}$ compositions (Fig. 6E-H), and a ~30-50 % mix of endmember $\Delta_{47}$ and $\Delta_{48}$ values (Fig. 6A-D), with the HMC endmember comprising a greater percentage of the mix at higher temperatures. For experiments with transformation temperatures of 20 and 60 °C, the measured $\Delta_{47}$ and $\Delta_{48}$ values during transformation fell below the modeled mixing line, which may have been from relatively higher analytical error in $\Delta_{48}$ measurements.

While the dominant factor in the enrichment of $\Delta_{47}$ values in HMC is likely the disequilibrium $\Delta_{63\ HCO3}$ values during transformation (Fig. 5), mixing may have been a significant contributing factor to the $\Delta_{48}$ values of HMC. The $\Delta_{47}$ mixing effect likely is relatively small because of the rapid equilibration (Schulz et al., 2006) and small variation among C isotopes between DIC pools (C isotopes affect $\Delta_{47}$ values due to the $^{13}$C substitution). The mixing effect may more substantially affect $\Delta_{48}$ values because oxygen isotopes had larger variation and slower equilibration during transformation (O isotopes have a larger impact on $\Delta_{48}$ values due to two $^{18}$O substitutions) (Fig. 5A-D). Mixing effects are both predicted to enrich $\Delta_{47}$ and $\Delta_{48}$ values of calcite (Eiler and Schauble, 2004; Defliese and Lohmann, 2015; Lucarelli et al., 2022), consistent with what is observed here (Fig. 6I).

### Transformation mechanisms

Previous work on non-classical models for mineral formation proposed that ACC and ACMC transforms to crystalline solids through either solid state transformation (Beniash et al., 1999; Politi et al., 2008; Weiner and Addadi, 2011, Gal et al., 2013) or dissolution and reprecipitation (Pontoni et al., 2003; Lee et al., 2007; Han and Aizenberg, 2008; Wolf et al, 2008; Bots et al., 2012; Hu et al., 2012; Gal et al., 2013; Ihli et al., 2013; Guiffre et al., 2015; Mavromatis et al., 2017; Dietzel et al., 2020; Purgstaller et al., 2021) (Fig. 8). If ACMC transforms into HMC purely by a solid-state process, the isotopic values of ACMC should be preserved in the HMC (Guiffre et al., 2015; Lammers and Koishi, 2021). On the other hand, if ACMC transforms into HMC by dissolution and reprecipitation, then isotopic values corresponding to the solution conditions at the time of crystallization should be recorded in the crystal.

The evolution of the chemical (Fig. 2) and anion stable isotopic data (Figs. 3, 4) presented here supports the transformation of ACMC to proceed by a dissolution-reprecipitation dominated process, where the dissolution of ACMC progressively alters the solution (Figs. 5, 6). These results support inferences based on measurements of cation composition. For a subset of the samples presented here, Purgstaller et al. (2021) concluded through Mg/Ca analyses that HMC was formed via the dissolution and reprecipitation mechanism. This was evidenced by the preferential dissolution of Mg during the dissolution process, and the temperature-dependent reincorporation of Mg, resulting in HMC that had very different [Mg] than the ACMC precursor. Additionally, the solution had a measured increase in the [Ca] during transformation, of which the dissolution of ACMC was the only source. In other experiments, the dissolution of ACMC has been shown to alter the cation isotopic composition of the surrounding fluid, resulting in the Ca and Mg isotopic composition of calcite reflecting a mix of the isotopic composition of ACMC and the solution (Guiffre et al., 2015).

### Oxygen isotope exchange kinetics

The data record relatively slow oxygen isotope exchange in the first and final experimental phases (the ACMC and HMC phases), and relatively rapid exchange of oxygen isotopes during the transformation from ACMC into HMC (Fig. 7A-D). The oxygen isotope exchange during transformation (Fig. 7E) and the oxygen isotope exchange with HMC (Fig. 7G) both appeared to proceed via pseudo-first-order reactions. The kinetic rate constant, k, increased with increasing temperature during the transformation from ACMC to HMC (t = 5 to 61 minutes), with calculated values of 0.00011 ($\pm 1.98 \times 10^{-5}$), 0.0001306 ($\pm 6.584 \times 10^{-6}$), 0.0001978 ($\pm 6.980 \times 10^{-5}$), and 0.000417 ($\pm 1.068 \times 10^{-4}$) for 10, 20, 40 and 60 °C, respectively (Fig. 7F, Table 2). For the final 3 HMC samples (1 week, 2 months, and 1 year of reaction time), k also increased with increasing temperature, with calculated k values of 1.959 $(\pm 1.205) \times 10^{-9}$, 5.540 $(\pm 3.386) \times 10^{-9}$, 4.944 $(\pm 1.394) \times 10^{-9}$, and 3.568 $\times 10^{-8}$ for 10, 20, 40 and 60 °C, respectively (Fig. 7H, Table 2). The calculated $E_a$ value for oxygen isotope exchange during the transformation from ACMC to HMC was 20.5 $(\pm 3.1)$ kJ/mol, and the $E_a$ value for oxygen isotope exchange during the HMC phase was 38.9 $(\pm 13.1)$ kJ/mol (Table 2). The k value for HMC transformed at 60 $^{o}$C does not have a calculated error due to only the samples from 1 week and 2 months of reaction time being used in the regressions. The sample from 1 year in the 60 $^{o}$C experiment was not used in the regression because it had a measured increase in the $\delta^{18}O_{carb}$ value between 2 months and 1 year. The experiment also had a negative $SI_{calcite}$ value measured in the samples at 1 week and 2 months, then an increase in $SI_{calcite}$ between 2 months and 1 year, likely indicating slight dissolution of HMC (Fig. S2). Additionally, the $[Ca]_L$ of the solution from the 60 $^{o}$C experiment increased during this same time interval (Fig. 2A).

The calculated apparent activation energy, $E_a$, had a value for oxygen isotope exchange during the transformation of ACMC to HMC was significantly lower than the $E_a$ value of isotopic exchange in the HMC phase (Table 2). This indicates that the transformation is not rate-limiting for oxygen isotope exchange, and that the slow isotopic exchange during the HMC phase is the rate limiting step towards equilibrium with water. The $E_a$ value during the transformation was near the upper bound for diffusion-controlled reactions of about 21 kJ/mol, indicating that molecular transport through the solution and surface-solution interface controls the oxygen isotope exchange rate (Lasaga, 1998) during transformation, with faster diffusive transport at higher temperatures from higher kinetic energy. The $E_a$ value for oxygen isotope exchange in HMC is typical of a surface-controlled reaction (Lasaga, 1998). This may indicate that reactions at the crystal surface are rate-controlling.

The calculated time to reach 99 % oxygen isotope equilibration between HMC and water, $t_{99}$, decreased significantly with increasing temperature, with $t_{99}$ values of 25299, 8118, 8125, and 699 days for 10, 20, 40 and 60 °C, respectively (Table 2). All $t_{99}$ values were greater than the length of the experiment, which agreed with the apparent oxygen isotope fractionation factors (Fig. 3D) that indicated none of the experiments reached oxygen isotope equilibrium within the experimental duration.

## NOVEL MECHANISMS FOR DISEQUILIBRIUM EFFECTS

Theoretically, the clumped isotope compositions of different carbonate minerals should be very similar, with only small effects of mineralogy, DIC speciation across most conditions, precipitation rate, and cation substitution into the mineral lattice (Schauble, 2006; Guo et al., 2009; Eagle et al., 2010; Hill et al., 2014, 2020; Tripati et al., 2015; Watkins et al., 2015). However, there is evidence for larger fractionations in natural samples, including biominerals (eg. Ghosh et al., 2006; Kimball et al., 2016; Spooner et al., 2016; Davies and John, 2019). These effects may be due to processes such as $CO_2$ hydration and hydroxylation generating kinetic effects in the DIC pool (Guo, 2020; Bajnai et al. 2020) or diffusion (Thiagarajan et al., 2011; Davies and John, 2019), and dual clumped isotopes has been shown to be a mechanism by which these effects can be probed (Bajnai et al., 2020; Lucarelli et al., 2022). Here we present evidence for new mechanisms where these effects could be generated. One potential origin for disequilibrium is dissolution of an amorphous precursor that drives disequilibrium in the DIC pool, leading to oxygen and dual clumped isotopic signatures of DIC that reflect a combination of two processes - precipitation of a crystalline phase from this transient DIC pool, and mixing of crystalline material formed from the evolving DIC pool. A related factor that may contribute to disequilibrium clumped isotope signatures in minerals is the progressive formation of crystalline products during several cycles of dissolution and reprecipitation. In our experiments, SEM images and XRD patterns showed that ACMC and HMC existed simultaneously during transformation, which may indicate successive dissolutions and reprecipitations occurred while the oxygen and clumped isotope signatures of the DIC pool evolved, which would drive mixing effects. These data suggest a highly dynamic environment, with the clumped isotope relationship to formation temperature affected by disequilibrium conditions in the solution that occur during the transformation from the amorphous precursor phase into crystalline HMC. Large changes in $\Delta_{47}$, $\Delta_{48}$, $\delta^{18}O_{carb}$, and $\delta^{18}O_{water}$, and modest changes in $\delta^{13}C_{carb}$ were measured during the transformation, congruent with dissolution of ACMC and reprecipitation of HMC. The HMC precipitated from ACMC transformed at lower temperatures was closer to achieving equilibrium clumped isotope values than HMC precipitated from ACMC transformed at higher temperatures. Modeling and experimental observations indicated that this was due to more extensive disequilibrium in DIC occurring during the time interval of transformation in experiments at higher temperatures.

The apparent activation energy ($E_a$) and kinetic rates constants (k) for oxygen isotope exchange with water at 10, 20, 40, and 60 °C during the transformation from ACMC to HMC and for fully crystallized HMC were calculated. The $E_a$ value during the transformation was characteristic of a diffusion-controlled reaction, while the $E_a$ value for HMC is characteristic of a surface-controlled reaction (Lasaga, 1998). Faster oxygen isotope exchange was observed during transformation compared to HMC, as evident by larger k values and a smaller $E_a$, indicating that oxygen isotope exchange during the HMC phase is rate limiting.

## MATERIALS AND METHODS

### Precipitation of ACMC

ACMC with 47.9 ±0.2 mol% Mg was synthesized following a protocol described in Konrad et al. (2016). For the synthesis, a 0.25 M (Ca,Mg)$Cl_2$ solution (Mg/Ca ratio = 2.1) and a 0.25 M $Na_2CO_3$ (pH 11.5) solution were prepared and pre-cooled in a fridge for 4 hours (T = 10 ± 2 °C). Ultrapure water (Millipore Integral 3: 18.2 M$\Omega$cm$^{-1}$, $\delta^{18}O_{water}$ = -9.4 ‰; VSMOW) and analytical grade chemicals (Roth) were used for the preparation of the stock solutions. 100 mL of the (Ca,Mg)$Cl_2$ solution was added into a beaker containing 100 mL of the $Na_2CO_3$ solution. Upon mixing, ACMC formed immediately and after a few seconds the solid was separated from solution by a 0.2 µm cellulose filter using a suction filtration unit. The ACMC was washed with pre-cooled water and transferred into a freeze-dryer (Virtis Benchtop 3L). After 12 hours, the freeze-dried ACMC was transferred into a desiccator with silica gel. The stoichiometric formula of the synthesized ACMC is $Ca_{0.52}Mg_{0.48}CO_3 \cdot 0.67H_2O$ (Purgstaller et al., 2021). Detailed information on the experimental setup and analytical procedures can be found in Purgstaller et al. (2021).

### Transformation of ACMC into HMC

The ACMC transformations were performed at 10, 20, 40 and 60 °C and are thus labelled as T_10°C, T_20°C, T_40°C and T_60°C (Table S1). For the ACMC transformations, 50 mM $NaHCO_3$ solutions were prepared in 150 mL gas-tight glass bottles using 90 % ultrapure water and 10 % of $^{18}O$-depleted water ($\delta^{18}O$ = -395 ‰; VSMOW). The prepared $NaHCO_3$ solutions (pH = 8.1 ±0.1) were kept at reaction temperatures 10, 20, 40 and 60 ±1 °C for 24 to 60 h to assure oxygen isotope equilibrium among the dissolved inorganic carbon (DIC) species present in the solution (Beck et al., 2005; Kluge et al., 2018). Subsequently, $MgCl_2 \cdot 6H_2O$ salt was added to the pre-cooled/heated $NaHCO_3$ solution to obtain a Mg concentration of 30 mM. A 150 mL borosilicate reactor containing 50 mL of the $NaHCO_3$-$MgCl_2$ solution was placed in an Easy Max$^{TM}$ 102 system (Mettler Toledo) to control the reaction temperature (10.0, 20.0, 40.0 or 60.0 ±0.1 °C) and stirring (200 rpm) of the solution during the experimental run. A pre-weighed amount of the synthesized ACMC material (1.5 g) was added into the buffered $NaHCO_3$-$MgCl_2$ solution and the pH of the reactive solution was adjusted to 7.62 ±0.01 by the automatic titration of a 2 M HCl solution (Schott; 118 TitroLine alpha plus) to prevent the precipitation of hydrous Ca- or Mg- carbonate phases, such as monohydrocalcite and nesquehonite (Purgstaller et al, 2017; Konrad et al., 2018; Xto et al., 2019). After 60 min of reaction time, the reactive solution was transferred into 100 mL gastight glass bottles and was kept at 10, 20, 40 or 60 ±2 °C over a period of 1 year. Homogeneous sub-samples of the experimental suspension (1.5 mL) were collected with a pipette at certain reaction times (Table S1), with the final samples collected at ~1 year. The solids were separated from the solution by a 0.2 µm cellulose acetate filter using a suction filtration unit and washed with ethanol. The solids were dried overnight (40 °C) and stored in a desiccator with silica-gel.

## Analytical methods for mineralogy and solution chemistry

The mineralogy of the dried precipitates was determined using X-ray diffraction (PANalytical X´Pert PRO). The Mg content of high Mg-calcite (in mol%) was calculated based on the shift of the characteristic $d_{104}$-peak value for HMC according to Goldsmith et al. (1961). The Mg content of the bulk solid (in mol%) was determined by digestion of samples with 6 % $HNO_3$ and analysis by inductively coupled plasma optical emission spectrometry (ICP-OES, Perkin Elmer Optima 8300 DV), with a precision of ±3 % using equation 1,

$$[Mg]_{solid} = [Mg]_s / ([Mg]_s + [Ca]_s) \times 100 \qquad (1)$$

where $[Mg]_s$ and $[Ca]_s$ are the ICP-OES measured concentrations (mol/kg) of Ca and Mg in the bulk solid. Aqueous Ca and Mg concentrations of the solutions were also measured via ICP-OES.

### Stable carbon, oxygen and dual clumped isotopic measurements

The stable carbon ($\delta^{13}C$), oxygen ($\delta^{18}O$), and carbonate clumped ($\Delta_{47}$ and $\Delta_{48}$) isotope ratios of the carbonate samples (ACMC and HMC) were determined using two Nu Perspective IS mass spectrometers at the University of California, Los Angeles using methods published elsewhere (Defliese and Tripati, 2020; Upadhyay et al., 2021). Briefly, for one mass spectrometer, here called Nu Perspective 1, was paired with a common acid bath where 0.48 to 0.52 mg of carbonate is weighed into silver capsules and placed into the sample carousel. Before analysis, the sample carousel is vacuum sealed before dropping samples into the vessel containing 90 °C, 105% phosphoric acid. The other mass spectrometer, Nu Perspective 2, was paired with a Nu Carb Sample Digestion System, where glass sample vials are cleaned with deionized water and dried overnight at 70 °C. Approximately 0.48 to 0.52 mg of sample is measured into each glass sample vial and placed into the sample carousel, which was contained within a chamber maintained at 70 °C. Prior to each sample analysis, 200 µL of 70°C, 105% phosphoric acid was injected into the sample vial and let to digest the carbonate sample for 20 minutes, liberating $CO_2$ gas. Sample digestion in individual vials eliminates potential isotopic memory effects that might be observed in common acid bath systems. The $CO_2$ gas was then dried and purified by cryogenic distillation and passes through an adsorption trap and an in-line GC column packed with PoraPak Type-QTM 50/80 and silver wool. The first part of the cryogenic distillation process dried the $CO_2$ gas with a dry ice-cooled ethanol trap (-78.5 °C). The second trap, liquid $N_2$-cooled trap (-196 °C), further purified the $CO_2$ by freezing out other gases that may be present. After the separation and purification steps, the $CO_2$ gas was transferred to the dual-inlet Nu Perspective IS for analysis of $\delta^{13}C$, $\delta^{18}O$, $\Delta_{47}$, and $\Delta_{48}$. A measurement consisted of three, 20-cycle blocks. Each cycle integrated over 20 seconds with 8 seconds of changeover delay, totaling 1200 seconds of integration per sample.

The stable carbon and oxygen isotope measurements ($\delta^{13}C$ and $\delta^{18}O$) of the solids and solutions were calculated according to the equations:

$$\delta^{13}\mathrm{C} = \frac{(13C/12C)_{sample} - (13C/12C)_{standard}}{(13O/12O)_{standard}} \times 1000 \tag{2}$$

$$\delta^{18}\mathrm{O} = \frac{(18O/16O)_{sample} - (18O/16O)_{standard}}{(18O/16O)_{standard}} \times 1000 \tag{3}$$

where the values are given in permil (‰). The $\delta^{13}C$ values are reported on the Vienna Pee Dee Belemnite (VPDB) scale. The $\delta^{18}O_{carb}$ was measured on the VPDB scale and were aligned to the Vienna Standard Mean Ocean Water (VSMOW) scale using the expression $\delta^{18}O_{VSMOW} = 1.03091\ \delta^{18}O_{VPDB} + 30.91$ (Coplen et al., 1983).

The clumped isotope composition was based on the deviations of the $^{18}O$–$^{13}C$–$^{16}O$ ($\Delta_{47}$) and $^{12}C$–$^{18}O$–$^{18}O$ ($\Delta_{48}$) abundances measured relative to stochastic distributions and were reported according to equations:

$$\Delta_{47}=\frac{R^{47}}{R^{47^*}}-1 \tag{4}$$

$$\Delta_{48}=\frac{R^{48}}{R^{48^*}}-1 \tag{5}$$

where $R^i$ is the ratio of the minor isotopologues relative to the most abundant isotopologue (*m/z* 44), and $R^{i*}$ are the expected stochastic ratios which are calculated using the measured abundance of $^{13}C/^{12}C$ ($R^{13}$) and $^{18}O/^{16}O$ ($R^{18}$) in the sample and the estimated abundance of $^{17}O/^{16}O$ ($R^{17}$). The latter ratio was estimated from $R^{18}$ ($^{18}O/^{16}O$) assuming a mass-dependent relationship between $^{18}O$ and $^{17}O$ (Daëron et al., 2016). The $\Delta_{47}$ and $\Delta_{48}$ values were reported in permil (‰), which implies the multiplication of a factor of 1000 for Equations 4 and 5. The analyses included carbonate standards pinned to the Intercarb-carbon dioxide equilibrated scale (I-CDES) at 90°C for $\Delta_{47}$ (Dennis et al., 2011; Bernasconi et al., 2021), and the CDES reference frame at 90°C for $\Delta_{48}$ (Fiebig et al., 2019). It is worth pointing out that the ACMC included certain amounts of structural water ($Ca_{0.52}Mg_{0.48}CO_3 \cdot 0.67H_2O$) and potential artifacts caused by oxygen isotope exchange of $H_2O$ during acidification and $CO_2$ production cannot be ruled out for samples containing ACMC (Table S1).

The stable oxygen isotopic composition of water of the $NaHCO_3$ solution ($\delta^{18}O_{water}$) was measured by the classic $CO_2$-$H_2O$ equilibrium technique (JR-AquaConSol, Graz, Austria) (Horita et al., 1989). The oxygen isotope composition was subsequently determined via continuous-flow isotope ratio mass spectrometry using a Finnigan DELTA$^{plus}$ mass spectrometer. The oxygen isotopic composition of the water of the solutions sampled during the experimental runs were measured by the wavelength-scanned cavity ring-down spectroscopy (WS-CRDS, Picarro). The precision for the measurements of $\delta^{18}O_{water}$ is <0.05 ‰ for both methods. The results were normalized versus the VSMOW scale. The apparent oxygen isotope fractionation factor between solid carbonate phase and water ($\alpha_{carb-water}$) is expressed by the equation:

$$\alpha_{carb-water} = \frac{18R_{carb}}{18R_{water}} = \frac{\delta^{18}O_{carb} + 1000}{\delta^{18}O_{water} + 1000} \tag{6}$$

where $^{18}R$ is the ratio of $^{18}O$ to $^{16}O$ in the solid carbonate and water.

## Parameters used for IsoDIC modelling

To estimate the evolution of the clumped and oxygen isotopic composition of $HCO_3^-$ during DIC-$H_2O$ isotope exchange in an aqueous solution, we used the IsoDIC model from Guo (2020). This numerical modeling software predicts kinetic clumped isotope fractionations in the DIC-$H_2O$-$CO_2$ system. The model simulates five key reactions (Reactions 1-5) that control isotope fractionation, and all related isotopologue reactions involving $^{12}C$, $^{13}C$, $^{16}O$, $^{17}O$, and $^{18}O$, for a total of 155 reactions.

$CO_2 + H_2O \leftrightharpoons HCO_3^- + H^+$ (Reaction 1)

$CO_2 + OH^- \leftrightharpoons HCO_3^-$ (Reaction 2)

$HCO_3^- \leftrightharpoons CO_3^{2-} + H^+$ (Reaction 3)

$HCO_3^- + OH^- \leftrightharpoons CO_3^{2-} + H_2O$ (Reaction 4)

$H_2O \leftrightharpoons H^+ + OH^-$ (Reaction 5)

The forward and reverse rate constants were estimated using equation 8,

$$k^* = \alpha_{KIE} \times k \quad (7)$$

where $k^*$ is the rate constant of the isotopically substituted reaction, $k$ is the rate constant of the isotopically non-substituted reactions, and $\alpha_{KIE}$ is the kinetic isotope fractionation factor for the isotopically substituted reaction. Isotopic equilibrium was assumed between $HCO_3^-$ and $CO_3^{2-}$ and $H_2O$ and $OH^-$ due to rapid equilibration via Reactions 3-5 relative to the reaction rate of hydration (Reaction 1) and hydroxylation (Reaction 2). Therefore, the only reactions that contribute to isotopic fractionation in the IsoDIC model are the forward and reverse $CO_2$ hydration and hydroxylation reactions (Guo, 2020). The full set of equations used are available in Guo (2020).

For all simulations, the modelled solution was set to be initially equilibrated at 10, 20, 40, and 60 °C with no DIC present ($\delta^{13}C_{DIC}$ = 0 ‰; $\delta^{18}O_{water}$ = 0 ‰), and the modelled $NaHCO_3$ added to the solution had an initial $\delta^{13}C_{DIC}$ of -2.8 ‰, and an initial $\delta^{18}O_{HCO3}$ value of 50 ‰. For simulations of $\Delta_{63\ HCO3}$, the modelled $NaHCO_3$ had an initial $\Delta_{63\ HCO3}$ of 0.308. For simulations of $\Delta_{64\ HCO3}$, the modelled $NaHCO_3$ had an initial $\Delta_{64\ HCO3}$ of 0.141 ‰. The experimental ACMC $\Delta_{47}$ value was 0.499 ±0.010, which corresponded to a $\Delta_{63\ HCO3}$ of ~0.305 ‰ (Hill et al., 2020), and initial $\delta^{13}C_{ACMC}$ was -2.8 ‰. The experimental $\Delta_{48}$ value for ACMC was 0.552 ±0.056, which would yield a $\Delta_{64\ HCO3}$ value of ~0.421 (Hill et al., 2020). This differences in the modelled versus experimental values for $\Delta_{64\ HCO3}$ and $\delta^{18}O$ likely result in the model underestimating the magnitude of disequilibrium in DIC during the trajectory towards equilibrium (see Discussion). The model has a total evolution time of 160 hours.

Differences in the modelled and measured values relative to expected equilibrium were calculated as follows:

$$\Delta\delta^{18}O = \delta^{18}O_t - \delta^{18}O_{eq} \tag{8}$$

$$\Delta\Delta_i = \Delta\Delta_{i\ t} - \Delta\Delta_{i\ eq} \tag{9}$$

where $\delta^{18}O_t$ and $\Delta\Delta_{i\ t}$ were the isotopic values at time t, and $\delta^{18}O_{eq}$ and $\Delta\Delta_{i\ eq}$ were the isotopic values at equilibrium (Mavromatis et al., 2012; Hill et al., 2020; Lucarelli et al., 2021).

### Mixing model

The mixing model from Lucarelli et al. (2022) was used to simulate isotopic values for the mixing of two endmembers. In the model, $\Delta_{47}$, $\Delta_{48}$, $\delta^{18}O$, and $\delta^{13}C$ values are assigned to each endmember. For each simulation temperature, 10, 20, 40, and 60 °C, one endmember was the initial ACMC isotopic values, and the other endmember was the final HMC $\delta^{18}O$ and $\delta^{13}C$ values, and an average of the HMC $\Delta_{47}$, $\Delta_{48}$, values. The reason an average value for HMC was only used for $\Delta_{47}$ and $\Delta_{48}$

is that the clumped isotope values did not observably evolve after crystallization, however, the $\delta^{18}$O and $\delta^{13}$C values continued to evolve after crystallization.

The model calculates $\delta^{45}$, $\delta^{46}$, $\delta^{47}$, $\delta^{48}$, $\delta^{18}$O, and $\delta^{13}$C values of $CO_2$ gas produced by phosphoric acid digestion of carbonate relative to a working gas (WG). The ratio of each endmember is entered into the model and the isotopic values of the mix are calculated. $\delta^{18}$O and $\delta^{13}$C values are given to the hypothetical WG. The slope and intercept for an empirical transfer function (ETF) are entered into the model. All isotopic values for model samples and the working gas, as well as the transfer function values, were based on experimental data taken from the Nu Perspective instruments. No acid fractionation factor was used, and model calculations were based on values determined in the I-CDES (Bernasconi et al., 2021) reference frame at 90 $^{o}$C. The model is available for download at https://github.com/Tripati-Lab/Lucarelli-et-al-D48exp2022.

### Calculation of oxygen and isotope exchange kinetics

The pseudo-first-order kinetic rate constant, k (sec$^{-1}$), and activation energy, $E_a$ (kJ mol$^{-1}$ K$^{-1}$) for the oxygen isotope exchange during the transition from ACMC to HMC and after HMC was fully crystallized were examined using experimental data and the Arrhenius equation:

$$k = A_o e^{\frac{-E_a}{RT}} \tag{10}$$

where R is the gas constant and T is the temperature in Kelvin. The rate constant was calculated using experimental $\delta^{18}O_{carb}$ data and the additional relationship (citation?):

$$ln\left(\frac{\delta^{18}O_{carb\ eq}-\delta^{18}O_{carb\ t}}{\delta^{18}O_{carb\ eq}-\delta^{18}O_{carb\ i}}\right) = ln(F_{\delta^{18}O} - 1) = -kt \tag{11}$$

$$F_{\delta^{18}O} = \left(\frac{\delta^{18}O_{carb\ t}-\delta^{18}O_{carb\ eq}}{\delta^{18}O_{carb\ i}-\delta^{18}O_{carb\ eq}}\right) \tag{12}$$

where $\delta^{18}O_{carb\ i}$ and $\delta^{18}O_{carb\ t}$ are the initial measured $\delta^{18}O$ values and $\delta^{18}O$ values at time t for the solid, and $F_{\delta^{18}O}$ is the fractional approach to oxygen isotope equilibrium values calculated from Mavromatis et al. (2012). A plot of $ln(F_{\delta^{18}O} - 1)$ versus reaction time (s) has a slope that is equal to -k. Equation 11 was also used to calculate the time to reach 99% oxygen isotope equilibration between HMC and water, $t_{99}$. The $\delta^{18}O_{carb\ eq}$ values were calculated using the following relationship from Mavromatis et al. (2012):

$$1000ln\alpha_{MgCaCO_3-H_2O} = \frac{18030}{T} - 32.42 + (6 \times \frac{10^8}{T^3} - 5.47 \times \frac{10^6}{T^2} + \frac{16780}{T} - 17.21) \times mol\%Mg \tag{13}$$

where $\alpha_{MgCaCO_3-H_2O}$ is the fractionation factor between $MgCaCO_3$ (here HMC) and water, T is the formation temperature in Kelvin, and mol%Mg is the measured mol% of Mg in the HMC. This equation accounts for the increase in oxygen isotope fractionation factors with an increase in [Mg] in the HMC (Mavromatis et al., 2012). Where k was able to be determined, ln(k) versus 1/T in Kelvin was plotted. The slope of this regression yielded $-E_a/R$ (Lasaga, 1998).

**Acknowledgments**: We thank lab members past and present for their work running standards, efforts in data entry, and contributions to discussions, the NAWI Graz Central Lab for Water, Minerals and Rocks for experimental and analytical support, and Ben Elliot and members of the Tripati Lab for their analytical support. This work was funded by DOE BES grant DE-FG02-83613ER16402. Jamie Lucarelli also acknowledges support as an early career fellow of The Center for Diverse Leadership in Science supported by the Packard and Sloan and Silicon Valley Community Foundations, and the Cota Robles and Dissertation Year Fellowships from University of California, Los Angeles. Bettina Purgstaller was funded through the Austrian science fund, project number T920-N29.

**Author Contribution Statement:** AT and MD initiated and designed the research, funded the project. AT, MD, and RE mentored the students and postdoctoral researchers. BP, AL, KG, and MD designed and carried out the ACC transformation experiment in MD's laboratory. RU, JL, and BP carried out the isotope geochemical measurements in AT and RE's laboratory. JL and BP analyzed the isotope data and performed calculations. JL and ZP did modeling calculations. JL and BP wrote the manuscript. JL, BP, RU, RE, MD, and AT provided insights into data interpretations. All authors edited and gave comments on the manuscript.

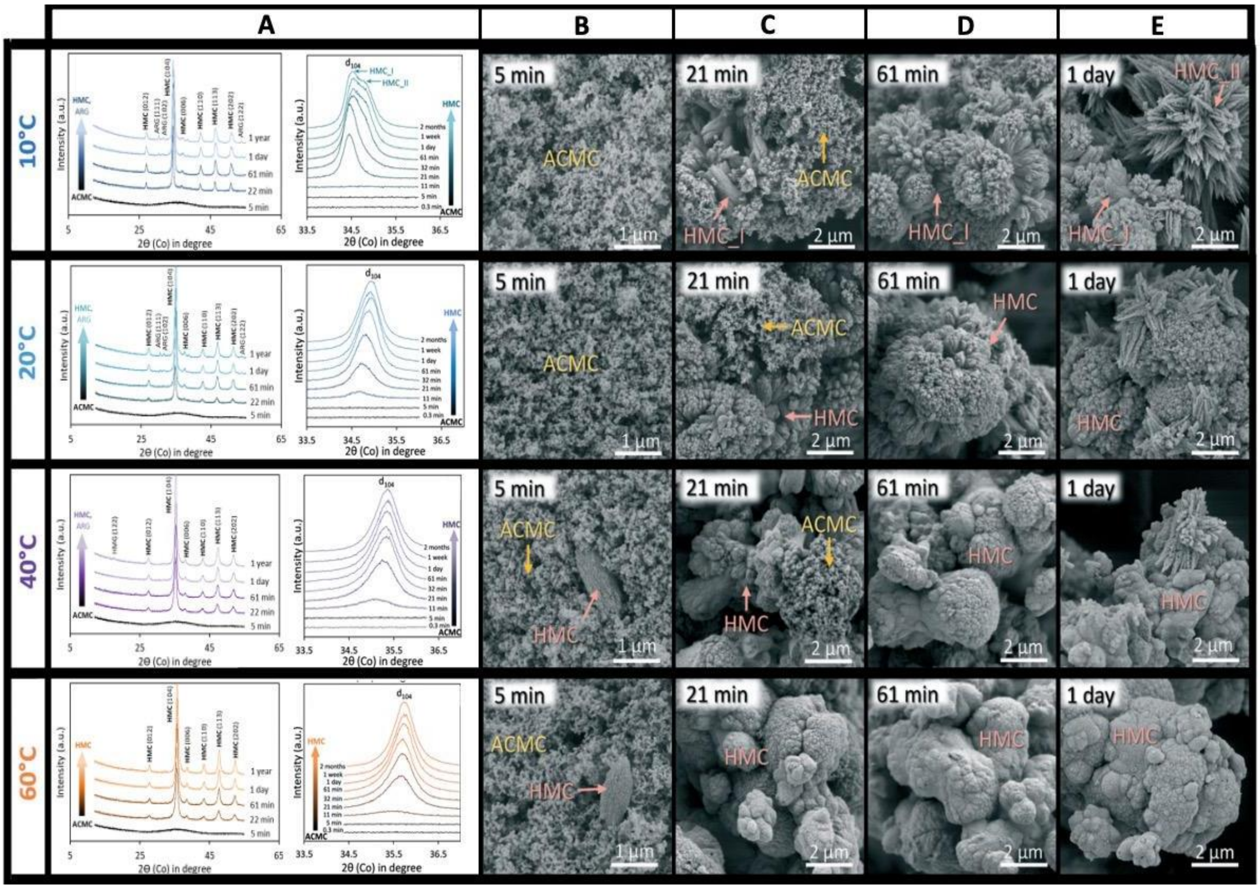

**Fig. 20.** XRD patterns (A) and SEM images (B-E) of solids were collected at multiple reaction times during ACMC transformation experiments at each experimental temperature (modified after Purgstaller et al., 2021). ACMC: amorphous calcium magnesium carbonate; HMC: high Mg-calcite; ARG: aragonite; HMG: hydromagnesite. Samples from 5 and 21 minutes contain a mix of ACMC and HMC, indicating successive dissolution-reprecipitation.

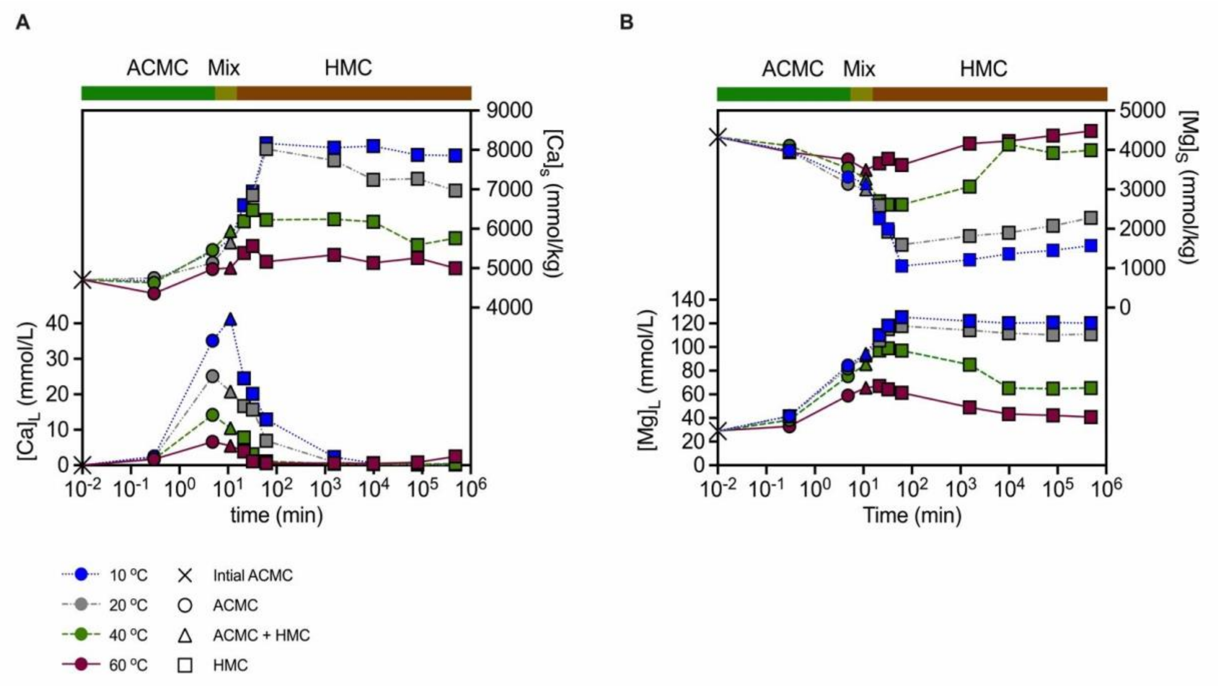

**Fig. 21.** Temporal evolution of (A) [Ca] in the reactive solution and solid, $[Ca]_L$ and $[Ca]_S$, and (B) [Mg] in the reactive solution and solid, $[Mg]_L$ and $[Mg]_S$. The final $[Mg]_s$ has a positive correlation to temperature.

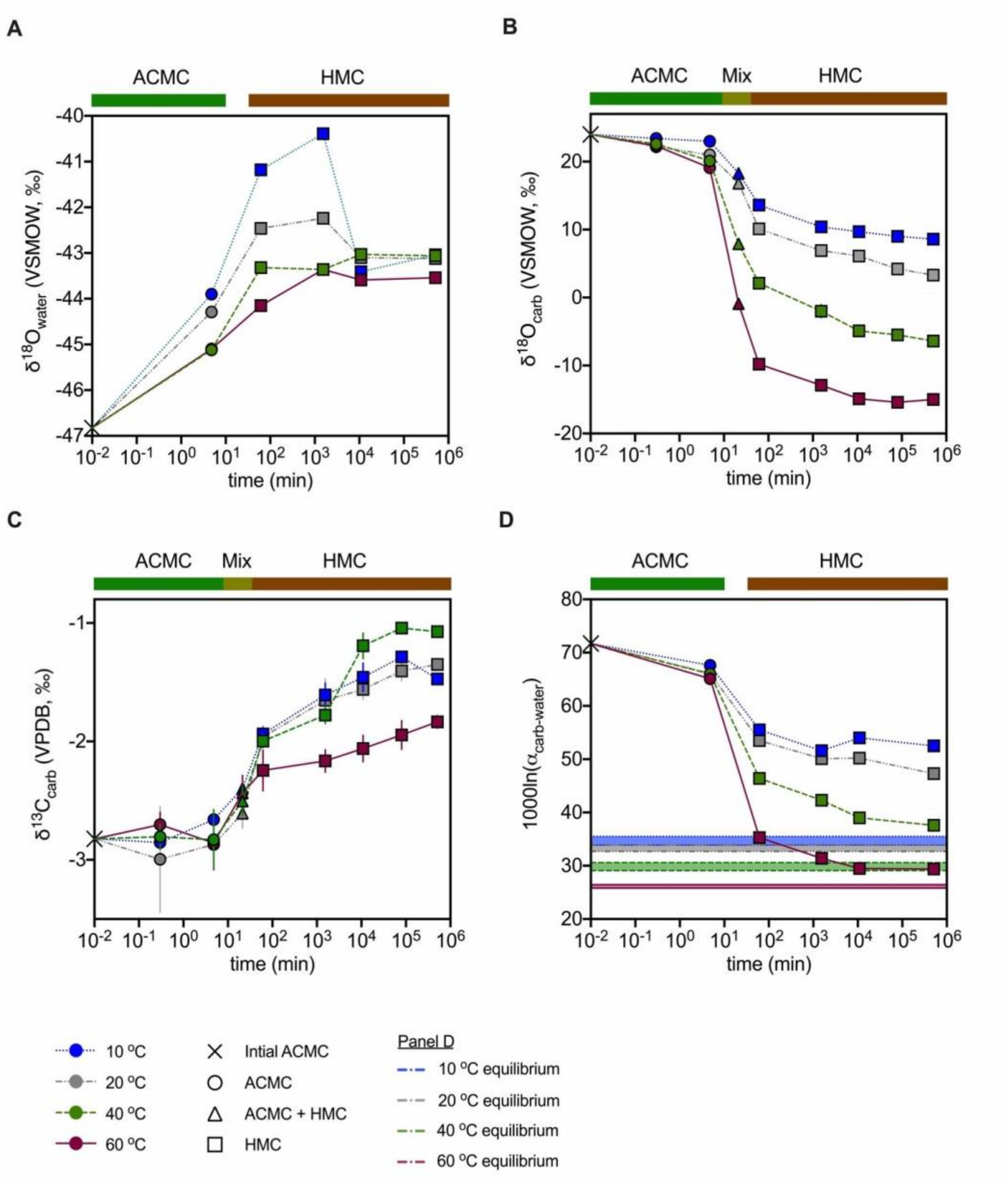

**Fig. 22.** Evolution of measured (A) oxygen isotope composition of the reactive solution ($\delta^{18}O_{water}$), (B) oxygen isotope composition of the carbonate solids ($\delta^{18}O_{carb}$), (C) carbon isotope composition of the carbonate solids ($\delta^{13}C_{carb}$), and (D) apparent oxygen isotope fractionation factor for the carbonate solid and water of the reactive solutions ($\alpha_{carbonate\text{-}water}$) as a function of reaction time at 10, 20, 40 and 60°C. The expected equilibrium $1000\ln(\alpha_{carb\text{-}water})$ values are calculated from Mavromatis et al. (2012). None of the experiments achieved oxygen isotope equilibrium between HMC and water within the experimental duration of ~1 year.

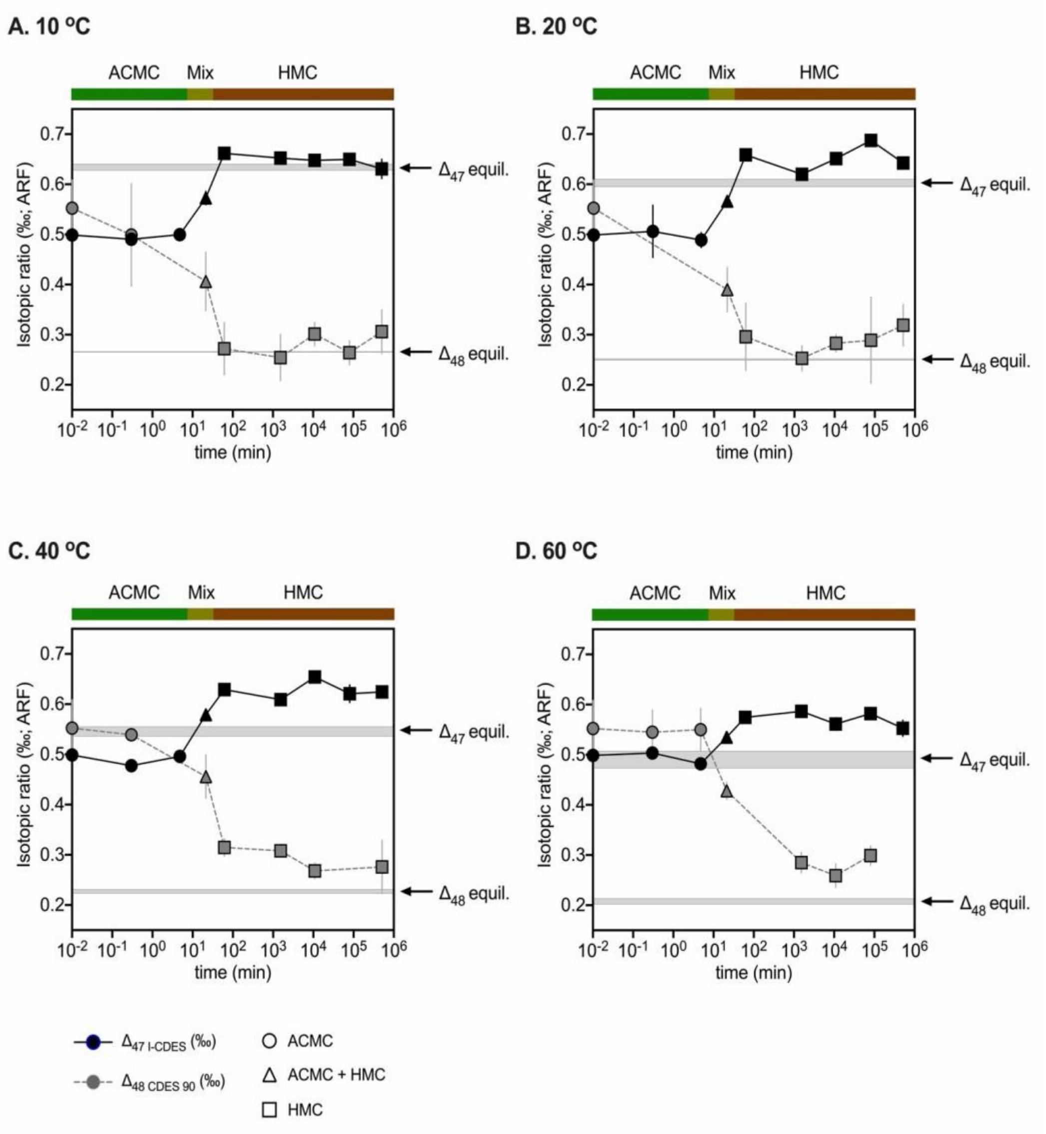

**Fig. 23.** Evolution of measured *Δ*47 and *Δ*48 as a function of reaction time at (A) 10°C, (B) 20°C, (C) 40°C and (D) 60°C. The grey bars are the range of calculated equilibrium values for each temperature, including values for calcite (Fiebig et al. 2021) and HMC (Hill et al., 2020). The average HMC values for *Δ*47 and *Δ*48 were quasi-constant and enriched relative to equilibrium for all experiments.

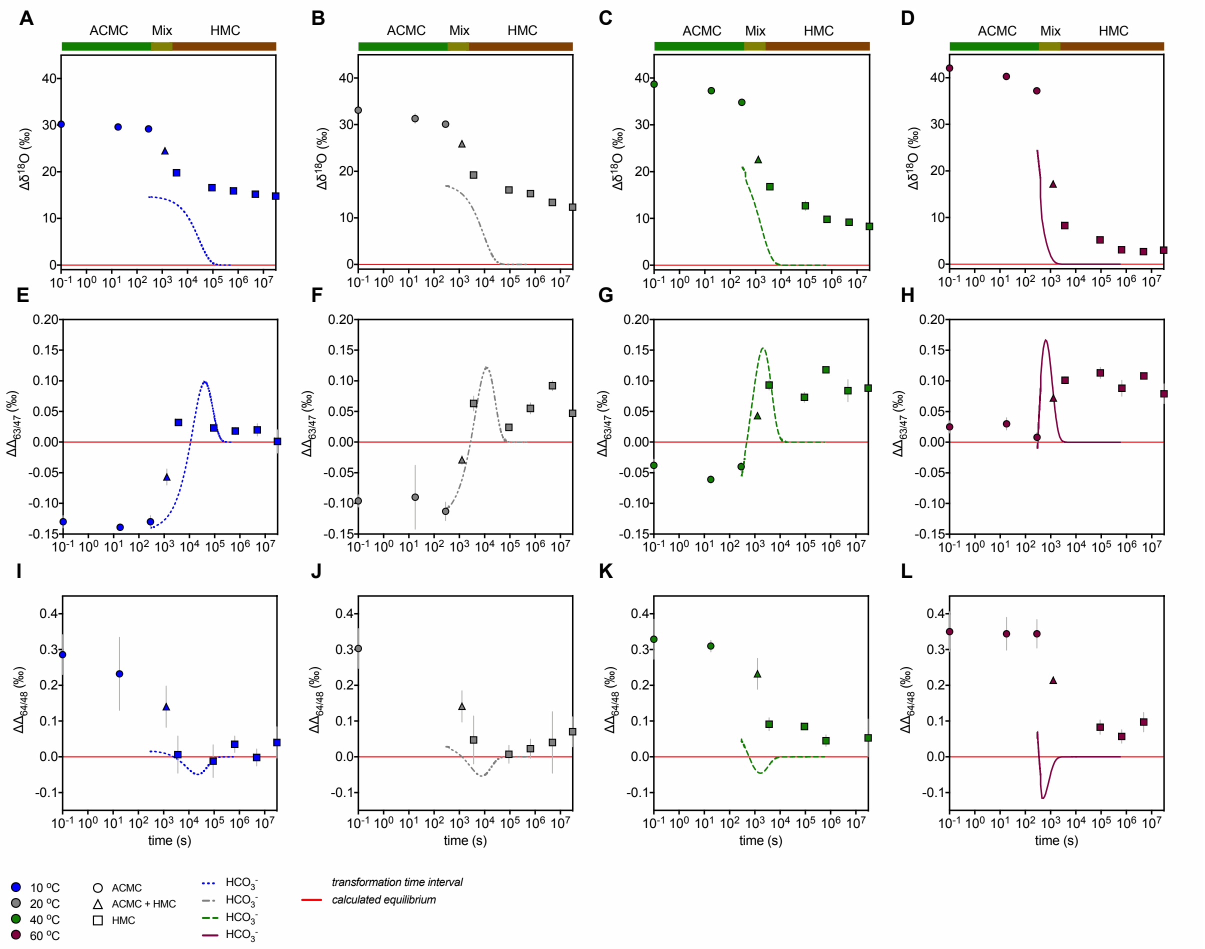

**Fig. 24.** Comparison of IsoDIC modeling results for the isotopic evolution of $HCO_3^-$ (lines) to measured values (data points) at each experimental temperature. Panels A-D show $\Delta\delta^{18}O$ for $HCO_3^-$ and measured solids; panels E-H show $\Delta\Delta_{63}$ for $HCO_3^-$ and $\Delta\Delta_{47}$ for measured solids; panels I-L show $\Delta\Delta_{64}$ for $HCO_3^-$ and $\Delta\Delta_{48}$ for measured solids. The vertical brown bar indicates the time at which transformation into HMC occurred, as indicated by XRD and SEM images. Overall, the extent of disequilibrium during the transformation from ACMC to HMC (brown bar) was recorded in the isotopic signatures of HMC.

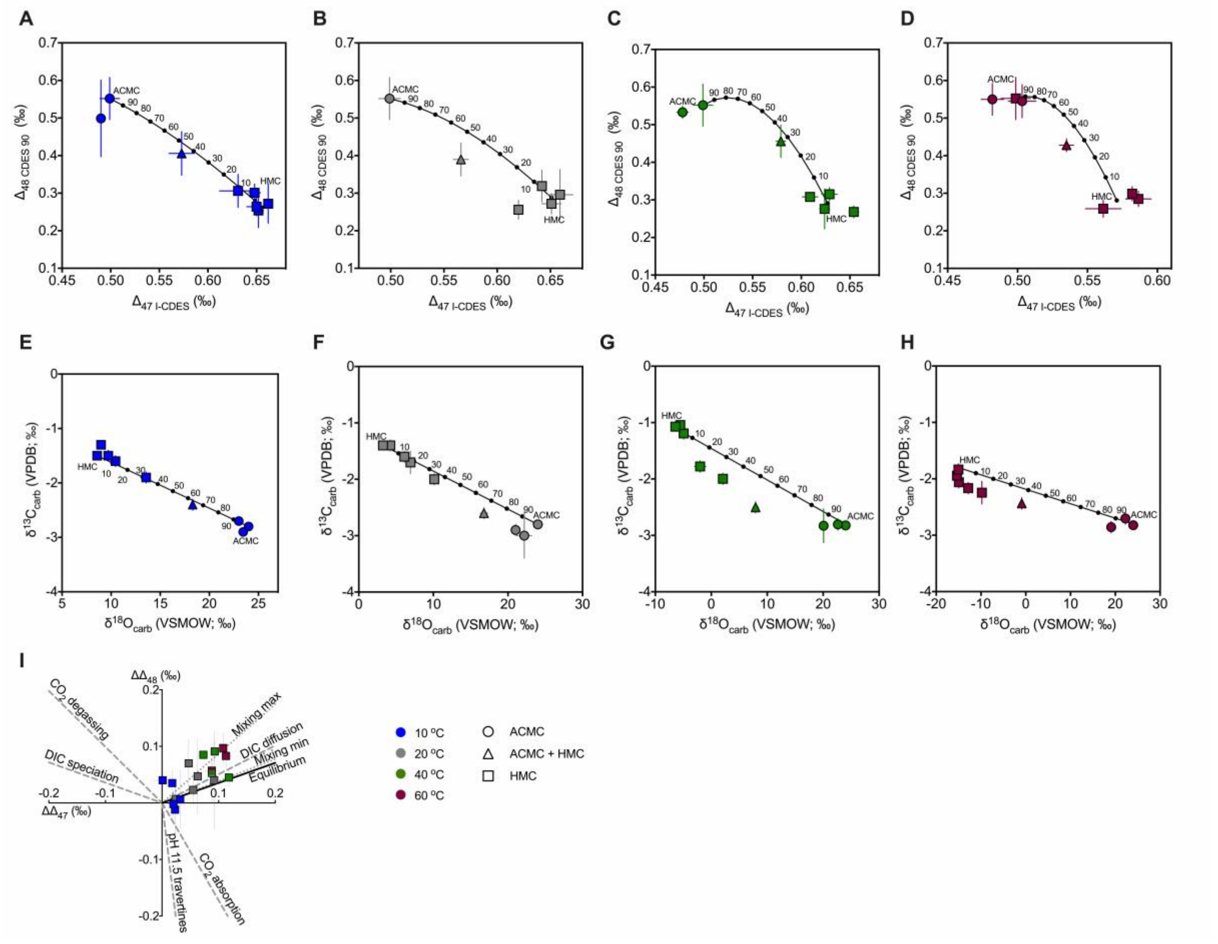

**Fig. 25.** Comparison of mixing model results (lines) to experimental data (filled symbols) at each experimental temperature. The gray line with round points indicates equilibrium mixing (Mavromatis et al., 2012; Hill et al., 2020). For $\delta^{18}O_{carb}$, the black line with square points indicates mixing where the endmembers are initial measured values for ACMC and final HMC values. For $\Delta_{47}$ and $\Delta_{48}$, the endmembers are the initial ACMC value and the average of the HMC values. The numbers on the mixing line indicate the percent contribution of the ACMC endmember. A-D show modeled and measured results for $\Delta_{47}$ and $\Delta_{48}$; E-H show modeled and measured results for $\delta^{13}C_{carb}$ and $\delta^{18}O_{carb}$. Panel I is a $\Delta\Delta_{47}$ versus $\Delta\Delta_{48}$ cross plot showing kinetic isotopic fractionations and mixing effects (Lucarelli et al., 2022) compared to data for HMC (symbols). The mixing relationships are not indicative of equilibrium mixing (gray lines), and instead provide evidence that the dissolution of ACMC altered the isotopic

composition of the surrounding solution, resulting in isotopic values for HMC that are offset from equilibrium.

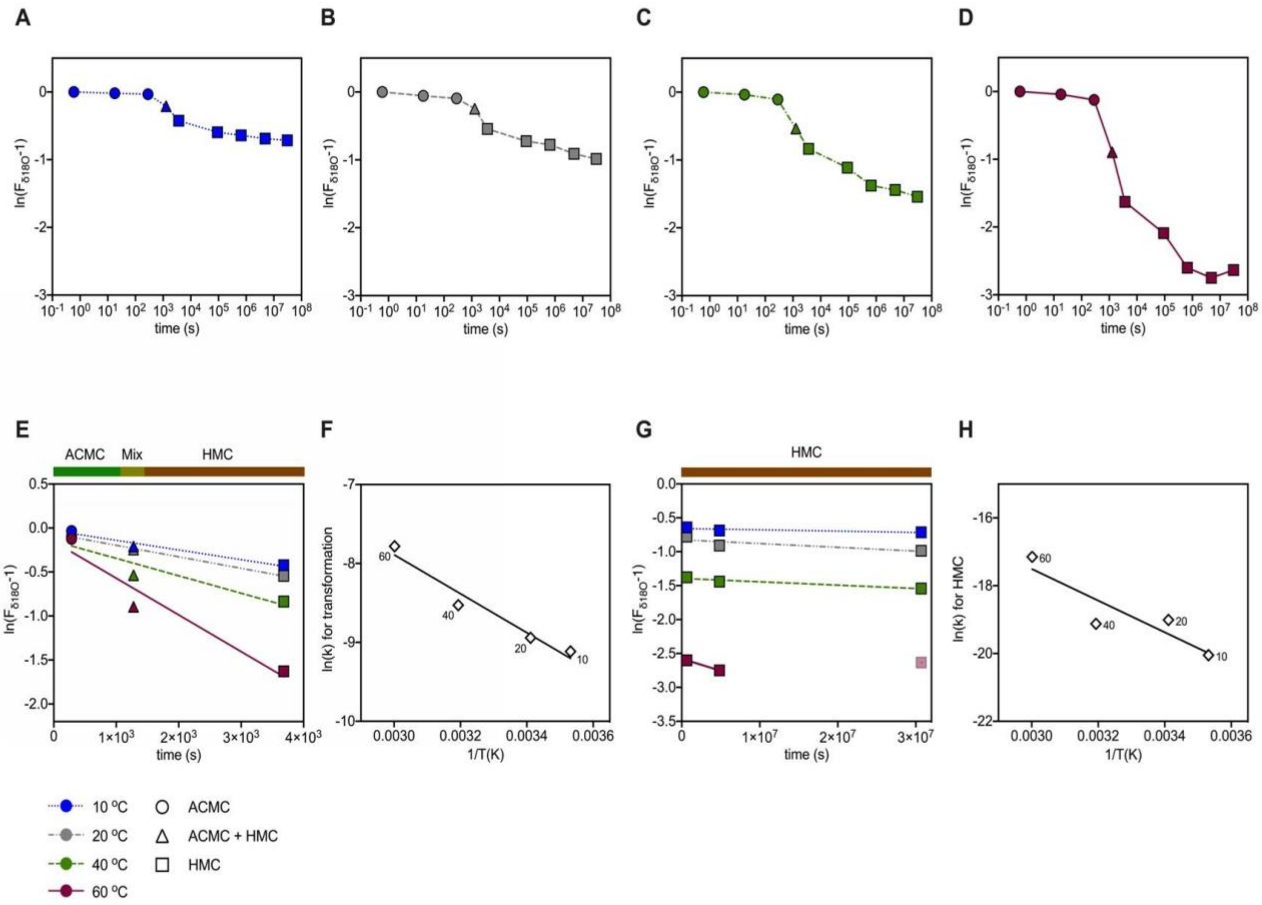

*Numbers on panels F and H indicate the temperature (ºC) of the precipitation solution*

**Fig. 26.** The temporal evolution for 1 year of the natural log of the fractional approach to expected oxygen isotope equilibrium, ln($F_{\delta_{18}O}$), for ACMC transformed into HMC at (A) 10°C, (B) 20°C, (C) 40°C and (D) 60°C. (E) is the temporal evolution of ln($F_{\delta_{18}O}$) during the transformation at 10°C, 20°C, 40°C and 60°C , which is comprised of the final ACMC sample, the mixed sample containing both ACMC and HMC, and the first measured HMC sample. (F) is the relationship during the transformation for ln(k) versus 1/$T$ in Kelvin, which was used to calculate $E_a$ for oxygen isotope exchange during the transformation. (G) is the temporal evolution of ln($F_{\delta_{18}O}$) for fully crystallized HMC at 10°C, 20°C, 40°C and 60°C. (H) is the relationship for fully

crystallized HMC for ln(k) versus 1/*T* in Kelvin, which was used to calculate $E_a$ for oxygen isotope exchange during the HMC phase of the experiments. These results indicate that there was relatively fast oxygen isotope exchange during the transformation from ACMC to HMC (triangles) compared to the ACMC phase (circles) and HMC phase (squares).

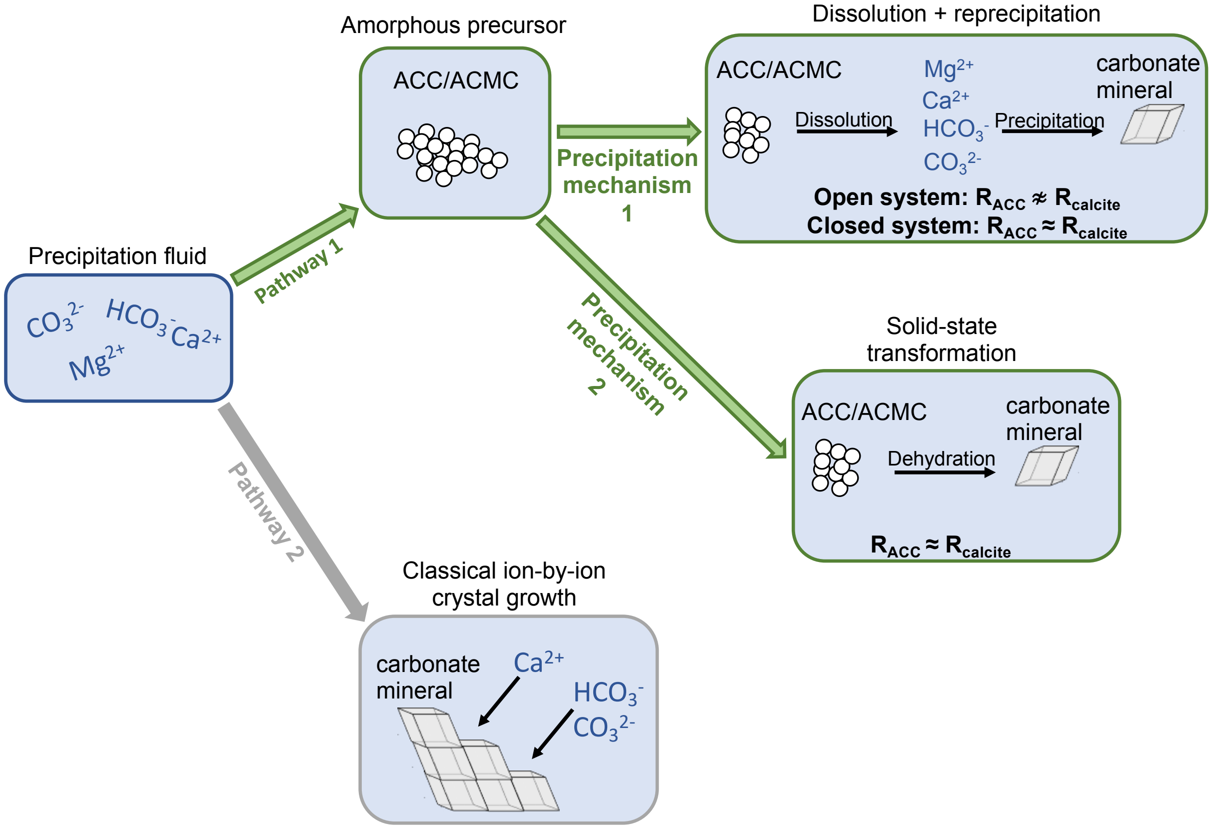

**Fig 27.** Potential reaction mechanisms for the formation of carbonate minerals from aqueous ions. The expected isotopic relationships are given when calcite is formed *via* an amorphous precursor, where $R_{ACC}$ is the ratio of heavy to light isotopes in amorphous carbonates and $R_{calcite}$ is the ratio of heavy to light isotopes in carbonate minerals. Studies of the isotopic signatures of the cation in transformation experiments (Guiffre et al., 2015; Mavromatis et al., 2017) and anion in the final mineral product (Dietzel et al., 2020) have invoked the dissolution and reprecipitation

mechanism. Structural studies have hypothesized solid-state transformation occurs via dehydration of amorphous carbonates (Beniash et al., 1999; Politi et al., 2008; Weiner and Addadi, 2011, Gal et al., 2013). These non-classical models contrast with classical models of crystal growth (Lammers and Koishi, 2021). The dual clumped isotope data supports a dissolution-reprecipitation dominated process, where the dissolution of amorphous carbonates progressively alters the solution.

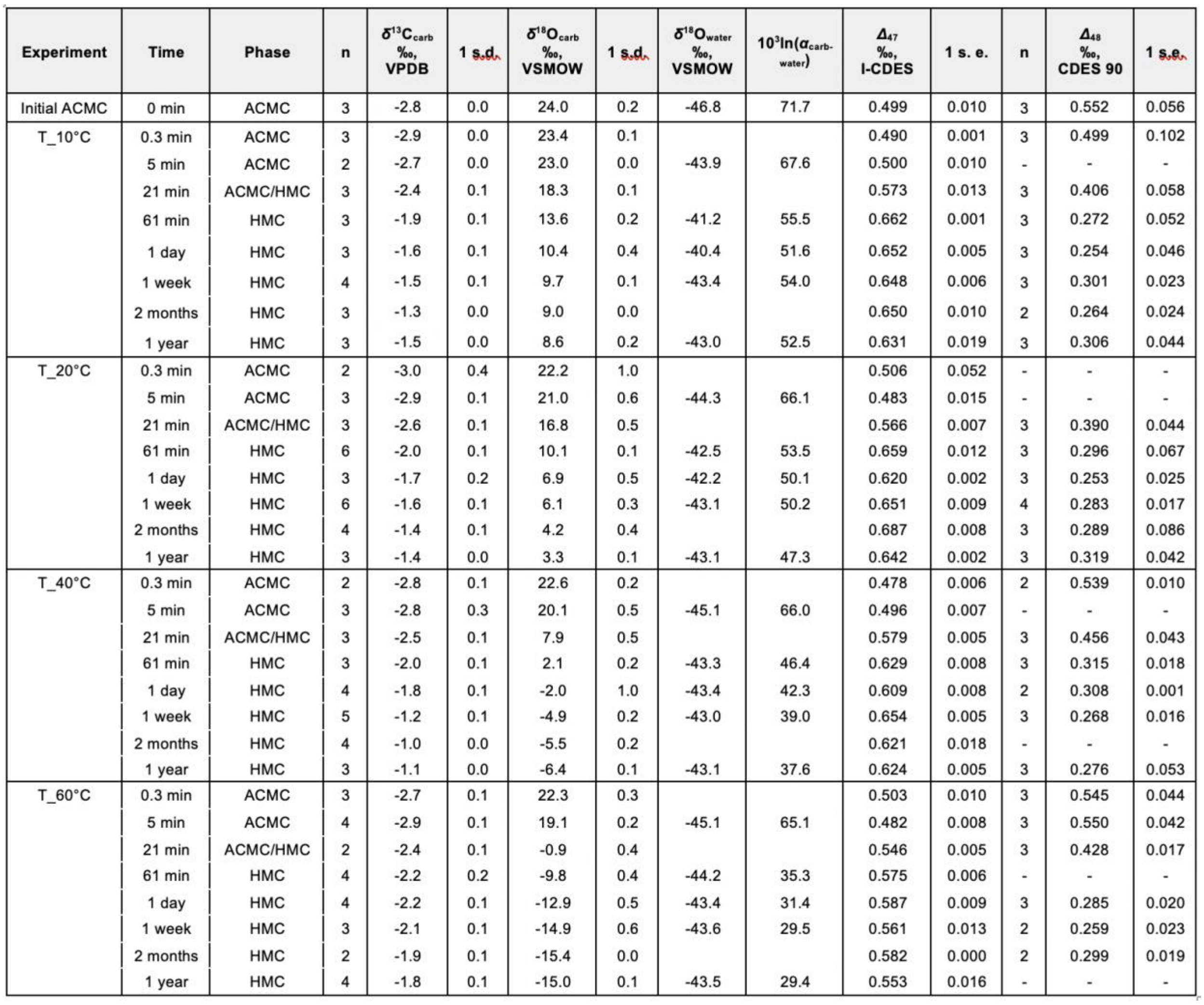

| Experiment | Time | Phase | n | $\delta^{13}C_{carb}$ ‰, VPDB | 1 s.d. | $\delta^{18}O_{carb}$ ‰, VSMOW | 1 s.d. | $\delta^{18}O_{water}$ ‰, VSMOW | $10^3\ln(\alpha_{carb-water})$ | $\Delta_{47}$ ‰, I-CDES | 1 s. e. | n | $\Delta_{48}$ ‰, CDES 90 | 1 s.e. |
|---|---|---|---|---|---|---|---|---|---|---|---|---|---|---|
| Initial ACMC | 0 min | ACMC | 3 | -2.8 | 0.0 | 24.0 | 0.2 | -46.8 | 71.7 | 0.499 | 0.010 | 3 | 0.552 | 0.056 |
| T_10°C | 0.3 min | ACMC | 3 | -2.9 | 0.0 | 23.4 | 0.1 | | | 0.490 | 0.001 | 3 | 0.499 | 0.102 |
| | 5 min | ACMC | 2 | -2.7 | 0.0 | 23.0 | 0.0 | -43.9 | 67.6 | 0.500 | 0.010 | - | - | - |
| | 21 min | ACMC/HMC | 3 | -2.4 | 0.1 | 18.3 | 0.1 | | | 0.573 | 0.013 | 3 | 0.406 | 0.058 |
| | 61 min | HMC | 3 | -1.9 | 0.1 | 13.6 | 0.2 | -41.2 | 55.5 | 0.662 | 0.001 | 3 | 0.272 | 0.052 |
| | 1 day | HMC | 3 | -1.6 | 0.1 | 10.4 | 0.4 | -40.4 | 51.6 | 0.652 | 0.005 | 3 | 0.254 | 0.046 |
| | 1 week | HMC | 4 | -1.5 | 0.1 | 9.7 | 0.1 | -43.4 | 54.0 | 0.648 | 0.006 | 3 | 0.301 | 0.023 |
| | 2 months | HMC | 3 | -1.3 | 0.0 | 9.0 | 0.0 | | | 0.650 | 0.010 | 2 | 0.264 | 0.024 |
| | 1 year | HMC | 3 | -1.5 | 0.0 | 8.6 | 0.2 | -43.0 | 52.5 | 0.631 | 0.019 | 3 | 0.306 | 0.044 |
| T_20°C | 0.3 min | ACMC | 2 | -3.0 | 0.4 | 22.2 | 1.0 | | | 0.506 | 0.052 | - | - | - |
| | 5 min | ACMC | 3 | -2.9 | 0.1 | 21.0 | 0.6 | -44.3 | 66.1 | 0.483 | 0.015 | - | - | - |
| | 21 min | ACMC/HMC | 3 | -2.6 | 0.1 | 16.8 | 0.5 | | | 0.566 | 0.007 | 3 | 0.390 | 0.044 |
| | 61 min | HMC | 6 | -2.0 | 0.1 | 10.1 | 0.1 | -42.5 | 53.5 | 0.659 | 0.012 | 3 | 0.296 | 0.067 |
| | 1 day | HMC | 3 | -1.7 | 0.2 | 6.9 | 0.5 | -42.2 | 50.1 | 0.620 | 0.002 | 3 | 0.253 | 0.025 |
| | 1 week | HMC | 6 | -1.6 | 0.1 | 6.1 | 0.3 | -43.1 | 50.2 | 0.651 | 0.009 | 4 | 0.283 | 0.017 |
| | 2 months | HMC | 4 | -1.4 | 0.1 | 4.2 | 0.4 | | | 0.687 | 0.008 | 3 | 0.289 | 0.086 |
| | 1 year | HMC | 3 | -1.4 | 0.0 | 3.3 | 0.1 | -43.1 | 47.3 | 0.642 | 0.002 | 3 | 0.319 | 0.042 |
| T_40°C | 0.3 min | ACMC | 2 | -2.8 | 0.1 | 22.6 | 0.2 | | | 0.478 | 0.006 | 2 | 0.539 | 0.010 |
| | 5 min | ACMC | 3 | -2.8 | 0.3 | 20.1 | 0.5 | -45.1 | 66.0 | 0.496 | 0.007 | - | - | - |
| | 21 min | ACMC/HMC | 3 | -2.5 | 0.1 | 7.9 | 0.5 | | | 0.579 | 0.005 | 3 | 0.456 | 0.043 |
| | 61 min | HMC | 3 | -2.0 | 0.1 | 2.1 | 0.2 | -43.3 | 46.4 | 0.629 | 0.008 | 3 | 0.315 | 0.018 |
| | 1 day | HMC | 4 | -1.8 | 0.1 | -2.0 | 1.0 | -43.4 | 42.3 | 0.609 | 0.008 | 2 | 0.308 | 0.001 |
| | 1 week | HMC | 5 | -1.2 | 0.1 | -4.9 | 0.2 | -43.0 | 39.0 | 0.654 | 0.005 | 3 | 0.268 | 0.016 |
| | 2 months | HMC | 4 | -1.0 | 0.0 | -5.5 | 0.2 | | | 0.621 | 0.018 | - | - | - |
| | 1 year | HMC | 3 | -1.1 | 0.0 | -6.4 | 0.1 | -43.1 | 37.6 | 0.624 | 0.005 | 3 | 0.276 | 0.053 |
| T_60°C | 0.3 min | ACMC | 3 | -2.7 | 0.1 | 22.3 | 0.3 | | | 0.503 | 0.010 | 3 | 0.545 | 0.044 |
| | 5 min | ACMC | 4 | -2.9 | 0.1 | 19.1 | 0.2 | -45.1 | 65.1 | 0.482 | 0.008 | 3 | 0.550 | 0.042 |
| | 21 min | ACMC/HMC | 2 | -2.4 | 0.1 | -0.9 | 0.4 | | | 0.546 | 0.005 | 3 | 0.428 | 0.017 |
| | 61 min | HMC | 4 | -2.2 | 0.2 | -9.8 | 0.4 | -44.2 | 35.3 | 0.575 | 0.006 | - | - | - |
| | 1 day | HMC | 4 | -2.2 | 0.1 | -12.9 | 0.5 | -43.4 | 31.4 | 0.587 | 0.009 | 3 | 0.285 | 0.020 |
| | 1 week | HMC | 3 | -2.1 | 0.1 | -14.9 | 0.6 | -43.6 | 29.5 | 0.561 | 0.013 | 2 | 0.259 | 0.023 |
| | 2 months | HMC | 2 | -1.9 | 0.1 | -15.4 | 0.0 | | | 0.582 | 0.000 | 2 | 0.299 | 0.019 |
| | 1 year | HMC | 4 | -1.8 | 0.1 | -15.0 | 0.1 | -43.5 | 29.4 | 0.553 | 0.016 | - | - | - |

**Table 15.** Isotopic data for the ACMC transformation experiments. Time refers to the experimental run time when the sample was taken.

| **Experimental phase** | **Experiment** | **k ($s^{-1}$)** | **$t_{99}$ (days)** |
|---|---|---|---|
| **Transformation From ACMC to HMC (0 min to 61 min)** | T_10°C | 0.00011 ($\pm 1.98 \times 10^{-5}$) | - |
| | T_20°C | 0.0001306 ($\pm 6.584 \times 10^{-6}$) | - |
| | T_40°C | 0.0001978 ($\pm 6.980 \times 10^{-5}$) | - |
| | T_60°C | 0.000417 ($\pm 1.068 \times 10^{-4}$) | - |
| | **Ea = 20.528 (±3.149) kJ/mol** | | |
| **Final 3 HMC samples (1 week to 1 year)** | T_10°C | 1.959 ($\pm 1.205$) $\times 10^{-9}$ | 25,299 |
| | T_20°C | 5.540 ($\pm 3.386$) $\times 10^{-9}$ | 8118 |
| | T_40°C | 4.944 ($\pm 1.394$) $\times 10^{-9}$ | 8125 |
| | T_60°C | $3.568 \times 10^{-8}$ | 699 |
| | **Ea = 38.862 (±13.104) kJ/mol** | | |

**Table 16.** Summary of the oxygen isotope exchange kinetics with water during the transformation of ACMC to HMC and for the final 3 HMC samples, including the pseudo-first-order kinetic rate constant, k ($s^{-1}$), apparent activation energy, $E_a$ (kJ/mol), and the time to reach 99 % oxygen isotope equilibration, $t_{99}$ (days).

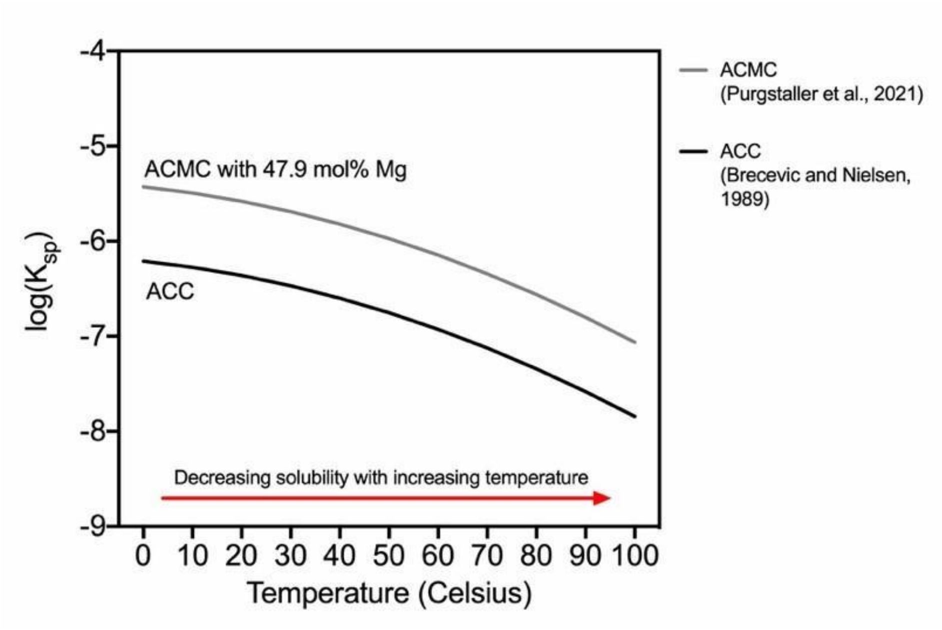

**Fig. S4.** Plot showing the relationship between the log of the solubility product constant, $K_{sp}$, and temperature for ACMC (Purgstaller et al., 2021) and ACC (Brecevic and Nielsen, 1989), which results in higher dissolution of both phases at lower temperatures.

| Experiment | Time | Composition | HMC | ARG | HMG | $[\mathrm{Mg}]_{\mathrm{XRD}}$ of HMC | $[\mathrm{Ca}]_{\mathrm{L}}$ | $[\mathrm{Ca}]_{\mathrm{S}}$ | $[\mathrm{Mg}]_{\mathrm{L}}$ | $[\mathrm{Mg}]_{\mathrm{S}}$ | $[\mathrm{Mg}]_{\mathrm{S}}$ |
|---|---|---|---|---|---|---|---|---|---|---|---|
| | min/day | | wt.% | wt.% | wt.% | mol% | mmol/L | mmol/kg | mmol/L | mmol/kg | mol% |
| Initial ACMC | 0 | ACMC | - | - | - | - | 0.00 | 4707 | 29.0 | 4326 | 47.9 |
| T_10°C | 0.3 min | ACMC | - | - | - | - | 2.5 | 4675 | 41.7 | 3980 | 46.0 |
| | 5 min | ACMC | - | - | - | - | 35.1 | 5416 | 84.3 | 3314 | 38.0 |
| | 11 min | ACMC | - | - | - | - | 41.3 | 5726 | 94.3 | 3144 | 35.4 |
| | 21 min | ACMC, HMC_I | - | - | - | I: 4.8 | 24.5 | 6596 | 110.1 | 2256 | 25.5 |
| | 61 min | HMC_I, HMC_II | - | - | - | I: 6.2, II: 14.5 | 12.9 | 8164 | 125.2 | 1057 | 11.4 |
| | 1 day | HMC_I, HMC_II, ARG | I: 56, II: 42 | 2 | 0 | I: 6.6, II: 15.4 | 2.3 | 8056 | 122.0 | 1212 | 13.0 |
| | 1 week | HMC_I, HMC_II, ARG | I: 57, II: 41 | 3 | 0 | I: 7.1, II: 16.3 | 0.6 | 8096 | 120.3 | 1363 | 14.4 |
| | 2 months | HMC_I, HMC_II, ARG | I: 56, II: 41 | 4 | 0 | I: 6.4, II: 15.8 | 0.3 | 7872 | 120.7 | 1453 | 15.5 |
| | 1 year | HMC_I, HMC_II, ARG | I: 53, II: 43 | 4 | 0 | I: 6.3, II: 15.9 | 0.26 | 7857 | 120.3 | 1574 | 16.6 |
| T_20°C | 0.3 min | ACMC | - | - | - | - | 2.1 | 4746 | 41.4 | 3973 | 45.6 |
| | 5 min | ACMC | - | - | - | - | 25.1 | 5134 | 81.8 | 3140 | 38.0 |
| | 11 min | ACMC, HMC | - | - | - | 11.9 | 20.8 | 5653 | 92.8 | 2998 | 34.7 |
| | 21 min | ACMC, HMC | - | - | - | 12.8 | 16.7 | 6188 | 105.6 | 2590 | 29.5 |
| | 61 min | HMC, ARG | - | - | - | 17.0 | 6.9 | 8021 | 117.7 | 1597 | 16.6 |
| | 1 day | HMC, ARG | 99 | 1 | 0 | 18.0 | 0.9 | 7733 | 114.2 | 1816 | 19.0 |
| | 1 week | HMC, ARG | 99 | 1 | 0 | 18.3 | 0.3 | 7244 | 111.6 | 1901 | 20.8 |
| | 2 months | HMC, ARG | 98 | 2 | 0 | 18.8 | 0.2 | 7269 | 110.4 | 2077 | 22.2 |
| | 1 year | HMC, ARG | 96 | 4 | 0 | 18.4 | 0.2 | 6969 | 110.9 | 2279 | 24.6 |
| T_40°C | 0.3 min | ACMC | - | - | - | - | 1.7 | 4628 | 38.3 | 4326 | 47.0 |
| | 5 min | ACMC | - | - | - | - | 14.2 | 5462 | 75.3 | 4104 | 39.3 |
| | 11 min | ACMC, HMC | - | - | - | 23.0 | 10.5 | 5939 | 85.5 | 3269 | 35.5 |
| | 21 min | HMC, ACMC | - | - | - | 28.4 | 7.8 | 6189 | 97.1 | 3530 | 30.4 |
| | 61 min | HMC | - | - | - | 29.7 | 1.1 | 6226 | 97.0 | 2697 | 29.6 |
| | 1 day | HMC | 100 | 0 | 0 | 30.3 | 0.4 | 6239 | 85.1 | 2612 | 33.0 |
| | 1 week | HMC, HMG | 94 | 0 | 6 | 29.7 | 0.3 | 6178 | 65.2 | 3070 | 40.1 |
| | 2 months | HMC, HMG | 91 | 0 | 9 | 30.9 | 0.3 | 5587 | 64.8 | 4139 | 41.2 |
| | 1 year | HMC, HMG | 90 | 0 | 10 | 29.6 | 0.47 | 5759 | 65.4 | 3922 | 40.9 |
| T_60°C | 0.3 min | ACMC | - | - | - | - | 1.7 | 4358 | 32.9 | 3943 | 47.5 |
| | 5 min | ACMC | - | - | - | - | 6.6 | 4976 | 58.9 | 3758 | 43.0 |
| | 11 min | ACMC, HMC | - | - | - | 34.2 | 5.5 | 5007 | 65.6 | 3492 | 41.1 |
| | 21 min | HMC, ACMC | - | - | - | 39.4 | 3.9 | 5386 | 67.1 | 3660 | 40.5 |
| | 61 min | HMC | - | - | - | 39.8 | 0.6 | 5165 | 61.3 | 3619 | 41.2 |
| | 1 day | HMC | 100 | 0 | 0 | 40.7 | 0.6 | 5337 | 48.9 | 4163 | 43.8 |
| | 1 week | HMC | 100 | 0 | 0 | 40.5 | 0.5 | 5133 | 43.3 | 4227 | 45.2 |
| | 2 months | HMC | 100 | 0 | 0 | 40.6 | 0.8 | 5258 | 42.2 | 4363 | 45.3 |
| | 1 year | HMC | 100 | 0 | 0 | 40.9 | 2.5 | 5000 | 40.8 | 4479 | 47.3 |

**Table S1.** Mineralogical and chemical composition of the solids and reactive solution obtained at certain reaction times during experiments performed from 10 to 60°C.

$[Mg]_{XRD}$ of HMC refers to the Mg content of HMC, while $[Mg]_s$ refers to the Mg content in the bulk solid. The data presented in this table is a subset of the data presented in Purgstaller et al. (2021).

## S1. Saturation Index

Aqueous speciation in the reactive solutions was calculated using the software PHREEQC and its minteq.4 database. The saturation index of the solution with respect to calcite ($SI_{calcite}$) is defined as:

$$SI_{calcite} = log\left(\frac{a_{Ca^{2+}} \cdot a_{CO_3^{2-}}}{K_{calcite}}\right) \quad \text{(S1)}$$

where $a_i$ denotes the activity of the *i*th species in aqueous solution. The values of the solubility product of calcite ($K_{calcite}$) in the temperature range from 10 to 60°C were derived from Plummer and Busenberg (1982).

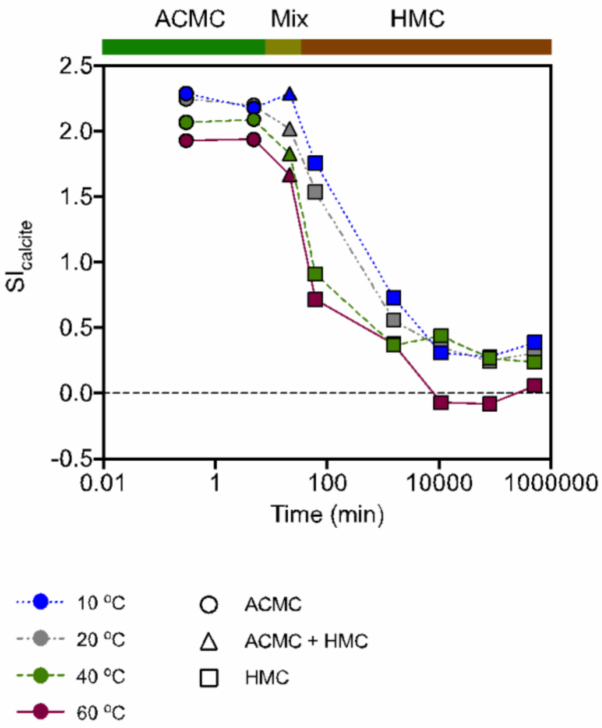

**Fig. S5.** Temporal evolution for reactions times up to ~1 year for $SI_{calcite}$ for ACMC transformed at 10, 20, 40, and 60 °C.

# REFERENCES

Addadi, L., Raz, S. and Weiner, S., 2003. Taking advantage of disorder: amorphous calcium carbonate and its roles in biomineralization. *Advanced Materials*, *15*(12), pp.959-970. https://doi.org/10.1002/adma.200300381

Agbaje, O.B., George, S.C., Zhang, Z., Brock, G.A. and Holmer, L.E., 2020. Characterization of organophosphatic brachiopod shells: spectroscopic assessment of collagen matrix and biomineral components. *RSC Advances*, *10*(63), pp.38456-38467. DOI: 10.1039/D0RA07523J

Albéric, M., Bertinetti, L., Zou, Z., Fratzl, P., Habraken, W. and Politi, Y., 2018. The crystallization of amorphous calcium carbonate is kinetically governed by ion impurities and water. *Advanced Science*, *5*(5), p.1701000. https://doi.org/10.1002/advs.201701000

Aufort, J., Raiteri, P. and Gale, J.D., 2022. Computational Insights into Mg2+ Dehydration in the Presence of Carbonate. *ACS Earth and Space Chemistry*. https://doi.org/10.1021/acsearthspacechem.1c00389

Atasoy, D., 2015. *Clumped Isotope Signals of Biogenic and Non-biogenic Carbonates* (Doctoral dissertation, University of Miami).

Bajnai, D., Fiebig, J., Tomašových, A., Milner Garcia, S., Rollion-Bard, C., Raddatz, J., Löffler, N., Primo-Ramos, C. and Brand, U., 2018. Assessing kinetic fractionation in brachiopod calcite using clumped isotopes. *Scientific Reports*, *8*(1), pp.1-12. https://doi.org/10.1038/s41598-017-17353-7

Bajnai, D., Guo, W., Spötl, C., Coplen, T.B., Methner, K., Löffler, N., Krsnik, E., Gischler, E., Hansen, M., Henkel, D. and Price, G.D., 2020. Dual clumped isotope thermometry resolves kinetic biases in carbonate formation temperatures. *nature communications*, *11*(1), pp.1-9. https://doi.org/10.1038/s41467-020-17501-0

Beck, W.C., Grossman, E.L. and Morse, J.W., 2005. Experimental studies of oxygen isotope fractionation in the carbonic acid system at 15, 25, and 40 C. *Geochimica et Cosmochimica Acta*, *69*(14), pp.3493-3503. https://doi.org/10.1016/j.gca.2005.02.003

Beniash, E., Addadi, L. and Weiner, S., 1999. Cellular control over spicule formation in sea urchin embryos: A structural approach. *Journal of structural biology*, *125*(1), pp.50-62. https://doi.org/10.1006/jsbi.1998.4081

Bernasconi, S.M., Müller, I.A., Bergmann, K.D., Breitenbach, S.F., Fernandez, A., Hodell, D.A., Jaggi, M., Meckler, A.N., Millan, I. and Ziegler, M., 2018. Reducing uncertainties in carbonate clumped isotope analysis through consistent carbonate-based standardization. *Geochemistry, Geophysics, Geosystems*, *19*(9), pp.2895-2914. https://doi.org/10.1029/2017GC007385

Bernasconi, S.M., Daëron, M., Bergmann, K.D., Bonifacie, M., Meckler, A.N., Affek, H.P., Anderson, N., Bajnai, D., Barkan, E., Beverly, E. and Blamart, D., 2021. InterCarb: A community effort to improve interlaboratory standardization of the carbonate clumped isotope thermometer using carbonate standards. *Geochemistry, Geophysics, Geosystems*, *22*(5), p.e2020GC009588. https://doi.org/10.1029/2020GC009588

Berner, R.A., 1975. The role of magnesium in the crystal growth of calcite and aragonite from sea water. *Geochimica et Cosmochimica Acta*, *39*(4), pp.489-504. https://doi.org/10.1016/0016-7037(75)90102-7

Bleuzen, A., Pittet, P.A., Helm, L. and Merbach, A.E., 1997. Water exchange on magnesium (II) in aqueous solution: a variable temperature and pressure 17O NMR study. *Magnetic resonance in chemistry*, 35(11), pp.765-773. https://doi.org/10.1002/(SICI)1097-458X(199711)35:11<765::AID-OMR169>3.0.CO;2-F

Bots, P., Benning, L.G., Rodriguez-Blanco, J.D., Roncal-Herrero, T. and Shaw, S., 2012. Mechanistic insights into the crystallization of amorphous calcium carbonate (ACC). *Crystal Growth & Design*, *12*(7), pp.3806-3814. https://doi.org/10.1021/cg300676b

Coplen, T.B., Kendall, C. and Hopple, J., 1983. Comparison of stable isotope reference samples. *Nature*, 302(5905), pp.236-238. https://doi.org/10.1038/302236a0

Daëron, M., Blamart, D., Peral, M. and Affek, H.P., 2016. Absolute isotopic abundance ratios and the accuracy of Δ47 measurements. *Chemical Geology*, 442, pp.83-96. https://doi.org/10.1016/j.chemgeo.2016.08.014

Davies, A.J. and John, C.M., 2019. The clumped (13C18O) isotope composition of echinoid calcite: Further evidence for “vital effects” in the clumped isotope proxy. *Geochimica et Cosmochimica Acta*, *245*, pp.172-189.

Eagle, R., Schauble, E., Tripati, A., Tütken, T., Fricke, H., Hulbert, R. and Eiler, J., 2010. ‘Clumped isotope’thermometry in bioapatite. *Geochimica et Cosmochimica Acta*, 74(12), p.A256. http://dx.doi.org/10.1016/j.gca.2010.04.029

Davies, A.J. and John, C.M., 2019. The clumped (13C18O) isotope composition of echinoid calcite: Further evidence for “vital effects” in the clumped isotope proxy. *Geochimica et Cosmochimica Acta*, 245, pp.172-189. https://doi.org/10.1016/j.gca.2018.07.038

DeCarlo, T.M., 2018. Characterizing coral skeleton mineralogy with Raman spectroscopy. *Nature Communications*, *9*(1), pp.1-3. DeCarlo, T.M., 2018. Characterizing coral skeleton mineralogy with Raman spectroscopy. *Nature Communications*, *9*(1), pp.1-3.

Defliese, W.F., Hren, M.T. and Lohmann, K.C., 2015. Compositional and temperature effects of phosphoric acid fractionation on Δ47 analysis and implications for discrepant calibrations. *Chemical Geology*, *396*, pp.51-60. https://doi.org/10.1016/j.chemgeo.2014.12.018

Defliese, W.F. and Tripati, A., 2020. Analytical effects on clumped isotope thermometry: Comparison of a common sample set analyzed using multiple instruments, types of standards, and standardization windows. *Rapid Communications in Mass Spectrometry*, *34*(8), p.e8666. https://doi.org/10.1002/rcm.8666

Dennis, K.J., Affek, H.P., Passey, B.H., Schrag, D.P. and Eiler, J.M., 2011. Defining an absolute reference frame for 'clumped'isotope studies of CO2. *Geochimica et Cosmochimica Acta*, *75*(22), pp.7117-7131. https://doi.org/10.1016/j.gca.2011.09.025

Dennis, K.J., Cochran, J.K., Landman, N.H. and Schrag, D.P., 2013. The climate of the Late Cretaceous: New insights from the application of the carbonate clumped isotope thermometer to Western Interior Seaway macrofossil. *Earth and Planetary Science Letters*, *362*, pp.51-65. https://doi.org/10.1016/j.epsl.2012.11.036

De Yoreo, J.J., Gilbert, P.U., Sommerdijk, N.A., Penn, R.L., Whitelam, S., Joester, D., Zhang, H., Rimer, J.D., Navrotsky, A., Banfield, J.F. and Wallace, A.F., 2015. Crystallization by particle attachment in synthetic, biogenic, and geologic environments. *Science*, *349*(6247). DOI: 10.1126/science.aaa6760

Dietzel, M., Purgstaller, B., Kluge, T., Leis, A. and Mavromatis, V., 2020. Oxygen and clumped isotope fractionation during the formation of Mg calcite via an amorphous precursor. *Geochimica et Cosmochimica Acta*, *276*, pp.258-273. https://doi.org/10.1016/j.gca.2020.02.032

Fernandez-Diaz, L., Putnis, A., Prieto, M. and Putnis, C.V., 1996. The role of magnesium in the crystallization of calcite and aragonite in a porous medium. *Journal of sedimentary research*, *66*(3), pp.482-491. https://doi.org/10.1306/D4268388-2B26-11D7-8648000102C1865D

Fiebig, J., Bajnai, D., Löffler, N., Methner, K., Krsnik, E., Mulch, A. and Hofmann, S., 2019. Combined high-precision∆ 48 and∆ 47 analysis of carbonates. *Chemical Geology*, *522*, pp.186-191. https://doi.org/10.1016/j.chemgeo.2019.05.019

Fiebig, J., Daëron, M., Bernecker, M., Guo, W., Schneider, G., Boch, R., Bernasconi, S.M., Jautzy, J. and Dietzel, M., 2021. Calibration of the dual clumped isotope thermometer for carbonates. *Geochimica et Cosmochimica Acta*, *312*, pp.235-256. https://doi.org/10.1016/j.gca.2021.07.012

Fry, B., 2002. Conservative mixing of stable isotopes across estuarine salinity gradients: a conceptual framework for monitoring watershed influences on downstream fisheries production. *Estuaries*, *25*(2), pp.264-271. https://doi.org/10.1007/BF02691313

Gal, A., Habraken, W., Gur, D., Fratzl, P., Weiner, S. and Addadi, L., 2013. Calcite crystal growth by a solid-state transformation of stabilized amorphous calcium carbonate nanospheres in a hydrogel. *Angewandte Chemie International Edition*, *52*(18), pp.4867-4870. https://doi.org/10.1002/anie.201210329

Goetschl, K.E., Purgstaller, B., Dietzel, M. and Mavromatis, V., 2019. Effect of sulfate on magnesium incorporation in low-magnesium calcite. *Geochimica et Cosmochimica Acta*, *265*, pp.505-519. https://doi.org/10.1016/j.gca.2019.07.024

Goldsmith, J.R., Graf, D.L. and Heard, H.C., 1961. Lattice constants of the calcium magnesium carbonates. *American Mineralogist,* 46, pp.453–459.

Giuffre, A.J., Gagnon, A.C., De Yoreo, J.J. and Dove, P.M., 2015. Isotopic tracer evidence for the amorphous calcium carbonate to calcite transformation by dissolution–reprecipitation. *Geochimica et Cosmochimica Acta*, *165*, pp.407-417. https://doi.org/10.1016/j.gca.2015.06.002

Ghosh, P., Adkins, J., Affek, H., Balta, B., Guo, W., Schauble, E.A., Schrag, D. and Eiler, J.M., 2006. 13C–18O bonds in carbonate minerals: a new kind of paleothermometer. *Geochimica et Cosmochimica Acta*, *70*(6), pp.1439-1456. https://doi.org/10.1016/j.gca.2005.11.014

Griesshaber, E., Kelm, K., Sehrbrock, A., Mader, W., Mutterlose, J., Brand, U. and Schmahl, W.W., 2009. Amorphous calcium carbonate in the shell material of the brachiopod Megerlia truncata. *European Journal of Mineralogy*, *21*(4), pp.715-723. https://doi.org/10.1127/0935-1221/2009/0021-1950

Guo, W., Mosenfelder, J.L., Goddard III, W.A. and Eiler, J.M., 2009. Isotopic fractionations associated with phosphoric acid digestion of carbonate minerals: Insights from first-principles theoretical modeling and clumped isotope measurements. *Geochimica et Cosmochimica Acta*, *73*(24), pp.7203-7225. https://doi.org/10.1016/j.gca.2009.05.071

Guo, W. and Zhou, C., 2019. Patterns and controls of disequilibrium isotope effects in speleothems: insights from an isotope-enabled diffusion-reaction model and implications for quantitative thermometry. *Geochimica et Cosmochimica Acta*, *267*, pp.196-226. https://doi.org/10.1016/j.gca.2019.07.028

Guo, W., 2020. Kinetic clumped isotope fractionation in the DIC-H2O-CO2 system: patterns, controls, and implications. *Geochimica et Cosmochimica Acta*, *268*, pp.230-257. https://doi.org/10.1016/j.gca.2019.07.055

Han, T.Y.J. and Aizenberg, J., 2008. Calcium carbonate storage in amorphous form and its template-induced crystallization. *Chemistry of Materials*, *20*(3), pp.1064-1068. https://doi.org/10.1021/cm702032v

Henkes, G.A., Passey, B.H., Wanamaker Jr, A.D., Grossman, E.L., Ambrose Jr, W.G. and Carroll, M.L., 2013. Carbonate clumped isotope compositions of modern marine mollusk and brachiopod shells. *Geochimica et Cosmochimica Acta*, *106*, pp.307-325. https://doi.org/10.1016/j.gca.2012.12.020

Henkes, G.A., Passey, B.H., Grossman, E.L., Shenton, B.J., Pérez-Huerta, A. and Yancey, T.E., 2014. Temperature limits for preservation of primary calcite clumped isotope paleotemperatures. *Geochimica et cosmochimica acta*, *139*, pp.362-382. https://doi.org/10.1016/j.gca.2014.04.040

Hill, P.S., Tripati, A.K. and Schauble, E.A., 2014. Theoretical constraints on the effects of pH, salinity, and temperature on clumped isotope signatures of dissolved inorganic carbon species and precipitating carbonate minerals. *Geochimica et cosmochimica acta*, *125*, pp.610-652. https://doi.org/10.1016/j.gca.2013.06.018

Hill, P.S., Schauble, E.A. and Tripati, A., 2020. Theoretical constraints on the effects of added cations on clumped, oxygen, and carbon isotope signatures of dissolved inorganic carbon species and minerals. *Geochimica et Cosmochimica Acta*, *269*, pp.496-539. https://doi.org/10.1016/j.gca.2019.10.016

Horita, J., Ueda, A., Mizukami, K. and Takatori, I., 1989. Automatic δD and δ18O analyses of multi-water samples using H2-and CO2-water equilibration methods with a common equilibration set-up. *International Journal of Radiation Applications and Instrumentation. Part A. Applied Radiation and Isotopes*, *40*(9), pp.801-805. https://doi.org/10.1016/0883-2889(89)90100-7

Hu, Q., Nielsen, M.H., Freeman, C.L., Hamm, L.M., Tao, J., Lee, J.R.I., Han, T.Y.J., Becker, U., Harding, J.H., Dove, P.M. and De Yoreo, J.J., 2012. The thermodynamics of calcite nucleation at organic interfaces: Classical vs. non-classical pathways. *Faraday Discussions*, *159*(1), pp.509-523.
https://doi.org/10.1039/C2FD20124K

Ihli, J., Kim, Y.Y., Noel, E.H. and Meldrum, F.C., 2013. The effect of additives on amorphous calcium carbonate (acc): janus behavior in solution and the solid state. *Advanced Functional Materials*, *23*(12), pp.1575-1585.
https://doi.org/10.1002/adfm.201201805

Kimball, J., Eagle, R. and Dunbar, R., 2016. Carbonate “clumped” isotope signatures in aragonitic scleractinian and calcitic gorgonian deep-sea corals. *Biogeosciences*, *13*(23), pp.6487-6505. https://doi.org/10.5194/bg-13-6487-2016

Kluge, T., John, C.M., Boch, R. and Kele, S., 2018. Assessment of factors controlling clumped isotopes and δ18O values of hydrothermal vent calcites. *Geochemistry, Geophysics, Geosystems*, *19*(6), pp.1844-1858. https://doi.org/10.1029/2017GC006969

Koishi, A., Fernandez-Martinez, A., Ruta, B., Jimenez-Ruiz, M., Poloni, R., Di Tommaso, D., Zontone, F., Waychunas, G.A. and Montes-Hernandez, G., 2018. Role of impurities in the kinetic persistence of amorphous calcium carbonate: A nanoscopic dynamics view. *The Journal of Physical Chemistry C*, *122*(29), pp.16983-16991. https://doi.org/10.1021/acs.jpcc.8b05189

Konrad, F., Gallien, F., Gerard, D.E. and Dietzel, M., 2016. Transformation of amorphous calcium carbonate in air. *Crystal growth & design*, *16*(11), pp.6310-6317. https://doi.org/10.1021/acs.cgd.6b00906.

Jacob, D.E., Wirth, R., Agbaje, O.B.A., Branson, O. and Eggins, S.M., 2017. Planktic foraminifera form their shells via metastable carbonate phases. *Nature communications*, *8*(1), pp.1-9. https://doi.org/10.1038/s41467-017-00955-0

Nielsen Lammers, L. and Koishi, A., 2021. Isotopic Tracers of Nonclassical Crystallization. In *Crystallization via Nonclassical Pathways Volume 2: Aggregation, Biomineralization, Imaging & Application* (pp. 167-198). American Chemical Society. DOI: 10.1021/bk-2021-1383.ch007

Lasaga, A.C., 1998. Kinetic Theory in the Earth Sciences. *Geological Magazine*. https://doi.org/10.1017/S0016756800234614

Lee, J.R., Han, T.Y.J., Willey, T.M., Wang, D., Meulenberg, R.W., Nilsson, J., Dove, P.M., Terminello, L.J., van Buuren, T. and De Yoreo, J.J., 2007. Structural development of mercaptophenol self-assembled monolayers and the overlying mineral phase during templated CaCO3 crystallization from a transient amorphous film. *Journal of the American Chemical Society*, *129*(34), pp.10370-10381. https://doi.org/10.1021/ja071535w

Lloyd, M.K., Ryb, U. and Eiler, J.M., 2018. Experimental calibration of clumped isotope reordering in dolomite. *Geochimica et Cosmochimica Acta*, *242*, pp.1-20. https://doi.org/10.1016/j.gca.2018.08.036

Loste, E., Wilson, R.M., Seshadri, R. and Meldrum, F.C., 2003. The role of magnesium in stabilising amorphous calcium carbonate and controlling calcite morphologies. *Journal of Crystal growth*, *254*(1-2), pp.206-218. https://doi.org/10.1016/S0022-0248(03)01153-9

Lucarelli, J., Carroll, H., Elliott, B., Eagle, R. and Tripati, A., 2021. Equilibrated gas and carbonate standard-derived paired clumped isotope (Δ47 and Δ48) values on the absolute reference frame. https://doi.org/10.31223/X5T318

Lucarelli, J.K., Purgstaller, B., Parven, Z., Watkins, J.M., Eagle, R., Dietzel, M. and Tripati, A., 2022. Paired Δ47 and Δ48 analyses and model calculations constrain equilibrium, experimentally-manipulated kinetic isotope effects, and mixing effects in calcite. https://doi.org/10.31223/X5NS7W

Markham, G.D., Glusker, J.P., Bock, C.L., Trachtman, M. and Bock, C.W., 1996. Hydration energies of divalent beryllium and magnesium ions: An ab initio molecular orbital study. *The Journal of Physical Chemistry*, *100*(9), pp.3488-3497. https://doi.org/10.1021/jp952531t

Mass, T., Giuffre, A.J., Sun, C.Y., Stifler, C.A., Frazier, M.J., Neder, M., Tamura, N., Stan, C.V., Marcus, M.A. and Gilbert, P.U., 2017. Amorphous calcium carbonate particles form coral skeletons. *Proceedings of the National Academy of Sciences*, *114*(37), pp.E7670-E7678. https://doi.org/10.1073/pnas.1707890114

Mavromatis, V., Schmidt, M., Botz, R., Comas-Bru, L. and Oelkers, E.H., 2012. Experimental quantification of the effect of Mg on calcite–aqueous fluid oxygen isotope fractionation. *Chemical geology*, *310*, pp.97-105. https://doi.org/10.1016/j.chemgeo.2012.03.027

Mavromatis, V., Purgstaller, B., Dietzel, M., Buhl, D., Immenhauser, A. and Schott, J., 2017. Impact of amorphous precursor phases on magnesium isotope signatures of Mg-calcite. *Earth and planetary science letters*, *464*, pp.227-236. https://doi.org/10.1016/j.epsl.2017.01.031

McConnaughey, T.A. and Gillikin, D.P., 2008. Carbon isotopes in mollusk shell carbonates. *Geo-Marine Letters*, *28*(5), pp.287-299. https://doi.org/10.1007/s00367-008-0116-4

Merkel, C., Griesshaber, E., Kelm, K., Neuser, R., Jordan, G., Logan, A., Mader, W. and Schmahl, W.W., 2007. Micromechanical properties and structural characterization of modern inarticulated brachiopod shells. *Journal of Geophysical Research: Biogeosciences*, *112*(G2). https://doi.org/10.1029/2006JG000253

Nielsen Lammers, L. and Koishi, A., 2021. Isotopic Tracers of Nonclassical Crystallization. In *Crystallization via Nonclassical Pathways Volume 2: Aggregation, Biomineralization, Imaging & Application* (pp. 167-198). American Chemical Society. DOI: 10.1021/bk-2021-1383.ch007

Passey, B.H. and Henkes, G.A., 2012. Carbonate clumped isotope bond reordering and geospeedometry. *Earth and Planetary Science Letters*, *351*, pp.223-236. https://doi.org/10.1016/j.epsl.2012.07.021

Plummer, L.N. and Busenberg, E., 1982. The solubilities of calcite, aragonite and vaterite in CO2-H2O solutions between 0 and 90 C, and an evaluation of the aqueous model for the system CaCO3-CO2-H2O. *Geochimica et cosmochimica acta*, *46*(6), pp.1011-1040. https://doi.org/10.1016/0016-7037(82)90056-4

Politi, Y., Arad, T., Klein, E., Weiner, S. and Addadi, L., 2004. Sea urchin spine calcite forms via a transient amorphous calcium carbonate phase. *Science*, *306*(5699), pp.1161-1164. https://doi.org/10.1126/science.1102289

Pontoni, D., Bolze, J., Dingenouts, N., Narayanan, T. and Ballauff, M., 2003. Crystallization of calcium carbonate observed in-situ by combined small-and wide-angle X-ray scattering. *The Journal of Physical Chemistry B*, *107*(22), pp.5123-5125. https://doi.org/10.1021/jp0343640

Purgstaller, B., Konrad, F., Dietzel, M., Immenhauser, A. and Mavromatis, V., 2017. Control of Mg2+/Ca2+ activity ratio on the formation of crystalline carbonate minerals via an amorphous precursor. *Crystal growth & design*, *17*(3), pp.1069-1078. https://doi.org/10.1021/acs.cgd.6b01416

Purgstaller, B., Goetschl, K.E., Mavromatis, V. and Dietzel, M., 2019. Solubility investigations in the amorphous calcium magnesium carbonate system. *CrystEngComm*, *21*(1), pp.155-164. DOI: 10.1039/C8CE01596A

Purgstaller, B., Mavromatis, V., Goetschl, K.E., Steindl, F.R. and Dietzel, M., 2021. Effect of temperature on the transformation of amorphous calcium magnesium carbonate with near-dolomite stoichiometry into high Mg-calcite. *CrystEngComm*, *23*(9), pp.1969-1981. DOI: 10.1039/D0CE01679A

Rodriguez-Blanco, J.D., Shaw, S. and Benning, L.G., 2008. How to make ‘stable’ACC: protocol and preliminary structural characterization. *Mineralogical Magazine*, *72*(1), pp.283-286. doi:10.1180/minmag.2008.072.1.283

Schauble, E.A., Ghosh, P. and Eiler, J.M., 2006. Preferential formation of 13C–18O bonds in carbonate minerals, estimated using first-principles lattice dynamics. *Geochimica et Cosmochimica Acta*, *70*(10), pp.2510-2529. https://doi.org/10.1016/j.gca.2006.02.011

Schmidt, M., Xeflide, S., Botz, R. and Mann, S., 2005. Oxygen isotope fractionation during synthesis of CaMg-carbonate and implications for sedimentary dolomite formation. *Geochimica et cosmochimica Acta*, *69*(19), pp.4665-4674. https://doi.org/10.1016/j.gca.2005.06.025

Schott, J., Pokrovsky, O.S. and Oelkers, E.H., 2009. The link between mineral dissolution/precipitation kinetics and solution chemistry. *Reviews in mineralogy and geochemistry*, *70*(1), pp.207-258. https://doi.org/10.2138/rmg.2009.70.6\

Schulz, K.G., Riebesell, U., Rost, B., Thoms, S. and Zeebe, R.E., 2006. Determination of the rate constants for the carbon dioxide to bicarbonate inter-conversion in pH-buffered seawater systems. *Marine chemistry*, *100*(1-2), pp.53-65. https://doi.org/10.1016/j.marchem.2005.11.001

Shamoto, S.I., Kodama, K., Imaki, T., Nakatani, T., Oshita, H., Kaneko, N., Masuko, K., Sakamoto, K., Yamaguchi, K., Suzuya, K. and Otomo, T., 2014. 2D neutron diffraction imaging on an ammonite. In *Proceedings of the 12th Asia Pacific Physics Conference (APPC12)* (p. 014011). https://doi.org/10.7566/JPSCP.1.014011

Spooner, P.T., Guo, W., Robinson, L.F., Thiagarajan, N., Hendry, K.R., Rosenheim, B.E. and Leng, M.J., 2016. Clumped isotope composition of cold-water corals: A role for vital effects?. *Geochimica et Cosmochimica Acta*, *179*, pp.123-141. https://doi.org/10.1016/j.gca.2016.01.023

Sun, C.Y., Stifler, C.A., Chopdekar, R.V., Schmidt, C.A., Parida, G., Schoeppler, V., Fordyce, B.I., Brau, J.H., Mass, T., Tambutté, S. and Gilbert, P.U., 2020. From particle attachment to space-filling coral skeletons. *Proceedings of the National Academy of Sciences*, *117*(48), pp.30159-30170. https://doi.org/10.1073/pnas.2012025117

Tarutani, T., Clayton, R.N. and Mayeda, T.K., 1969. The effect of polymorphism and magnesium substitution on oxygen isotope fractionation between calcium carbonate and water. *Geochimica et Cosmochimica Acta*, *33*(8), pp.987-996. https://doi.org/10.1016/0016-7037(69)90108-2

Thiagarajan, N., Adkins, J. and Eiler, J., 2011. Carbonate clumped isotope thermometry of deep-sea corals and implications for vital effects. *Geochimica et Cosmochimica Acta*, *75*(16), pp.4416-4425. https://doi.org/10.1016/j.gca.2011.05.004

Uchikawa, J., Chen, S., Eiler, J.M., Adkins, J.F. and Zeebe, R.E., 2021. Trajectory and timescale of oxygen and clumped isotope equilibration in the dissolved carbonate system under normal and enzymatically-catalyzed conditions at 25° C. *Geochimica et Cosmochimica Acta*, *314*, pp.313-333. https://doi.org/10.1016/j.gca.2021.08.014

Upadhyay, D., Lucarelli, J., Arnold, A., Flores, R., Bricker, H., Ulrich, R.N., Jesmok, G., Santi, L., Defliese, W., Eagle, R.A. and Carroll, H.M., 2021. Carbonate clumped isotope analysis (Δ47) of 21 carbonate standards determined via gas-source isotope-ratio mass spectrometry on four instrumental configurations using carbonate-based standardization and multiyear data sets. *Rapid Communications in Mass Spectrometry*, *35*(17), p.e9143. https://doi.org/10.1002/rcm.9143

Wang, Y.W., Kim, Y.Y., Stephens, C.J., Meldrum, F.C. and Christenson, H.K., 2012. In situ study of the precipitation and crystallization of amorphous calcium carbonate (ACC). *Crystal growth & design*, *12*(3), pp.1212-1217. https://doi.org/10.1021/cg201204s

Watkins, J.M. and Hunt, J.D., 2015. A process-based model for non-equilibrium clumped isotope effects in carbonates. *Earth and Planetary Science Letters*, *432*, pp.152-165. https://doi.org/10.1016/j.epsl.2015.09.042

Weiner, S. and Addadi, L., 2011. Crystallization pathways in biomineralization. *Annual review of materials research*, *41*, pp.21-40. https://doi.org/10.1146/annurev-matsci-062910-095803

Weiss, I.M., Tuross, N., Addadi, L.I.A. and Weiner, S., 2002. Mollusc larval shell formation: amorphous calcium carbonate is a precursor phase for aragonite. *Journal of Experimental Zoology*, *293*(5), pp.478-491. https://doi.org/10.1002/jez.90004

Wolf, S.E., Leiterer, J., Kappl, M., Emmerling, F. and Tremel, W., 2008. Early homogenous amorphous precursor stages of calcium carbonate and subsequent crystal growth in levitated droplets. *Journal of the American Chemical Society*, *130*(37), pp.12342-12347. https://doi.org/10.1021/ja800984y

Xto, J.M., 2019. *In situ studies on the crystallisation of amorphous calcium carbonate and the role of magnesium ions in calcium carbonate polymorph selection* (Doctoral dissertation, ETH Zurich). https://doi.org/10.3929/ethz-b-000370593

Zheng, Y.F. and Hoefs, J., 1993. Carbon and oxygen isotopic covariations in hydrothermal calcites. *Mineralium Deposita*, *28*(2), pp.79-89. https://doi.org/10.1007/BF00196332

# SUMMARY

In Chapter 1, we measured the $\Delta_{47}$ and $\Delta_{48}$ values for a suite of standards and samples and compared their values to theoretical equilibrium clumped isotope values for calcite. We determined that the majority of measured values were indistinguishable from theoretical equilibrium. We constructed equilibrium regressions for $\Delta_{47}$-$\Delta_{48}$, $\Delta_{47}$-temperature, and $\Delta_{48}$-temperature using the data from this study combined with published data. We also determined temperature-dependent acid digestion fractionation factors for when calcite mineral is digested in phosphoric acid. These values are useful for comparison of measured values to theoretical mineral clumped isotope values.

In Chapter 2, we constrained equilibrium and kinetic isotope effects from hydration and hydroxylation reactions in calcite, and mixing effects in calcite, using both experimental and modeling approaches. We precipitated calcite under controlled temperature (5 to 25 $^{o}$C) and pH (8.3 to 11.0) with and without the enzyme carbonic anhydrase. We used the samples at low pH with carbonic anhydrase to constrain equilibrium $\Delta_{47}$-$\Delta_{48}$, $\Delta_{47}$-temperature, $\Delta_{48}$-temperature, $\Delta_{47}$-$\delta^{18}$O, and $\Delta_{48}$-$\delta^{18}$O relationships. We determined characteristic clumped and oxygen isotope slopes for hydration and hydroxylation kinetic isotope effects using samples precipitated without carbonic anhydrase at high pH. The measured isotopic values were compared to box model results, which predicted that calcite which precipitates at a faster precipitation rate will inherit larger kinetic isotope effects from hydration and hydroxylation relative to calcite precipitated at slower precipitation rates. Additionally, we used two calcite samples with different $\Delta_{47}$, $\Delta_{48}$, and $\delta^{18}$O values as endmembers in mixing experiments.

We demonstrated the nonlinear mixing of dual clumped isotope values and validated our results using a numerical model.

In Chapter 3, we report the dual clumped isotope composition of amorphous carbonates and transformation products. We precipitated ACMC at 10 °C under isotopic disequilibrium conditions, and transformed the ACMC into HMC at 10, 20, 40, and 60 °C. The $\Delta_{47}$, $\Delta_{48}$, and $\delta^{18}O$ values evolved considerably during transformation, and $\delta^{18}O$ values continued to evolve in fully crystallized HMC while $\Delta_{47}$ and $\Delta_{48}$ were quasi-constant. The clumped and oxygen isotope values of HMC were not consistent with equilibrium values, with the extent of disequilibrium dependent on temperature. Modeling simulations of the dissolved inorganic carbon (DIC) pool predicted disequilibrium isotopic values and rapid isotopic evolution during the transformation period from the dissolution of ACMC, which is the time interval when the isotopic values of HMC are recorded. A comparison of measured isotopic values, modeling, scanning electron microscope imaging, and x-ray diffraction patterns suggested that the crystal formed successively. The disequilibrium clumped and oxygen isotope values in HMC formed from ACMC may be due to isotopic disequilibrium in the DIC pool during transformation, and mixing effects from multiple episodes of dissolution and reprecipitation during crystallization.